Hα IMPACT POLARIZATION AS A SOLAR AND ASTROPHYSICAL PARTICLE DIAGNOSTIC

by

Lyndsay Fletcher

Thesis
submitted to the
University of Glasgow
for the degree of
Ph.D.

Astronomy and Astrophysics Group,
Department of Physics and Astronomy,
University of Glasgow,
Glasgow G12 8QQ

March 1993

ProQuest LLC.
789 East Eisenhower Parkway
P.O. Box 1346
Ann Arbor, MI 48106 – 1346

To my mother and father
To Rachel and David

Table of Contents

Summary

This thesis is concerned chiefly with the development and application of three different models for the generation of impact polarization in the Hα line, during solar flares. It also includes work on the possible production of impact polarization ion the stellar source SS433. In chapter 1 the observational background to the solar work is described, followed by a general introduction to the current ideas about the solar chromosphere in which the Hα excitation is thought to occur. A summary is also given of the processes involved in solar flares and the various emissions resulting. The atomic physics needed for the calculations in the following chapters is described in the second part of the introductory chapter.

Chapter 2 outlines the methods of calculation of background emission and the general numerical techniques which will be used in future chapters. It then discusses the generation of impact polarization by beams of intermediate energy protons impacting the chromosphere. The main result of this chapter is that the proton beam model is found to put unrealistically large demands on the total energy budget for the flare and, contrary to the conclusions of previous work, is not considered capable of explaining the observations.

Chapter 3 is concerned with the excitation of polarized radiation by high energy electron beams scattering in the collisionally thick chromosphere whilst having their motion affected also by a converging chromospheric magnetic field. It is found, in general to be a successful model, in terms of explaining the polarization magnitude and orientation, and also in accounting for the sporadic appearances of accompanying HXR signatures. Included in this chapter is a discussion of the application of the method of solving Fokker-Planck equations using stochastic simulations.

Chapter 4 moves away from excitation by beams associated with the transfer of energy from the corona to the chromosphere and considers the possibility that the response of the atmosphere to impulsive phase energy input is the generation of fragmented, relatively low energy upflows of ionised material which through their interaction with surrounding neutral material excite impact polarized radiation. This model is successful at explaining the direction, the area and the timescales of the polarization observations, and the polarization fraction generated is, with conservative choices of atmospheric and flow parameters, of the same order of magnitude as that observed.

Chapter 5 moves away from impact polarization as a purely solar particle diagnostic and discusses the generation of impact polarized Hα radiation in the optical bullets of SS433, as a result of the supposed interaction of the bullets with the ionised wind from a stellar companion. Here it is

found that under a wide range of bullet physical conditions, a considerable polarization fraction is to be expected if the wind interaction model is correct.

Chapter 6 is a final short chapter discussing the shortcomings of the work so far carried out in the chromospheric flare investigations, and proposing ways in which it could be extended and improved. In particular it is suggested that the effects of radiative transfer of polarized radiation, and of the magnetic fields in the chromosphere be studied in an attempt to explain temporal and spatial variations in the observed polarization fraction. Comment is made on the extension of the Hα impact polarization diagnostic to other astrophysical sources.

Preface and Acknowledgements

This thesis, which has grown from a passing interest in curious observations of linearly polarized radiation seen in some solar flares, aimed at the outset to thoroughly treat the production of this radiation in the sun, and to find a model for its generation which would complement the present understanding of processes occuring in solar flares. As is usually the case in solar physics it has not been possible to say that the radiation is an unambigious signature of one particular process or one particular beam type, and possibly the major contribution of the work is to further extend the barrage of diagnostics with which we attack the solar flare. But I hope that the interest which I have shown in the subject may encourage others to continue searching for and analysing the polarization, more and more reports of which are appearing, and to continue developing this diagnostic which I think is a particularly useful one, providing as it does information on particle distribution energy *and* geometry.

The original research chapters of this thesis, chapters 2,3,4 and 5 have been published or are expected to be published in letter or paper form in *Astronomy and Astrophysics*. Material from the thesis has been presented at various conferences, seminars and workshops around the world.

Over the course of the three and a half years it took to research and write this thesis my fascination with astrophysics and particularly with the Sun has grown. I personally do not believe that we will ever be able to sit back with our arms folded saying "there, that's the flare problem / dynamo problem / neutrino problem all wrapped up". Instead I anticipate that we will continue to finely dissect the observations and the theory, getting ever closer to the truth, whilst with every new satellite mission the Sun gives us something new to ponder. This is not a pessimistic point of view however, because with something new to look at we will never get bored.

During the research and part of the writing of this thesis I was the holder of an SERC postgraduate research studentship. I am grateful to the SERC of the UK for this award and for other payments allowing me to attend conferences etc. I am also grateful to the DSS for financial assistance almost as generous as that from the SERC.

The work of this thesis was carried out whilst I was a research student in the Astronomy and Astrophysics group, part of the Department of Physics and Astronomy, University of Glasgow, and I am indebted to every group member in one way or another, for making my seven and a half years here enjoyable and productive. I know that this group is one of the most friendly, diverse, innovative and entertaining collections of people to be found anywhere, and I hope that I will

always be welcome in the top floor of whatever building they end up in. My first debt is to my friend and supervisor, Professor John C. Brown who, although not always easy to track down, was always ready to listen to the latest trials and tribulations, to sort out what the science and the problem really was, and convince me that everything wasn't down the pan after all. I have learned much from him, not least of which is never to let a problem die. Thanks to John and his family for many good times. I must thank Dr. Alec MacKinnon with whom I shared an office for two years, for scientific discussions which I can't remember and a general attitude to science which I can. Thanks for taking me up some Munros too. I also shared an office with Dr. Graeme Stewart, who wasn't a doctor then but beat me to it. Thanks go to him for many years of companionship and for revealing to me some of the secrets of electron - positron plasmas. Dr. David Alexander did more than he realises to keep up my confidence all through my time at Glasgow - I thank him for that, and for his willingness to help with the science, the Suns and stupid questions. He is particularly good at stupid questions. Additional scientific input to chapter 4 came from Professor Jan Kuijpers of the Sterrekundig Instituut, Utrecht. I am grateful to him and to the Instituut for their assistance. Many other students and staff of the department, past and present are owed thanks for, amongst other things, providing piano accompaniment and many laughs (Martin), a benchmark for the speed at which a thesis *should* be written (Colin), a benchmark for the speed at which a thesis *shouldn't* be written (Richard), a source of strange noises and irreverential behaviour (Moray), chips, ceilidhs and an ever-cheerful smile (Keith), pub visits, whenever required (Geoff), jokes, stories and polarization (Kenneth), much appreciated female company (Giotta), a fountain of knowledge on the Arts and most operating systems (Andy), some electrifying moments (Jaber), some rather good drunken pictures from Crieff (Steve) and for invaluable assistance with all the computers (Alan). I also want to mention Carolyn, Christine and all the 'theory gang' with whom I spent many enjoyable Friday evenings. Thanks must in addition go to John Simmons for, amongst other things, some very good home made bread, and to Anne and Declan for getting me to the choir on time, and for getting me singing again in the first place. And what thesis in the last few years would be complete without a special thank-you to Daphne for tea and biccies, for a chat and a laugh in the morning, and for keeping me right wherever matters bureaucratic arose.

Outside the department there are several people who deserve special thanks. I graduated over three years ago with Suzie, Siobhan and Elaine and I know that our friendship will have withstood the strains that thesis writing causes. Thanks to Kenneth for more years and more raucous evenings than I care to remember. Thanks to Hazel for the tea and the whisky and the encouragement and dear friendship she has given as a flatmate for the past two years.

The past three and a half years have been made incalculably easier and more enjoyable by the presence (at a distance) of Peter Wheatley, my best friend, my confidant, my punchbag, my shield and my entertainer, who appeared at the very beginning of my thesis and despite unfavourable conditions has made it to the end and beyond. I hope that I have given and can continue to give Pete as much love and support as he has given me.

Finally I want to say thank you to my family, to whom this work is dedicated. I have always had a warm and happy and stimulating environment at home, even in troubled times, and there is no doubt that without the continual encouragement, praise, friendship, food and love from number 41 I could not have attained this peaceful and fulfilled state of being and, less importantly, this thesis.

Chapter 1. Introduction

§1.1 The Solar Chromosphere and Chromospheric flares.

In this section a review is given of the observations of polarized Balmer α (hereafter Hα) emission in chromospheric flares. These are put in context, with a brief outline of chromospheric structure and emission in the quiet and in the flaring sun. Hα thermal emissions in the flare atmosphere, and the general features of chromospheric flares are described.

§1.1.1 The Observations of Polarized Emission from Solar Chromospheric Flares

The chief purpose of this thesis is to attempt to explain observations made over the last 10 years or so of polarized Hα emission in chromospheric flares. (Polarization occurring during solar flares has also been observed in other chromospheric and transition region lines, noteably the UV line of SI at 1437Å (Hénoux et al, 1983), but Hα polarization is better documented. Also, the Hα transition has been the subject of extensive theoretical and experimental studies, meaning that relevant parameters such as excitation cross-sections, transition probabilities etc., are easily available and reliable, and the atomic processes occurring are relatively easy to understand.) The observations and initial modelling work is recorded in a number of papers by Hénoux and co-workers at the Observatoire de Paris, (see Hénoux *et al* 1983a,b; Hénoux 1986, Hénoux 1990, Hénoux *et al* 1990), but independent observations were made recently by Metcalf *et al* (1991) confirming the broad features reported by the Paris group. These main features are;

1) The polarized emission occurs at the time of chromospheric Hα brightening during flares. In the majority of cases it occurs during the rise of soft X-ray emission, but does not have any associated hard X-ray emission (although the Metcalf observation demonstrates a good correlation between the HXR and polarization timings).

2) The area over which polarization is seen is large. The observations of Hénoux *et al* (see Hénoux 1990) show a polarization fraction of $> 2.0\%$ occuring, at the time of maximum emission, over $\sim$ one half of an area of 2×10^{19} cm^2. At other times the fraction is greater than ~ 0.1 of this area.

3) The emission is observed to last for up to 30 minutes.

4) The mean direction of the polarization vector is towards disc centre.

Each of these main features narrows down the set of possible conditions giving rise to the emission. The area and timescales of the observations suggest strongly to us that the process causing the polarization is not directly associated with the primary acceleration mechanism or the associated particle beams, which tend to occur on rapid timescales (a few minutes or less) and over small areas $\sim 10^{17}$ to 10^{18} cm^2 (assuming a thick target electron beam model of flare heating, Canfield et al,1991). It is possible that the polarization occurs as part of the slower response of the atmosphere to the initial energy input. The coindidence in timing with the rise of the soft X-ray further suggests an association with the thermal part of the flare. These facts are of course only part of the story, and modelling to attempt to reproduce the observed polarization features, in the thermal scenario, and in the case of the polarization being caused by the primary beam, will allow us to discriminate on other grounds.

The July 17th 1982 observations by Hénoux *et al* (1990) will now be described in detail. The Hα flare patrol heliograph at Paris observatory, was used to make the observations. This instrument incorporates a rotating half- wave plate polarimeter and a monochromatic Hα filter with 0.75Å bandpass. A complete polarimetric map of the Hα emitting area is made every minute. Two flaring regions were present at the time of the observations, at 11N 38W and 17N 29W. Observation centred on the more westerly flare. A map of this flare observation at polarization maximum has been reproduced here (fig 1.1) from Hénoux (1990) showing the presence of linear polarization spatially concurrent with Hα bright patches in active regions. This covers an area of approximately 2 x 10^{19} cm ^{2} in a matrix of 90 by 90 pixels, one pixel being one arc second. The polarization fraction exceeds 2% in a significant fraction of the observed area, over a period of some 35 minutes. Although it is not possible to follow the variation of degree of the polarization with high spatial resolution, it is possible to view the change in the relative numbers of pixels with polarization greater than the 2% level, on timescales of a minute - this shows large variation - going from 0.1 to 0.5 of all pixels in one minute (fig 1.2) The rise of the mean level of polarized emission from this region appears to coincide with the rise of the total Hα emission level, although the pixels of polarized emission extend beyond the Hα bright patches. In the brightest Hα patches, the net direction of the polarization vector is consistently towards the centre of the solar disc. Figs 1.3a,b show the azimuthal distribution of the time integrated polarization directions in both the eastern and the western flare, whose disc-centre directions are respectively $14° \pm 2$ and $28° \pm 3$. The azimuthal distributions of the polarizations show strong peaks at, respectively, $20° \pm 5$ and $35° \pm 5$. A comparison is also made of the distribution of one-minute integrated emission vector direction before and after the maximum (figs 1.4), showing a more pronounced peak before maximum than after. Possible interpretations of this and of the observed wide deviations from the disc centre direction will be discussed in future sections.

As mentioned before, the other sets of observations, by the Paris group and by Metcalf *et al*, confirm the timescale and direction of the polarization as outlined above, but when attempting to model the polarization production process we use the large area flare observed by Hénoux.

We now present a review of the structure, emission and flaring behaviour of the solar chromosphere, in which the Hα line is formed, going on in the second half of this chapter to consider the atomic processes leading to the generation of polarization.

§1.1.2 Chromospheric Structure and Emission

Firstly we will consider briefly the structure of the 'quiet sun', i.e. those regions of the solar atmosphere whose activity is not dominated by a strong magnetic field. These are considerably less complicated than magnetic regions. But even for a section of the chromosphere not magnetically dominated (i.e. not part of the flaring or 'active sun') it is difficult to stratify the atmosphere and give a unique temperature or density with depth dependence. This is because, especially high up in the chromosphere, the matter is irregularly distributed in the chromospheric fine structure; spicules, the chromospheric network (a threading of dark lines visible in the Hα line centre, defining the supergranulation structure in the underlying high photosphere), fibrils, mottles etc. For this reason, Vernazza, Avrett and Loeser (VAL) (1981) have developed a number of chromospheric models for the various features visible in the solar chromosphere. However, we describe here only the 'average' quiet sun chromosphere - the region in the centre of the magnetic field interior where the field strength is at a minimum (as classified in VAL) before going on to the situation in a chromospheric region undergoing flaring activity.

In this work we follow Athay (1985) in defining the chromosphere as that portion of the solar atmosphere lying between temperature minimum and T = 25000K, in which the temperature gradient is negative (i.e. the temperature increases outwards). This region can be split into two, the lower and upper chromosphere. Referring to the standard semi-empirical quiet-sun chromosphere of Vernazza, Avrett and Loeser (see fig 1.5) the lower chromosphere lies between temperature minimum and the first plateau in temperature at about 6000K. In this region flux tubes anchored in the photosphere are well constrained by gas pressure and the larger part of the material present is free from magnetic fields. (The low non-magnetic chromosphere - the material collected within the flux tubes constitutes the low magnetic chromosphere.) However, moving upwards in the chromosphere, as the temperature rises, the density and pressure of the atmosphere rapidly decrease and the flux tubes, no longer constrained by gas pressure, expand. The whole region is then magnetically dominated. This part is termed the 'upper chromosphere' and it is processes occuring

here which are to be studied in this thesis. It will therefore be necessary to pay attention to the effects of the chromospheric magnetic field at all times.

The main feature of radiation from the chromosphere as that it is dominated by absorption and emission spectrum lines. Observations of the sun at eclipse show most obviously the splendours of the tenuous corona, but during the last few seconds before totality and the first few seconds thereafter, a bright red sliver of chromosphere is visible - the colour revealing strong emission in Hα . The calcium K line at 3933Å - indicative of a temperature in the region of 6000K, is also strong (observed in non-limb emission) Other lines from highly ionised states of magnesium, carbon and potassium reveal regions with temperatures of the order 10000K, although the intensity of this emission suggests that the volume of high temperature material is relatively small. The high photosphere/low temperature chromosphere can be traced by molecular emissions - from the CN molecule for example, as well as rare earth elements and neutral metals. The reason that such a number of distinct spectral lines can be observed is that the entire chromosphere is effectively optically thin to all spectral lines, except the Lyman series, and all photons generated in this region (through collisional excitation by thermal electrons) escape - having suffered only slight wavelength shifts into the line wings. There is also a component of chromospheric radiation that is actually scattered photospheric radiation - it is difficult to separate this from the locally generated radiation - thus it can be difficult to work out chromospheric emission properties. However, some EUV lines (eg, Ca IV at 1549Å) cannot be formed by scattering of photospheric radiation and unambiguously trace chromospheric emission.

The chromospheric spectrum is complex, reflecting a complex structure. The theory of radiative transfer in non-LTE atmospheres must be applied if an adequate description of the chromosphere is to be found. For a detailed discussion on this difficult subject, Mihalas's text on Stellar Atmospheres is excellent (Mihalas 1978), and much of what follows has been learned from this, and a number of other sources (Durrant (1988), Thomas and Athay (1961), Sturrock(1986)).

A Brief description of the Current Chromospheric Model.

Even the low non-magnetic chromosphere is difficult to describe. The radiative equilibrium LTE model (i.e., all energy transported by radiation), together with hydrostatic equilibrium, which adequately describe the temperature and pressure run of the radiative photosphere, fall at the first hurdle in the chromosphere - the presence of a temperature minimum. In a non-grey (frequency dependent continuum opacity) plane-stratified atmosphere in LTE the temperature is expected to be a monotonically decreasing function of distance outward, a series of slow plateaus interrupted by

narrow regions of sharp temperature decreases where the particular dominant (eg, hydrogen line) transition becomes optically thin, and radiates energy from that region. According to the semi – empirical VAL model, and other standard reference models such as the Harvard Smithsonian reference atmosphere, the behavior of the outer layers of the sun is quite different (see fig 1.5). The VAL model temperature structure passes through a minimum at a value of 4300K, just above the photosphere. A detailed theoretical model by Athay (1970) places the temperature minimum at 4330K also. From here the temperature climbs outwards, and it is necessary thermodynamically to have non - radiative energy deposited locally to sustain the increase. The temperature structure is then defined by the balance between chromospheric energy input and radiative cooling. Briefly, the favoured heating mechanism is dissipation of acoustic and magneto - acoustic waves generated by turbulent convective motions in the photosphere, and propagated upwards along the magnetic field. The magnetic field strength appears to be important in the heating efficiency - the correlation between local field strength and enhanced chromospheric brightness is good. In the quiet cell interiors the heating appears to be by short period (< 1 min) acoustic waves, while in the bright cell boundaries, longer period (3 min) waves are visible, in CaII and in Hα lines. Both analytical and numerical treatments of the generation and propagation of these waves give the result that wave power is concentrated in frequencies in agreement with those observed in the various parts of the chromospheric structure, which strongly supports the wave – heating hypothesis.

Chromospheric cooling is by line losses. The major sources of radiative loss in the low and middle chromosphere are hydrogen and helium lines - these being the most abundant elements. Higher up in the chromosphere and transition region, other partially ionised trace elements play a major role in radiative cooling. The initial temperature rise is moderated by continuum emission from the H^- ion, which is formed by a neutral hydrogen atom gaining a free electron (liberated from one of the metallic elements, which are ionised to some degree at the top of the photosphere). This emission is a slowly varying function of temperature. The temperature climbs fairly rapidly until the cross section for capture of a free electron has decreased. At this point, emission from the lower lines of neutral hydrogen starts to dominate. However here the temperature is high enough for hydrogen to start ionising and this process provides an energy sink, keeping the temperature almost constant at 7000K for 1000 kilometers. When the hydrogen is almost completely ionised, it no can longer cool efficiently and the temperature rises rapidly. A second narrow temperature plateau occurs where the chromosphere becomes optically thin to Lyman α emission - being the most common transition this has supply for Lymanα emission comes directly from the non-radiative sources described above, the second plateau should extend further, since the hot corona indicates that the non-radiative heating sources are still operating around these heights. It has been suggested that the non-radiative energy is first dissipated in the overlying layers and then conducted downwards

to power the Lymanα flux. In this case coronal conditions limit the amount of cooling and the width of the plateau. It is evident that conductive processes also have to be considered. At high altitudes, emissions from Carbon, Nitrogen, Oxygen, Neon, Magnesium and Silicon dominate at temperatures of greater than 10^5 K. The temperature continues to rise through the transition region and into the corona.

§1.1.3 The Semi - Empirical Flare Chromosphere

We refer above to 'semi-empirical' chromospheric models, and it is these which we use as our references for atmospheric parameters in the calculations which follow. Like the quiet chromosphere, the flare chromosphere has been modelled semi-empirically (Machado *et al* (1980), hereafter MAVN). Briefly, a semi-empirical model is one in which a temperature structure is calculated, by trial and error, which yields the best possible overall fit to the strength and shape of a number of important spectral lines. The equations of hydrostatic equilibrium, of statistical balance and non – LTE radiative transfer are then solved self consistently over the emitting region to yield density distributions of protons, electrons and of atomic particles in various level of excitation. This is a complicated nonlinear procedure involving the calculation of absorption and emission coefficients, ionisation levels, radiative fluxes etc. throughout the atmosphere and ensuring that the relevent equations are satisfied globally and locally. These model atmospheres have the decided benefit of fitting well the observations without having to make ad hoc assumptions as often happens in theoretical modelling. This makes them more reassuring to use, but they are limited in various ways. Firstly, there are gaps in the present understanding of the necessary atomic physics - for example, the theory of redistribution of photons within the spectral lines, which is a problem when trying to calculate the exact line shapes. Secondly, there is no guarantee that the temperature solution found for a particular set of lines is unique for those lines, particulary if the number is limited. This can be helped by choosing lines which cover a wide range in temperature. Thirdly, there is no guarantee that important physical laws, including energy conservation are satisfied throughout the atmosphere! Fourthly, the models so far developed are single component models - a pure hydrogen model is assumed when calculating densities, optical depths etc. Also, any given model, developed to explain the average of a few observations, may not have any generality. We use the semi-empirical models because of their observational input, and because for flare atmospheres no others with sufficient structural detail are available. Nonetheless, as we use them we are aware of their limitations.

Overall in the energised chromosphere we expect to see higher temperatures and pressures than in the quiet chromosphere. Changes in temperature mean of course that atomic processes which are

significant to chromospheric structure and energy balance, like hydrogen ionisation, will happen at different heights. For example, the feature that we see immediately on comparing the semi - empirical models for quiet and flaring chromosphere, is the presence of a deeper and hotter temperature minimum in the flaring chromosphere.

Table 1.1

model	**temperature(K)**	**height(km)**
Quiet Sun	4300K	500
Flare F1	4820K	350
Flare F2	4960K	275

n.b. all heights are quoted with respect to the position in the atmosphere at which the optical depth = 1 at λ of 5000Å . This position is referred to as $\tau_{5000} = 1$, and is the standard position of the top of the photosphere.

The average particle densities increase by approximately an order of magnitude over the quiet sun values. The changes in density and temperature means that emission in certain spectral lines is enhanced, and the line shapes are also changed. The Hα line profile can go from line centre absorption of up to 80% in the quiet sun to emission at 2 to 3 times the continuum in the flaring sun, as a result of changes in optical depth and scattering. The line is also broadened - this is interpreted as being due to Stark broadening in the line wings, and in the line centre as due possibly to macroturbulence in the higher temperature part of the chromosphere.

§1.1.4 Hα Emissions in the Flare Chromosphere

The Hα emission of the thermal chromospheric plasma (henceforth 'the background') comes primarily from collisional excitation of ambient neutral hydrogen atoms to level 3 by free electrons – followed by downwards transitions occuring spontaneously. In addition, upper states may also be populated following recombination of free electrons onto protons. The ratio of the two populating processes is given by

$$\frac{\mathcal{R}_{rec}}{\mathcal{R}_{ex}} = \frac{n_e n_p \alpha_{rec}}{n_e n_1 C_{1\rightarrow 3}} \qquad 1.1$$

α_{rec}, the recombination coefficient, is given by

$$\alpha_{rec} = 3.262 \times 10^{-6} e^{\frac{\chi}{kT}} n^{-3} T^{-3/2} E_i(\frac{\chi}{kT}) \qquad 1.2$$

where $E_i(\chi \backslash kT)$ is the exponential integral function. n is the principal quantum number of the level to which recombination occurs and χ is the excitation potential of that number. $C_{1\rightarrow 3}$ is the

thermal excitation coefficient of the 1 to 3 transition. It is given by

$$C_{1\rightarrow 3} = \int_{\chi}^{\infty} v\sigma_{1\rightarrow 3} f(v) dv \qquad 1.3$$

the product of the electron Maxwellian, the number density of atoms in the lower level of excitation and the excitation cross section. The Maxwellian is given by

$$f(v) = \frac{4}{\sqrt{\pi}} \left(\frac{m_e}{2kT}\right)^{\frac{3}{2}} v^2 e^{\frac{-mv^2}{2kT}} \qquad 1.4$$

The emission from both of these processes as a function of position in the chromosphere is shown in figs (1.6a,b) for the models F1 and F2. In the dense low chromosphere recombination dominates, but falls off rapidly as collisional excitation takes over when the temperature rises. Beyond the transition region and corona, there is little collisional excitation since the hydrogen is practically all ionised, and population of level 3 by recombination dominates. However, at T = 10^6K, the total number of recombinations to level 3 is $\sim 6 \times 10^4$ cm^{-3} s^{-1} which is negligibly small compared to the rate of excitation in the lower temperature regions. De-excitations from level 3 occur spontaneously - we can see this by comparing the timescales for collisional and for spontaneous de - excitations in the chromospheric material. the timescale for collisional de-excitations is the mean-free path between de-exciting collisions divided by the mean velocity of the electrons;

$$\tau_{coll} \sim \frac{l_{coll}}{v_{th}} \sim (n_e \sigma_{3\rightarrow 2} v_{th})^{-1}$$

The spontaneous de – excitation timescale is

$$\tau_s = [A_{3\rightarrow 2}]^{-1} \qquad 1.6$$

Putting in values of chromospheric temperature $\sim$ 10000K, electron number density,$\sim 10^{11}$cm s^{-1} and the collisional de - excitation cross section at the thermal velocity give $\tau_{coll} \sim 5.7 \times 10^{-4}$ s, whereas $\tau_s \sim 2.28 \times 10^{-8}$ s.

It is apparent from looking at the density variation in the MAVN model atmosphere that the neutral hydrogen number density decreases rapidly outwards, but that temperature is increasing in the same direction. The velocity - integrated Maxwellian distribution function is a monotonically increasing function of temperature - therefore there is a maximum in thermal Hα emission at the best trade - off position between the rising Maxwellian and the falling neutral hydrogen number density. This maximum Hα emission rate, from the simple methods used here, occurs in F1 at 1429.5km, and in F2 at 1102.5km. However the net emission rate depends in addition on the opacity of the atmospheric material. MAVN, who take into account the optical transfer in the line, state that the Hα line centre is formed at about 1428km in F1 and at about 1090km in

F2. In our calculations we will assume that the atmosphere is completely optically thin above a certain level and completely optically thick below. Plots of the calculated line-centre optical depth, viewing in the local vertical direction (figures 1.7a,b) show that in the region of strong emission the chromosphere is rapidly changing from being optically thin to thick, and for this reason the effect of moving the 'optical boundary' by small amounts will be investigated.

§1.1.5 The Hα Flare Event. Morphology and Emissions

Hα flares had long been observed optically before x-ray instruments were available to detect the high energy emissions also present in the active flaring sun. Hα flares are observed as a brightening in the chromosphere, and are morphologically classified broadly as 'compact' or 'two–ribbon'. Two-ribbon flares are associated with an erupting solar prominence, and occur in two lines mapping the opposite polarity footpoints of loops in a magnetic 'arcade' aligned with the prominence. The other type of flare, the compact flare, is associated with single or small groups of small flaring loops, and is generally insufficiently resolved for identification of footpoints. The triggering of both types of flare seems to be similar - being due to reconfiguration of the coronal magnetic field. It is not always clear to which class any one flare belongs, since the magnetic topology may be convoluted or unresolved in that no clear pattern of footpoints emerges. The flare of July 17th covered a large area in Hα and from figure 1.1 appears to have a fairly complex shape, but it is not clear whether it was a compact or two ribbon type.

Hα emission maps both the impulsive and the gradual phases of the flare, with the impulsive phase being characterised by strong broadening of the Hα line, which then decays as the atmosphere returns to its pre-flare state. The impulsive phase processes have been modelled by Canfield and Gayley (1987), who, on the basis of 3 timescales involved, have identified this emission with impulsive electron beam bombardment of the chromosphere, ionization response of the chromosphere and, on the longest timescale (>10s) with hydrodynamic response, i.e. large scale motion of the heated chromosphere. The gradual phase has been studied by, amongst others, Acton *et al* (1982) and Antonucci *et al* (1990) who conclude that the Hα line profile is indicative of a heated chromosphere, moving hydrodynamically in response to energy injection in the impulsive phase. The distinction between these two phases and different physical behaviours will be important later in this thesis, in helping to pinpoint the source of observed Hα line polarization.

The presence of linearly polarized Hα emission in solar flares was first reported by Hénoux and Semel (1981) and Henoux *et al* (1983), and was interpreted by them as the first observation of impact polarization in an astrophysical object. It cannot immediately be attributed to the impact

excitation process – other sources of linear polarization must first be ruled out. The Stark and Zeeman effect are the prime candidates. Stark polarization, occuring when a strong electric field splits energy levels, has been ruled out on grounds of calculations of the expected magnitude of the effect which turns out to be far lower than that observed. If the electric field is just that of the ambient electrons and ions, the expected polarization turns out to be less than 0.5% rather than the 2-3% observed (Hénoux and Semel, 1981). Were the polarization due to the Zeeman effect - the splitting and ordering of upper states by a strong magnetic field, then we would expect it to be observed whilst any magnetic field in the active region is present, rather than being correlated so well with the Hα brightening. Overall, impact polarization by anisotropic particle distributions such as beams looks like the most favourable candidate.

§1.1.6 The Flare as Observed at Other Wavelengths.

It will be useful here to outline the signatures of solar flares at wavelengths other than optical, since these give a picture of what is happening in parts of the flare other than the chromosphere. Whatever models we arrive at for the Hα production mechanism can then be compared with what is already inferred from these various signatures. We will see also that there is a certain amount of argument over the interpretation of flare emissions, and indicate how the observations of impact polarization may be of help in setling the questions. Figure 1.8 is a summary of emissions at several wavelengths as a function of time.

We begin at the low energy end of the electromagnetic spectrum, with radio waves. These have been observed since the early 1940's, but were not spectrally resolved until the 1950's, with the advent of the radio spectrograph, nor spatially resolved until the late 60's when the radio heliograph started to resolve metric wavelengths. Later, use of the large arrays of radio telescopes and aperture synthesis techniques, opened the centimetric wavelengths to spatial scrutiny. Radio emission occurs in 'bursts', which can be classed into five distinct types.

Type I *noise storms*, are in the frequency range 40 - 400 Mhz, have a duration of hours or days, and occur in the atmosphere above active regions. These are not generally flare associated. Superimposed on these emissions are type I *bursts* which are narrower in bandwidth

Type II bursts are observed to start near the impulsive phase of the flare. They consist of two slowly drifting bands of emission at the fundamental and first harmonic of the local plasma frequency. They are associated with collisionless MHD shocks moving upwards through the corona.

Type III bursts, or fast drift bursts, can happen during the flare impulsive phase, and appear also as lower frequency storms in the wake of the flare, which drift rapidly downwards in frequency. The widely accepted view is that they are generated by streams of electrons propagating outwards

into the corona, presumably excited by the flare. The emission is from electron plasma (Langmuir) waves, generated by electron streams with energies of $\leq$ 25keV. The observed rapid drift downwards in frequency is thought to be a consequence of the decrease in density of the excited plasma as one moves further out into the corona.

Type IV bursts are continuum radiation which normally occur after type II bursts in flares. Continuum metric and decimetric radiation is observed to be stationary but a component of the metric radiation at 10^3 to 10^4 kHz moves through the corona, often associated with the ejection of coronal material -either in the form of a moving shock front, an expanding magnetic arch, or an ejected plasmoid. Each shows a different time profile. The emission may be accounted for by plasma emission and also by gyrosynchrotron emission - electromagnetic radiation generated as electrons spiral in magnetic fields.

Type V bursts are continuum components often associated with type III's

So flare associated solar radio emission appears to indicate the presence of high energy electrons moving into the upper solar atmosphere, during the impulsive phase and for several hours or even days thereafter. Motion is in the form of streams, and also bulk motions in the case of type IV's. Closely associated with radio type IV's, and also indicating the presence of energetic electrons are microwave bursts. These lie in the region of the e-m spectrum extending from 10s of GHz to 100s of MHz, and may be caused by plasma emission, by gyrosynchrotron emission, by thermal Bremsstrahlung or possibly by masering action. There is no apparent spectral structure. The bursts can be classified as impulsive and also microwave type IV's, and gradual bursts. Impulsive bursts, which are of interest here track hard X-ray bursts but lag by $\sim$ 1s. When observed with 100 millisecond time resolution the time profile of the microwave emission appears to be a 'smeared-out'version of the noisy hard X-ray time profile, which suggests that the HXR and microwave emissions are from related particle populations. Interpretation of the emissions in terms of gyrosynchrotron radiation leads to a value of electron energy of $\geq$ 100keV, and the site of the emission during the impulsive phase appears to be at the top of the coronal loop at whose footpoints HXR and Hα emission is observed to be polarized.

The optical UV, and EUV flare radiation comes from the energised chromosphere and transition region, and is interesting in helping to interpret the gradual or thermal phase of the flare. From numerous atomic lines, e.g., the Balmer lines of Hydrogen, HeI, CaII H and K lines, MgII and Na D, formed either by recombination or by excitation, it is possible to deduce the temperature structure and particle density of the heated atmosphere. Also, by observing the time sequence of maximum brightening of a variety of lines it is possible to follow the increase in temperature throughout the atmosphere as a function of time. Assuming that the brightening was due to the

conductive flow of energy, by this method, Lemaire *et al* obtained conductive timescales of 10's of seconds.

An additional optical event which does exhibit an impulsive component is the white light flare (WLF) emitting a flat spectrum from $\lambda = 6000$Å to 4000Å , but increasing in intensity by a factor of 2 - 3 at shorter wavelengths. WLF's occur only when the HXR emission exceeds a certain value, and show an impulsive and a gradual phase tracking radio and HXR emission. The favoured mechanism for their production is the heating of the lower chromosphere and upper photosphere - by particle beams, by EUV or soft X-ray irradiation, or by dissipation of Alfvèn waves or small scale currents. The beam heating model gives constraints on the beam - flux necessary to heat these deep layers. If the source of the heating were electron beams they would require an energy flux of 10^{12} to 10^{14} ergs cm^{-2} s^{-1} which is considered too large for reasonable flare energy budgets. Proton beams would require 10^{10} ergs $cm^{-2}s^{-1}$ in protons above 6 MeV which is more acceptable. Further comment will be made on this in a later discussion on proton versus electron beam flare models.

Soft X-ray emission, with wavelength 1 to 8Å is observed in line and continuum. This radiation indicates the presence of a thermal plasma at temperatures 1 - 2 x 10^6K. Dominating the line emission are lines from highly ionised states of Calcium and Iron. Methods exist (see, eg, Gabriel 1972) for using line intensities as diagnostics of temperature and density of the emitting plasma, but important also is their use in studying the large scale dynamics of the flare - heated atmosphere. Line widths and line shifts may posible give information on turbulent velocities and bulk velocities of plamsa components respectively (eg Antonucci *et al* 1984) although it has also been pointed out (Emslie and Alexander 1987) that broadening is a natural consequence of differential line-of-sight velocities of the plasma over the entire emitting region, and that line asymmetries, instead of being fitted by one or two plasma components travelling at discrete velocities, is more easily explained by a multithermal plasma with a continuous velocity distribution. These latter interpretations are important in that they are consistent with the behaviour of a thick-target electron-heated atmosphere.

Hard X-ray emission, with photon energies between 10 and 100keV, is recognised as the onset of the flare, and was first observed in balloon-borne observations in 1959 (Peterson and Winkler). Satellite observations followed, amongst them the imaging and burst spectrometers on board the SMM satellite, and most recently soft and hard X-ray imaging instruments on board the Japanese Yohkoh satellite, launched in 1991. Impulsive HXR flares are most frequently observed, and are especially important in the global picture, since they map the processes by which it is expected the majority of the flare energy is released and transported. They have long been interpreted as

bremsstrahlung emission from nonthermal 10-100keV electrons in a thick target (Brown 1971, Lin and Hudson 1971). The time development is spiky on a timescale of 5 to 10 seconds and the whole emission lasts for a period of a few minutes. HXR spectra are most often fitted by one or more power-law forms - i.e. $I(\epsilon) = I_o \epsilon^{-\gamma}$ with γ typically taking values between 3 and 8. Assuming the spectrum to be formed by thick target bremsstrahlung allows estimation of the total power contained in beam electrons - this turns out to be energetically demanding of the system, since the emission process is highly inefficient - of the order of 10^{-5} of the total beam energy is converted to HXR's. For this reason an alternative model has been proposed whereby the radiation is produced by a confined population of hot electrons. This is energetically less demanding than the beam model in terms of its HXR bremsstrahlung production, which occurs with a higher efficiency.

The thick target model predicts that the vast majority of Bremsstrahlung emission generated by an unimpeded, largely unscattered beam will be produced in the low corona/transition region and will appear on the solar disc as distinct loop footpoints. In some flares such footpoints are observed, but these also show considerable coronal components (MacKinnon, 1985) and many observations show only the coronal components (eg Tsuneta *et al* 1984). This suggests that the coronal loop column depth encountered by the electron is greater than or comparable to that encountered in the transition region, or possibly that part of the electron population is somehow confined in the corona, for example by a magnetic bottle. (See future discussion on the "trap-plus-precipitation" model. Occasionally extended bursts of HXR emission are also observed (eg Vilmer *et al* 1982) which can also be successfully explained by this model.

Finally γ – rays are the highest energy radiative signatures observed from the sun, occuring in line and continuum, and signifying the presence of particles of several MeV/nucleon, involved in nuclear excitation processes. The strongest observed line is at 2.223 MeV and is emitted following the capture of neutrons onto protons. This is a delayed line, as opposed to a prompt line, since a time lapse of up to 100 seconds arises between the production of the neutron involved in the capture process and the emission of the photon. The delay is because the neutron (produced in the disintegration of ^{4}He and other nuclei) must be slowed by collisions before the capture cross-section is large. Similarly, the 511kev line from positron-electron anihilation requires the positron formed in a previous nuclear reaction to slow down sufficiently for the reaction to take place. Prompt lines are, for example, nuclear de-excitation lines, in which a nucleus excited by collision with an energetic particle decays with emission of a photon - there is no time lapse, save the lifetime of the excited state, between the initial excitation and the γ – ray emission. γ – ray bursts are impulsive phase phenomena and prompt line emission occurs within a second or so of the HXR burst, indicating that the same mechanism accelerates particles for both processes. Since the energy of particles

involved is so large they are able to traverse the corona and chromosphere and consequently γ - ray emission comes from the low chromosphere and high photosphere. Detailed modelling of γ - ray spectra is summarised by Ramaty and Murphy (1987) who have had considerable success with their methods.

§1.1.7 Models of the Flare Process - an Overview.

The processes leading to the visible signatures of a solar flare are still a matter of fierce debate, despite having been studied for many years. This possibly indicates the complexity of the subject - a testing ground for kinetic plasma physics, MHD, atomic physics, and more. The number and diversity of observations testify to the many ways in which the flare is 'diagnosed'. Various diagnostics allow limits to be placed on particle populations, with different emissions belying the presence of various energies of particles. There is some concensus of opinion, which extends as far as saying that the flare energy comes from the coronal magnetic field, as this is the only energy reservoir large enough to power the emissions seem from a typical flare. There is certainly enough energy up there, but its conversion on short timescales requires particular conditions. Magnetic structures in the corona are large and their MHD evolution is slow, whereas coherent particle emissions occur on timescales of less than a second. This has led to the idea that particles are accelerated in highly localised regions where the field is reconnecting, having been forced into an energetically unfavourable configuration. In the case of the compact flare the widely accepted model is the emerging flux model of Heyvaerts *et al* (1977), in which new flux breaking from the photospheric surface rises rapidly in the force free region and encounters existing flux above. Magnetic reconnection occurs at the interface as shown in fig (1.9). The two ribbon flare proceeds by a different mechanism. Here an existing arcade structure is subject to shear or compression forces as the arcade footpoints, frozen into the photosphere, follow the turbulent photospheric velocity. When some critical amount of shear or twist is reached , the arcade becomes unstable and material erupts outwards, followed by reconnection of the field below the erupting filament (see fig 1.10) Having associated reconnection and acceleration there are two big questions. 1) By what physical mechanism do particles in the reconnection region gain energy from the reconnecting field and 2) How are the particles transported from this region to the lower atmosphere where they give rise to radiative signatures? The first question has been tackled in a number of ways which can only be outlined here. The article by Heyvaerts (1981) provides an excellent summary. There are a few basic mechanisms possible. Most directly connected to the process of magnetic reconnection in a shearing magnetic field (tearing mode instability) is the generation of induced electric fields parallel to the magnetic fields which accelerate particles in a small volume. This small volume is a problem since a large number of particles is accelerated. There must therefore be other mechanisms

which amplify the initial acceleration. The first of these is wave - particle interaction, in which particles gain energy through resonances with plasma waves generated in the acceleration region (eg,Cerenkov or Cyclotron resonances). Coupling of particles to waves occurs most strongly when the resonance condition $\omega = \underline{k}.\underline{v}$ is satisfied - ω being the wave frequency, $\underline{k}$ its wave - number and $\underline{v}$ the particle velocity. The wave spectrum may be turbulent in form , and may either be generated by the fluctuating electric field in the acceleration region, or by a particle beam. The former is a case of strong turbulence - the field fluctuations generate an electric pressure or 'ponderomotive' force, which accelerates charged particles away from the turbulent region. Turbulence generated by an existing particle beam is obviously not the initial acceleration mechanism, but may aid in the triggering of further magnetic energy transfer to ambient particles. Electrostatic double layers are another possibility for acceleration. These are regions of charge seperation, across which a large potential drop develops. The mechanism of formation is still somewhat of a mystery, although they have been observed in laboratory plasmas (Volwerk, 1992). If the thermal energy of particles on either side of the double layer is much less than the potential drop, then the particles will be accelerated across the drop. Another plasma discontinuity - or rather a group of - hydrodynamic shock fronts may provide a source of acceleration. Particles reflecting from such shocks gain energy from them, and the Fermi mechanism - whereby a series of such reflections increases the momentum of the reflecting particle, is capable of efficient acceleration to high energies.(The Fermi mechanism can also operate under reflection from plasma waves.) Shock fronts are also subject to MHD instabilities, generating waves which can resonate with particles.

The second point, particle transport, is of more interest here - specifically we would like to know whether for example, the particles are in the form of a highly non - thermal beam, a conduction front or some other distribution, and whether the energy is carried predominantly by electrons, by protons or by a mixture of both. A lot of effort has gone into deciphering the radiative emissions in an effort to answer these questions and also possibly to find out something about the medium which is being heated. If these facts can be deduced it may be possible to use them to place constraints on the primary acceleration mechanism.

Proton or Electron Beams - Evidence for Rival Models

The most popular and enduring interpretation of the various radiations is that they are due to a beam of high energy electrons from the corona, although proton beams and neutral beams have also been mooted. The arguments seem to centre over the production of HXR impulsive bursts (see Brown *et al* 1990, Haisch, Strong and Rodono 1991), although other frequency bands may be important here also - e.g., WLF and γ - ray emissions. Below the main points of the e^-/p^+ debate

are summarised.

The electron beam model invokes a non - thermal flux of electrons, accelerated near the top of a coronal loop, with a distribution of energies above some rather arbitrary cut - off value, normally around 20 keV, injected over an area of less than about 10^{19} cm^2 (Hoyng *et al* 1976). The HXR emission is e^- - p^+ Bremsstrahlung, and heating of the low corona, transition region and chromosphere is due to collisional energy loss of the electrons on the target particles. Heating produces the flare thermal or gradual phase.
The p^+ model takes two forms – high energy and low energy. The high energy version (eg, Emslie and Brown 1985, Heristchi 1986) involves a beam of protons of energy greater than about 40 MeV which produce HXR's through p^+ - e^- Bremsstrahlung. Alternatively, a beam of protons of 0.1 to 10 MeV is postulated (Simnett and Strong 1984), although the means by which this could produce HXR emission is not clear - the production of a thermally emitting plasma at loop footpoints seems most plausible.

Both models have problems, observational and theoretical. The thick - target electron beam model makes some very specific predictions about the site and directivities of HXR production, and the associated emissions in microwaves and type III radio bursts. These, while not being completely refuted by present observations, are consistent only for particular target conditions, which of course must agree with independent determinations. γ - ray emission seen with some HXR bursts lead to the possibility that in some flares a large part of the energy is carried by proton or ion beams - the occurence of white light flares suggests this also. With the proton beam model there are there problems with reconciling the expected and observed sites of HXR production and also with the size of the individual proton energies involved. HXR emission is observed up to 20MeV which would require 40 GeV proton energies. In addition, if the same proton beam produced the HXR and the γ - ray flux the beam flux necessary for the HXR observations, assuming the thick target model, would lead to a γ - ray flux in one case three orders of magnitude larger than that observed (Emslie and Brown 1985). On balance the thick target proton beam seems to fare no better, on observational grounds, than the thick target electron beam.

Both models are subject, to a greater or lesser degree, to the same theoretical problems. The need to find a rapid and efficient acceleration mechanism is pressing, and the electrodynamic conditions of charged beam propagation in terms of ambient plasma response is not well understood. Both models are evidently problematic and certain of the outstanding questions may possibly be answered by alternatives; for example, a neutral beam model, or the trap plus precipitation model, which will be discussed in Chapter 3.

§1.1.8 Motivation for studying Impact Polarization in Chromospheric Flares.

It would be rewarding to have an observation capable of discriminating unambiguously between the various scenarios, and doubly rewarding if Hα line polarization was that observation. Unfortunately, the diagnostics outlined above are all alike in that they indicate that radiative signatures are as dependent on 'target' conditions as they are on the parameters of the energy source for the emission, and Hα polarized lines are certainly no exception. However, these Hα polarization observations certainly have a useful contribution to make. In particular, because the energy at which the cross section for the process maximises is rather low, there is the exciting possibility that they can be used to trace low - energy protons - observation of the only other proposed diagnostic - the emission of Doppler shifted Lyman α photons (MacKinnon, 1989) has not yet been attempted. The presence of low energy protons in the chromosphere may lend weight to the neutral beam model or the low energy proton beam model of flares, but it is hard to see how high energy protons could be sufficiently collisionally degraded to give rise to the Hα observations. It is possible in addition to investigate not only energy but also the angular distribution of particle populations which exist during flares, since, as we shall later see the orientation of the polarization vector depends partly on this. For example the "trap - plus - precipitation model" is one case in which the distribution is not purely beam -like but in different parts of the trap will be peaked at different angles to the field. This model appears to be a hopeful way of adapting the generally accepted thick target electron beam model so that it better fits the observational evidence, and merits attention for this reason. In the forthcoming chapters attempts will be made to interpret the polarization observations in the context of various flare models and we hope, despite the uncertainties imposed by our lack of knowledge of the target conditions, to be able to pinpoint the most likely scenario giving rise to its production.

§1.2 Atomic Physics Background

In this section the atomic processes underlying the production of polarized impact radiation will be described. The complex quantum mechanical formulation of the problem will not be treated. Instead an approach based on ideas of excitation cross sections and transition probabilities is used. General theoretical results are then particularised to the case of the Hα transition, and a comparison between theoretical and experimental results is made.(A detailed treatment of atomic excitations is to be found in Mott and Massey, 1965, and the standard reference for excitation of polarized radiation is Percival and Seaton 1959. Results from these works are summarised in what follows.

§1.2.1 Introduction

The production and polarization of impact radiation has been studied, theoretically and experimentally, by many of the famous names of physics, among them Oppenheimer, Penney, Mott and Bethe, and has provided a testing ground for the many and varied theoretical models of atomic interactions. As an experimental atomic physics topic it is also a most fruitful field of study, providing insight into the processes occuring during the collision of two atomic particles. For example,the polarized radiation emitted following the impact of a beam of electrons on an atomic target depends on the the relative populations of angular momentum substates excited, and consequently the cross sections for excitation of these substates. Optical emission from the substates is not easily resolved, the energy splitting being small, but the deconvolution of the polarization fraction can, theoretically, lead to reliable cross-section values (McConkey, 1988). Unfortunately, the polarization observations at this time are not of sufficient accuracy to use in what is essentially an inversion problem. However, it is expected that in the near future suitable measurements can be made.

Another experimental area in which impact polarization is now proving useful is in the study of one of the simplest collisions - that between a proton and a neutral hydrogen atom at low velocity - that is, velocity less than the orbital velocity of the atomic electron. At these velocities the pair of interacting particles pass through quasi-molecular states. The coupling of the molecular orbitals, and the excitation cross sections can be deduced by observing the polarization of their de-excitation radiation (see e.g. Hippler *et al*, 1990, Kaupilla *et al*, 1970).

Polarized impact radiation also lends itself as a diagnostic in astrophysical situations where charged particles traverse partially neutral targets. The polarization fraction of radiation emitted from the targets gives rough limits on the relative velocities of target and charged particle, whilst the sign, or orientation of the polarization vector can give information on the charged particle direction. This aspect is particulary nice. Coupled with some knowledge of the physical conditions in the target, and the magnitude of the polarization fraction, a more refined estimate of velocity can be made, and limits set on the system geometry.

§1.2.2 The generation of polarized radiation.

In the following sections the processes leading to the excitation of polarized impact radiation will be described and the theoretical treatment briefly outlined. If a ground-state (1s) atom is excited through collision with an electron or proton, an atomic electron is raised to one of the upper

energy levels (n) of that atom , and enters also a particular angular momentum and magnetic substate (lm_L). From here there are two ways it can de-excite. It can, under certain density conditions, be collisionally de-excited by the thermal particles in the target medium, in which case the characteristics of the resulting photon depend both on the properties of the state nlm_L, and on the energetics of the collision. Alternatively it can de-excite naturally in the decay time for the upper state. Transitions which occur with the highest probability are known as "allowed" transitions. These follow the selection rules

$$l \rightarrow l \pm 1$$

$$m_L \rightarrow m_L, m_L \pm 1$$

The Hα transition under consideration in this thesis is an allowed transition. "Forbidden" transitions do not obey these rules. The optical electric dipole selection rules arise from calculating the first order term in the expansion of the time dependent bracket $\langle \beta_i | H_p | \beta_f \rangle$ - which is proportional to the transition probabiliy. β_i and β_f are the initial and final state wavevectors and H_p is the perturbation Hamiltonian. Lower order terms in the expansion give rise to the electric quadrupole and the magnetic dipole selection rules. Such transitions occur, but on far longer radiative timescales and are only visible in astrophysical objects under certain conditions. For example, normally the upper levels - the 'metastable' levels - of such transitions are collisionally de-populated before de-exciting spontaneously. However, if the gas is of very low density and the collisional lifetime is therefore longer than the radiative lifetime, the transition will be observable.

An allowed transition may still de-excite collisionally - this will depend on the spontaneous transition probability for the transition (A_{nlm_L}) which gives the inverse of the lifetime of the upper state, and on the collision cross section, velocity and number density of the colliding particles, which combine to give the collisional lifetime in the medium. If the collisional lifetime is shorter than the radiative lifetime then the information about the initial excitation process will be lost.

The cross section for excitation of a ground level electron to an upper substate is dependent not only on the energy of the exciting or impacting particle, but also on its direction of entry, relative to the orientation of the atom. The orientation in space is defined by the quantization axis, about which the electronic wave functions are cylindrically symmetric. In general the direction of the quantization axis can be arbitrarily assigned to an atom, though, in some cases it is externally imposed. Consider a target in some angular momentum state $l \neq 0$ in the presence of a strong magnetic field . Here, the atomic magnetic dipoles μ (produced by the "circulation" and spin of the electrons) will couple with the external field $\mathbf{B}$ and experience a torque $\tau = \mu \times \mathbf{B}$ which will tend to orientate the dipole along along the field, and parallel to it, which is the lowest

energy configuration (ΔE = potential energy of orientation = $-\mu.\mathbf{B}$). When the upper state de-excites the photons (or rather the electric dipoles which we consider as emitting the photons) have a preferred orientation in space, given by the transition probability matrix, and the emitted light is observed to be polarized. By contrast, in a ground - state target in which the particles have established a thermal distribution, their quantization axes are randomly orientated and any radiation thermally excited has zero net polarization. But, if the transition from lower to upper state is excited by an anisotropic distribution of charged particles, e.g. a beam, a direction is imposed on the system, and the resultant de-excitation radiation is found to be polarized. Below we indicate how, by considering the scattering of the exciters, excitation cross – sections and thence polarization fractions may be calculated.

We restrict considerations to the simple case of an atom with one optically active electron (in particular hydrogen). When a charged particle of initial momentum k_i approaches the atom it exerts a perturbing field on the electron which may raise it to a higher state. The charged particle will itself be perturbed from its orbit and will scatter from its original path. If a system of co - ordinates is defined with the original path of the atom as the OZ - axis and polar angles θ and ϕ as shown in fig. (1.11), the probability of the charged particle scattering into a solid angle $d\omega$ in the direction (θ,ϕ), having excited a particular quantum substate β (where β is shorthand for the complete set of quantum numbers of the state) is given by the scattering function $f_b(\theta,\phi)$, which is related to the scattering cross-section $\sigma_b(\theta,\phi)$ by

$$\sigma_\beta(\theta,\phi) = \frac{k_\beta}{k_1}|f_\beta(\theta,\phi)|^2 \qquad 1.7$$

where the term k_β/k_1 arises because the above equation is essentially a continuity equation for the charged particle flux. If instead of a single collision we have collisions excited by a beam of identical particles then the number of particles crossing unit area per unit time initially is proportional to the incident momentum $\underline{k_1}$, and after the scatterings is proportional to $\underline{k_\beta}$, the momentum with which they leave, having excited state β. The scattering functions $f_b(\theta,\phi)$ can be worked out from the interaction of the travelling wave of the electron and the orbital wave function of the optically active electron, in a variety of perturbation schemes - $f_\beta(\theta,\phi)$ being related to the wave function of the scattered charged particle at an infinite distance from the scattering centre. (For example, the simplest scheme, the Born approximation, describes adequately interactions where the relative velocity of target and exciter is high - in this approximation the charged particle wave function is described by a plane wave, which when combined with hydrogenic wave functions renders simple the solution of the Schrödinger equation in the case of impact of electrons on hydrogen.) To calculate the total cross section for excitation of the particular state β it is necessary to integrate the scattering function over all solid angles. Thus the total cross section for excitation of state β

by a charged particle incident along the polar axis with momentum $\underline{k_1}$ is

$$Q_\beta = \frac{k_\beta}{k_1} \int \int |f_\beta(\theta, \phi)^2| \sin\theta d\theta d\phi$$

Obviously these cross sections are different for different β's - particular states will become preferentially populated by beam excitation and, as in the case of alignment by a magnetic field, the result of excitation by a beam is the production of aligned upper states which de-excite, according to the transition probabilities, producing polarized radiation. The directional dependence of the transition probability is crucial here. Upper states de-exciting via dipole transitions do not do so in such a way that the dipoles are isotropically distributed. If this were the case there would be no polarization. Instead it is possible to calculate values $A_\beta(z)$ and $A_\beta(x)$ (or $A_\beta(y)$, these directions being equivalent in the co-ordinate system which we have defined.) These are probabilities for de-excitation with dipole in the z-direction and in the x-direction, and we will see in equation 1.10 how these combine with the excitation cross-sections to yield the line polarization.

To calculate the polarization fraction resulting from collisional excitation followed by de-excitation between energy levels (n quantum number) it is necessary to sum across all magnetic (m_L) sub-states excited (although a full calculation should take into account spin-orbit and nuclear spin coupling). To relate the atomic quantities – the cross sections and the transition probabilities – to the quantities observed, the polarization fraction P is defined by

$$P = \frac{I_\parallel - I_\perp}{I_\parallel + I_\perp} \qquad 1.9$$

where $I_\parallel$ is the observed intensity of emitted photons with dipole vector parallel to the incident beam direction, (OZ) and $I_\perp$ is the intensity of photons with dipole vector perpendicular to the incedent direction and the line of sight (OY). In terms of the directional transition probabilities from a state with principal and orbital angular momentum numbers $n_2 l_2$ to lower state $n_1 l_1$ the equation becomes

$$P_{n_2 l_2 \to n_1 l_1} = \frac{\sum_{m_L}[A_{m_L}(z) - A_{m_L}(y)]Q_{m_L}}{\sum_{m_L}[A_{m_L}(z) + A_{m_L}(y)]Q_{m_L}} \qquad 1.10$$

This is now ready to have slotted into it theoretical (or in some cases experimental) values of the transition probabilities and cross sections. Of course the excitation cross sections vary with the energy of the impacting particle, therefore so too will the resulting polarization.

Excitation by Protons and Electrons.

It has been mentioned already that the cross section for a particular transition depends on the energy with which the particle is incident, however, in expression 1.7 for Q_β the incident particle

mass cancels out in the fraction $k_\beta \backslash k_1$. It is in fact only the particle velocity that is of interest here - in theory any singly charged particle travelling at a given velocity will be equally effective at atomic excitations. So although the theoretical and experimental results which will be outlined in the following sections have been derived and measures for electron impact excitation, they should apply equally well to excitation by proton impact. At high velocities where the perturbation to the orbital electron is well approximated by an electric field pulse, this will be true, however moving to much lower energies it is possible that other interactions will occur - indeed as has already been mentioned, polarization is particularly useful in studying the quasi-molecular states formed in low energy collisions between protons and hydrogen atoms. We will see later some experimental comparisons at lower energies.

§1.2.3 The Hα Transition

For the case of the Hα transition, with which this thesis is primarily concerned, the relevant cross sections and polarization fractions following electron impact have been studied in some depth, and a composite of the results of various experimental and theoretical studies is shown in figs (1.12) to (1.14). The production of an Hα photon by collision involves the excitation from 1s to 3s,p or d, followed by spontateous de - excitation to level 2. The selection rules for the 3-2 transition mean that only 3s-2p, 3p-2s and 3d-2p excitations are permitted dipole transitions. The net cross section for the total 3-2 transition is calculated as a linear sum of all three excitation cross sections, $\sigma_{1s-3s}, \sigma_{1s-3p}$ and σ_{1s-3d} with coefficients proportional to the fraction of transitions going from the upper 3 state to a level 2 state. The total Hα emission cross section is

$$\sigma(H\alpha) = \sigma(3s) + 0.118\sigma(3p) + \sigma(3d) \qquad 1.11$$

The polarization fraction for the entire line is a sum over the values calculated for individual angular momentum states

$$P_{90} = \frac{1}{\sigma_{90}(H\alpha)} \Sigma_l B_l \sigma_{90}(3l) P_{90}(3l) \qquad 1.12$$

where the B_l's are the coefficients appearing in the cross section sum. P_{90}, σ_{90}(Hα) and $\sigma_{90}(3l)$, $P_{90}(3l)$ are quantities observed at 90° to the beam direction.

We see that the excitation cross sections by electrons, for all levels rise to a maximum at around 30 eV, corresponding to a velocity of $3.25 \times 10^8 \text{cms}^{-1}$. The velocity of the ground state electron in hydrogen, according to the Bohr theory is 2.18×10^8 cms^{-1}. So as we might expect it becomes easier to excite an upward transition as the energy of the impacting particle increases, but only whilst the exciting particle is moving slowly with respect to the atomic electron, so that it is in proximity for long enough to seriously perturb the orbital wave function. As it moves faster and

faster the excitation cross section decreases again as the moving particle's influence on the orbital electron decreases.

§1.2.4 Comparison Between Theory and Experiment

Although the agreement between theoretical and experimental evaluations of cross sections is often poor in terms of magnitude, all efforts agree on the broad characteristics - an increase to a maximum at a few times the electron orbital velocity, followed by a slow decrease. At low energies the various approximations can give very different cross – section values. Here there are many effects which must be taken into account in the interaction between charged particle and neutral target. The target can be distorted by the approach of the charged particle which changes the energy levels and makes the orbital wave functions asymmetrical. There is the possibility that, in the case of electron excitation, the orbital and impacting electron will actually change places. At particular velocities there may be resonances between the wave functions of the impacting particle and the orbital electron. These and other effects are taken into account in a great number of low - energy approximations - some of which agree better with experimental values than others. At the high energy end all the approximations tend to converge. The situation with polarization calculations is not quite so good. Fig (1.14) shows the results of theoretical and experimental attempts at this. The main area of contention is at threshold - here a simple theoretical argument should apply. In the collision of the electron and atom, angular momentum must be at all times conserved. We start with a target initially in the ground state - 1s - a state of zero angular momentum, and an electron beam also of zero angular momentum. At threshold, if an electron excites the upper level, it must then leave with zero energy and hence zero angular momentum, so to satisfy the conservation conditions the atom may only occupy excited states also with zero angular momentum, the $m_l = 0$ states. This reduces the magnetic substate excitation cross sections, appearing in equation (1.10) to particularly simple forms, and the resulting theoretical threshold polarization is $\frac{3}{7}$ for the 3p state and $\frac{57}{119}$ for the 3d state (Syms *et al* 1975). (The 3s state de-excitation results in zero net polarization.) These are combined in the normalised sum to give a total threshold polarization for the Hα line. The resultant value is $\sim 45\%$. Experiments have, however, given values for the polarization fraction which decrease with energy towards zero at threshold as can be seen in fig 1.15 although it must be conceded that the error bars on the experimental points are very large. This type of discrepancy is apparent also when studying other atomic transitions - for example the Hg $7^1D - 6^1P$ transition, as shown in fig (1.15), has an experimentally measured threshold value of zero, and a theoretical value of 60%. Still, the generally held opinion (cf Mott and Massey 1965, Syms *et al* 1975) appears to be that experimental methods are still inaccurate and difficult, especially at threshold where the cross sections and hence emitted intensities are small compared

with background counts, and the strong theoretical arguments for threshold polarization values should not be disregarded.

The polarization fraction is negative when the intensity of photons polarized parallel to the beam direction exceeds that polarized perpendicular the the beam direction - and is positive value when the converse is true. Theoretical values go negative at an electron energy of 120 eV, whereas existing experiments do not show any negative polarization, although the values above 60eV are unarguably declining towards zero, and it is probable that although the rate of decline may be different, the polarization fraction will cross zero at a high energy. At high energies the cross - sections and intensities are once more small, so there will again be considerable experimental difficulties in this region - although here the quoted error bars are smaller, and the data should be reliable. The small squares in the plot are the values used this thesis - matched to an analytic approximation at high beam energy. These values are not in fact a totally independent measurement of polarization; instead measured values (Mahan *et al* 1974) of the excitation cross sections (to states n_l) are used in the summation expression 1.12, but σ_{nlm_l} values used in 1.10 are calculated in the Born approximation.

The data described and shown above all relates to electron impact excitation, and as mentioned before, there may be differences between proton and electron cross sections at low velocities. Measurements have been made (Park *et al.* 1976) of excitation of atomic hydrogen to the n = 3 state, although no investigation was made of the angular momentum substate cross sections. The data extend from 15 keV to 200keV impact energy - ie, 1.7×10^8 to 6.2×10^8 cm s^{-1}, normalised to the Born approximation value at 200 keV. A comparison between this and cross section values for impact by electrons of the same velocity is made in figure 1.16. evidently the n=3 state proton excitation cross section is approximately twice the electron excitation cross section. Ideally proton experimental data should be used in our calculations but there is insufficient detail available. For the calculation of polarization fractions the excitation cross sections to angular momentum and magnetic substates are necessary. In the absence of such information for protons we are forced to use electron data although this is not entirely satisfactory. Since the de - excitation of the 3s state does not result in polarized radiation (it being spherically symmetric), the relative populations of the 3p and 3d states are very important. Park *et al* state that in the excitation of hydrogen by protons the $1s \rightarrow 3d$ transition represents a small fraction of the n = 3 excitation, whereas the electron data of Mahan *et al* demonstrate that the $1s \rightarrow 3d$ excitation cross section is $\sim$ 40% of the total $1 \rightarrow 3$ cross section at velocities of 2.6×10^8 cm s^{-1}, 15% at velocities $\sim 6.2 \times 10^8$ cm s^{-1}, but falling to $< 5\%$ above this. Theoretical work by Franco and Thomas (1971) on the $1s \rightarrow 3s$ and $1s \rightarrow 3p$ transitions and by Bhadra and Ghosh (1971) on the $1s \rightarrow$ 3d transition,

in the Glauber approximation indicates that on average, if this approximation is to be trusted, the 3p cross section is slightly larger when excited by a proton than when excited by an electron of the same velocity, whereas the 3d cross section is slightly lower. So by using electron data for protons with velocity $< 6.2 \times 10^8$ cm s^{-1} (200keV) we may be overestimating the 3d population, but ,since the total n=3 cross section is smaller for electrons, we may be underestimating the 3p population. The Glauber approximation is unfortunately another high energy approximation but is better than the Born or other 'impulse' approximations in that it takes into account the interaction of the incident particle with the target particle. At high energies there is no problem - approximations and experiments alike tend to converge for protons and electrons. Still it is not clear that the Glauber approximation gives us reliable information at low incident velocities. Therefore we shall stick to the electron data.

One minor disadvantage with using the electron data is the range which it covers. We have electron data from around the excitation energy of 13.6eV, but if this is converted to the energy of a proton with identical velocity, we only have information down to 25.3 keV, and protons of below this energy are capable of exciting Hα transitions. All the theoretical work and experimental work indicates that the cross sections begin to decline if the charged particle velocity is less than 3.25×10^8 cms^{-1}, and in practice, when dealing with proton beam of greater velocity than this (i.e. $\sim$ 100 keV) we neglect the contribution from low energy ($<$ 25.3keV) protons. As is illustrated in fig 1.17, a 10keV proton beam will traverse a column depth of order $10^{16} cm^{-2}$ which is negligible compared to the 10^{18} cm^{-2} already traversed by the 100 keV beam of which it is the tail (so the number of Hα excitations by this tail will also be small). However, we will carry out some calculations in chapter four where the protons involved are all of energy of $\sim$ 50 to 100 eV and obviously here we will need to have some estimate of the excitation cross section.

§1.2.5 The High Energy Approximations

We need total values for excitation cross section and polarization fraction for any energy of impacting particle, since in calculations we will be dealing with beams or flows of particles with continuous energy distributions. To this end we use interpolating splines to approximate the available data, and then attempt to match these with analytic approximations valid at high energies. The two approximations chosen are the Bethe approximation applicable to the upwards transitions satisfying the optical dipole selection rules (i.e., 1s - 3p) (MacFarlane 1974, Inokuti 1971) and the first Born approximation, for those which do not (i.e., 1s-3d). The Bethe approximation is essentially a simplification of the Born approximation made by replacing the interaction potential $V(r_1, r_2)$ of target (1) and particle(2) with its asymptotic form for large radial distances r_2. The resulting

form for the Bethe asymptotic cross section is

$$\sigma_n = \frac{4\pi/a_0^2}{(E\backslash Ry)} \frac{f_n}{(\Delta E\backslash Ry)} ln\left(\frac{4C_n E}{Ry}\right)$$

where Ry is the Rydberg energy, f_n is the transition optical oscillator strength and C_n depends on the generalised oscillator strength. The transition optical oscillator strength is a number which arises in the classical treatment of the absorption of radiation, where the atom is considered to be composed of oscillating electrons, being forced by the radiation field, and f_n is the number of classical oscillators or the eqivalent number of electrons in the atom. The generalised oscillator strength, defined for a collision involving a transfer of momentum K from projectile to target particle, is $f_n(K)$ and is the extension of the radiation field concept to a sitiuation where the oscillators are forced also by the field of the projectile. In the limit of K tending to zero, the generalised oscillator strength tends to the optical oscillator strength. The number C_n is a constant for a particular transition, related to the generalised oscillator strength integrated over all possible values of momentum transfer. Its exact theoretical calculation for hydrogen is possible, and results are summarised in Inokuti (1971). The graph of $\ln C_n$ vs (E/Ry) is shown here (fig 1.18). From this graph $\ln C_n$ is read and has the value 0.25 ± 0.01.

The first Born approximation takes the form

$$\sigma_n = \frac{\epsilon}{E a_o^2} \langle \beta_1 | r^2 | \beta_n \rangle \qquad 1.14$$

where a_o is the Bohr radius. In practise we keep the energy dependence of the cross section $\sigma =$ Const/E, but match to experimental data at high energies to get the constant.

The polarization fraction is obtained in the Bethe approximation, by defining, for individual particle interactions, the quantization axis in the direction of momentum change of the incident particle, and averaging over many interactions. Both the Born and the Bethe approximations allow only transitions with change in magnetic quantum number $\Delta m_L = 0$ with respect to individual particle quantization axes. This defines the permitted lower substates and hence the polarization fraction in the case of the 3d-2p transition

Figures 1.19 and 1.20 show a composite of the low and high energy values of cross section and polarization fraction. The points are data and the line is the interpolating spline fit to the data matched to the high energy approximation. The points on this line are precisely those which are used in the calculations. The 3d matching is not certain since only an asymptotic rather than an energy dependent value of polarization fraction is given, and the slope of the high energy section (and more importantly, where it crosses the axis) depends on what energy is sufficiently high to be

treated as infinite in this context. Here a value of 1000 keV is chosen - i.e., at 1000 keV and above, the polarization fraction is -24.6% and a straight line joins 1000 keV and the last experimental data point.

§1.2.6 Treatment of a Distribution of Particle Velocities and Pitch Angles.

The results outlined so far really only describe single collisions (or a succession of identical collisions) but it is necessary to be able to extend these to the case where the exciting particles enter the target with a range of velocities and a distribution in angle. The general form for the calculation of polarization in such a case is given in Hénoux *et al* (1981). The method is to calculate the polarization Stokes' parameters in a generalised co-ordinate system. The Stokes' parameters which we are interested in are combinations of intensities and are defined with reference to a particular axis as $Q = I_{\parallel} - I_{\perp}$ and $I = I_{\parallel} + I_{\perp}$, so that the polarization is $P(\theta) = Q(\theta) \backslash I(\theta)$. Q and I for a cylindrically symmetric distribution are defined as follows

$$Q(\theta) = \sin^2\theta \int_{v_{th}}^{\infty} \frac{P_{90}(v)(3J_2 - J_0)v\sigma(v)}{3 - P_{90}(v)} dv \qquad 1.16a$$

$$I(\theta) = 2\int_{v_{th}}^{\infty} \frac{(J_0 - P_{90}(v)J_2)v\sigma(v)}{3 - p_{90}(v)} dv + \sin^2\theta \int_{v_{th}}^{\infty} \frac{P_{90}v\sigma(v)(3J_2 - J_0)}{3 - P_{90}(v)} dv \qquad 1.16b$$

In these expressions the particles have a cylindrically symmetric velocity distribution, and viewing is at an angle θ to the axis of symmetry. $P_{90}(v)$ is from eqn. 1.12. The angular information is contained in the terms J_0 and J_2 which are the zeroth and second moments of the distribution function, given by

$$J_n = \int_{-1}^{1} f(v,\mu)\mu^n d\mu \qquad 1.17$$

μ being the pitch angle cosine. In the case of a unidirectional beam with distribution function $f(v)\delta(\mu - 1)$ the moments become

$$J_o = f(v) = J_2$$

Therefore a unidirectional beam viewed at 90° has a polarization of

$$\mathcal{P}(90) = \int_{v_{th}}^{\infty} \frac{f(v)P_{90}(v)v\sigma(v)}{3 - P_{90}(v)} dv \Big\backslash \int_{v_{th}}^{\infty} \frac{f(v)v\sigma(v)}{3 - P_{90}(v)} dv \qquad 1.18$$

In a thick-target situation the function $f(v)$ is in fact changing with position. This must be carefully treated. First consider the general case where we wish to calculate the polarization emitted over a uniform cylinder of length $l = z_1 - z_0$ and of cross section A, by particles with an evolving, cylindrically symmetric distribution function. Since the radiation intensities are additive, it is imperative that we calculate

$$\mathcal{P}_{TOT} = \frac{\int_{vol} I_{\parallel} dV - \int_{vol} I_{\perp} dV}{\int_{vol} I_{\parallel} dV + \int_{vol} I_{\perp} dV} = \frac{\int_{vol} Q dV}{\int_{vol} I dV} = \frac{A\int_{vol} Q(z)dz}{A\int_{vol} I(z)dz} \qquad 1.19$$

rather than first evaluating the polarization as a function of volume and integrating over volume - the polarization fraction is not an additive quantity. Going back to the unidirectional beam incident this time along the z - axis, the quantity which must now be calculated is

$$\mathcal{P}_{TOT}(90) = \int_{z_o}^{z_1}\int_{v_{th}}^{\infty} \frac{f(v,z)P_{90}(v(z))v(z)\sigma(v(z))}{3-P_{90}(v(z))}dv(z)dz \Big\backslash \int_{z_o}^{z_1}\int_{v_{th}}^{\infty} \frac{f(v(z))v(z)\sigma(v(z))}{3-P_{90}(v(z))}dv(z)dz \qquad 1.20$$

In the case of an arbitrary cylindrical distribution, the function moments must be calculated as a function of depth and included in the above integral. A factor introduced in Hénoux *et al* to describe the spread of the distribution function - the *anisotropy factor* b is given by

$$b = \frac{3J_2 - J_0}{2J_0}$$

For a distribution function which does not change, and a viewing angle of 90°, multiplying the 'unidirectional' result by this anisotropy factor will make the appropriate reduction in polarization fraction, but in a collisionally thick medium there is obviously no such simple method. Scattering will, however, always lead to a decrease in the anisotropy factor, therefore an upper limit to the polarization from a scattering cylindrical distribution could be obtained by calculating the anisotropy factor at the point of injection, to use as a constant multiplying factor, rather than recalculating as a function of depth. In the next chapter we deal only with unidirectional proton beams in which case the initial anisotropy factor has value one, and, since proton beams do not scatter significantly, does not decrease significantly until the very end of the proton trajectory, when its velocity is not significantly above the local thermal velocity. When dealing with electron excitation the scattering is a much more important consideration, and in fact, in chapter 3, which is concerned with mirroring electron beams, the anisotropy factor must be evaluated as a function of position.

We have by no means provided a full description of the process of impact excitation, and by omitting the quantum mechanical analysis using state represention we have made the argument considerably less elegant, but more immediately understandable than it could have been. But all that is necessary for the analysis of future chapters is summarised, and with this, and a familiarity with the immediate flare environment, as provided in §1.1, we may now proceed with investigating various models for the excitation of polarized Hα radiation.

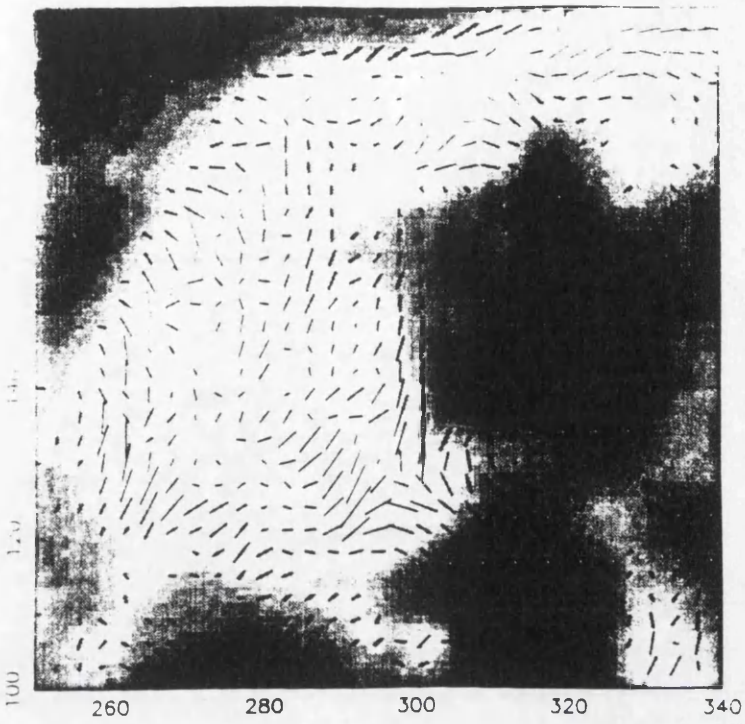

Fig 1.1 Polarization map of 17th July 1982 flare (Hénoux 1990).
1 pixel = 1 arc second

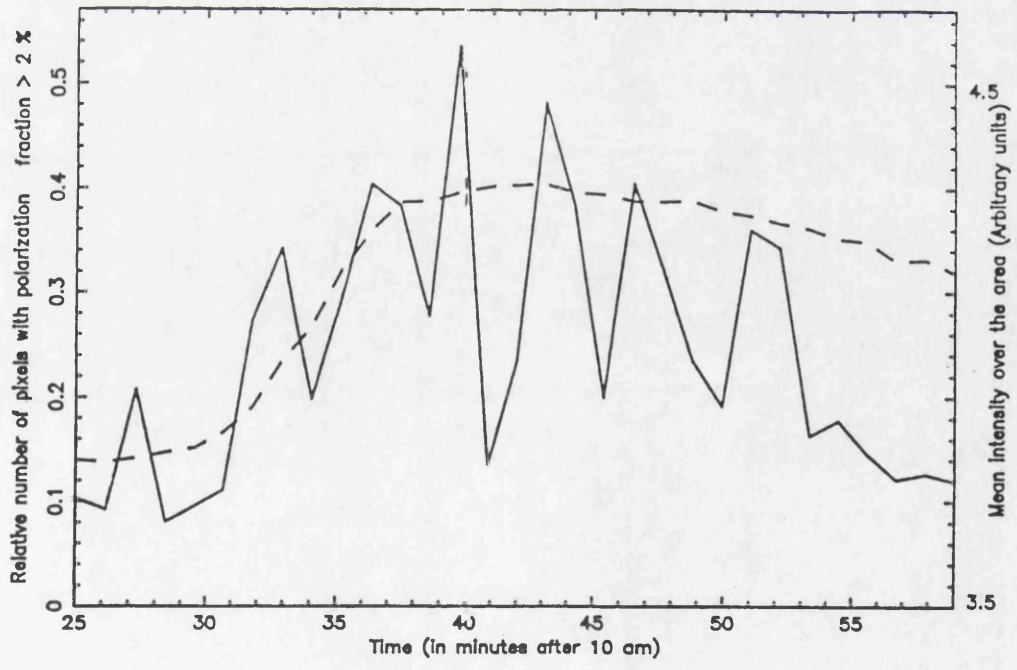

Fig 1.2 Time variation of fraction of pixels showing 2% polarization.

- - - - - relative number of polarization pixels

——————— mean intensity of Hα

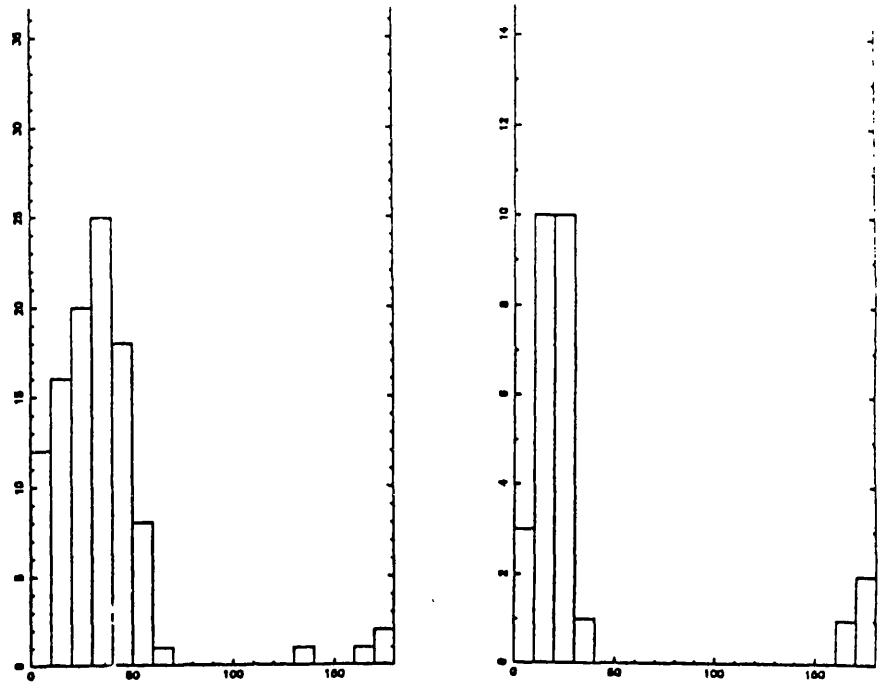

(a) Eastern flare ——— (b) Western flare

Fig 1.3 Azimuthal distribution of 13 minute integrated polarization vector.

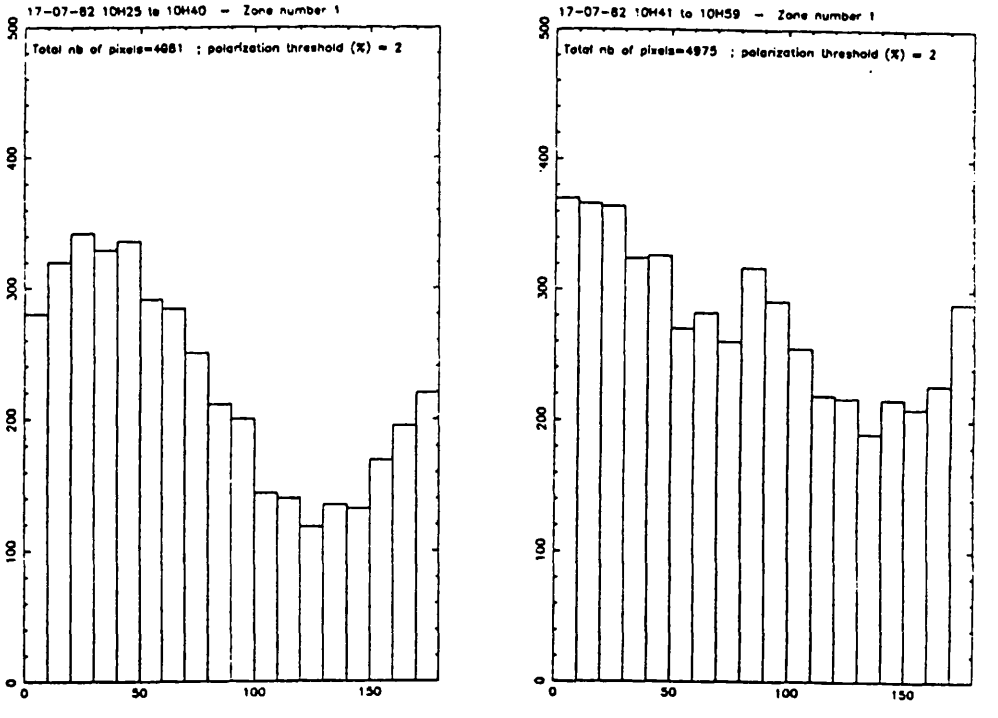

Fig 1.4 Azimuthal distribution of 1 minute integrated polarization vector.

(a) During rise (10.25 - 10.40) (b) After maximum (10.41 - 10.59)

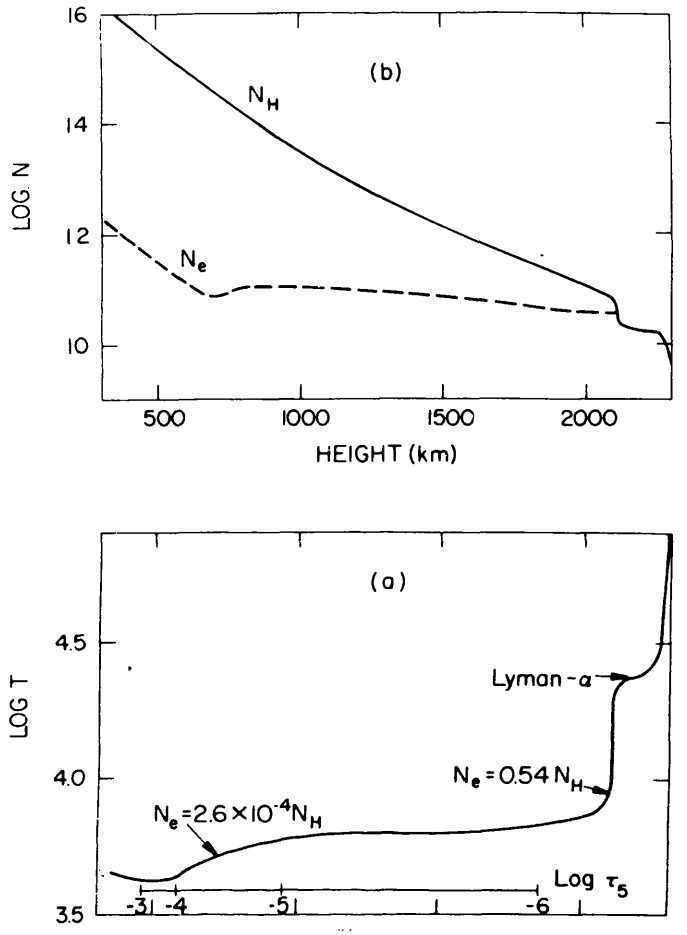

Figure 1.5 Quiet sun model atmosphere of Vernazza *et al* (1981).

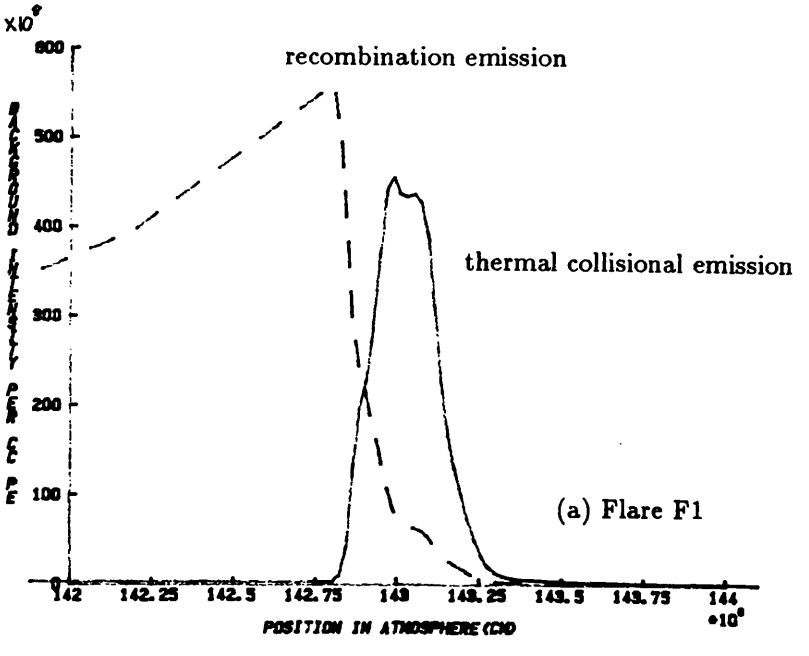

Fig 1.6 Intensity of themally generated and recombination Hα ($cm^{-3}\ s^{-1}$).

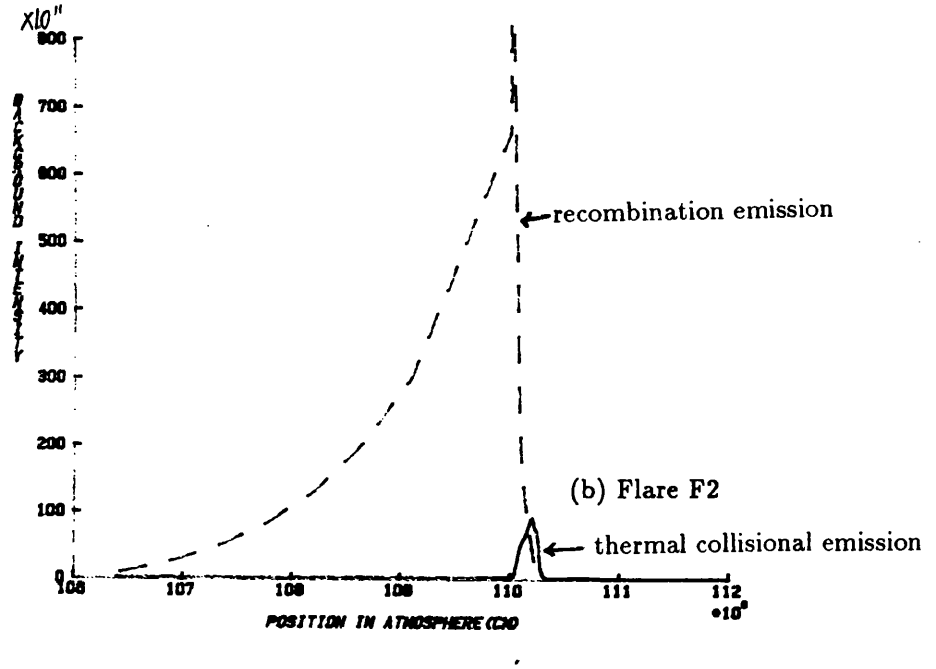

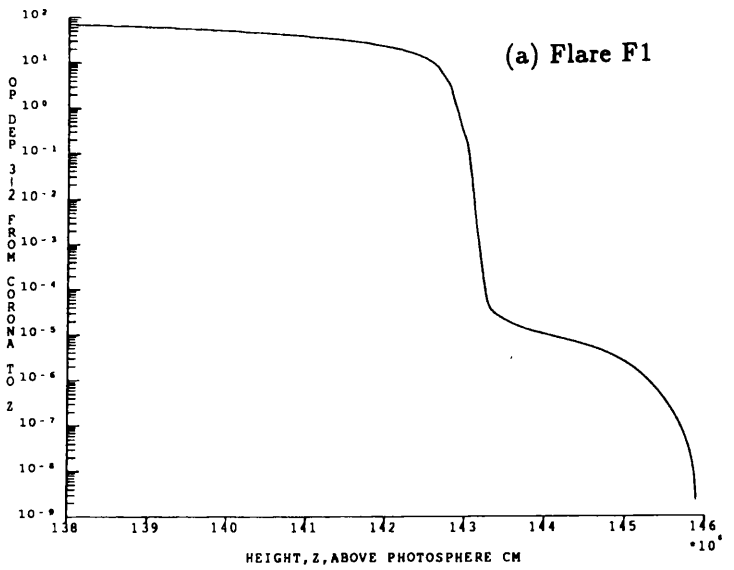

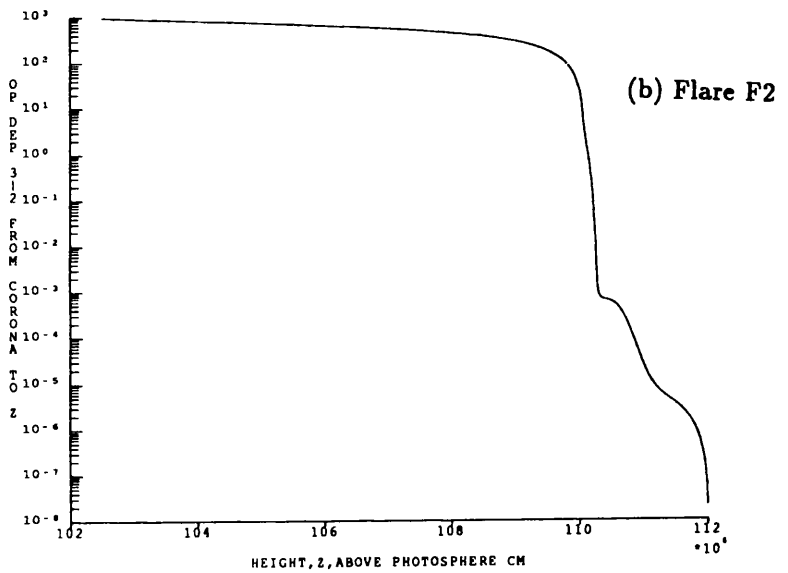

Fig 1.7 Calculated Hα line centre optical depths.

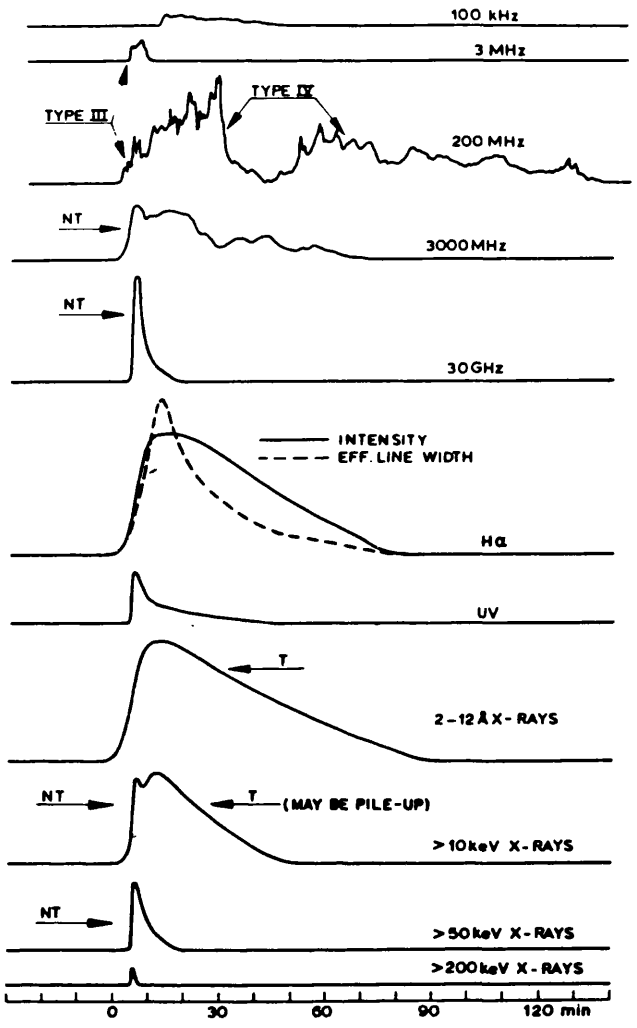

Fig 1.8 Summary of typical flare emissions as a function of time.

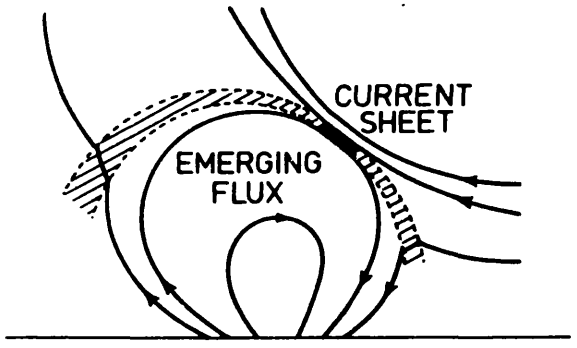

Fig 1.9 Compact flare reconnection - Emergent flux model (Heyvaerts *et al* 1977).

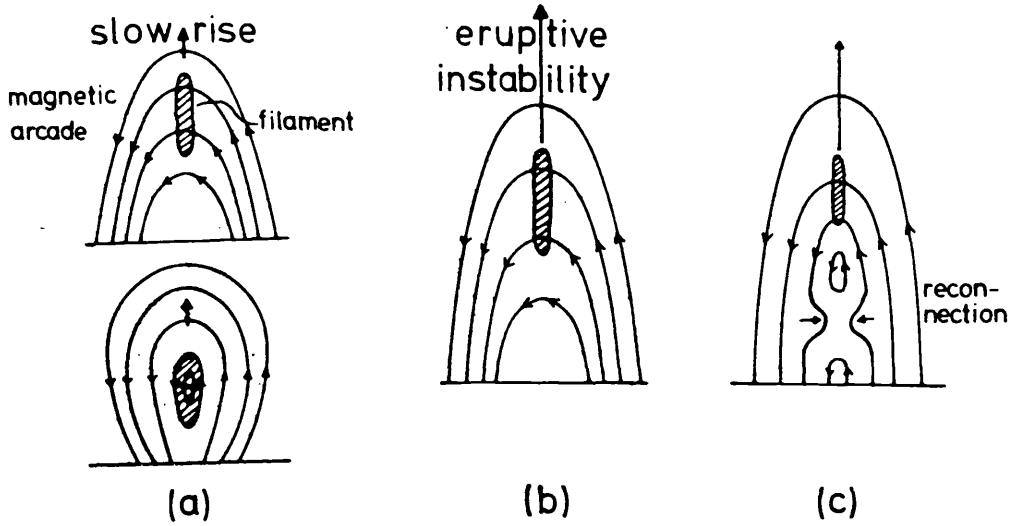

Fig 1.10 2-ribbon flare reconnection (From Priest, 1981).

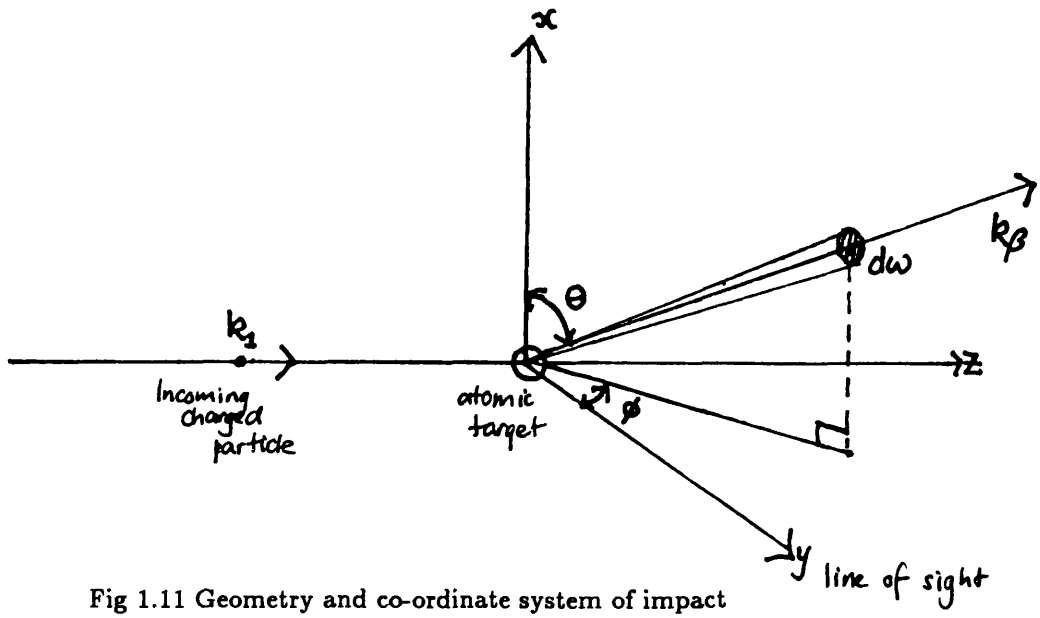

Fig 1.11 Geometry and co-ordinate system of impact

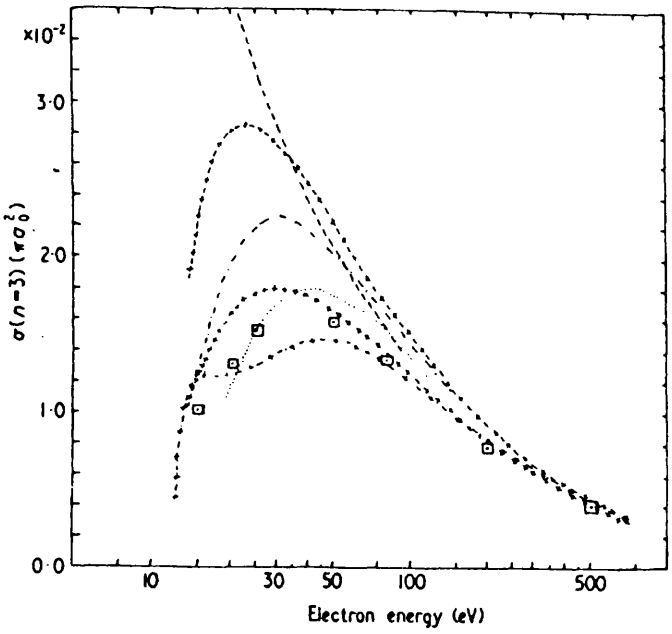

Fig 1.12 Total n=3 excitation cross-section (Mahan *et al* 1976).

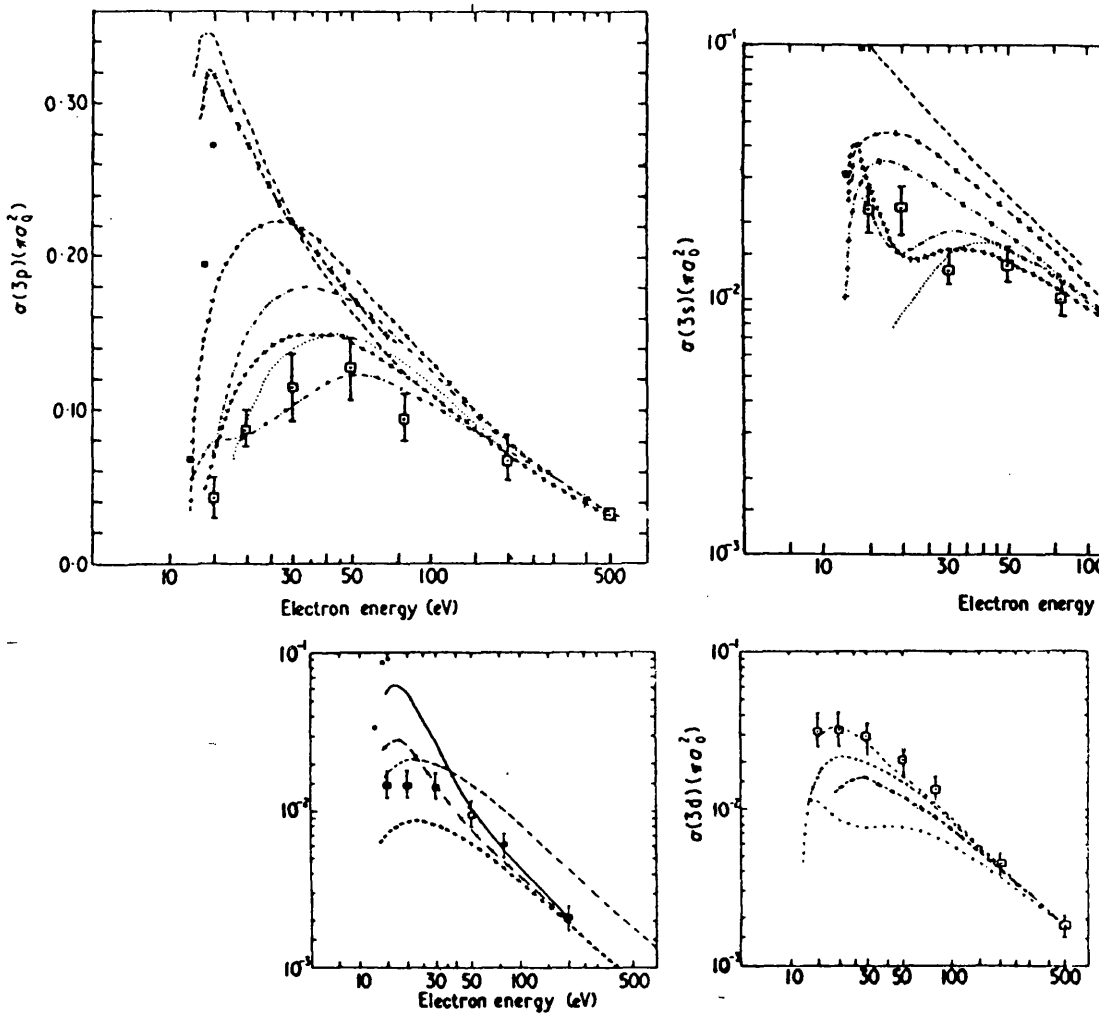

Fig 1.13 Individual 3s, 3p and 3d Cross sections (Mahan *et al* 1976).

In all figures, the lines are a variety of theoretical calculations which, although not agreeing at low energy, converge at high energy. The points in boxes are experimental points which are used in the calculations in this thesis. For details of the approximations used in generating the curves see Mahan *et al* 1976.

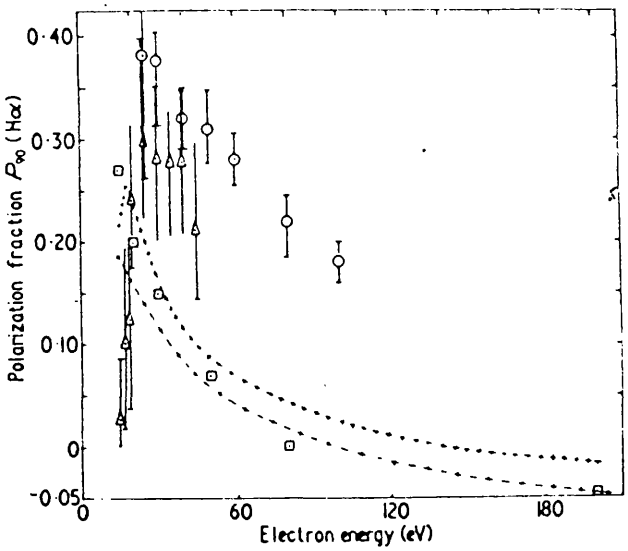

Fig 1.14 A composite of various sets of experimental measurements and theoretical calculations of the Hα line polarization fraction. The values used in this thesis are those in the small boxes. For details of the sources see Syms *et al* 1975

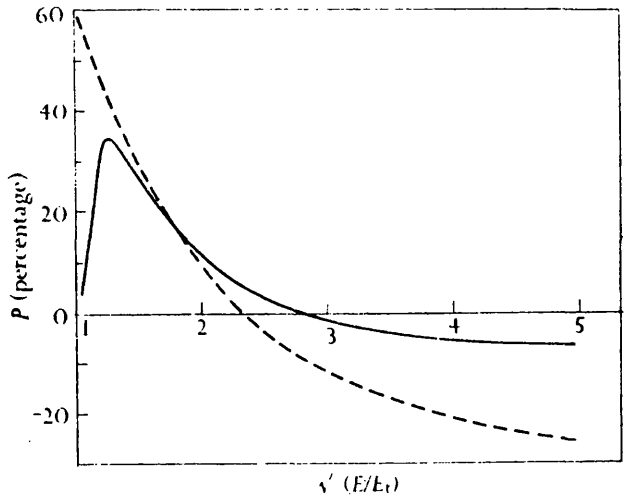

Fig 1.15 Observed (full line) and theoretical (dotted) polarization fraction in the Hg line (from Mott and Massey, 1965).

Fig 1.16 Total hydrogen n=3 excitation cross section by protons (full line) and electrons (dashed).

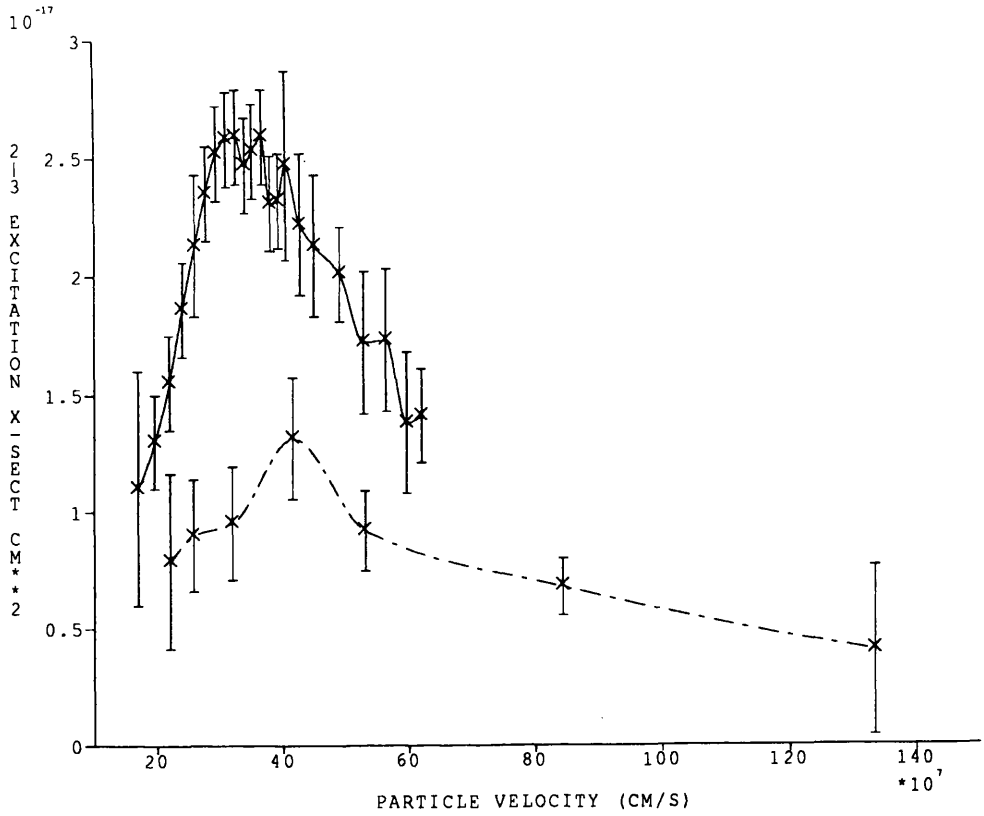

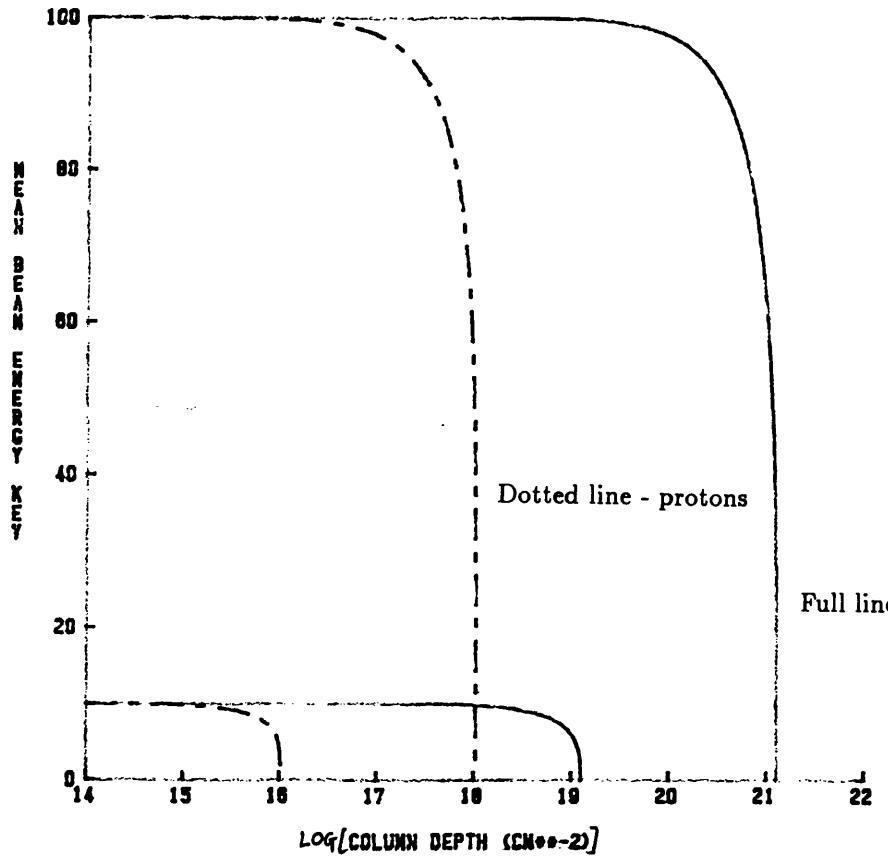

Fig 1.17 Beam energy as function of column depth traversed for beams with initial energy of 10keV and 100keV. Full line - electrons. Dotted line - protons.

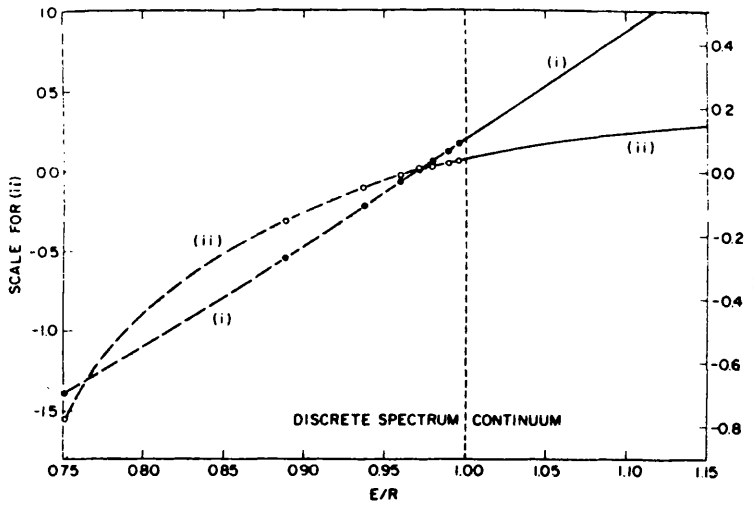

FIG. 15. The parameter ln c_E for excitation and ionization from H(1s) as a function of E. The data are taken from I63 and I66. The abscissa is E/R, so that the interval $0.75 < E/R < 1$ corresponds to the discrete spectrum and the interval $1 < E/R$ to the continuum. The points shown on curve (i) represent ln c_n in the discrete spectrum for $n = 2, 3, 4, 5, 6, 7, 10$, and 15. Curve (i) in the continuum shows ln c_E. Notice the smooth continuation at the ionization threshold $E/R = 1$, where $\lim_{n\to\infty}$ ln $c_n = 0.092955$. Curve (ii) represents (R^2/E) (df/dE) ln c_E in the continuum, and the open circles on curve (2) show $\frac{1}{2}n^3M_n^2$ ln c_n in the discrete spectrum again for $n = 2, 3, 4, 5, 6, 7, 10$, and 15. The plot is also smoothly continuous at $E/R = 1$, where $\lim_{n\to\infty}\frac{1}{2}n^3M_n^2$ ln $c_n = 0.07264$.

Fig 1.18 C_n, function of generalised oscillator strength as function of level energy in Rydbergs (Inokuti 1971).

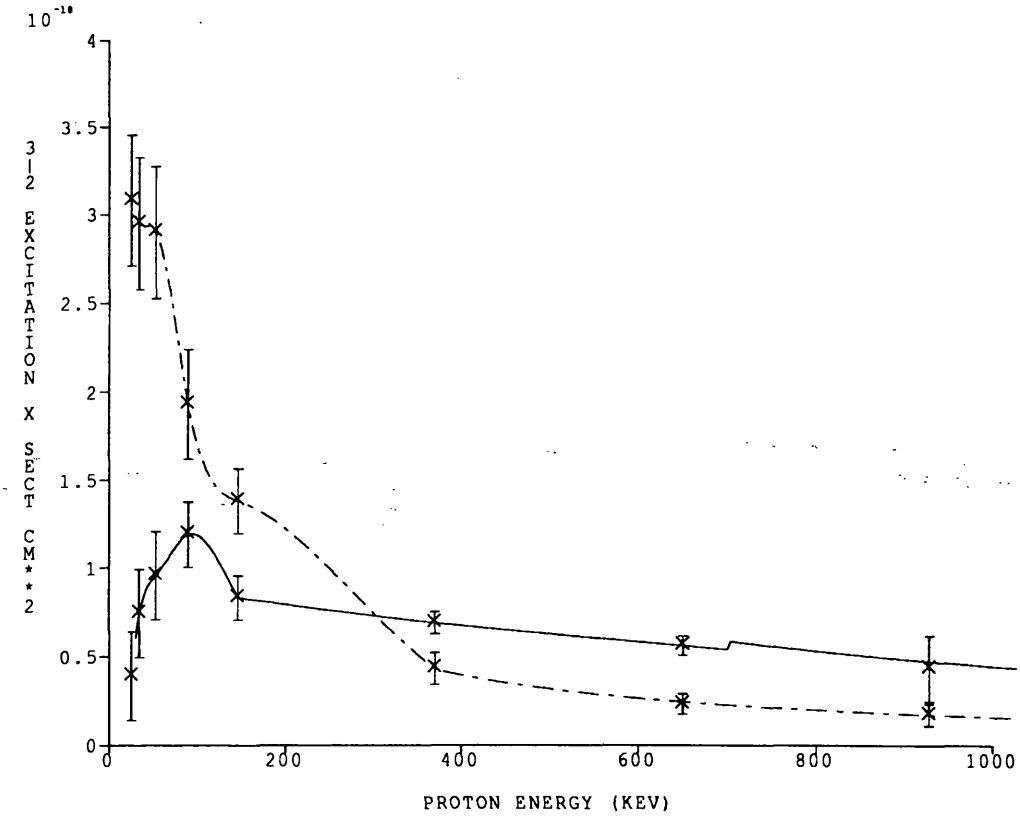

Fig 1.19 Matching of n=3 high energy cross section approximations with experimental data.

full line - electrons dotted line - protons

Fig 1.20 Matching of high energy polarization approximation with experimental data.

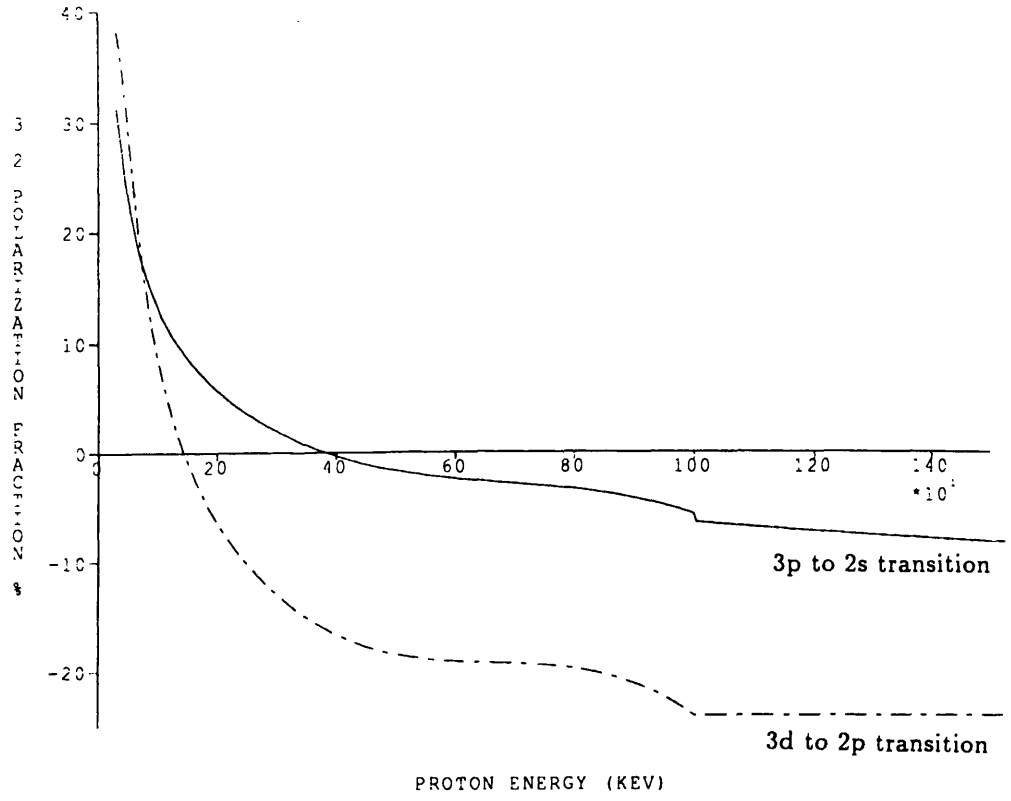

Chapter 2. The Proton Beam Model.

Introduction.

In this chapter we will investigate a model for the formation of Hα linear polarization based on the interaction of low and intermediate energy protons with neutral hydrogen in the solar chromosphere. This model has previously been discussed by Henoux *et al* (1990) - however we here point out some limitations of their treatment and faults with their model, and reassess the model and its results with more physically realistic parameters. We find that whilst still being a plausible candidate for the production of the polarization, low and intermediate energy protons place too great requirements on the energy budget of the flare to be considered in all but the most extremely energetic of flare events.

In formulating this model we will also introduce many ideas and methods which will be used throughout the remainder of the thesis, e.g., the thick target calculation and the calculation of optical depth and thermal emission of the chromosphere

§2.1.1 Target Conditions

In the form of a beam, protons and electrons will both cause emission of some polarized radiation in a collisionally thick medium, but the two beam types will evolve differently as they proceed through the target, and this is all important, since both the mean beam energy and its degree of anisotropy at any given position determine the magnitude and direction of polarization excited. It is necessary therefore to consider the evolution of a particle beam in a collisionally thick medium.

Firstly we will distinguish between the "warm" and "cold" target approximations. The criterion for describing a target as cold is given by

$$\frac{E}{kT} \gg \frac{m}{m_e} \qquad 2.1$$

where the target (electron) temperature is T, and the energy and mass of the test particles ('beam' particles) which have been introduced are E and m respectively. This is equivalent to saying that the beam speed is much greater than the thermal speed of the electrons (and therefore also of the protons) in the target and the distribution of relative velocities is highly peaked in the beam direction and close to the beam speed - the target particles may then be considered initially stationary. The warm target condition is that the beam particle speed is between the electron and proton thermal speeds. In a thermally relaxed ionised hydrogen target the electron thermal speed

is $m_p \backslash m_e$ times the proton thermal speed, and the warm target condition is that

$$\frac{m}{m_e} \gg \frac{E}{kT} \gg \frac{m}{m_p} \qquad 2.2$$

In the warm case, the target particles may transfer energy to the beam particles and the diffusion of the beam is more important. The equations for energy loss and pitch angle evolution of a beam in a cold target will later be compared with those for a warm target. We indicate below the particle energies above which the flare atmospheres of Vernazza, Avrett and Loeser (1981) can be considered cold.

Table 2.1

	Corona	Transition Region	Chromosphere
temperature	10^7 K	5×10^5 K	10^4 K
electron beam	E $\gg$ 850eV	E$\gg$ 40 eV	E$\gg$1eV
proton beam	E$\gg$ 1.5MeV	E$\gg$ 75keV	E$\gg$ 2keV
velocity cm s^{-1}	v$\gg 1.7 \times 10^9$	v$\gg 3.75 \times 10^8$	v$\gg 6.0 \times 10^8$

It is evident that the chromosphere can be considered a cold target to all but the lowest energy proton and electron beams, whereas the corona will have to be treated as a warm target for the low energy proton beams being modelled here.

§2.1.2 Coulomb collisions

The interaction between beam and target charged particles takes place via the interaction of their Coulomb fields. The results we reproduce here are applicable to cold target collisions. The coulomb interaction of two charged particles of masses m_1 and m_2, charges $z_1 e$ and $z_2 e$ can be described in the centre of mass frame. In this frame the deflection of each particle is equal, with value θ, given by

$$\tan\frac{\theta}{2} = \frac{z_1 z_2 e^2}{m_o b v^2} \qquad 2.3$$

where the reduced mass of the system is $m_0 = m_1 m_2 \backslash (m_1 + m_2)$ and b is the " impact parameter" that is, the mimimum distance of approach of the two particles in the absence of the Coulomb force. Let particle 1 be the 'beam particle' and particle 2 the 'target particle'. We are interested then in what happens in the frame of the target particle, since this is the frame of the chromosphere - and also the observer's frame. In the observer's frame, therefore, the beam particle approaches the target particle with velocity $(0, 0, v_z)$ (the z direction is the initial particle direction and the (x, y) plane is perpendicular to this). Since the Coulomb force is spherically symmetric we can consider the beam particle to scatter with a velocity component in an arbitrary direction in the (x, y) plane - the x direction will do. In this case, in the frame of the observer, the final velocity

(v_x, v_y, v_z) of the beam particle is given by

$$v_f = \frac{v}{(m_1 + m_2)}(m_1 \cos\theta + m_2, 0, m_1 \sin\theta)$$

We can then work out the energy lost per collision, ΔE, viz

$$\Delta E = \frac{m_o^2}{m_2} v^2 (1 - \cos\theta) \qquad 2.4$$

The $(1 - \cos\theta)$ term can be expanded in the small angle theta, and a substitution made from equation(2.3), giving $\Delta E \sim 2(z_1 z_1 e^2)^2 \backslash b^2 v^2 m_2$. Comparing the energy lost by a beam particle of velocity v, encountering a proton at impact parameter b, with that lost by an identical encounter with an electron, we see that $m_p \backslash m_e$ times more energy is lost to the electron than to the proton - a particle beam loses energy on the *electrons* in the target. (The massive ions act as almost fixed scattering centres.) The change in velocity of the beam particle as a result of the collision is

$$\Delta v_{\|} = \frac{m_o}{m_1} v(1 - \cos\theta) \qquad 2.5a$$

$$\Delta v_{\perp} = \frac{m_o}{m_1} v \sin\theta \qquad 2.5b$$

Again taking the small angle limit, $\theta \sim \Delta v_{\perp} \backslash \Delta v_{\|}$ and using another expansion in small angle θ reveals that, as we would expect, the largest changes in angle arise through collisions with the heavier protons.

We here summarise results from Emslie 1978. The evolution of energy and direction of a typical beam particle, initially travelling in the z direction, as it undergoes many collisions at different impact parameters is approximated by calculating mean time-rates of change in a manner involving integration over all values of impact parameter, up to some limit beyond which the target particles no longer affect the motion of the test particles. In a medium in which the particle density is a function of position it is convenient to have the rates of change as a function of position in the medium, rather than as a function of time, and a change of variables $d\backslash dt = nvd\backslash dN$ is made, where N is the column density of protons, free and in hydrogen. The ionisation is described by a factor x, such that $n_p = n_e = xn_h$ and $n_{h_0} = (1 - x)n_h$ where n_{h_0} is the number density of neutral hydrogen present. Under these conditions the energy and velocity equations in a cold plasma appear as follows, (from Emslie 1978)

$$\frac{dE}{dN} = \frac{-K}{\mu E}[x\Lambda + (1 - x)\Lambda'] \qquad 2.6a$$

$$\frac{dv_z}{dN} = \frac{-K v_z}{2\mu E^2}[3x\Lambda + (1 - x)\Lambda"] \qquad 2.6b$$

for an electron beam and

$$\frac{dE}{dN} = \frac{-K}{\mu E}\left(\frac{m_p}{m_e}\right)[x\Lambda + (1 - x)\Lambda'] \qquad 2.7a$$

$$\frac{dv_z}{dN} = \frac{-Kv_z}{2\mu E^2}\left[\left(\frac{m_p}{m_e}\right)x\Lambda + \frac{1}{2}(1-x)\Lambda''\right] \qquad 2.7b$$

for a proton beam. In these expressions, the constant $K = 2\pi e^4 {z_1}^2 {z_2}^2$, and we introduce the parameter μ the pitch angle cosine; $\mu = v_z \backslash v$. The parameters Λ, Λ' and Λ'' are the Coulomb Logarithm, the "effective Coulomb logarithm" (Brown 1973) and the "effective collision logarithm" (Emslie 1978).

$$\Lambda = ln\left(\frac{m_o v^2 r_c}{z_1 z_2 e^2}\right) \qquad 2.8a$$

$$\Lambda' = ln\left(\frac{\zeta m_e v^2}{1.105\chi}\right) \qquad 2.8b$$

$$\Lambda'' = ln\left[\frac{1}{\alpha}\left(\frac{m}{m_e}\right)\left(\frac{v}{c}\right)\right] \qquad 2.8c$$

ζ is a factor set equal to 1 or 2, depending on whether the bombarding particles are electrons or protons, χ is the ionisation potential of hydrogen and α is the fine structure constant. The Coulomb logarithm arises from the integration over impact parameter of the changes in energy and velocity arising from the collision of two charged particles. It is also the logarithm of the ratio of a maximum or cutoff impact parameter, r_c, to that impact parameter which results in a 90° deflection of the test particle. The cutoff is usually chosen as the radius of the plasma Debye sphere,

$$R_D = 6.9\left(\frac{T}{n_e}\right)^{1\backslash 2} \qquad 2.9$$

since in an ionised target a beam particle at the centre of this sphere is shielded from the electrostatic influence of particles outwith the sphere. The effective Coulomb logarithm is an analagous quantity but arrived at through consideration of inelastic collisions of charged particles with neutrals, in which any of the upper atomic levels may be excited. A similar integration of the momentum transferred over all possible values of impact parameter is performed, followed by summation over all excited upper states. In the simplest case the expression for momentum transfer is calculated in the first Born scattering approximation at high energy and a suitable limit at low energy (see Mott and Massey 1965) where the Born approximation is not valid. The effective collision logarithm arises from considering the parallel velocity change, or the pitch angle scattering of a beam particle following a collision with a neutral, again using the first Born approximation and integrating the particle scattering function over pitch angle. There is no allowance in the derivation of Emslie for low energy collisions, therefore the value of the effective collision logarithm will be incorrect at low energies. Fortunately the fact that protons are the bombarding particles means that pitch angle scattering can always be neglected (see later) and we never need to use the effective collision logarithm. Note that that the presence of other atomic nuclei is here ignored as in the solar atmosphere they will be in sufficiently small quantities to have little effect on energy loss. However the presence of electrons liberated from these other species mean that in the upper

chromosphere n_e can exceed n_h by a few percent (see figures 2.1a and b) - in which case we may not use the relation $n_e = xn_h$ and must use the empirically determined values for the electron density.

Setting boundary conditions E_o and μ_o enables solution of equations 2.6 and 2.7, in terms of initial mean pitch angle and energy at column depth zero. The solutions, written below for a completely ionised hydrogen gas, will allow us to compare the behaviour of a proton beam and an electron beam in terms of how rapidly the variation with column depth of energy and pitch angle proceeds. For electrons:

$$E = E_o\left[1 - \frac{3K\Lambda N}{\mu_o E^2}\right]^{\frac{1}{3}} \qquad 2.10a$$

$$\mu = \mu_o\left[1 - \frac{3K\Lambda N}{\mu_o E^2}\right]^{\frac{1}{3}} \qquad 2.10b$$

for protons:

$$E = E_o\left[1 - \left(\frac{m_p}{m_e}\right)\frac{2K\Lambda N}{\mu_o E_o^2}\right]^{\frac{1}{2}} \qquad 2.11a$$

$$\mu = \mu_o\left[1 - \left(\frac{m_p}{m_e}\right)\frac{2K\Lambda N}{\mu_o E_o^2}\right] \qquad 2.11b$$

These solutions - the behaviour of energy, velocity and pitch angle with column depth, are graphed in figures 2.2 a,b,c and d. It can be seen that an electron of a given energy travels farther than a proton of the same energy. However when considering atomic impact excitation we are concerned with the particle velocities and if equations 2.9 and 2.10 are re-expressed in terms of this it is apparent that a proton injected at $N = 0$ with velocity v will traverse $m_p \backslash m_e$ times the column depth of an electron also injected at v, before it attains the local thermal velocity. (Similarly with pitch angle evolution - electrons scatter faster than protons of the same velocity but slower than those of the same energy.)

§2.1.3 Discrimination between proton and electron beams.

The energy and pitch angle variation in a thick target, plus geometrical arguments can now be used to identify the type and velocity of beam which must be responsible for producing the impact polarization seen in the chromosphere. From experiments in atomic physics we know that a low velocity beam is more efficient at producing Hα impact radiation, as is seen on examining values of the cross section and the polarization fraction of impact emission in the Hα line. These maximise at low values of the relative speed between the target and projectile particles - rather than at high values. The maximum value of both parameters occurs at around 2.65×10^8 cms $^{-1}$ (30 eV for electron beams and 60 keV for proton beams), but if an electron beam were to be injected

into the chromosphere and arrive in the neutral hydrogen rich layers of the chromosphere (density $\sim 10^{11-12}$) cm^{-3} with a velocity of 2.65×10^8 cms $^{-1}$ it would lose its energy and be scattered through 90° from its initial direction on a lengthscale of $\sim$ 100 cm. So although it would generate polarized radiation it would never be observable, since the thermal Hα producing layers, against whose emission it is competing, are $\sim$ 5km thick and are themselves strong Hα emitters. However a proton beam of the same velocity could generate sufficient polarized radiation to be observable over the thermal background - it practically maintains its initial pitch angle distribution, over large column depths, and a proton travelling at 2.65×10^8 cms $^{-1}$ thermalises on a length scale of $\sim$ 10 km. Of course, a higher velocity electron beam, penetrating deeper into the chromosphere could generate observable polarization and even though the excitation cross-section decreases with velocity we could always demand a higher beam flux to compensate. Nonetheless there is a way in which we can distinguish between a low energy proton beam and a high energy electron beam.

We know from theory (fig (1.15)) that the polarization fraction of impact excited Hα radiation becomes negative above an impact velocity of around 6.5 x 10^8cm s^{-1}. This means that as the velocity increases, the polarization vector, which was previously observed in the direction parallel to the beam of exciting particles, goes to zero and reappears in the direction perpendicular to the beam direction. Now transfer the beam and observer to the solar geometry (figure 2.3). A system of axes is defined in which the beam direction is chosen as the $z-$ axis, and is in the local vertical, the x axis lies in the plane containing the z-axis and the line of sight of the observer, and the y axis is perpendicular to these two. The beam need not of course be in the local vertical direction - it is guided by the local magnetic field above the region and is in the field direction, whatever that may be. Here we assume that the field in the chromosphere and in the corona is nearly vertical (but note that in the very low density transition region the field fans out rapidly because of decreasing gas pressure and is no longer vertical) and for a simple geometric picture we can at present use a vertical beam. The polarized Hα emitting area is a sufficiently small and distant part of the solar disc that all of it is observed in the same plane, at very nearly the same angle ψ to the local vertical. The polarization emitted by atoms excited in this geometry, from equation 1.9 is $P = I_{\|} - I_{\perp} \backslash I_{\|} + I_{\perp}$, and is at a maximum when viewed at 90°. The parallel electric vector of the photon is in the beam direction, whilst the perpendicular vector is normal to the plane containing the beam direction and the line of sight - the y direction. (nb There is cylindrical symmetry here - if we look in any ϕ direction for a given θ the parallel vector always has the same magnitude.) If the intensity in the z direction is larger than that in the y direction then the polarization vector is oriented along the z direction and the polarization which we see will be projected so that it appears to be in the disc centre direction. This is what is observed during solar flares. If the perpendicular vector were larger, the net polarization would be at right angles to the

disc centre direction. So if the polarization is produced by a beam of particles then a low velocity beam results in a polarization vector directed towards the disc centre (a positive polarization in this geometry), whilst a high velocity beam gives a polarization vector perpendicular to the disc centre direction (a negative polarization), contrary to observations.

On this basis we can eliminate the high velocity vertical electron (or proton!) beam and limit our consideration of vertical beam distributions to intermediate or low energy proton beams. However, note here that if we have a distribution of high velocity particles present, which peaks in the local horizontal direction then there is the possibility that a polarization fraction in the beam centre direction will result. This geometry will be further discussed in chapter 3.

§2.1.4 The Background Emission

Any beam generated polarized Hα must compete with the ambient thermal emission of the solar atmosphere, which acts as a 'diluting' component of the radiation. It is important that the background radiation field is carefully calculated since (as we shall clearly see) innocent - looking approximations can result in great under- or overestimates of the the total polarization resulting. Thermal Hα emission of the background comes primarily from collisional excitation of ambient neutral hydrogen atoms to level 3 by free electrons, with some of the level 3 population coming from recombination also. Downwards transitions occur spontaneously from level 3 to 2, resulting in the emission of an Hα photon. A discussion of these matters appears in §1.1.6. In their 1990 paper Hénoux *et al* calculate the beam and thermal excitation rate under the assumption that all thermal Hα emanates from a narrow, uniform temperature layer. They assume that this layer is at temperature $9\times\ 10^3$K, which lies within the temperature range of the most strongly emitting region (as shown in fig 1.6) of $\sim 8.5 \times 10^3$ K to 2.6×10^4 K. But we show here approximate value is not really adequate. The dominant excitation process is collisional excitation by electrons in a Maxwellian distribution (cf eq 1.14) and the number of electrons above the excitation threshold, E_o, of 12.1 eV is very temperature sensitive. We integrate the Maxwellian from the threshold velocity to infinity (giving the total number of electrons with sufficient energy to excite level 3), viz

$$n_e(E > E_o) = n_e \int_{v_0}^{\infty} \frac{4}{\sqrt{\pi}} \left(\frac{m_e}{2kT}\right)^{3\backslash 2} v^2 e^{-mv^2\backslash 2kT} dv \qquad 2.12a$$

$$= n_e Q(\frac{3}{2}, x_o) \qquad 2.12b$$

where Q is the Incomplete Gamma function, and $x_o = E_o\backslash kT$. It is instructive to calculate this for the two temperature extremes of $\sim 8.5 \times 10^3$K to 2.6×10^4K and also for the value employed by Hénoux *et al*, of 9×10^3K. Between the low and the high temperature regions the electron

density varies from 2.25×10^{12} cm^{-3} to 1.09×10^{12} cm^{-3} - approximately a factor of 2. (Likewise the number density of level one hydrogen.) However the Incomplete Gamma function varies from 3.02×10^{-5} to 1.29×10^{-2} over the same temperature range. Evaluated at 9×10^3K, the incomplete gamma function has value 7.80×10^{-5}. Therefore the assumption of a constant temperature in the excitation region leads in this case to a gross underestimation of the thermal component of the emission.

Somewhat secondary to the effect of the uniform temperature approximation is that, in the model of Hénoux *et al* no account is taken of emission from the region which the beam crosses and also that which it does not reach - only this one layer (of unspecified thickness) is considered. In a full treatment, emission from all parts of the atmosphere above the point where it becomes optically thick to Hα should be considered, regardless of whether or not the beam reaches these regions. Also assumed by Hénoux *et al* is that the the Hα thermal excitation cross section, σ_{th}, is single valued and constant throughout the excitation volume. It is assigned a value of $\sigma_{th} = 5.5 \times 10^{-17}$ cm^2 (which is claimed to be the threshold value, although the experimental value near threshold (Mahan 1976) is actually an order of magnitude smaller.) In a Maxwellian electron distribution the number of electrons per unit energy decreases as energy increases and at temperatures where $E_{th} \sim E_o$ it is reasonable to say that the majority of electrons capable of exciting the $1 \rightarrow 3$ transition will be at or just above the threshold energy, but in the full calculation excitation by the entire population is included, with the excitation cross section varying according to experimental findings. In figures 2.4a and 2.4b we graph the rate $q_{1,3}(T)$ of emission of photons, per cubic centimetre per second, due to thermal processes, calculated including all of the above mentioned corrections, for flare atmospheres F1 and F2. We can compare the result of the exact calculation with that arising from the approximation in figures 2.5 a and b. In these figures the total Hα intensity visible at the solar surface (obtained by integrating over depth the number of photons emitted per unit volume) is plotted against the position down to which we carry out the integration - that is, the position at which we place the optical boundary. The upper solid line is the result of the full calculation, and the lower dotted line is what is obtained when a uniform temperature of 3×10^9 K is assumed throughout the atmosphere. Evidently, regardless of where we place the optical boundary (within the range of the calculation in figures 2.4a and 2.4b, the total thermal intensity calculated by the approximate method is smaller than that calculated by the exact method - sometimes by several orders of magnitude.

As mentioned above, we must also consider the instrumental effects on the measured Hα flux. The measurements of the polarization were made using an Hα filter with a bandpass of 0.75Å about the Hα line centre. Line emission from a thermal gas is of course broadened by a variety of

mechanisms - Stark broadening in a high density gas, Doppler broadening, natural broadening. The result of a calculation made of the total line intensity will include some fraction which in reality lies outwith the bandpass of the filter. In the solar chromosphere, Stark broadening (broadening due to perturbations by ambient charged particles) affects Balmer series lines formed in high density regions - especially the high order lines. The electron density in the thermal Hα forming regions, of approximately 10^{12}, is not sufficiently high to Stark broaden the Hα line significantly - instead the predominant broadening mechanism is Thermal Doppler broadening - in which the emitted line photons are red or blue shifted due to the thermal velocity of the emitting atoms in the line of sight of the observer. The actual values of the full-widths at half-maximum due to Stark and Doppler effects in the Hα line are

$$\delta\lambda_S = 4.85 \times 10^{-9} n_e^{\frac{2}{3}} \frac{(2s)^4}{(s^2-4)} \sim 0.012\mathring{A} \qquad 2.13a$$

$$\delta\lambda_D = \lambda_o \sqrt{\frac{3kT}{m_h c^2}} \sim 0.34\mathring{A} \qquad 2.13b$$

for approximate Hα forming region parameters of T$\sim$ 10^4K and $n_e \sim 2.2 \times 10^{12}$ cm^{-3}.m_h is the mass of the hydrogen atom. What is the effect on the relative intensities of thermal and beam-excited emission of subtracting the fraction of emission falling outwith the bandpass? It is essentially the same population of level one hydrogen atoms that are emitting both the thermal and the non-thermal components of the Hα line, therefore one might expect the same proportion of the total emissions to be outwith the bandpass. But the intensity of the thermal component depends on the local electron number density as well as on the local level 1 hydrogen number density, whilst the non-thermal emission depends on the latter, and on the spectrum of beam particles at the emission position. So the two types of emission can vary differently with depth. The temperature and therefore the width of the Doppler profile also varies with depth. It is possible that, for example, the larger part of the thermal emission, coming from slightly hotter regions, is outside the bandpass, but that the majority of emission generated by a beam which has reached cooler regions is not broadened so much. This is only one example of what could happen and it is worthwhile to calculate precisely the effect of thermal Doppler broadening as a function of depth on the total thermal and non-thermal components of emission. The Doppler broadened line profile has the form

$$\psi(\eta) = \frac{I_o}{\sqrt{\pi}\eta_o} e^{-(\eta \backslash \eta_o)^2} \qquad 2.14$$

where $\eta = \delta\nu \backslash \nu_o = v \backslash c$, $\psi(\eta)d\eta$ is the number of photons in normalised shifted frequency range η to $\eta + d\eta$, I_o is the total line intensity at $\eta = 0$ and $\eta_o = v_{th} \backslash c$ To calculate the fraction of the total intensity lying within the bandpass,$\delta\mu_f$ of the filter, we integrate over $-\delta\nu_f \backslash 2\nu_o$ to $+\delta\nu_f \backslash 2\nu_o$ The semi-integral can be written in terms of the standard integral

$$\int_0^x e^{-t^2} dt = \sqrt{\frac{\pi}{2}} erf(x) \qquad 2.15$$

erf(x) being the error function. Since the line profile is symmetric about $\eta = 0$, the total intensity fraction can be simply calculated using a NAg routine to evaluate the erf function and multiplying by $\sqrt{\pi}$. Figs 2.4a,b show the comparison between the thermal intensity passed by the filter and the total intensity. In both F1 and F2, the difference between 'filtered' and 'unfiltered' intensities is $\sim$ 20%. In all future calculations, of polarized and of unpolarized emission, the 'filtered' intensities are used.

§2.1.5 The Calculation of Optical Depth in the Chromosphere.

Figs (2.5 a,b) show the values obtained for total Hα number flux (photons per cm^2 per sec) as a function of the position of the optical boundary (the position at which the atmosphere becomes completely optically thick), but as yet we have not indicated how the position of the optical boundary is calculated. It is obviously an important factor. For example, were the optical boundary at a position of 1.42×10^8 cm in model F1, the total visible emission calculated by the approximate method is a factor 100 smaller than that from the exact method; at 1.43×10^8 cm it is a factor 10^4 too small.We assume that Hα photons are absorbed predominantly by level 2 hydrogen in the chromospheric material. The optical depth is therefore the product of level 2 hydrogen number density and line centre absorption cross-section integrated over depth. The line centre optical depth for transition $n_3 - n_2$ is given by

$$\sigma_{\lambda_{3-2}} = \frac{3\lambda_{3-2}}{8\pi}\left(\frac{m_h}{2\pi kT}\right)^{\frac{1}{2}} A_{3-2} \qquad 2.16$$

The plot of optical depth versus position for model F1 shows that the atmosphere can be considered essentially optically thick below a depth of $\sim 1.425 \times 10^8$ cm ($\tau \sim 10$). The variation between optically thin and optically thick occurs over a very short distance - around the position where the neutral hydrogen number density increases rapidly. But the position of $\tau \sim 1$ is $\sim 1.429 \times 10^8$ cm. Referring back to figure 2.4a we see that if the optical boundary is around 1.429×10^8 cm the correctly calculated emission is considerably larger than the estimated value - of the order of 10^3 times larger. This is mainly because the estimated temperature of 9×10^3K is lower than the actual temperature of the region of the maximum emission, and the thermal excitation function increases quite dramatically with increasing temperatures. The situation is not so clear cut with flare F2. The estimated temperature of 9×10^3K is close to the actual temperature at the peak emission so the estimate of Hénoux is not too far out. However the full calculation intensity is still more than an order of magnitude greater than the approximate calculation. Figures 2.6 b shows that the optical depth is changing very rapidly just at this position of maximum emission. According to the numerical data from which 2.6b is plotted the optical depth is exactly 1 at a position of 1.1015×10^8 cm. The numerical results over a spread of just 10 km about the position

of maximum emission are summarised here, indicating the rapid change in this region.

Table 2.2

Postion of Optical Boundary	Total Thermal Intensity photons/cm^2/s (Approx.)	Total thermal intensity photons/cm^2/s (Full Calc.)
1095km	1.78×10^{18}	2.78×10^{19}
1100km	9.76×10^{16}	1.03×10^{19}
1105km	1.12×10^{11}	9.44×10^{16}

Evidently the aproximate method of calculating thermal Hα intensity once again gives an incorrectly low value.

§2.1.6 The Basis of the Thick Target Calculation of Beam - Excited Polarized Radiation

If at position z in the solar atmosphere the intensities of polarized and of thermal radiation produced per unit volume by a nonthermal particle distribution are $I_{pol}(z)$ and $I_o(z)$ respectively, and the polarization fraction of the polarized component is $P(z)$, then the net polarization observable from this unit volume is given by

$$P_{net}(z) = \frac{I_{pol}(z)P(z)}{I_{pol}(z) + I_o(z)} \qquad 2.17$$

In the solar atmosphere thermal excitation processes are operating also, in which case Equation 2.12 must have included in it a term for the thermal background radiation. This term is added to the I Stokes' parameter on the denominator (the I Stokes' parameter simply the nonthermal total Hα intensity generated per unit volume per unit time). If powered by a beam, the non-thermal excitation process is not operating in one single narrow layer - it occurs throughout a finite volume and the intensity and polarization of the emission changes as the beam energy degrades. The Stokes' parameters of the polarization must be integrated over volume, as was indicated in §1.2.6. The total polarization is

$$\mathcal{P}_{TOT}(90) = \frac{Q_{TOT}}{I_{TOT}}$$

where (from equations 1.16)

$$Q_{TOT} = \int_{z_o}^{z_1}\int_{v_{th}}^{\infty} \frac{f(v,z)v(z)[\Sigma_{l=1,3}P_{l,90}(v)\sigma_{l,90}(v)]\mathcal{T}(z)}{3-\Sigma P_{l,90}(v)} dv(z)dz \qquad 2.18a$$

and

$$I_{TOT} = \int_{z_o}^{z_1}\int_{v_{th}}^{\infty} \frac{f(v,z)v(z)[\Sigma_{l=1,3}\sigma_{l,90}(v)]\mathcal{T}(z)}{3-[\Sigma_{l=1,3}P_{l,90}(v)]} dv(z)dz + \int_{z_o}^{z_1} I_o(z)\mathcal{T}(z) \qquad 2.18b$$

Notice two things about these equations - firstly that since the target is collisionally thick, velocity is a function of position, and secondly that it is necessary to sum over the cross sections and polarization fractions of all the angular momentum substates seperately, since they all vary with velocity in different ways. The factor $\mathcal{T}(z)$ which has now been introduced is a transfer function - describing the absorption, emission and scattering of polarized radiation through the solar atmosphere. In practice, the transfer of polarized radiation in a non-transparent atmosphere is a nasty problem to solve, although numerical treatments do exist (Rees 1987), and analytic treatments for the case of single scattering by an electron are being developed in the context of an intrinsically polarized star viewed through a circumstellar envelope (Fox, 1993). However, we will not perform explicit calculations of this effect, but will bear in mind, when summarising the results of our simulations, that the result of transfer is depolarization. We use a transfer function which is a step function, with value 1 down to where the atmosphere becomes optically thick to Hα (at z_0) and zero below. z_1 is the point in the upper atmosphere where Hα production ceases because there is no longer any neutral hydrogen present.

For any particular beam type the function $f(v,z)$ can be calculated, and equations 2.18a,b numerically integrated - a process which is described in the following sections for two different beam types.

§2.2 Mono - Energetic Beam.

Although we aim to model a beam with a physically reasonable distribution, in particular a power-law distribution, we present some initial calculations for a mono-energetic beam. (It is sensible to do such relatively simple calculations first before complicating the situation by having more than one particle energy injected at a time.) Since we know roughly where the bulk of the atmospheric neutral hydrogen is, we should be able to interpret the polarization profiles in terms of the energy which the beam has as it reaches the hydrogen rich area. This may be be of help when discussing power-law beams, in which case there will be a 'smearing' effect due to having a particle energy distribution at each height.

A mono-energetic beam has a distribution function given by

$$f(v,z) = F_o\delta(v(z))$$

where F_0 is the total injected beam flux, and $v(z)$ (or rather $E(z)$) is calculated using equation 2.6 or 2.7. This form of beam flux renders equations 2.17 simple, since the integral over velocity disappears, and the remaining integral over z is simply multiplied by F_0. The equations to be

integrated are then

$$Q_{TOT} = F_0 \int_{z_1}^{z_0} \frac{n_1(z)\Sigma_{l=1,3}[\sigma_{l,90}P_{l,90}]v(z)T(z)}{3 - \Sigma_{l=1,3}P_{l,90}} dz \qquad 2.18a$$

$$I_{TOT} = F_0 \int_{z_1}^{z_0} \frac{n_1(z)\Sigma_{l=1,3}\sigma_{l,90}v(z)T(z)}{3 - \Sigma_{l=1,3}P_{l,90}} dz + \int_{z_1}^{z_0} n_h(z)n_e(z)c_{1\rightarrow 3}T(z)dz \qquad 2.18b$$

Where $c_{1\rightarrow 3}$ is the thermal excitation coefficient (§1.1.4).

§2.2.1 Computational method

It is not possible to find neat functional forms for the quantities in the integrals above. The only feasible method is to evaluate the integrands numerically as a function of position, and integrate using a suitable NAg routine - D01GAF integrates a function which has been specified at a number of values (using a four-point finite difference method). There are several steps in the numerical procedure - the first of these is to obtain values for atomic and atmospheric data at the position values to be used in the integration. (Note that the atomic data depends only on particle velocity which depends only on position.) The atomic and the solar data used is too sparse for accurate computations - we need more points of evaluation than the data provides. It is therefore necessary to interpolate between the data points, using routines from the NAg libraries. In the case of the atomic data, it is also necessary to "patch" the experimental, low energy end of the energy range onto the theoretical high energy end, as described in section (1.2.5). This data does not vary too rapidly, and the interpolation routine is able to cope with the rise and fall of the cross sections without becoming unstable. Figs 1.19 and 1.20 show examples of the patched data and the experimental data points. There are 'glitches' in the curves, which may manifest themselves as similar glitches or instabilities in the resultant calculations. But overall, the fit is good and the curve smooth. The chromospheric data is grouped in three broad sections. Density and temperature parameters vary slowly and smoothly in the low chromosphere; $dT\backslash dz \sim$ 5K km^{-1}, and the data points here are spaced over $\sim$ 25km . There follows a region in which the change is rapid $dT\backslash dz \sim$ 7500K km^{-1} and data at 0.25 km intervals is given. In the high chromosphere and transition region the parameters are still changing rapidly but are given at intervals of $\sim$ 2km. When an attempt was made to fit this region with a single interpolation it was observed that the results were unstable and gave negative values for density and temperature. To avoid this problem it was thought reasonable to take the log_{10} of the density and temperature values, to interpolate this set of slowly varying values, and then generate the structure. This still resulted in a reconstruction which was unstable between the widely spaced data, since the spline functions generated fitted the rapidly varying data at the expense of the slowly varying data. It was decided to split the interpolation in two - slowly and rapidly varying regions - which proved very satisfactory, giving a smooth interpolation fitting the data to better than 0.1%.

Now we describe the steps in the integration. The atmosphere is split vertically into a large number of height intervals and at the intersection between the 'i'th and 'i+1'th interval we have an 'evaluation point', z_i, which is associated with array elements A_i and B_i (for the I and Q Stokes parameters respectively). At each z_i, values of the atmospheric parameters are calculated using interpolating splines, followed by the ionisation fraction, the Debye length and the thermal Hα emission. At z_0 the beam energy is E_0, and throughout the atmosphere, the 'i'th beam energy value is related to the 'i-1'th energy value by

$$E_i = \left(E_{i-1}^2 - 2n_i(z_i - z_{i-1})K(z_{i-1}, E_{i-1}) \right)^{1\backslash 2} \qquad 2.19$$

n_i is the density (of protons) at z_i. $K(z_i, E_i)$ is a function of both depth and energy - viz

$$K(z_i, E_i) = \pi e^4 \left(x(z_i)\Lambda(E_i) + (1 - x(z_i)\Lambda'(E_i) \right) \qquad 2.20$$

This is only a slowly varying function of energy but, since it is simple to evaluate, it is included in the calculation for completeness. Once the energies E_i have been found, the cross sections for excitation of each of the atomic substates and polarization fractions corresponding to these values are calculated. We are now in a position to evaluate the integrands in expressions 2.18a,b for the Stokes' parameters, which are stored in arrays A_i and B_i. To account for the effect of the 0.75 Åfilter bandwith, the array entries are multiplied by the fraction of total intensity falling within the bandwidth (equation 2.15) The set of data (z_i, A_i) and (z_i, B_1) are then integrated numerically, using NAg routine EO2BAF. The Q parameter integration is divided by the I parameter integration, and the result is the total polarization, when viewed at 90° to the beam direction. (This value must subsequently be corrected the effects of viewing the incedent proton direction at an angle other than 90°). There are problems with this integration scheme. Divisions in height must be sufficiently small in the region where density and temperature are increasing rapidly that the energy evolution of particles entering the region can be followed in detail - e.g., in equation 2.19, if the interval in column depth given by $n_i(z)(z_i - z_{i-1})$ is large ($\sim 10^{18}$) a proton of energy $E_{i-1} = 100$ keV is reduced to $E_i = 0$ within the space of this one division. The cross section and polarization fraction maximise between 0 and 100keV, but are small at these extremes. Since it is only the energies at the evaluation points that matter in the calculation, the resulting polarization fraction is an underestimate. Of course, if the number of evaluation points is increased the run time increases also. To find an acceptable trade - off between time and accuracy, the programme was run several times with the number of points increasing by a constant additive factor until the polarization percentages resulting from subsequent runs differed by no more than 0.1% (absolute). It can be seen (figure 2.7a) that the results are not smooth for certain parameter choices. In figure 2.7a, the region of calculation was extended into a part of the atmosphere where the density and temperature vary so rapidly that it was not possible to make divisions in height small enough -

if the difference between two adjacent height points was less than a certain amount ($\sim 10^{-2}$ km) the interpolation routine did not recognise the two points as distinct and the routine failed. The jagged profile in the figure is a result of injected 'beam particles' of different energies all stopping in the same interval in the atmosphere because it was not possible to increase the resolution further, but underlying shape of the profile, is sufficient to show the basic behaviour.

As mentioned above, the results of the calculation are polarization fractions viewed at 90° to the beam direction. The effect of viewing at an angle other than 90° is a reduction in the polarization. Let the observations of polarization be made at an angle θ to the beam direction where $\theta \neq 90°$. The observed fraction $P_{obs}(\theta)$is then related to P_{90} by

$$P_{obs}(\theta) = \frac{P_{90} \sin^2 \theta}{1 - P_{90} \cos^2 \theta} \qquad 2.21$$

which can be solved for a given observation to give the equivalent polarization at 90°. θ is the heliographic angle - the angle between the line of sight to the flare and the local vertical, which can be worked out from the heliocentric latitude and longitude (δ, λ) viz

$$\cos \theta = \cos^{-1}\left(\frac{\cos \lambda}{\cos \delta}\right) \qquad 2.22$$

For the July 17th 1982 flare, (δ, λ) = (11N,38W) the observed fraction of 2.0 % translated into an equivalent 90° value of 5.5%. We now compare this value with those obtained from numerical integration.

The procedure outlined above for calculating the net polarization fraction is followed, for a number of initial beam energies and figures 2.7 a,b,c and d, and 2.8 a-d show the variation of the net polarization fraction observed at 90° from the beam direction, as a function of beam particle energy input at the top of the chromosphere - this is arbitrarily chosen as the last point of the Machado *et al* (MAVN) atmospheric model, the effects of the overlying material being included later. Both F1 and F2 have been studied. The first comment to make is that for a given resultant polarization fraction, the total proton flux input to model F2 is far higher than that input to model F1. This is a consequence of the increased thermal emission in F2. Secondly, the peak polarization arises at a higher beam energy in F2 than in F1. Since the column depth traversed before reaching the neutral-hydrogen rich layers is greater in F2 than in F1, higher energy particles are required to reach them and still have sufficient energy to excite polarization. Note that for each model, plots are made corresponding to a number of positions of the optical boundary. Since the modelling approximation that we make - i.e. that the atmosphere changes discontinously from completely optically thin to completely optically thick, is patently not true, we must make sure that the results of our calculations do not depend to critically on precisely where we place the

boundary. (Note though, looking at the way the optical depth varies it is not too bad, and is, in any case, the only one we can make if we wish to ignore radiative transfer.) We therefore test the effects of moving the optical boundary position. Obviously we do not wish to place it in the two extremes (see figures 2.6 a,b) - optical depth below about 10^{-3} or above about 10, but we vary its position in the region in which the optical depth is changing rapidly. Placing the optical boundary within the optically thick region, above about 10, would be equivalent to neglecting the depolarizing effect of the optically thick material which emission from below the boundary must traverse, and hence overestimating the resulting polarization. On the other hand, placing it in the optically thin region would result in the emission from the hydrogen rich layers being discounted, with only the meagre emissions from the upper atmosphere being included.

In each plot, the four lines show polarizations from a variety of proton fluxes. Not surprisingly, the higher the proton flux, the higher the net polarization. Notice also that as the position of the optical boundary is lowered, the beam energy giving maximum polarization increases . Let us examine in detail the results for model F1,given in figures 2.7a - d. Below is a table summary of the results of the four graphs.

Table 2.3

position of op. boundary (km)	**optical depth**	**Energy (keV) at max^m polarization**	**Flux(min) protons cm $^{-2}s^{-1}$**
1431	5.4×10^{-3}	65	10^{18}
1430	0.19	70	5×10^{17}
1429	1.02	75	5×10^{17}
1428	3.16	75	1×10^{17}
1425	12.5	100	10^{16}

The third column is the energy at which the polarization fraction maximises, the fourth is the approximate minimum flux of particles at this energy necessary to produce a polarization fraction comparable with that seen. Both these parameters vary little over the optical depth range range 0.19 to 3.16. With the optical depth set at much less than 1, the flux required to get a large polarization fraction increases, as has been suggested would be the case. Similarly, a large polarization fraction is obtained for a significantly smaller flux if the position of the optical boundary is set too low. This is because the column depth of neutral hydrogen whose emission escapes increases dramatically as the position of the boundary is lowered. Both beam - excited and thermal emissions rise. But since the thermal emission emanates predominantly from the slightly higher temperature regions, above a height of $\sim 1.428 \times 10^8$ cm, and moving the boundary downwards is 'exposing'

more low temperature material, the relative increase in thermal emission is not large. However, the beam excitation, which depends on the beam energy and the hydrogen density, but not the temperature, is greatly enhanced, since we see emission from increasingly hydrogen rich regions. So the maximum flux necessary decreases significantly, from 5×10^{17} to 10^{16} protons $cm^{-2}s^{-1}$. We notice also that as the position of the optical boundary is lowered, (which increases the depth of the atmosphere included in the calculation) the beam energy for which the polarization maximises increases. If the boundary is at optical depth 5.4×10^{-3} the polarization fraction maximises for a beam energy of 65 keV, whereas at 12.5, it maximises at just over 100keV. We can easily explain this effect. The impact excitation cross section maximises at a value of about 60 keV for protons, and if the beam is monoenergetic, all protons attain this energy at the same position. Recall that the number density of atoms in level 1 increases as height in the atmosphere decreases. Then the beam energy at injection which gives maximum polarization is that which has been degraded to $\sim$ 60keV just above the optical boundary. As the position of the optical bounday is lowered, it requires a higher energy of injection for this condition to be met. Below is a table of the beam, parameters for model F2. The same trends appear as in model F1.

Table 2.4

position of op. boundary (km)	optical depth	Energy (keV) at max^m polarization	Flux (min) protons $cm^{-2}s^{-1}$
1103	8.3×10^{-4}	100	5×10^{20}
1102	0.11	130	5×10^{19}
1101	1.57	155	10^{19}
1100	20.9	191	10^{17}

Let us consider the implications of the modelling for the proton beam driven picture of Hα impact polarization. We consider firstly the results for flare model F1, which is the less energetic of the two flares. All the graphs peak strongly at an energy of 65 to 100 keV, with virtually no emission from beams entering the chromosphere with energy less than 60 keV. Such beams have had their mean energies reduced to less than the Hα excitation energy before they have encountered significant numbers of level 1 hydrogen atoms (n_1). As mentioned before, it is most reasonable, in terms of the assumptions made in our modelling, to put the boundary at 1.429×10^8 cm. The appropriate graph shows a maximum in polarization fraction at about 70 keV with the graph crossing the zero line at $\sim$ 200 keV. There is no significant polarization from beams of less than 60 keV. We can understand the shape of the graph in terms of the relative intensity of non-thermal (polarized) and thermal emission from various energy beams. This depends primarily on the ratio of the thermally emitting column depth (of level 1 hydrogen) to the (level 1) column depth traversed by the beam whilst the

beam energy is such that the excitation cross section is near maximum (between energies of 80 keV and threshold, say). Initially 60 keV proton beams traverse 9.34×10^{14} cms^{-2} of n_1 before reaching threshold energy, compared with the thermally emitting column depth of $\sim$ 9.46 10^{15} $n_1$cms^{-2} (with optical boundary at 1.429×10^8 cm) so we expect the relative intensity of collisional to thermal emission to be small. With 70 keV initial energy, the beam traverses 9.5×10^{15} n_1 cms^{-2} of n_1 before reaching threshold. The relative intensity is therefore larger. However, as the beam energy at the top of the chromosphere increases further, the beam traverses significant n_1 column depths whilst the beam particle energy is high. The excitation cross section decreases, and more and more of the collisional Hα emissions are produced with negative polarization fractions, until at an injection energy of greater than 200 keV the net polarization fraction is shown by the graphs to be negative. This would manifest itself as a polarization vector lying perpendicular to the disc centre direction, in contradiction to observations. This allows us to completely rule out mono - energetic beams of mean energy above 200 keV as the source of polarization.

With the optical boundary at 1.429×10^8 cm, only 70keV protons with a flux of 5×10^{17} protons cm^{-2} give a polarization fraction large enough to be in agreement with observations. In terms of total energy flux arriving at the top of the chromosphere, this works out as 5.6×10^{10} ergs cm$^{-2}s-1$. This is not an enormous energy flux by the standards of the impulsive phase of solar flares, but its duration and area are large. We can decide on the grounds of the total energy transferred whether excitation by a monoenergetic proton beam is feasible. If it is to account for the entirety of the polarization observed in July 17th 1982 flare, the beam must sustain 5.5% polarization (= 2.0% plus correction for angle of observations) for 30 minutes over an area of more than 3.6 x 10^{18}cm^2 - at times $\sim 8 \times 10^{18}$ cm^2 - which gives an energy budget for protons arriving at the chromosphere of $\sim$ 4 x 10^{32} ergs, which is an extremely large flare energy. And we have still not taken into account that the beam must first traverse the corona and lose energy there before encountering the chromosphere. In the flare corona of 10^7K, the cold target approximation for energy loss is no longer valid, and it is necessary to use a warm target treatment. This is briefly described below.

Warm Target Approximation

The warm target equations are somewhat more complicated than those for a cold target (see Trubnikov, 1966). The proton energy degradation equation for a fully ionised target approximates to

$$\frac{dE}{dN} = \frac{-2\pi e^4 \Lambda}{\mu E}\left(\frac{m_p}{m_e}\right)\left(1 - \frac{3\sqrt{\pi}}{4x^{3/2}}\right)^{-1} \qquad 2.23$$

where $x = (m_e/m_p)(E/kT)$. Figure (2.9) illustrates the difference between the proton stopping

depth calculated with the cold target and the warm target approximations at a temperature of 10^6 K. The dashed line illustrates the cold target extrapolation into an inappropriate region (from Tamres 1986). Evidently, using the cold target approximation gives a stopping depth considerably smaller that which would actually exist -ie the protons traverse a greater column depth in a warm medium than in a cold one. If the target is not completely ionised an additional term for the energy and velocity changes on the neutral particles must be added, but as was mentioned before, most of the beam energy is lost to the ambient electrons in the target, therefore the above expressions will be approximately correct. In the flare corona, hydrogen will be completely ionised anyway, (but it is possible that other cooler and unionised regions of the chromosphere will satisfy the warm target condition for certain beam energies).

Equation 2.23 solves to give a quartic for $E_1^{1/2}$, the beam energy at coronal injection, in terms of E_o, the energy of the beam entering at the top of the chromosphere, and the total coronal column density N. N can be calculated from data given in the semi empirical flare models. An overlying mass column density is quoted in MAVN for each of the flare atmospheres. For Flare F1 it is 3.14×10^{-4} g cm^{-2}, or 1.88×10^{20} protons cm^{-2} and for F2 it is higher at 3.46×10^{-3} g cm^{-2}, or 2.16×10^{21} protons cm^{-2}. The quartic is

$$E_1{}^2 - E_0{}^2 + 3\sqrt{\pi}U^{3\backslash 2}(E_1^{1\backslash 2} - E_0^{1\backslash 2}) = \frac{K\Lambda N}{\mu} \qquad 2.24$$

This is the solution for a completely ionised plasma. U is the ratio $E\backslash kT$ and μ is the proton pitch angle cosine, which we take as zero. It is necessary to find the roots E_1 of this equation, but the solution, although analytically possible, is messy. It is easier to solve by means of a Newton-Raphson iterative method. A convergence to 0.1% was demanded. The results of the calculation are shown in figure 2.10. The energy with which the beam arrives at the top of the chromosphere is along the x - axis, and the corresponding energy with which it must have been injected at the top of the corona is up the y - axis. Two curves are plotted for model F1 and F2. These show that for flare F1 the energy of protons at the top of the corona is a factor of approximately 1.5 larger than that of protons at the top of the chromosphere, in Flare F2 this factor is 5 - 10 depending on E_0.

We can now use all this information to set a lower limit on the total energy in a mono-energetic, low energy proton beam, necessary to power the observed impact polarization. In model F1 the maximum polarization occurs when $E_0 = 70$ keV, which corresponds to an E_1 of ~ 150 keV. The result arrived at for the total energy contained in the proton beam with an entirely cold target must therefore be multiplied by ~ 2, bringing the required total energy up to 8×10^{32} ergs. It is

unusual to have a flare with total energy larger than $\sim 10^{32}$ ergs, and it looks, from this analysis, as if the mono-energetic proton beam model of polarization is too energetically demanding to be reasonable, because of the large flare area and duration. It is possible however that model F1 is an inappropriate atmospheric model - as it describes the atmosphere deduced in a class of small flares whereas F2 describes that appropriate for a larger flare. Identical analysis is carried out using the F2 atmosphere, but because this atmosphere is on average denser and hotter than F1, it requires 1) larger beam energy to penetrate to the hydrogen - rich layers and 2) a larger beam flux to generate sufficient polarized intensity to be visible over the thermal background. The graphs for optical depths between 0.19 and 3.16 show that the polarization peaks at between 130 and 155 keV, and that only a flux of between 1 and 5 $\times 10^{19}$ protons cm $^{-2}s^{-1}$, or an energy flux at the chromosphere of $0.25 - 1.04 \times 10^{13}$ ergs $cm^{-2}s^{-1}$ is big enough to generate the required polarization fraction. Referring to graph 2.10 we see that the beam energy at the point of injection in the corona would have to be 2250 keV. To generate the observed polarization fraction in a flare atmosphere of the type described by F2 requires a colossal $2 - 13 \times 10^{35}$ ergs in total, which is totally unreasonable.

§2.2.3 Varying Atmospheric Parameters

The MAVN flare model atmospheres were devised in the flash phases of two small groups of flares - one group of Hα class F flares and the other of class N flares. Although they span a range of conditions, it is possible that they do not adequately represent the flare of July 17th 1982 with which we are concerned - particularly since each flare observation on which the MAVN models were based lasted no more than 4 minutes each, whereas the polarization duration is much longer ($\sim 2 \times 10^3$ s). It is likely that the atmosphere is returning to its cooler pre-flare state during at least the latter part of the polarization observations. It is thought that during the flare gradual phase the the hot corona cools, on a conduction timescale given by

$$\tau_c = \frac{3nkL^2}{KT^{5\backslash 2}} \qquad 2.25$$

where L is the length of the overlying loop, K is the classical conductivity. If we assume a coronal temperature of $10^6 - 10^7 K$, a loop length of 10^9 cm and a density of 10^{10} particles $cm^{-2}s^{-1}$ then the timescale on which the corona cools is 10^3 seconds. If the transition region and chromosphere are heated, during the gradual phase, by conduction from the corona, then after 10^3 seconds they too will start to cool as the coronal heat source becomes exhausted. The investigation of a flare atmosphere which is not so hot (or dense) as those given in F1 and F2 is thus justified.

Vernazza, Avrett and Loeser (1980) have as mentioned already, developed a series of semi - empiri-

cal model atmospheres representing various parts of the quiet sun. We choose to use the parameters from their model C ' the mean quiet sun '. There are other models more representative of conditions in the cooling chromosphere - i.e., brighter than the mean quiet sun, and magnetically active, but only for model C are the necessary data on hydrogen level populations presented. It would not be a simple matter to calculate corresponding values for a more suitable model, as the atmosphere is not in LTE, and there are significant departure coefficients to be evaluated. Additionally, the data presented for models apart from C include only the total hydrogen (atomic and ionised) number density, and the total electron number density, liberated from all species present, are given. To use the Saha-Boltzmann equation to evaluate populations we need specifically the proton number density and the number density of electrons due to the ionisation of hydrogen. In the absence of these values we cannot attempt the calculations.

It is obvious, we feel, that a hotter and denser flare atmosphere will only increase demands on the proton beam model, since there will be greatly enhanced thermal emission. Therefore we do not study an example of this.

We calculate the polarization resulting only for one value of the position of the optical boundary - chosen using the same criteria as were employed in models F1 and F2 - ie that the optical depth equals one and is changing rapidly. Figure 2.11a shows the variation of optical depth with depth,and it is evident that the value $\tau = 1$ does not lie in the region of most rapid variation, so the that, as might be expected, the effect of having a cooler atmosphere is to depress the level of thermal Hα and hence to allow formation of observable polarization for low fluxes of protons - as few as 10^{14} protons cm^{-2} s^{-1}, with an energy of 100keV each. The variation of polarization fraction with beam energy for fluxes from 10^{14} to 10^{16} proton cm^{-2} s^{-1} is shown in figure 2.11b. The necessary energy and flux give an energy budget of only 10^{29} ergs at the top of the chromosphere. To calculate the injection energy we use a coronal column depth an order of magnitude smaller than that of F1. With this value there is negligible difference between coronal and chromospheric injection energies, so the total energy budget in the quiet sun remains at 10^{29} ergs. This is certainly a reasonable energy for a flare, but should only be considered as an **absolute** lower limit, since the atmosphere is too cool for a realistic post-flare atmosphere, where we expect that the temperature will be higher and the thermal emission will be enhanced above the quiet sun value.

§2.2.4 Conclusions of the Mono-energetic Proton Beam Model

From the above discussions we conclude that it seems highly unlikely that a monoenergetic proton

beam could cause the observed linear Hα polarization during solar flares, on the grounds that the energy required in the beam in all reasonable scenarios, greatly exceeds that expected in even a large flare. We have tested two solar atmospheric models and the more energeric flare requires a more energetic, higher number density proton beam to produce the polarization than the smaller flare does. We have produced plots of the variation of polarization with beam energy for a variety of positions of the "optical boundary" and in so doing hope to estimate the absorption, but not the depolarization effect of radiative transfer. Note that any depolarization by the atmosphere can lead only to the demands on the energy budget increasing. We have also repeated the calculation using a quiet sun model as we recognise that the flare models of MAVN may not represent the entire likely range of atmospheric conditions during a flare, particularly towards the end of the thermal phase when the atmosphere is cooler (but still most likely above the temperature of the quiet sun) . But within all these variations the monoenergetic beam remains an unlikely if not impossible candidate.

§2.3. A Power - Law Beam Spectrum

Having seen the behaviour of a monoenergetic beam and understood the variation of the polarization fraction in terms of the variation of the excitation cross section and of the beam transport processes, we will add complexity to the system by changing the beam spectrum to a power law. This form of spectrum is chosen since it is 1) reasonably easy to deal with and 2) justified (in the case of electrons anyway) on the basis of observations of X-ray spectra, which also exhibit a power law spectrum near the time of maximum burst intensity. Brown (1971) showed that using the Bethe-Heitler form of the cross-section for electron Bremsstrahlung, such spectra could be analytically inverted to yield the energy spectra of the particle population producing them, in which case a power law of smaller spectral index results. The mathematical description of a power law spectrum is

$$\begin{aligned} F(E) &= F_1 E^{-\delta} \qquad E \geq E_c \\ F(E) &= 0 \qquad\quad E < E_c \end{aligned} \tag{2.26}$$

$F(E)dE$ is the number of particles of energy in the range E to E + dE per cm^2 per second. δ is the 'power law index', F_1 is a constant related to the total beam flux, N_o (see later), and the cut off energy, E_c which the lowest particle energy present. The number of particles in a power law spectrum increases with decreasing energy. By multiplying (2.13) by E and integrating from E_c to ∞ we calculate the total energy residing in the beam. The value is

$$E_{TOT} = \frac{1-\delta}{2-\delta} F_o E_c \tag{2.27}$$

Evidently $\delta > 2$. In the case of an electron beam producing hard x-rays the cutoff is generally taken as 20 keV, (this is called into dispute by some authors eg Simnett (1985) and it is somewhat

of an ad-hoc value). However, in proton-driven models of solar flares (Simnett 1985), no such cut-off value is defined or suggested, although a power law spectrum is still invoked. There must of course be a cut-off energy if the total beam energy is to be finite.

The value of δ for certain energy ranges has been deduced using satellite observations of energetic proton events (see Svestka, 1976). However observations do not extend as far down as 100's of keV. At high energies, δ is large, ~ 5, and averages at a value of 2.9 for energies 20 - 80 MeV. It is not possible to fit the entire solar proton event with one power law index. The average electron spectral δ is ~ 4. Low values of δ mean that the bulk of the energy resides in the high energy part of the spectrum - the spectrum is "hard". A "soft" spectrum has a high δ. We will investigate the production of polarized radiation by beam with a variety of values of δs and E_cs.
As in the case of a monoenergetic beam, we choose an initially unidirectional, vertical proton beam since it is obvious that as the most extreme case of an anisotropic distribution, the polarization it generates is larger than any other angular distribution (for a given velocity distribution). The effects of a cylindrically symmetric anisotropic distribution can be introduced by including the *anisotropy factor* as defined in Henoux et al (1983) and described in section (1.2.6)

§2.3.1 Preliminary Discussions on the Effect of a Power Law Spectrum

The mono-energetic beam was clear to follow since the excitation cross section and polarization fraction maximised for all particles at the same time. It is in retrospect obvious that the maximum polarization will occur more or less when the energy of beam particles when in the most hydrogen rich regions is the optimum for exciting the Hα transition. With a power law beam there may be a fraction of the total population at any given position which is exciting polarization with a positive direction but there will certainly always also be a fraction (possibly bigger) exciting polarization with a negative direction, since the beam spectrum is continous and extends to infinity (theoretically). From our work on the mono - energetic beam we know the particle energy at the top of the chromosphere which produces the highest positive polarization fraction, and for a power law beam to produce a similarly high polarization we must have a large proportion of the injected particle population concentrated around this energy, without having too many in the high energy tail. With an appropriate power law it is possible, at all points in the atmosphere, to have a fraction of the particles at the optimum excitation energy, efficiently generating polarization whereas particles in a monoenergetic beam attain this optimum excitation energy in only a narrow region. But it is expected that the bulk of the polarization must still be generated in the relatively narrow hydrogen rich layers, by particles starting out at ~ 70 keV (from the monoenergetic beam calculation). So the most efficient form of power law spectrum will be one with a cut-off energy

of $\sim$ 70 keV, and with a high power law index. We have already seen that protons with energy $<$ 70 keV produce essentially no polarization, so lowering the cut-off energy would not help at all, and only increase the total energy necessary. High energy protons similarly do not substantially increase the total impact emission, and will in fact decrease the net polarization through the generation of negatively polarized photons. It is not obvious that a power law beam will ever be as efficient at generating polarization as a monoenergetic beam.

The calculation is similar to that carried out for the mono-energetic beam, with the added complication that there is an additional integration to be done, over the beam energy spectrum at each depth evaluation point, before the integration over depth is performed. The term $f(v,z)$ appearing in equations 2.17a,b is replaced by $F(E(z))$ - dependent on both variables. The Stokes' Q and I parameters are now given by

$$Q_{TOT} = \int_{z_1}^{z_0} n_1(z) \int_{\epsilon_{min}(z)}^{\infty} \frac{P_{90}(E(z))\sigma(E(z))F(E(z))}{3 - P_{90}(z)} dEdZ \qquad 2.28a$$

$$I_{TOT} = \int_{z_1}^{z_0} n_1(z) \int_{\epsilon_{min}(z)}^{\infty} \frac{\sigma(E(z))F(E(z))}{3 - P_{90}(z)} dEdZ + \int_{z_1}^{z_0} n_h(z) n_e(z) c_{1\to 3} T(z) dz \qquad 2.28b$$

The infinite upper limit of the integrals cannot of course be replicated in a numerical routine, but since the beam flux, the polarization fraction and the cross-section all decrease as energy increases, the integral will converge, and a suitably high upper limit can be chosen to give a result to any specified accuracy. $\epsilon_{min}(z)$ is the lowest energy in the beam at position z. The relationship between $\epsilon_{min}(z)$ and the cut-off energy at the top of the chromosphere is given by equation 2.11a i.e.,

$$\epsilon_{min}(z) = E_c \left[1 - \left(\frac{m_p}{m_e}\right) \frac{\mathcal{K}N}{\mu_o E_c^2}\right]^{\frac{1}{2}} \qquad 2.29$$

This decreases with depth and eventually will reduce to the mean thermal energy of the target. However for computational simplicity in other parts of the calculation we do not actually evaluate cross sections and polarization fraction for energies less than about 28keV, since this is the lowest energy experimental data point used in the interpolation routine. At $z = 0$, $F(E, z_0) = F_0(E_0) = F_1 E_0^{-\delta}$. F_1 is related to the total number flux, F_{tot} and the energy cut - off of the initial proton beam, since

$$F_{tot} = \int_{e_c}^{\infty} F_1 E_0^{-\delta} dE$$

enabling us to write

$$F_1 = (\delta - 1) F_{tot} E_c^{\delta - 1} \qquad 2.30$$

E and E_0 are related to one another through equation 2.11a, which has the form

$$E = E_0 \left[1 - \left(\frac{m_p}{m_e}\right) \frac{\mathcal{K}N}{\mu_o E_o^2}\right]^{\frac{1}{2}}$$

where in the full expression for a partially ionised plasma , K is given by

$$\mathcal{K} = 2\pi e^4(x\Lambda + (1-x)\Lambda')$$

We require an explicit form for $F(E(z))$. In the absence of inelastic collisions, proton number flux is conserved, $F_0(E_0)dE_0 = F(E(z))d(E(z))$ and $F(E(z))d(E(z))$ is the number of protons at position z with energies in the range E to $E + dE$, which started out at z_0 with energies in the range E_0 to $E_0 + dE_0$. We can then write

$$F(E(z)) = F_0(E_0)\frac{d(E_0)}{dE(z)} \qquad 2.31a$$

$$= F_1 E_0^{-\delta}\left(\frac{E}{E_o}\right) \qquad 2.31b$$

$$= (\delta-1)F_{tot}E_c^{\delta-1}E^{-1}(E(z)^2 + \left(\frac{m_p}{m_e}\right)K(z,E)N(z))^{-(1+\delta)\backslash 2} \qquad 2.31c$$

by substitution from equations (2.30) and (2.11a), and putting $\mu_o = 1$ for a unidirectional beam which, in its initial progress, is not scattered significantly in angle. However, the protons are being scattered by Coulomb collisions and they will **eventually** have their energies reduced to that of the background population, in which case they will not generate impact polarization because 1) they are below E_{th}, the threshold energy, and 2) their distribution becomes isotropic. Additionally in this calculation we must define a fraction $fr(z_o, z)$ which is the fraction of the total particle flux at z_o which arrives at z having sufficient energy to excite Hα radiation. To satisfy this criterion, a particles must have left z_o with an energy $E'(z_o, z)$ given by

$$E'(z_0, z) = (E_{th} + 2KN(z))^{1\backslash 2} \qquad 2.32$$

Particles with energy less than E' at z_o will not excite Hα impact radiation at z. The total number from the initial injected population which will do so is given by

$$\int_{E'(z_o,z)}^{\infty} F_1 E_o^{-\delta} dE_o$$

and the fraction $f(z)$ is given by

$$fr(z_o, z) = \frac{\int_{E'(z_o,z)}^{\infty} F_1 E_o^{-\delta} dE_o}{F_{tot}} = \left(\frac{E'(z_o, z)}{E_c}\right)^{1-\delta} \qquad 2.33$$

Substituting the expressions for $F(E(z))$ into equations 2.28a, b we have

$$Q_{TOT} = \int_{z_1}^{z_0} n_1(z) \int_{\epsilon_{min}(z)}^{\infty} \frac{fr(z_0,z)P_{90}(E)\sigma(E)F_1(E^2 + (m_p\backslash m_e)\mathcal{K}N(z))^{-(\delta+1)\backslash 2}}{3 - P_{90}(z)} T(z)dEdz \qquad 2.34a$$

$$I_{TOT} = \int_{z_1}^{z_0} n_1(z) \int_{\epsilon_{min}(z)}^{\infty} \frac{fr(z_0,z)\sigma(E)F_1(E^2 + (m_p\backslash m_e)\mathcal{K}N(z))^{-(\delta+1)\backslash 2}}{3 - P_{90}(z)} T(z)dEdz$$
$$+ \int_{z_1}^{z_0} n_h(z)n_e(z)c_{1\to 3}T(z)dz \qquad 2.34b$$

We proceed with the integration as follows. As with the mono-energetic beam case we have an set of evaluation points, but this time energy has a seperate identifier, and our arrays for the integrands in the Stokes' parameters expressions are now $A_{i,j}$ and $B_{i,j}$. i counts position and j counts energy. This time, values of $P_{90}(E_j)$ and $\sigma(E_j)$ are calculated at a set of points E_j, for energy values from 28 to 10000 keV (the lower and upper limits of the energy integration), and the atmospheric parameters, are calculated at a set of points z_i. At each grid intersection (i,j) the value of $K(z_i, E_j)$ is found. Array elements $A_{i,j}$ are calculated

$$A_{i,j} = \frac{fr(z_0, z_j)P_{90}(E_j)\sigma(E_j)F_1(E_j^2 + (m_p \backslash m_e)\mathcal{K}(E_j, z_i)N(z_i))^{-(\delta+1)\backslash 2}}{3 - P_{90}(E_j)}T(z_i) \qquad 2.35a$$

$$B_{i,j} = \frac{fr(E_0, E_j)P_{90}(E_j)\sigma(E_j)F_1(E_j^2 + (m_p \backslash m_e)\mathcal{K}(E_j, z_i)N(z_i))^{-(\delta+1)\backslash 2}}{3 - P_{90}(E_j)}T(z_i)$$
$$+ n_h(z_i)n_e(z_i)c_{1\rightarrow 3}(z_i)T(z_i) \qquad 2.35b$$

The first set of calls of the numerical integration routine EO2GAF are to perform the integration over energy - i.e. a value of $i = n$ is set and the data points read into the routine are $(E_j, A_{n,j}), (E_j, B_{n,j})$. At n, the value $\epsilon_{min}(z_n)$, the beam cut - off energy at (z_n) is calculated (2.29), and any array elements with $E_j < \epsilon_{min}(z_n)$ are not included in the integration.

The results of this integration over energy are then used in a futher call of DO1GAF, to perform the final integrals over position, with results Q_{TOT} and I_{TOT} - the ratio of which is the final polarization. The whole process is somewhat lengthy and exhaustive of computing time, but is reliable - if the number of evaluation points is made sufficiently high.

§2.3.2 Variation of Beam Parameters

The three parameters which can be varied are F_{tot}, δ and E_c. We shall first investigate the dependence of polarization on E_c, the beam cut-off energy. Figures 2.12 a,b,c, and 2.13 a,b,c, show this dependence, for values of power - law index from 3 to 5 and for a number of total beam fluxes. Both F1 and F2 graphs are plotted for optical boundary at $\tau = 1$. As we expect the polarization fraction maximises for a value of cut - off energy equal to the energy of the mono-energetic beam which generated maximum polarization in calculations in the earlier part of this chapter - i.e., 70keV in F1 and 150 keV in F2. For very low cut-offs the polarization is small, but unlike the mono-energetic beam case, there is always a fraction of the population with sufficient energy to excite Hα impacts. So whilst a mono-energetic beam of less than 70keV gives virtually no net polarization, for any value of beam flux tested, a low cut-off but high flux power-law beam could generate a visible net polarization fraction.

The graphs cross the axis from positive to negative polarization at values of cut-off energy lower than the energy at which the same thing happens with a mono - energetic beam. For example, all particles in a 150keV mono-energetic beam in model F1 excite positive polarization in the neutral-hydrogen rich layers, but in a power-law beam with cut-off at 150keV there is a sizeable fraction of particles exciting negative polarization.

We next investigate what happens when δ is varied and the other two parameters held constant. As δ is increased the spectrum steepens and the number of particles at low energy is increased relative to those at high energy. On the basis of the mono – energetic situation we expect that an increase in the number of low and intermediate energy particles in the spectrum will lead to an increase in the observable polarization, but in a spectrum that is too steep it may be the case that the vast majority of particles have energies too low to take them as far as the hydrogen rich layers - depending on the cut-off value. We have also seen that protons above a certain energy produce a negative polarization fraction, therefore as power law index decreases the total polarization will decrease. The variation of polarization fraction with power law for a constant flux beam and cut - off energy is shown in figures 2.14 a,b,c,d and 2.15 a,b,c,d. The graphs extend only to a value of $\delta = 2$, since a smaller value is unphysical (i.e if the total energy contained in a power law beam is calculated, a spectral index of less than two gives an infinite total energy value.) We see the expected behaviour of the polarization fraction in all graphs save that plotted for flare F1, with a cut-off energy of 20keV. In this case the cut-off energy was deliberately placed far below the energy which a proton injected at the chromosphere needs to excite significant Hα radiation. The result is an initial slight increase in polarization as the population of intermediate energy protons increases relative to the high energy population, but as the spectrum shifts towards being dominated by very low energy protons, the polarization fraction decreases towards zero. Note that the power law beam in extreme circumstances can produce more polarization for a given beam flux than can a mono-energetic beam - for example, graph 2.14 c shows that a polarization fraction of more than 20% is possible with a flux of 5×10^{16} protons cm^{-2} s^{-2} and a high power law index whereas a mono-energetic beam of 70keV energy and the same flux only produces 1.75%. The same is true for F2 - figure 2.15 shows that a power law beam of $\delta = 8$, cut-off $\sim$ 150 keV and beam flux 10^{19} protons cm^{-2} s^{-2} generates 12.5% and a mono-energetic beam of energy 150 keV can only muster 2%. The improvement in polarization yield although surprisingly large, is understandable since, as was mentioned before, there are particles present at all depths in the chromosphere with the optimum Hα excitation energy. It remains to be seen, however, what the total energy (rather than flux) of these beams are.

The Optimum Beam Parameters and Total Energy Necessary

It is clear that to optimise the polarization yield by a power-law spectrum, it should have a cut-off energy of 70keV in model F1 and 150keV in model F2. As high a power-law index as possible is desirable, although little variation occurs for values of δ above about 8 in model F1, or 10 in F2 as the spectrum tends more and more towards the 'ideal' mono-energetic beam. There have been no indications in theoretical work on low - energy proton models of what the spectral cut - off or power-law index should be. In the electron beam model the cut - off is generally taken at 25keV, with a power law index somewhere between 3 and 5. Observations of very high energy (MeV) protons indicate a power law index of 5, but the average over measurements at all energies (but not less than a few hundred keV) is 2.9. There is no clue about what happens at low energies, but it seems reasonable to choose a value of $\delta = 3 - 5$. The total energy flux in a power law beam is given by equation 2.30

$$E_{TOT} = \frac{1-\delta}{2-\delta} F_o E_c$$

We calculate immediately the total energy necessary to power the Hα polarization at the point of injection in the corona. The relationship between the spectral cut-off in the corona and at the chromosphere is given in equation 2.29, and it is this value that is used in the calculation of E_{TOT}, which is then multiplied by the area and duration of the flare to give the total energy in ergs, which is plotted in figures 2.16 a,b,c for models F1, F2 and the quiet sun. We assume that the power law index is maintained - which is very nearly true, since we see from the almost straight line relationship of figure 2.10 that the effect of the warm target coronal portion is to add a constant to the injection energy at the chromosphere, so the spectrum is essentially just shifted up in energy by a constant value. To find the total energy contained in a beam of higher total flux, it is necessary only to multiply the energy read off the graph by the ratio of the desired flux to that for which the graph is plotted.

Dealing first with model F1 we look at figures 2.12. The horizontal lines are drawn at 5.5%, the value which the polarization must attain. For $\delta = 4$ the minimum flux which gives 5.5% polarization is of the order of 10^{17} protons cm^{-2} s^{-1} but at the low energy end there is evidently a range of combinations of flux and cut-off energy which could give the observed polarization; 10^{17} and 70 keV, or 10^{18} and 30keV for example. But since the total energy depends on the product of these two numbers, evidently the first pair yields the lowest total. According to figure 2.16a, the total energy contained in a beam with these parameters is 2.5×10^{32} ergs. For $\delta = 5$, the necessary flux and cutoff are 5×10^{16} and 70keV, corresponding to the slightly smaller total energy budget of 1.25×10^{32} ergs. If the power law index were permitted to take a higher value of 7 or 8 above then we could further reduce the required total energy, to around 10^{31} ergs, but we really have no justification for imposing such a high power law index.

As we might expect, model F2 makes higher demands on the total beam energy. With a cut -off energy of 140keV and $\delta = 4$ a beam flux of10^{18} protons cm^{-2} s^{-1} is required. If $\delta = 5$ the requirement is 10^{17} to 10^{18} protons cm^{-2} s^{-1}. Referring to 2.16b, we see that this leads to a total energy of 3×10^{34} ergs ($\delta = 4$) or $2.5 \times 10^{33-34}$ ergs ($\delta = 5$). Once again, if the power law index is permitted to increase, the energy requirement can be reduced by an order of magnitude.

For completeness, a quiet sun calculation has also been performed. With this model we find that the energy budget can be reduced to 10^{29}ergs, for reasonable values of the power-law index.

§2.3.3 Conclusions of the Power-Law Beam Modelling

Using a power-law form for the beam spectrum we find that it is possible to reduce the total energy necessary to power an Hα polarized flare. The reduction depends on both the beam cut-off energy and the power-law index. For all atmospheric models tested there is a particular value of cut-off energy for which the polarization generation process is most efficient (i.e., highest polarization fraction) but it seems that the efficiency increases monotonically with the power-law index. After a value of $\delta = 8 - 10$ (depending on the cut-off energy and flare atmosphere model) there is no further significant increase in the polarization fraction obtained. We have no theoretical or observational guide to what the power law index should be at energies of less that an MeV or so, but above this energy the mean value of δ is 4. We are therefore most interested in the results for $\delta = 3, 4, 5$. With these values we can get the total beam energy necessary down to 2.5×10^{32} ergs in F1 and 2.5×10^{33} ergs in F2. These values are smaller than those obtained in the monoenergetic beam model, but are still very high total energies except when considering extremely large flares.

§2.3.4 Conclusions to Chapter Two.

In this chapter we have re-examined the proton-beam model of Hα impact polarization and have found that when more attention is paid to the effects of temperature and density variations in the atmosphere the model becomes unfeasible on the grounds that the total energy in the beam is at least 10^{32} ergs (in a low temperature flare atmosphere). This total cannot reasonably be decreased, unless we allow the atmosphere to be a quiet sun atmosphere, which, given the increase in Hα emission and soft (plus sometimes hard) X-rays observed during the Hα polarization observations (signalling an increased temperature) is not very likely. In addition, if factors such as beam anisotropy are included the total energy necessary can only increase. To enable this model to work within the energy constraints it would be necessary to have an atmosphere which is collisionally much thinner above the neutral hydrogen rich layers than are the flare atmospheres of Machado *et al*, so that proton beams would not have to be injected at such a high energy to arrive

at the hydrogen-rich layers with optimum excitation energy. This we could do by insisting that the temperature of these layers is so high that the atmosphere is essentially a warm target from the corona to the point of non-thermal Hα excitation, but this would demand an extremely abrupt transition region and would also run the risk of greatly increasing the recombination Hα from the overlying layers as the temperature increases without a density decrease. Alternatively we could insist that the hydrogen rich layers are a little cooler than in the MAVN models, with the result that the thermal emission would be decreased, but then we would again have the problem of explaining the enhanced thermal flare Hα . Finally, we could resort to creating for these few Hα flares a small class of very high energy, extended flares whose extremely high energy is not manifested in way other than the presence of polarization. This is clearly not a satisfactory thing to do. We do note however that the difficulties with the proton beam model come primarily from the physical size and duration of the flare. Proton beams can generate impact polarization, and it is possible that, if ever observed, impact polarization in smaller and shorter flares could be proton beam generated.

In conclusion, on the basis of the work of this chapter we do not believe that the proton beam model of Hα impact polarization *in the flares studied* is consistent with current ideas about flare energetics or flare atmospheres and although we cannot reject it outright are forced to consign it to the class 'unlikely models'.

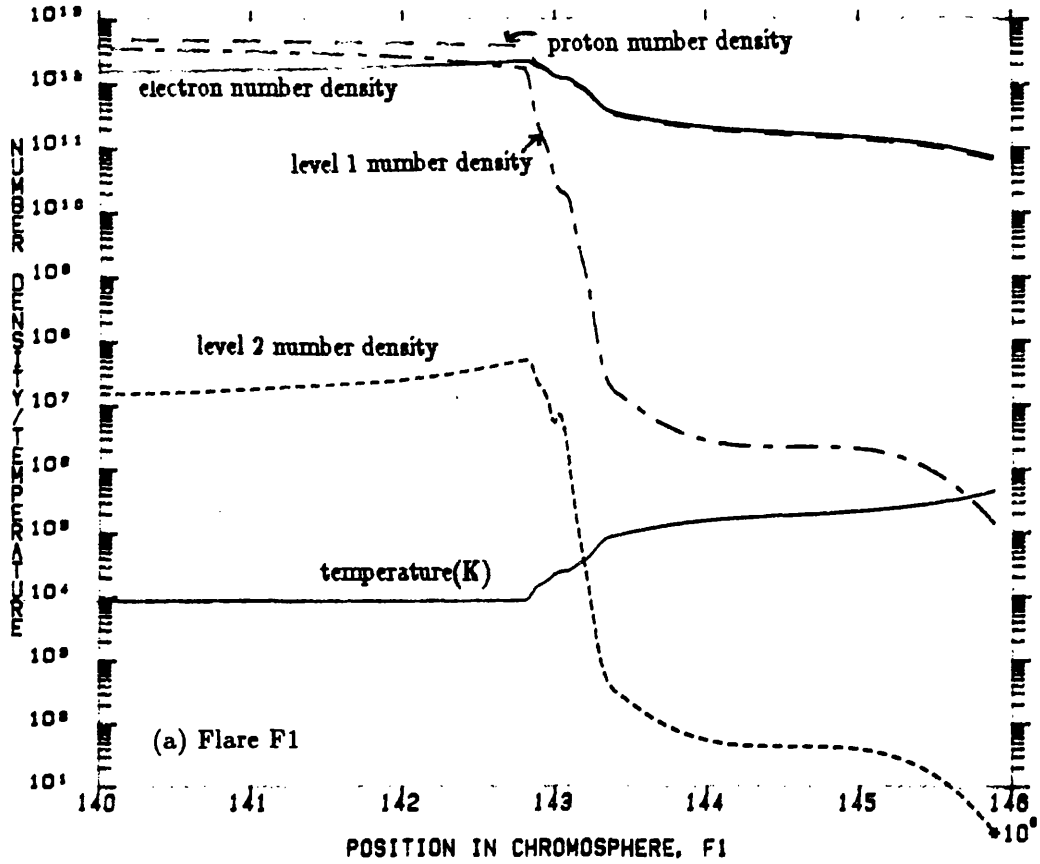

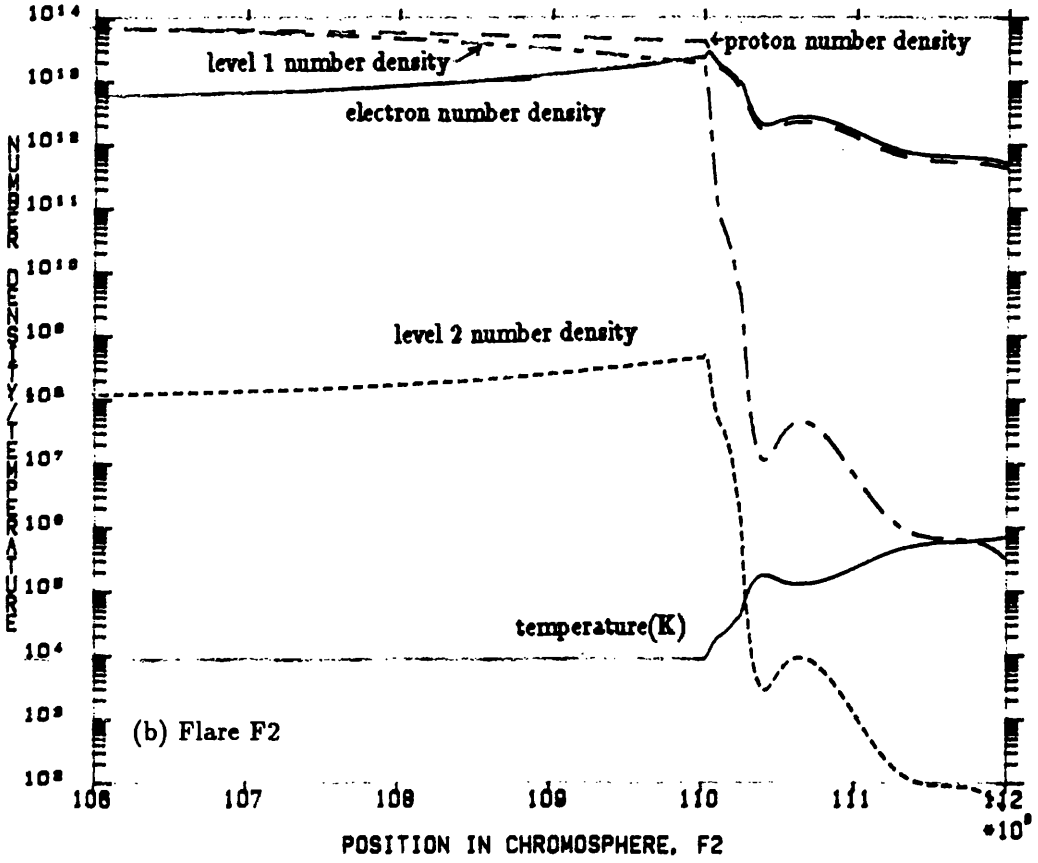

Fig 2.1 Chromospheric flare models of Machado *et al* (1980)

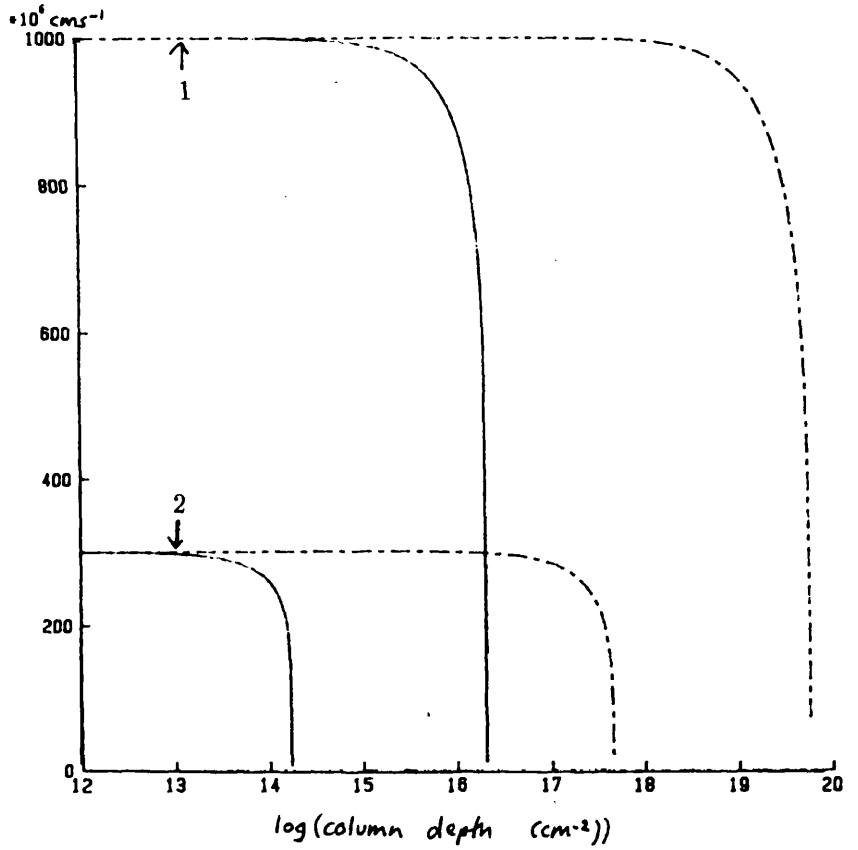

Fig 2.2a Variation of beam velocity with column depth, for beams with initial velocity of (1) 10^9 cm s^{-1} and (2) 3×10^8 cm s^{-1}.
Dotted line - protons. Full line - electrons

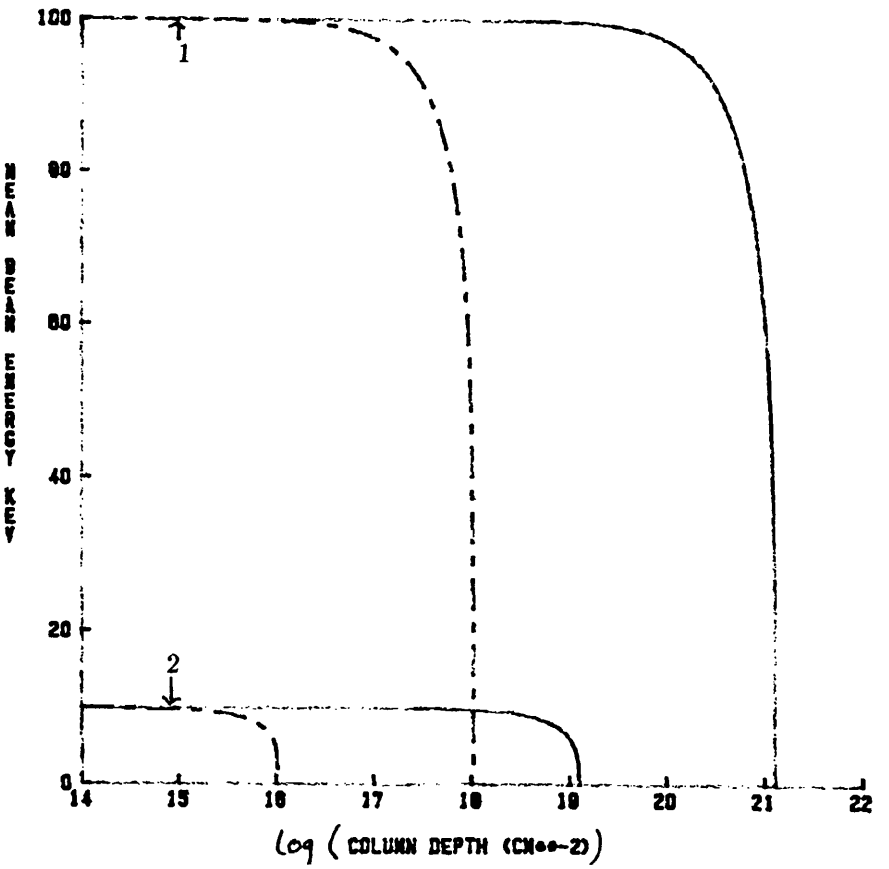

Fig 2.2b Variation of mean beam energy with column depth,
for beams with initial energy of (1) 100 keV (2) 10 keV

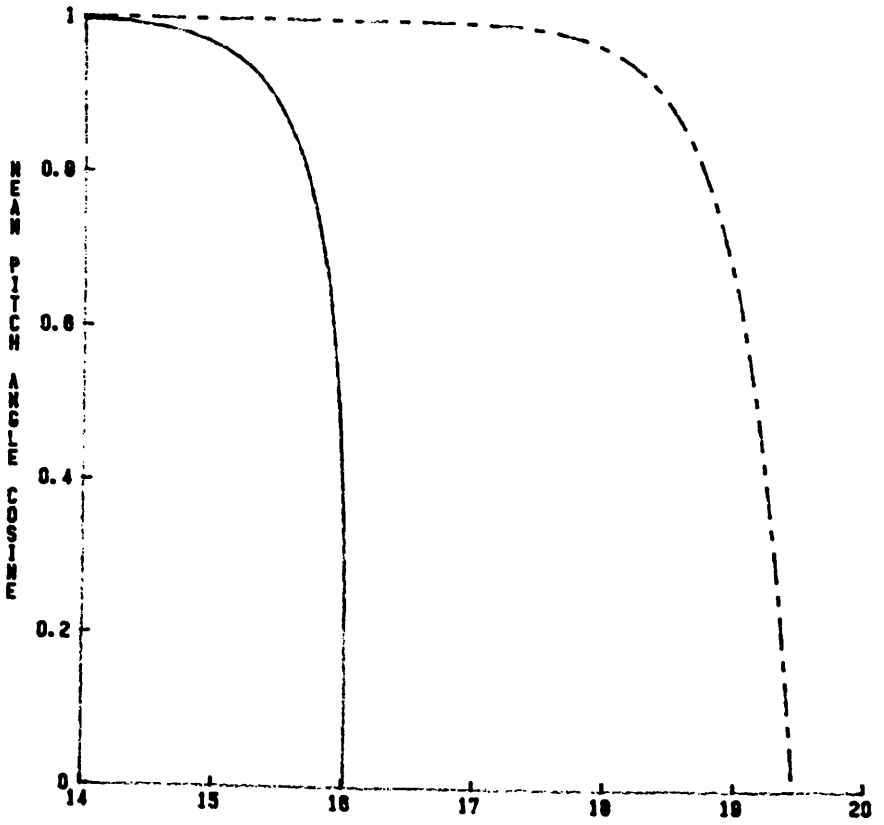

Fig 2.2c Variation of mean beam pitch angle cosine with column depth.

initial value = 1

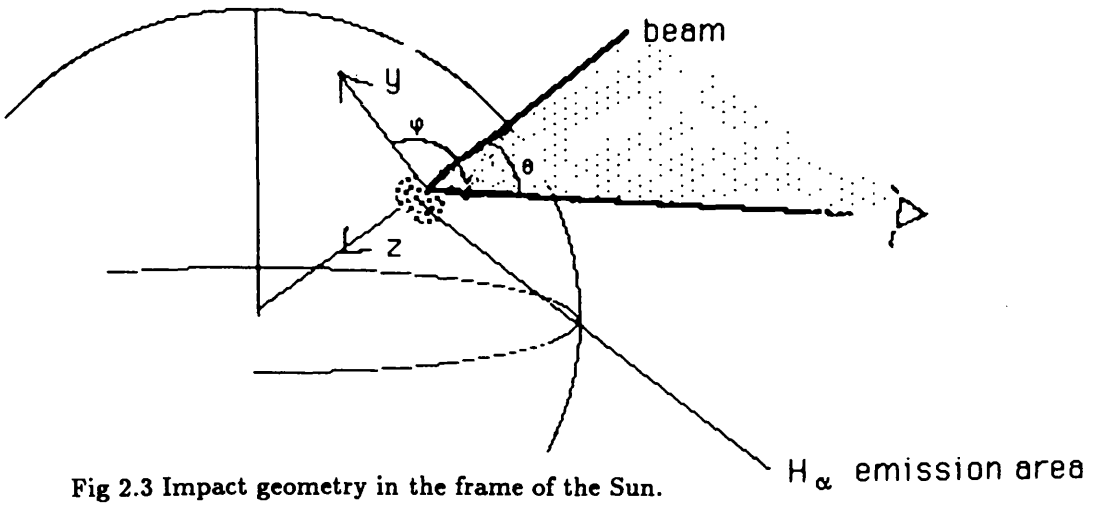

Fig 2.3 Impact geometry in the frame of the Sun.

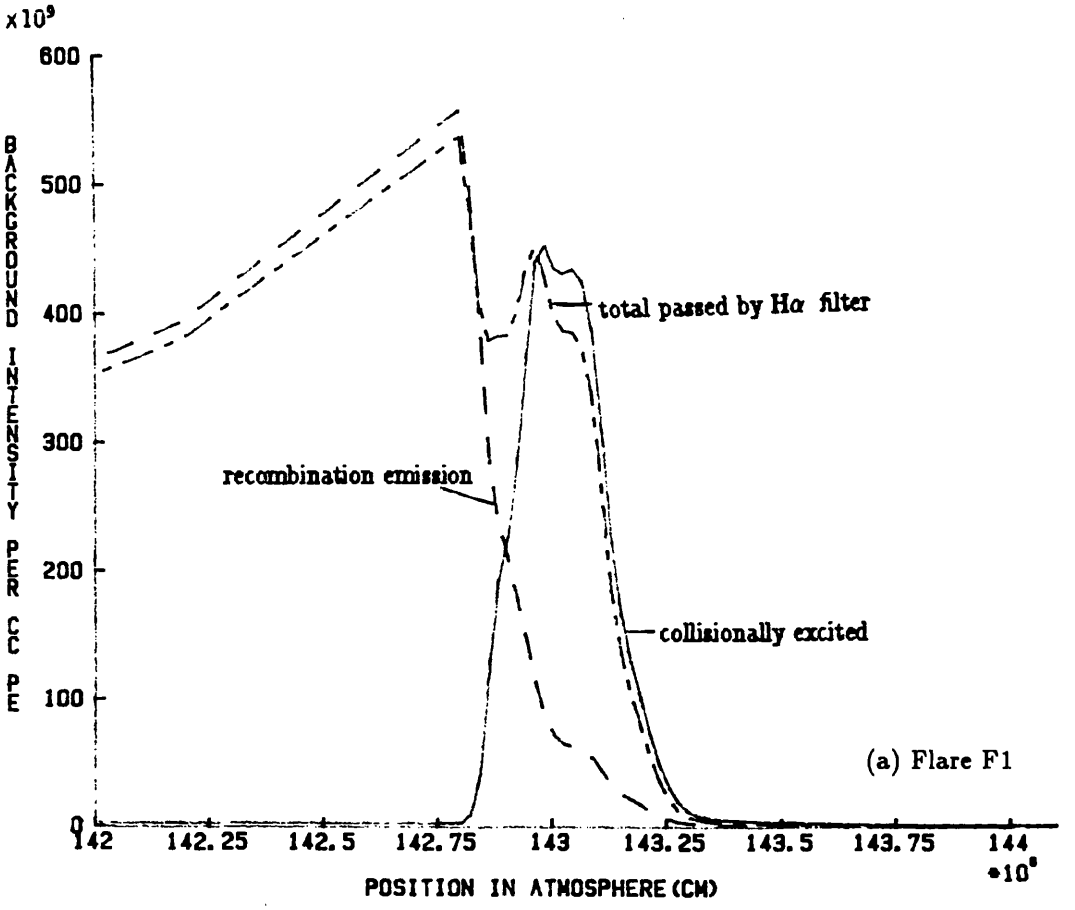

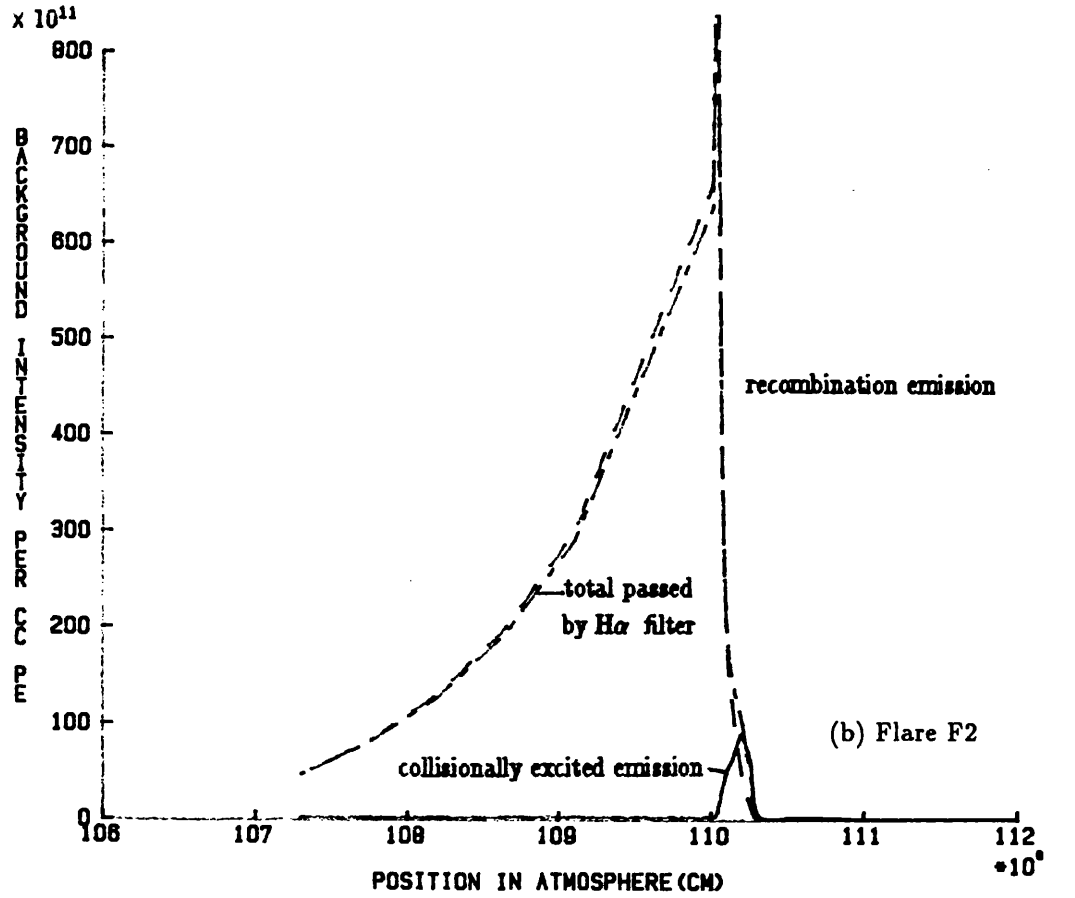

Fig 2.4 Emission rate of thermal and recombination Hα photons ($cm^{-3}\ s^{-1}$) and total passed by filter

Fig 2.5 Hα number flux at chromospheric surface ($cm^{-2}\ s^{-1}$).

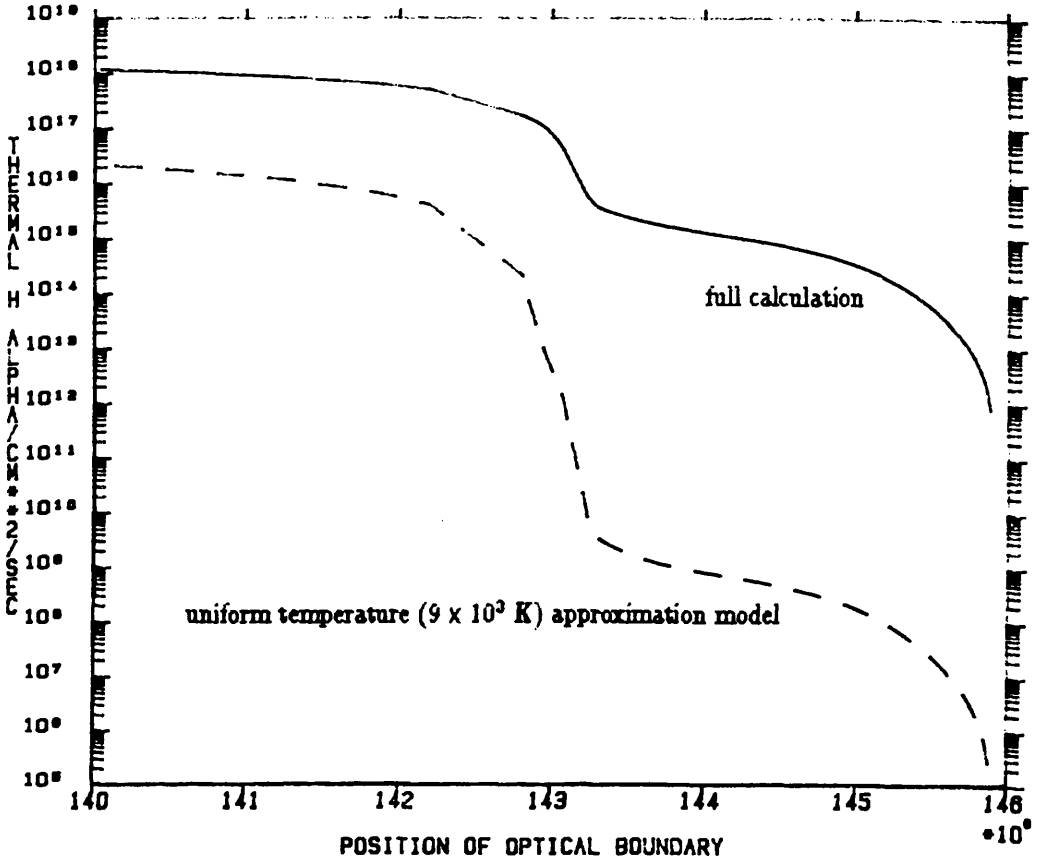

(a) Flare F1

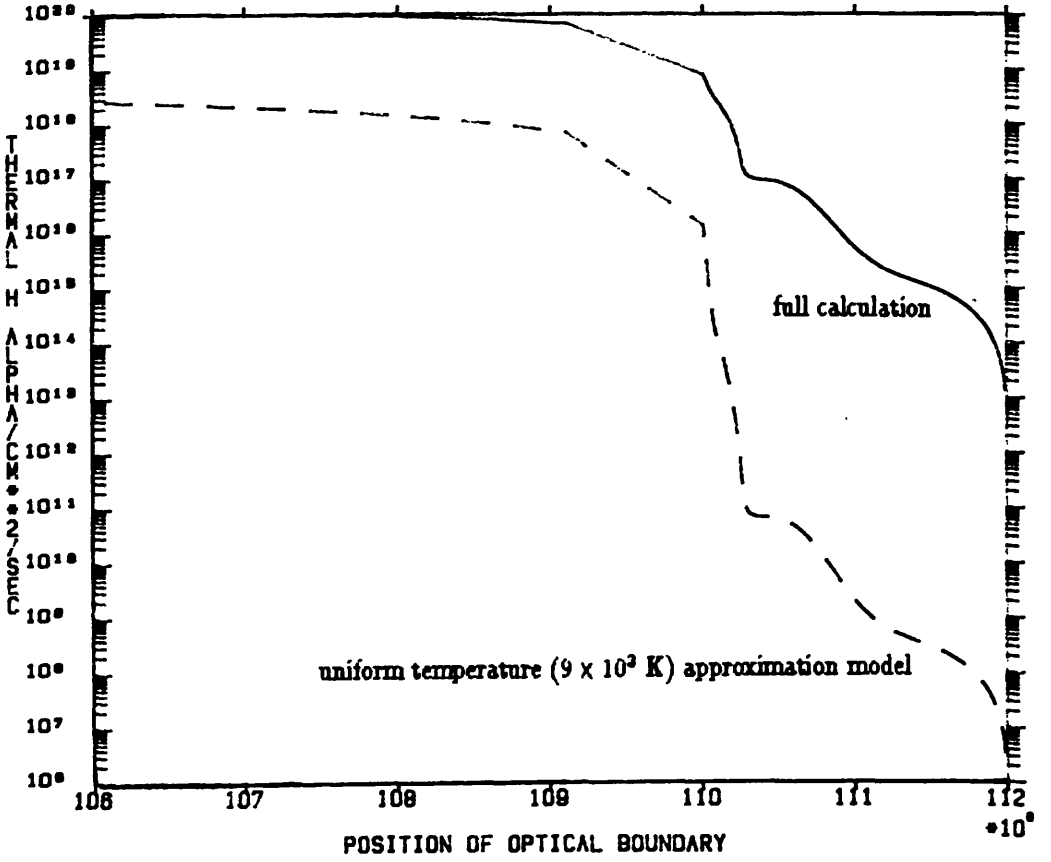

(b) Flare F2

Fig 2.6 Optical depth in the Hα line

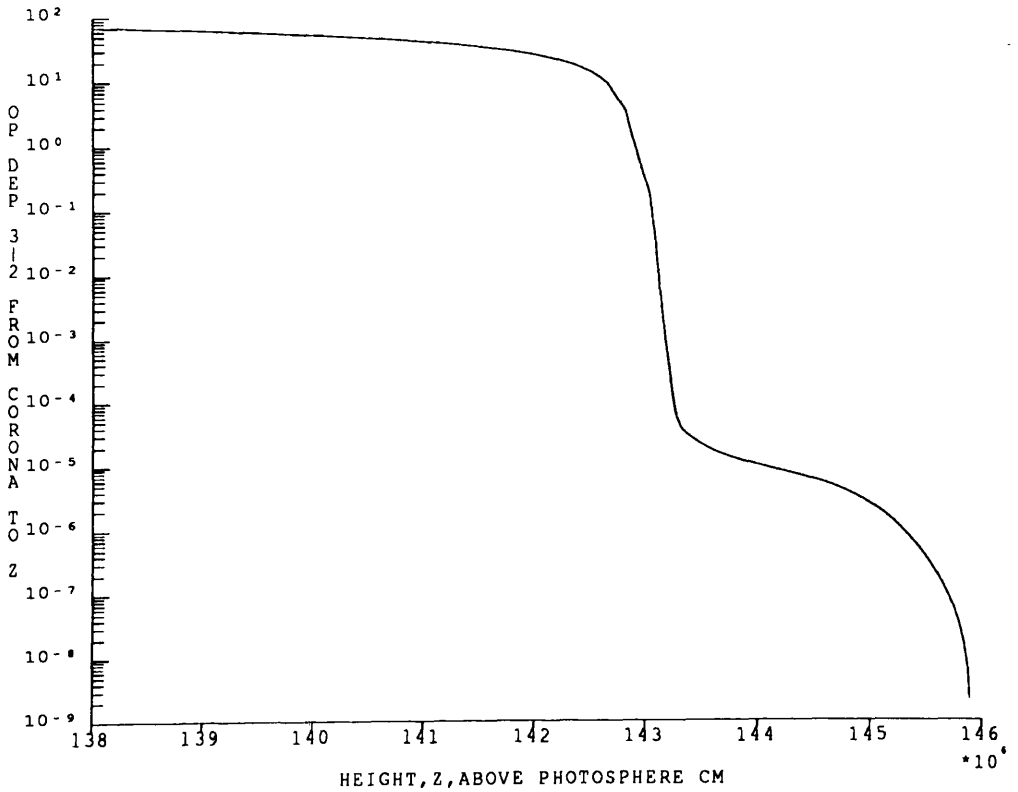

(a) Flare F1

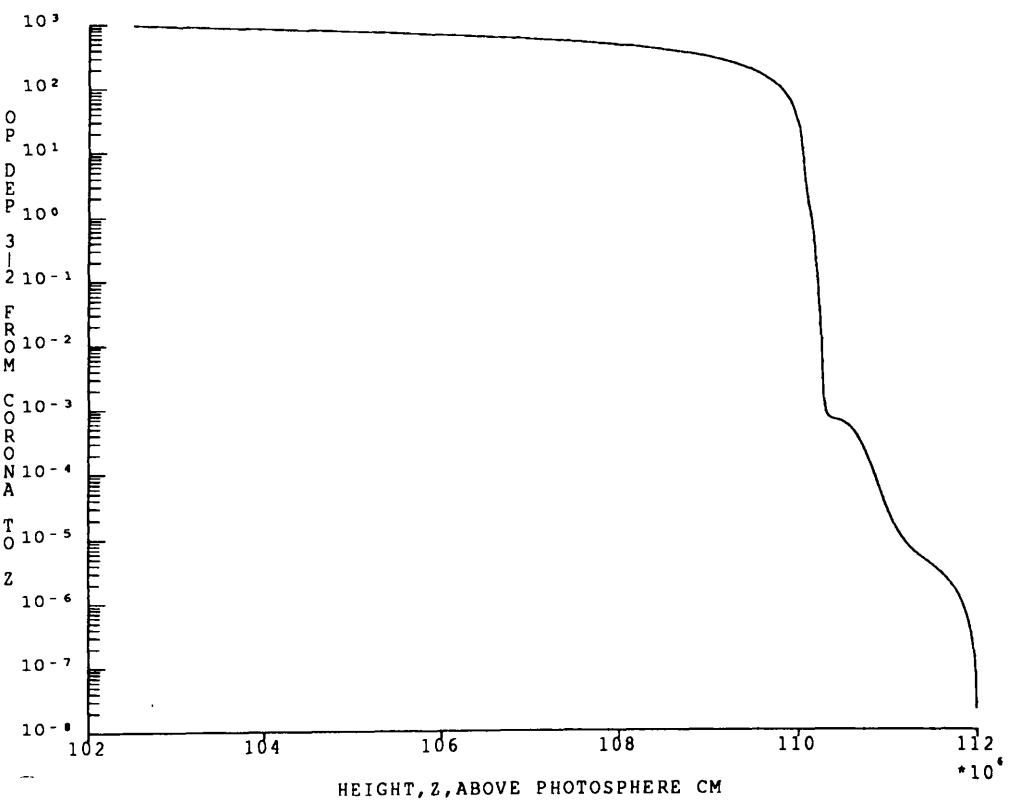

(b) Flare F2

Fig 2.7 Polarization fraction from chromosphere F1 as a function of proton beam energy

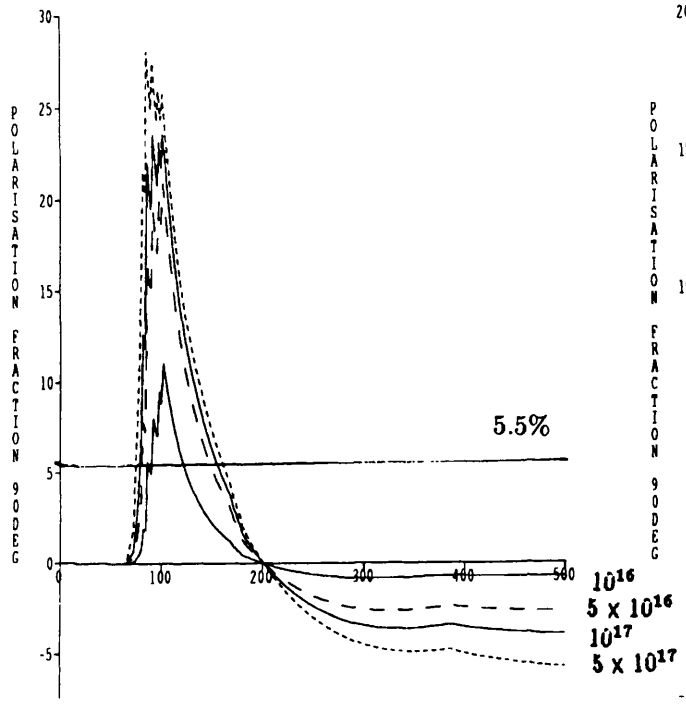

(a) with optical boundary at 1.425×10^8 cm

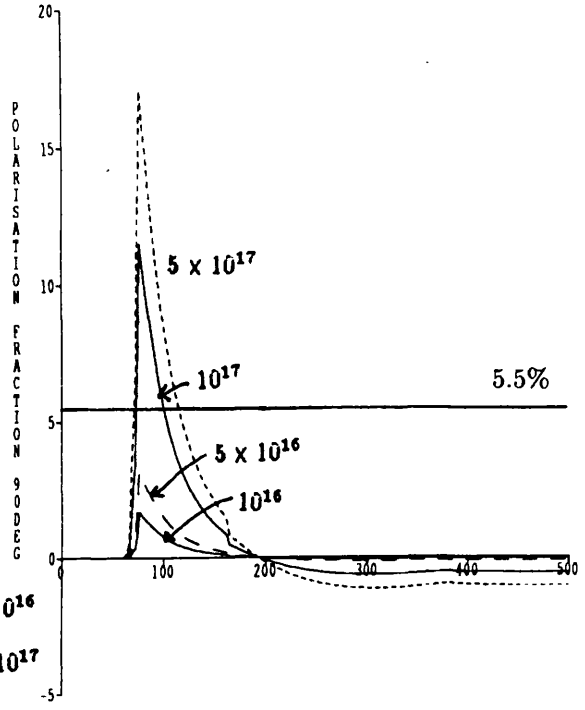

(b) with optical boundary at 1.428×10^8 cm

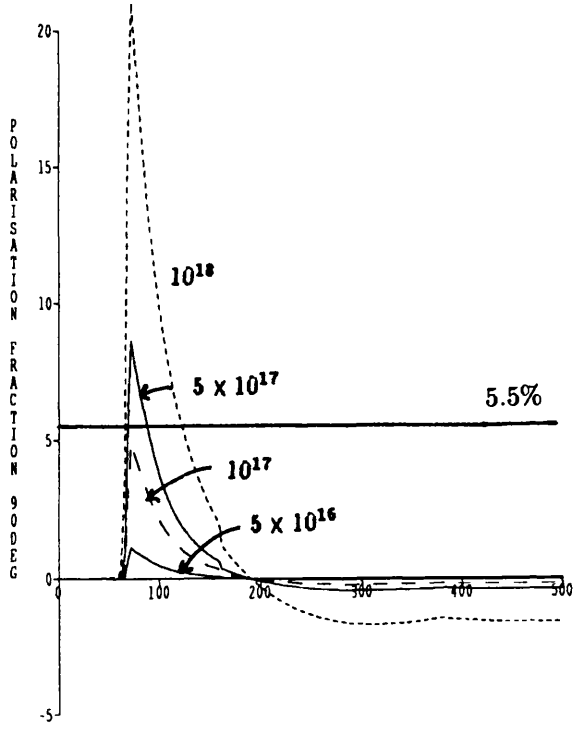

(c) with optical boundary at 1.429×10^8 cm

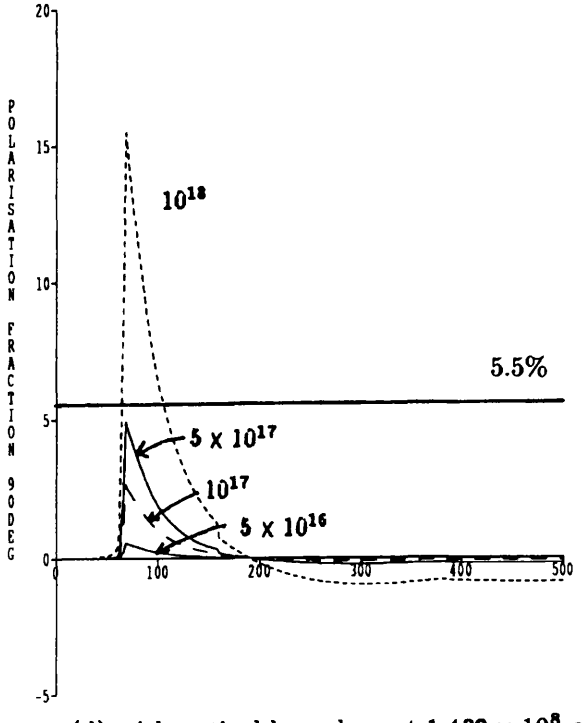

(d) with optical boundary at 1.430×10^8 cm

Fig 2.8 Polarization fraction from chromosphere F2 as a function of proton beam energy

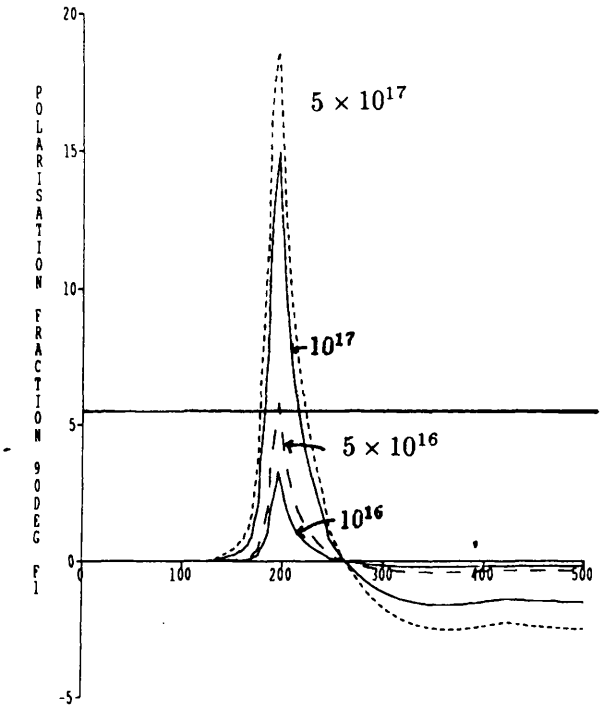

(a) with optical boundary at 1.100×10^8 cm

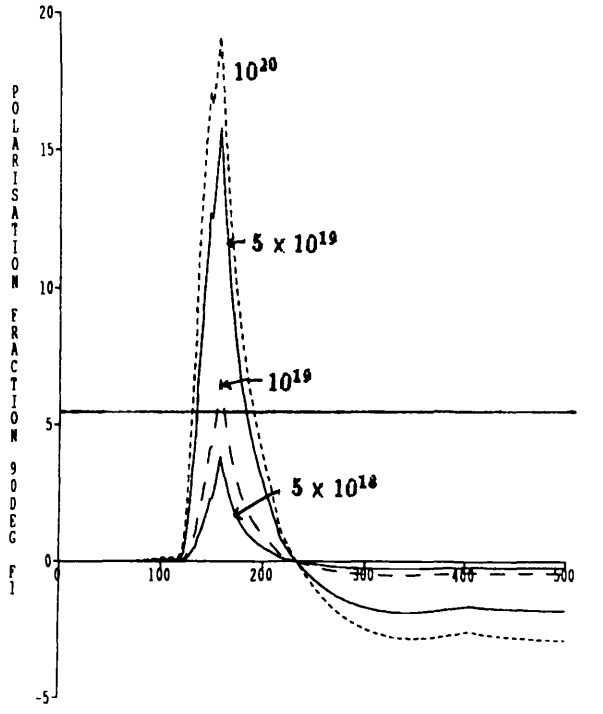

(b) with optical boundary at 1.101×10^8 cm

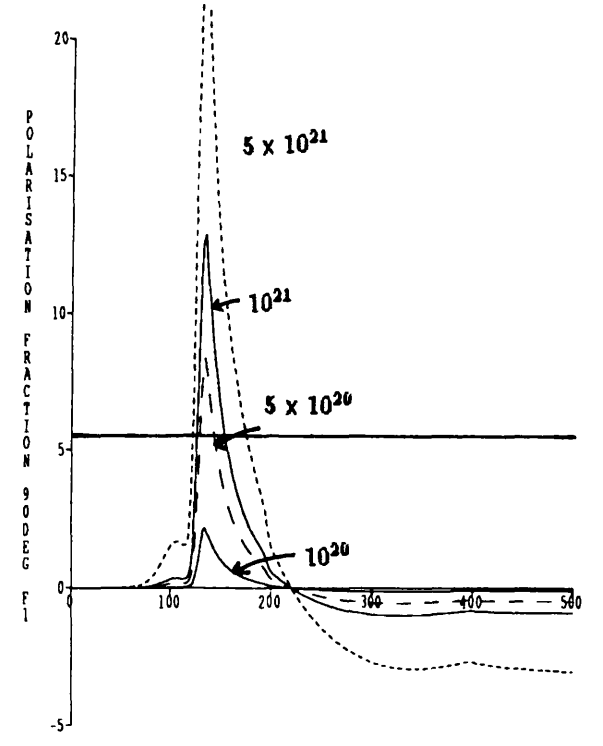

(c) with optical boundary at 1.102×10^8 cm

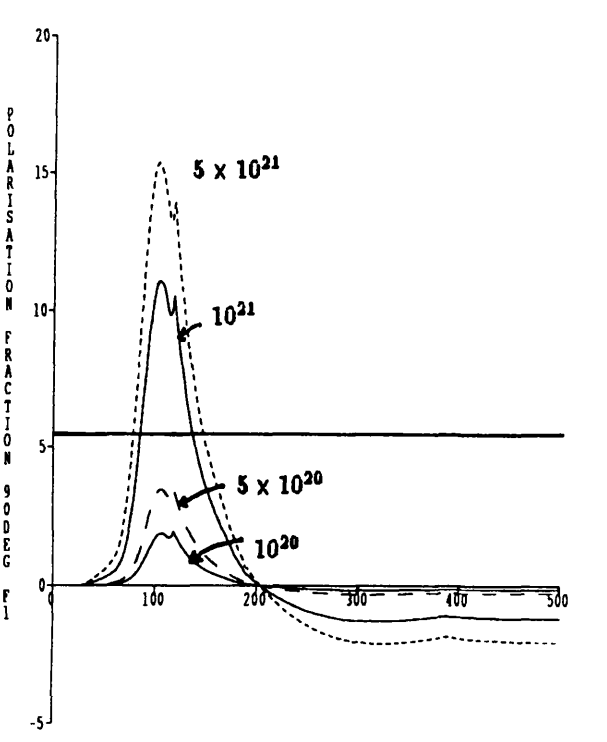

(d) with optical boundary at 1.103×10^8 cm

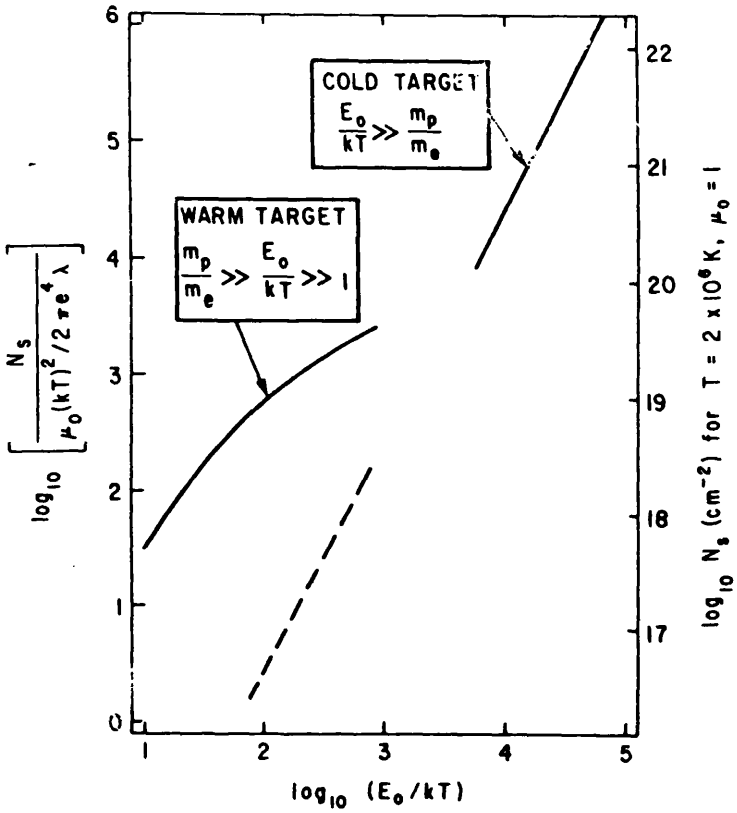

Fig 2.9 Comparison of warm and cold target stopping depths (Tamres 1985)

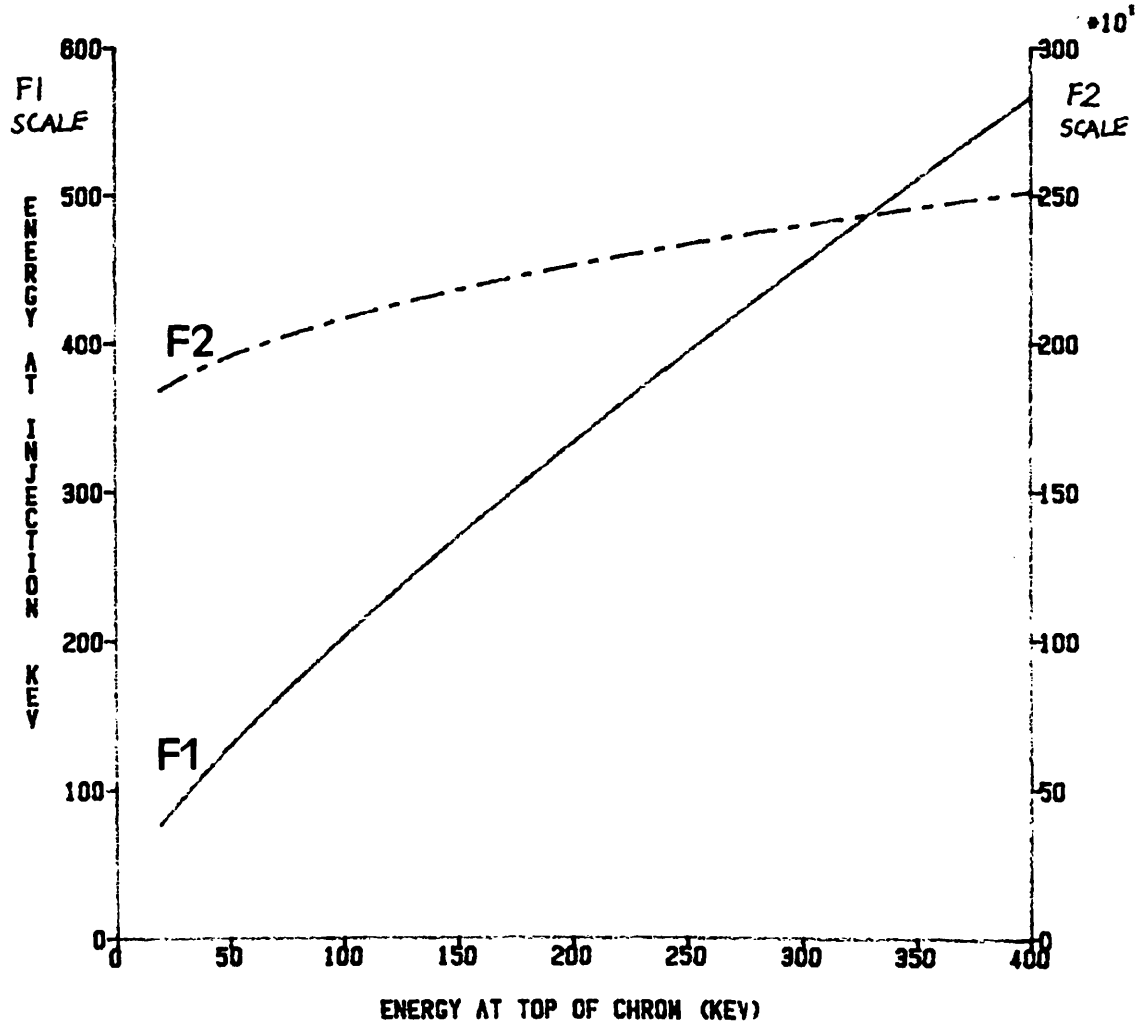

Fig 2.10 Proton energy at coronal acceleration site as a function of the energy it has on entering the chromosphere.

Fig 2.11(a) optical depth in the Hα line in the quiet sun chromosphere

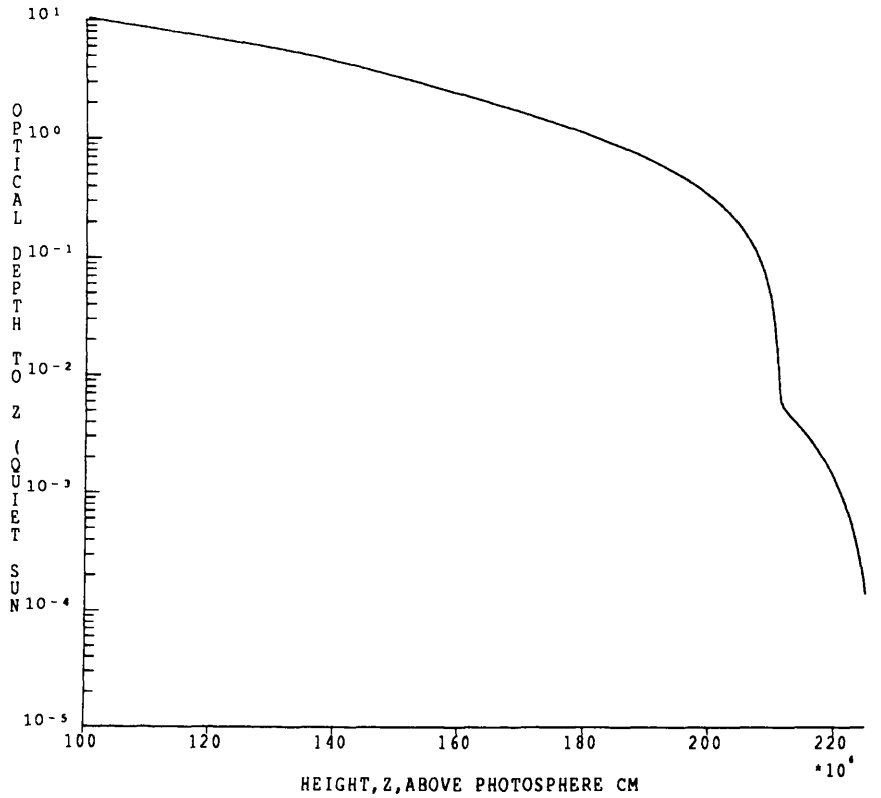

Fig 2.11(b) Polarization fraction as a function of proton beam energy in the quiet sun chromosphere.

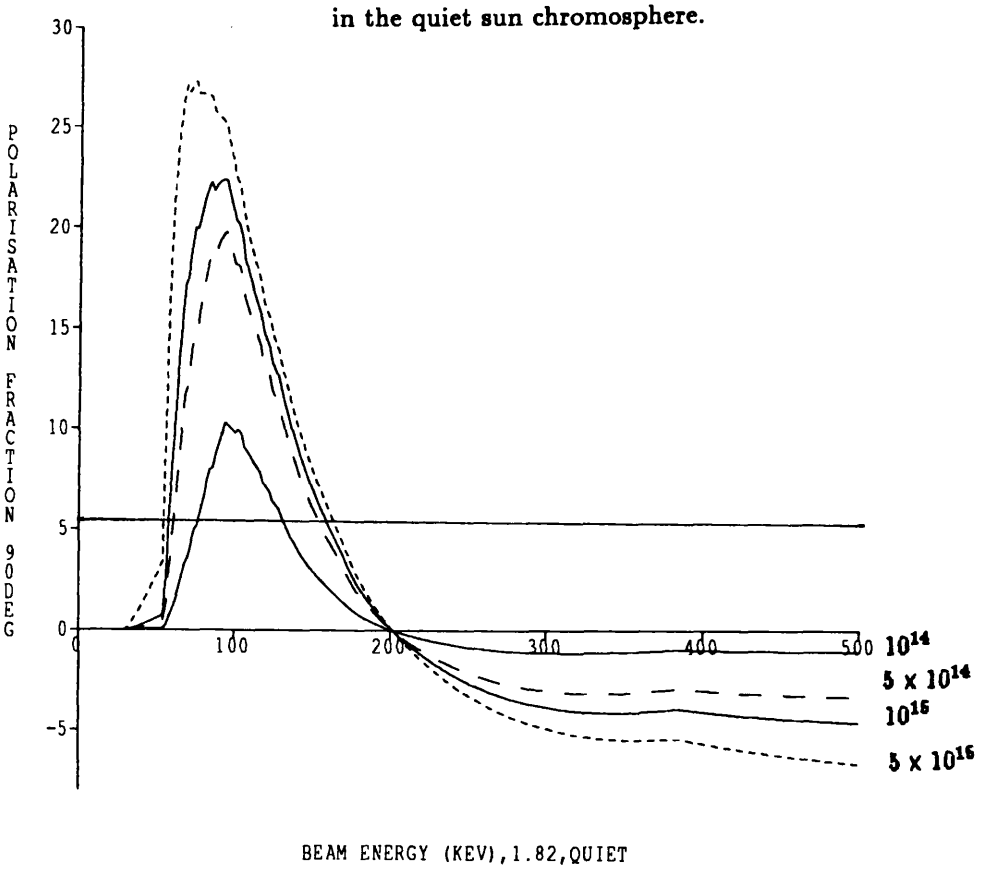

Fig 2.12 Variation of net polarization fraction with beam cut-off energy, model F1

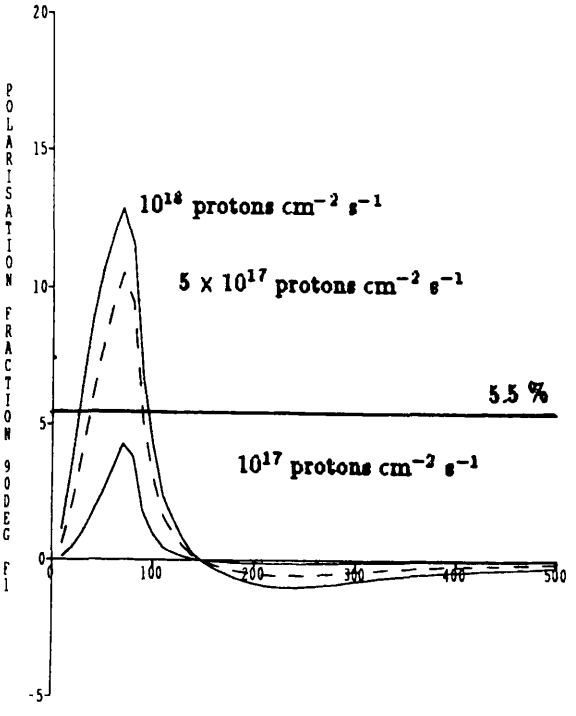

(a) $\delta = 3$

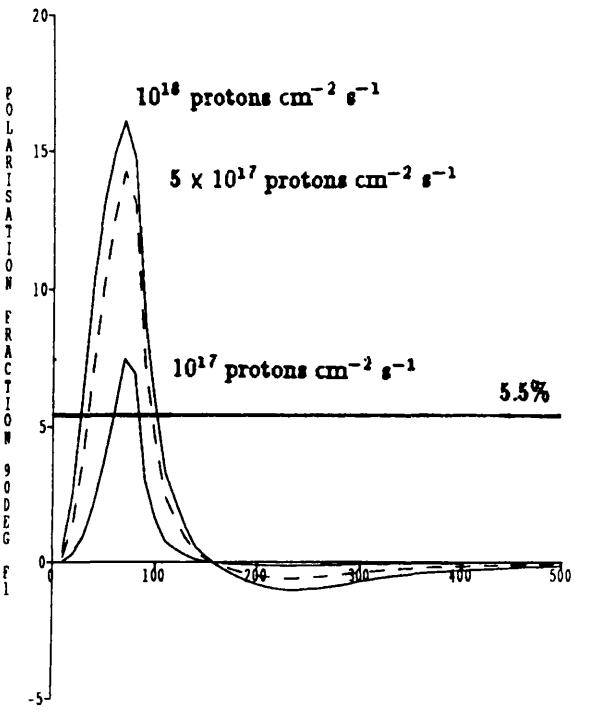

(b) $\delta = 4$

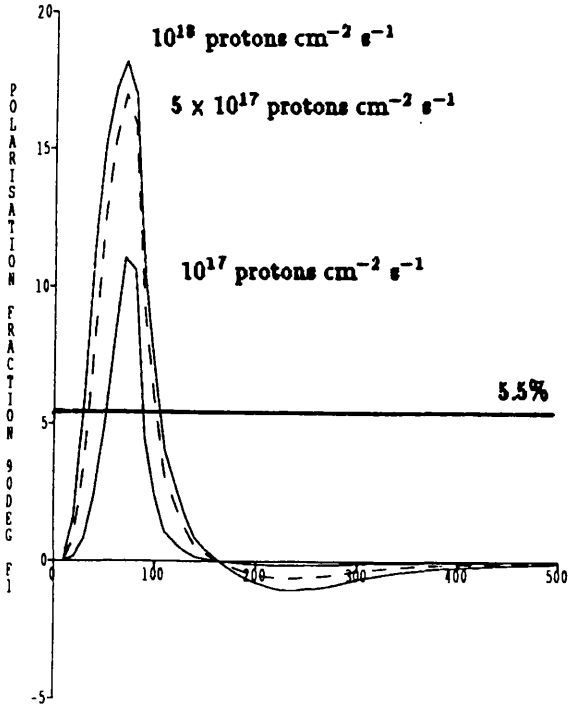

(c) $\delta = 5$

Fig 2.13 Variation of net polarization fraction with beam cut-off energy, model F2

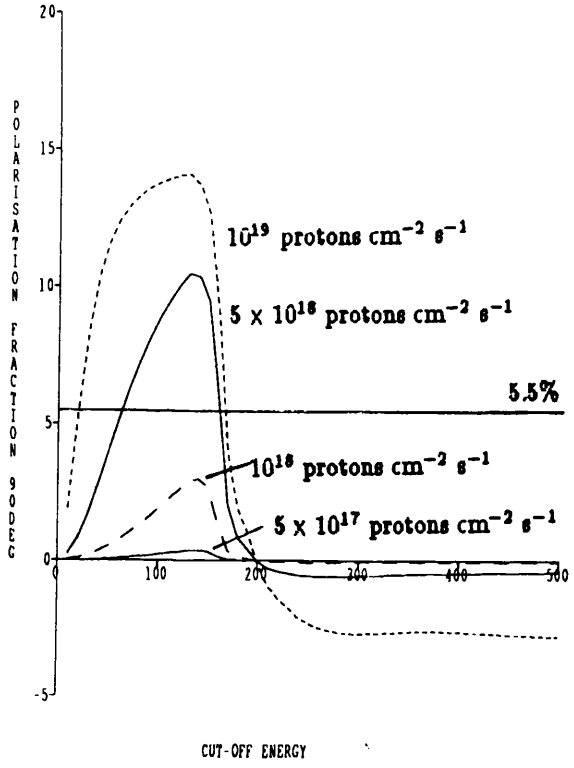

(a) $\delta = 3$

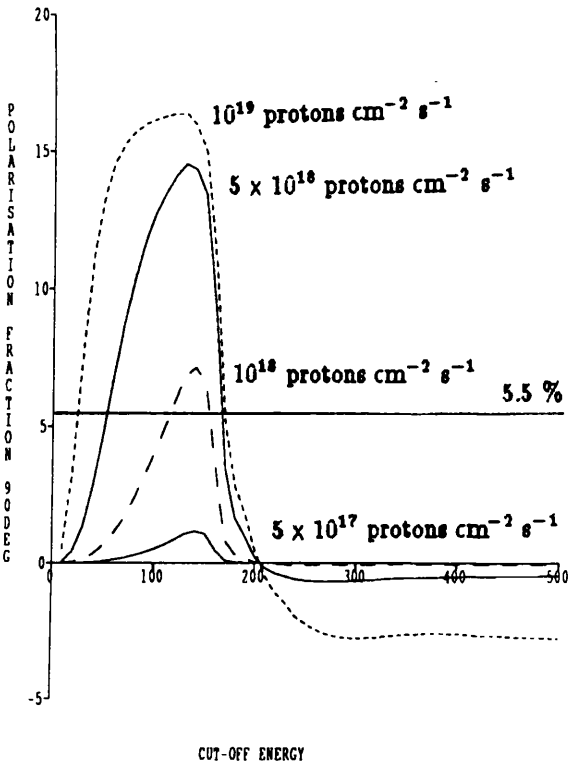

(b) $\delta = 4$

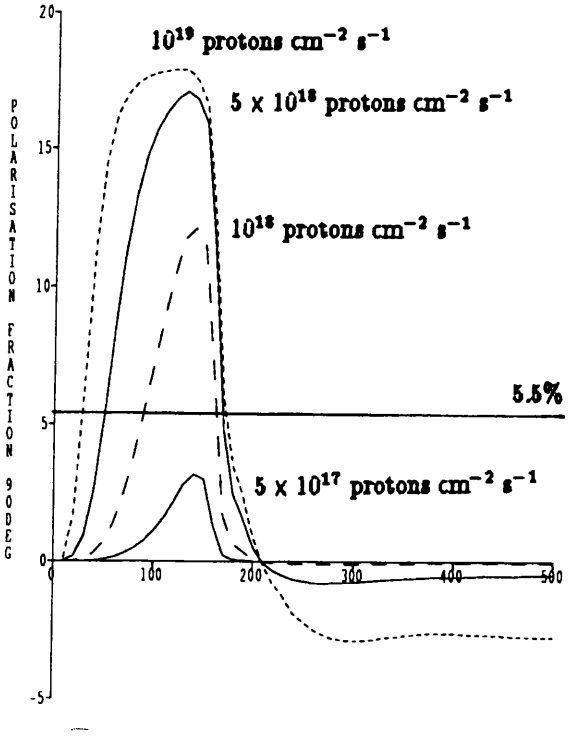

(c) $\delta = 5$

Fig 2.14 Variation of net polarization fraction with beam power-law index, model F1

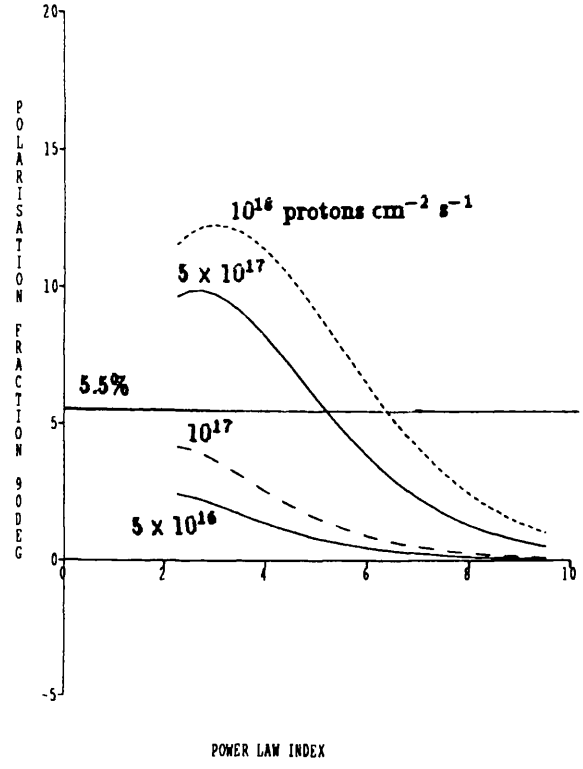

(a) cut-off energy = 20 keV

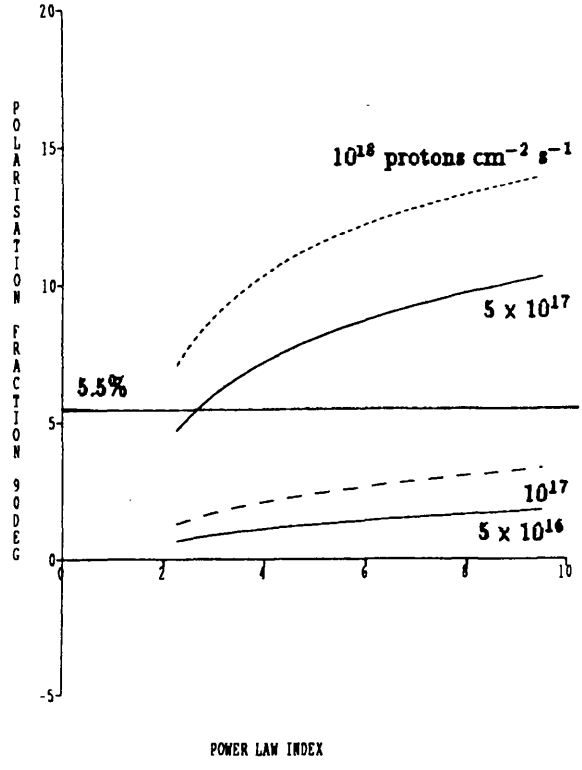

(b) cut-off energy = 40 keV

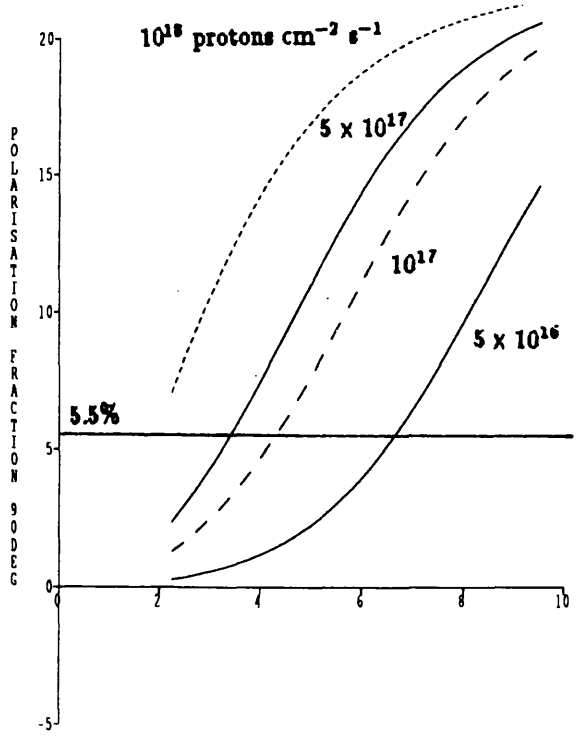

(c) cut-off energy = 70 keV

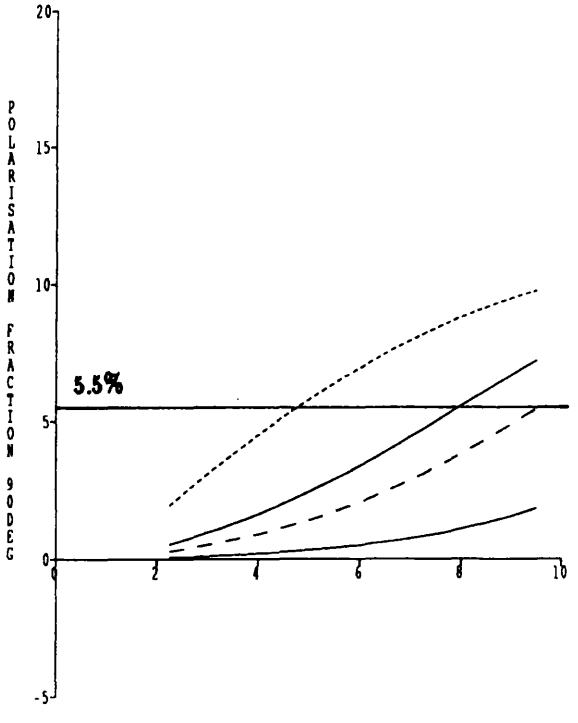

(d) cut-off energy = 100 keV

Fig 2.15 Variation of net polarization fraction with beam power-law index, model F2

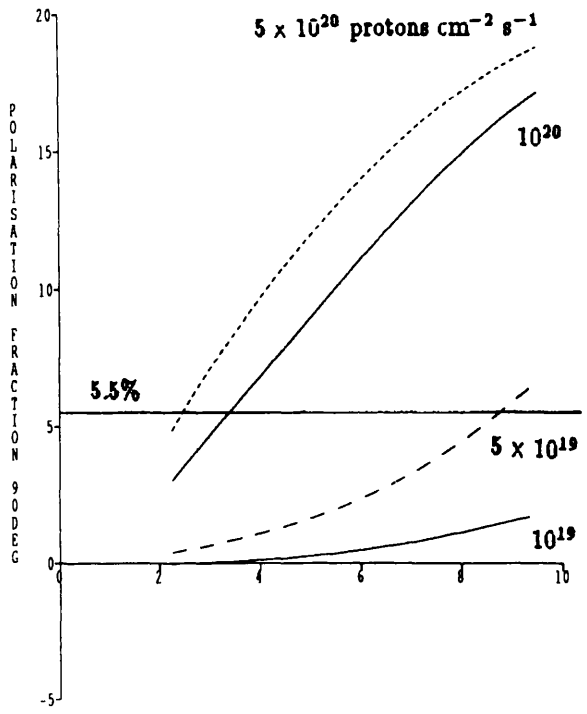

(a) cut-off energy = 70 keV

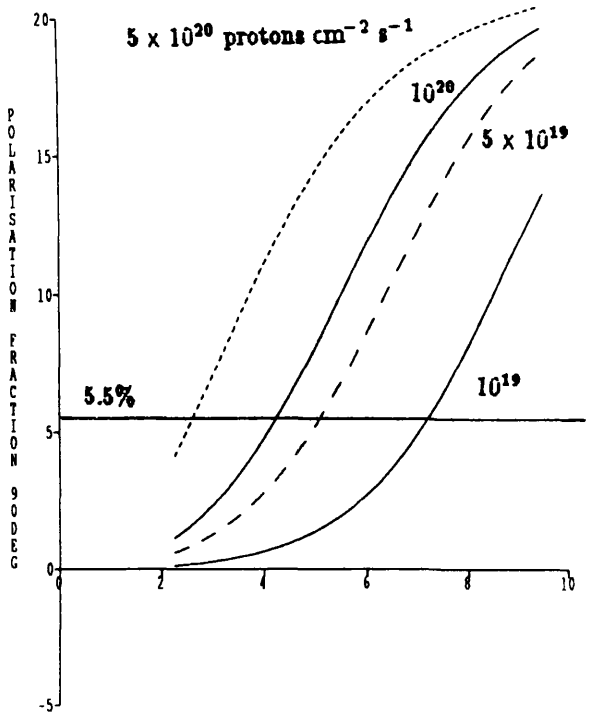

(b) cut-off energy = 100 keV

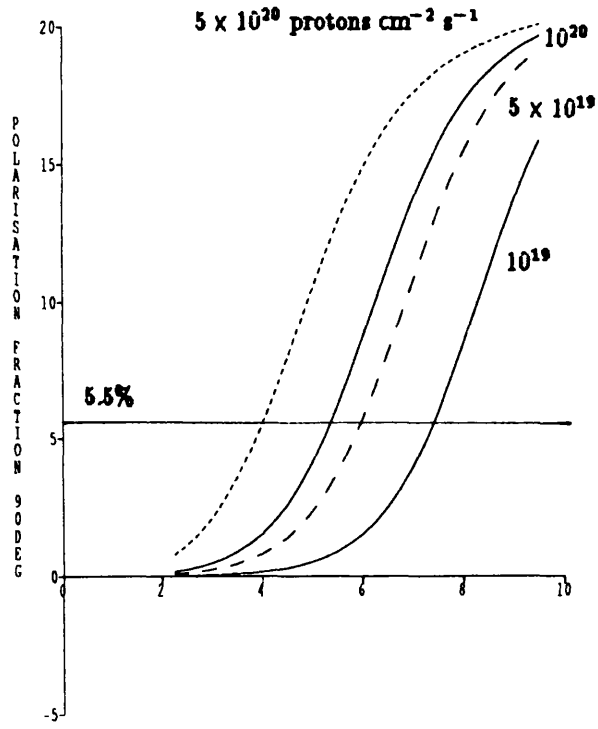

(c) cut-off energy = 150 keV

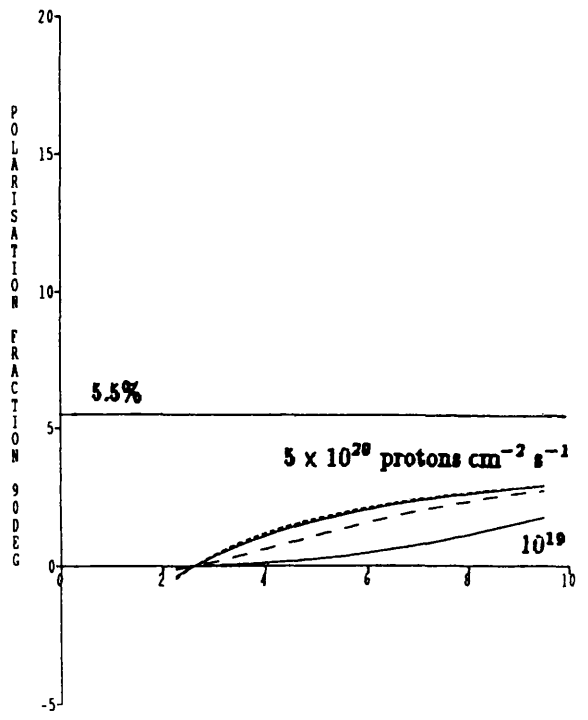

(d) cut-off energy = 200 keV

Fig 2.16 Total energy in a power-law beam needed to power polarization observed as a function of cut-off energy, for various values of δ

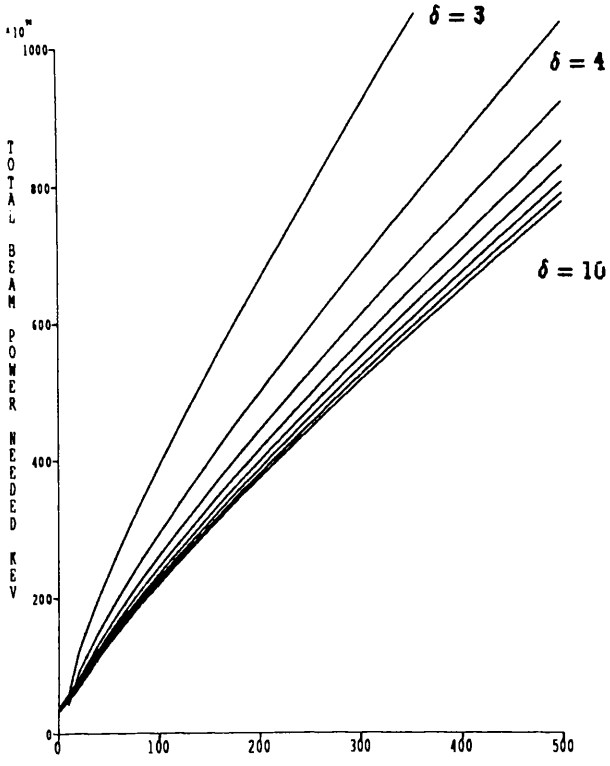

(a) in model F1
beam flux of 10^{17} protons cm^{-2} s^{-1}

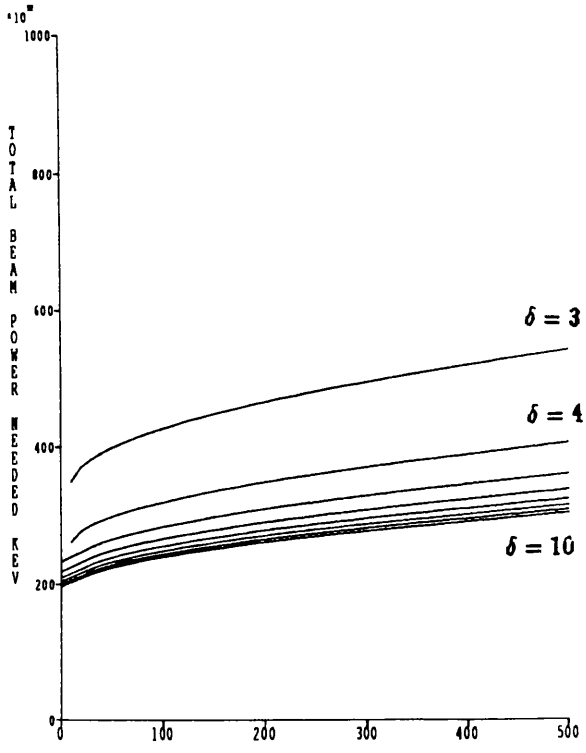

(b) in model F2
beam flux of 10^{18} protons cm^{-2} s^{-1}

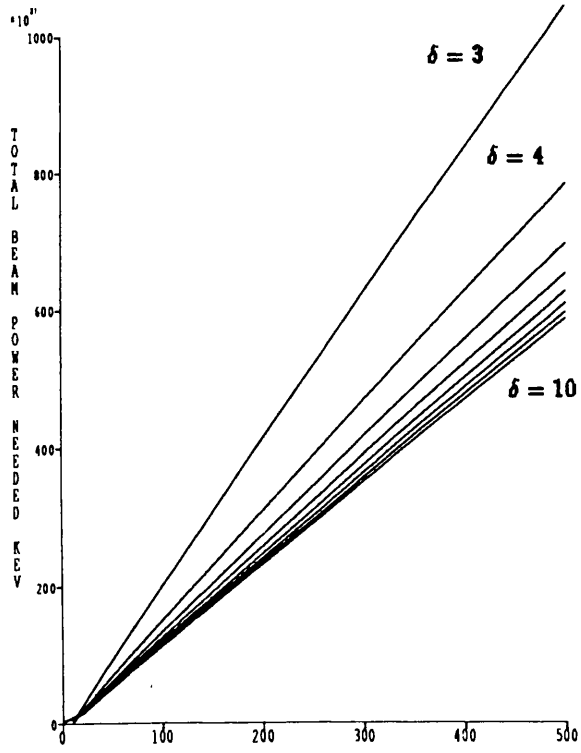

(c) in the quiet sun
beam flux of 10^{14} protons cm^{-2} s^{-1}

Chapter 3. A Mirroring Electron Model.

§3.1 Introduction - The Thick Target Electron Beam Model

As an alternative to proton beam impact polarization we now investigate the possibility that electron beams are at the root of the polarized line emission. Electron beams have long been accepted as a likely candidate for the transfer of energy from the corona to the chromosphere during the flare. The thick-target electron beam model in its most basic form invokes a spectrum of electrons accelerated in the corona which, guided by the coronal magnetic fields, impinges upon the atmosphere below and produces the HXR signature of the flare impulsive phase. When it encounters the large increase in density in the transition region - the thick target regime, the beam gives up its energy in Coulomb collisions, heating the atmosphere and leading to the onset of the thermal flare impulsive emissions followed by the flare gradual phase. This could be called a 'one pass' picture - the beam proceeds unimpeded and the entire HXR signature results from the single pass that the beam particles make through the low chromosphere and transition region. As has been outlined in chapter 1, the evidence for this version of the thick – target electron beam model is not conclusive. The proposed 10 to 100 keV electron beams can generate the observed amount of HXR emission in a 'one pass' model, which predicts that the HXR generation should come exclusively or predominantly from the thick target region - the low corona and transition region, whereas satellite observations by Hinotori (Tsuneta *et al* 1984) sometimes observed HXR emission occuring solely in the high corona, and earlier observations from the Solar Maximum Mission Hard X-Ray Spectrometer which do show the desired 'footpoint' emission, do not, in the light of further analysis (MacKinnon *et al* 1985) agree with a one pass model. These too show significant emission in higher coronal regions. In addition, the sudden and rapid increase in target density as the beam encounters the transition region means that heating of this part of the atmosphere would be intense , and numerical simulations of this scenario all predict rapid upwards 'evaporation' visible in soft X-ray lines. Evaporation of some sort does occur, as is evidences by the soft X - ray brightening, but the interpretation of the soft X - ray line blue shifts is unclear. Some authors take the large blue shifts as indicative of high velocity motion of a single plasma component, but Alexander (1990) and Emslie and Alexander (1987) claim that the observations are consistent with gentle evaporation of a multithermal plasma, viewed obliquely.

A proposed trap – plus – precipitation model goes some way to alleviating these problems. In this model particles are somehow confined to the higher regions, only a small fraction escaping to cause the observed HXR footpoints, the rest remaining in the corona where they produce the coronal component. Since a smaller energy flux would arrive at the transition region, ablation of

the atmosphere would be much less severe. The trapping is of charged particles with non - zero pitch angle, by converging magnetic fields. Trapping of charged particles by a 'magnetic bottle' is a familiar phenomenon in the study of confined fusion plasmas, where mirror machine design of reactor uses (rather unsuccessfully) this principle. Such machines are unsuccessful because end losses are unacceptably high, but research into controlling plasmas in this way continues. Trapping also arises in the Earth's magnetosphere. The converging fields at the poles means that charged particles in the atmosphere may be reflected there, and can remain for a long period in the Van Allen radiation belts found above the equatorial regions. High energy particles leaking from the ends of the trap give rise to the aurorae. A magnetic flux tube anchored in the photosphere and rising up through the chromosphere and into the corona will expand as the surrounding pressure decreases. The resulting field convergence at the flux tube footpoints can act as a trap to coronal particles.

§3.1.2 The Magnetic Trap

A particle of charge q, mass m, moving with velocity $\underline{v}$ in a magnetic field $\underline{B}$ and an electric field $\underline{E}$ is subject to the Lorentz force

$$F_L = q(\underline{E} + \frac{\underline{v} \times \underline{B}}{c}) \qquad 3.1$$

We consider the case $\underline{E} = 0$. In a in a highly conducting medium such as the corona, spatial charge separations leading to local electric fields are not maintained except when driven by the beam itself. We neglect $dB\backslash dt$ electric fields. The effect of the Lorentz force is to make a charged particle execute a helical path about the field direction with Larmor radius

$$r_L = \frac{mvc}{qB} \qquad 3.2$$

The sum of the particle potential and kinetic energy in the field is conserved at all points on the path (cf Spitzer 1962). When the field which is guiding and influencing the particle motion varies, the Lorentz radius and the particle velocities parallel and perpendicular to the field direction vary also. It is found (see, eg.Tandberg-Hanssen and Emslie, 1988) that there are various conserved quantities - the adiabatic invariants of the motion of the particle. The one of interest here is the first invariant, which relates the particle momentum perpendicular to the field direction and the magnitude of the field

$$\frac{p_\perp^2}{B} = constant \qquad 3.3$$

If the field increases then so does the perpendicular particle momentum. But since $p_\perp = mv_\perp$ and $v_\perp^2 + v_\parallel^2 = constant$ (in a collisionless medium), the particle's velocity parallel to the field must decrease. This may be expressed by writing

$$\frac{1-\mu^2}{B} = \frac{1-\mu_o^2}{B_o} \qquad 3.4$$

where μ and B are the cosine of the particle pitch angle and the local field strength, with the subscript 'o' denoting these parameters at some (arbitrary) point of injection. At the point where $\mu = 0$ all the particle momentum is perpendicular to the field direction. Here the particle mirrors, and the mirroring field strength B_m is then given by $1 - \mu_o^2 = B_o \backslash B_m$.

A particle injected at B_o with pitch angle $\mu > \mu_o$ will not mirror at or before B_m but will instead form part of the loss–cone distribution - those particle which have sufficient initial parallel momentum to escape the trap. In the solar case it is these loss cone particles which enter the low atmosphere and cause footpoint emission and chromospheric heating, whilst the trapped coronal particles generate the coronal hard X-rays (and other coronal emissions such as microwave and radio bursts). Note, however, that the adiabatic invariant is invariant only in a lossless medium - which the transition region and chromosphere most certainly are not. In the coronal part of a magnetic loop the collisionless approximation may be reasonable if the collisional loss timescale is much greater than the escape time from the trap. But in the dense chromosphere it is necessary to include the effects of energy degradation and pitch angle scattering by Coulomb collisions. Other sources of scattering - eg by Alfvén waves are not considered at present, although our solution of the evolution equation is of such a form that it will be possible, as a future project, to add additional scattering terms.

Before describing the treatment of this problem we will review briefly existing work on the trap-plus-precipitation model, comparing its predictions of HXR and SXR emission with what has been observed, and also describe recent work on the transition region and chromospheric field structure, since this must be prescribed in our mirroring model.

§3.1.3 Support for the Trap - Plus - Precipitation Model.

Recent work by, amongst others, Vilmer (1986) on extended hard X-ray emission and Alexander (1990), MacKinnon (1990) and McClements(1990) on hard X-ray bursts has tackled the application of the trap - plus - precipitation model (originated by Kane 1974 and quantified by Melrose and Brown 1976) by a number of different analytical and theoretical methods. The work of Alexander (1990) using a mean scattering treatment (i.e. one in which the evolution of a particle having the mean energy and pitch angle of the entire distribution is followed) and that of MacKinnon (1990) using a perturbation solution, have given good agreement with a full numerical treatment (McClements 1990a) of the evolution in pitch angle and energy of a particle distribution trapped in a coronal magnetic bottle. In his calculation, Alexander determines the observed HXR spectrum for a range of values of $\mathcal{R}$, the ratio of coronal to chromospheric emission. Using a value of the total

precipitated particle flux in agreement with that arrived at in the calculations of Li *et al* (1989) on soft X-ray emission, Alexander finds that the predicted HXR spectrum compares favourably with observations. This work considers isotropic injection of electrons into the loop, as does that of MacKinnon (1990) who finds that using a perturbation solution of the evolution equation, values of $\mathcal{R}$ are quantitatively consistent with the broad temporal evolution and energy variation of observed $\mathcal{R}$, for a simple form of injection profile. The work of Vilmer *et al* (1982) explains observations of gradual phase hard X-rays in the flare of 14th August 1979 in terms of a well - trapped coronal population of electrons which is added to by subsequent injection pulses, resulting in an extended ($\sim$ 10 min) HXR profile of several peaks.

The above evidence for the trap - plus - precipitation model is encouraging, and to date the model appears to be the best that we have. As such it should be studied in the context of Hα polarized emission. But in addition to this, the observational (and theoretical) fact that converging magnetic fields exist in the chromosphere (for evidence see the next section), demands that if we are to study any model involving electron beams, which scatter, then magnetic trapping must be included.

§3.1.4 Atmospheric Model and Magnetic Field Structure

In the problem of generation of impact polarization we are interested solely in what happens in the chromosphere. We do not therefore concern ourselves with the behaviour of electrons in the corona, where the warm target approximation (see §2.1.1) of electron scattering may be appropriate, but deal only with the cold target region of the transition zone and chromosphere (cold to electrons with energies $\gg$ 40eV). The flare model atmospheres of Machado *et al* are once again used.

It is necessary not only to have values of the magnetic field in the chromosphere, but also to have some form for the field convergence between these two points, since the location of the maximum rate of field convergence is where the majority of electrons will mirror. In Hagyard (1984) we are presented with average quiet sun sunspot field gradients of 0.1 to 0.3 Gauss km^{-1}. One method used by the author is to calculate field strengths from Zeeman splitting observations in the transition region of CaIV at 1548Å, and in the photoshere of FeI at 5250Å, formed at roughly known heights, but in addition magnetograph observations of the horizontal components of the field at the solar surface are used along with the div.$\mathbf{B}$ = 0 condition to deduce the underlying field convergence. These methods yield the same results, within experimental error. There is only one source of direct experimental measurement of the coronal field strength and this is the Zeeman effect observed in optical lines in coronal prominences - which are cool dense material suspended in magnetic fields above the solar surface and may not be representative of either the mean coronal field, or that in hot flare loops such as those with which we are concerned. Other

sources of indirect field measurments are the microwave and radio emission from the corona, caused by various plasma oscillations, about which we shall not go into detail here (but see the summaries by Dulk and MacLean 1978, Hurford 1992). However problems with this data include uncertainty about the position of the region from which the emission emanates, and therefore about the plasma properties, doubt about precisely which mechanisms are responsible for which signatures, and the innately complex theory involved in interpreting radio emissions, which are very sensitive to local conditions. Extrapolation of photospheric fields using potential field analysis is the most reliable method of calculating magnetic fields from $1.1R_{\odot}$ out to distances of about $1.4R_{\odot}$. Beyond this region the method is not reliable. Since we are concerned with loops of length approximately 10^9 cm or $\sim 0.02R_{\odot}$, the extrapolated field values are not really suitable. The best we can do is to turn to the work of Takakura (1972) who calculated the field using radio emission (gyrosynchrotron emission) from a flare region, arriving at values betweeen 220 and 370 gauss at a height of 1.4×10^3 km. Coronal fields of this order will be used in our calculation.

Keller *et al* (1990) have calculated the photospheric field strength using very high spatial resolution images of two magnetically broadened iron lines, whose intensity ratio is almost totally insensitive to everything except the local magnetic field value. At the formation height of these lines (approximately 500 km above $\tau_{5000} = 1$) they find a field strength of $\sim$ 1000 - 1200 Gauss, but at $\tau_{5000} = 1$ this has risen to $\sim$ 2000 Gauss. The chromospheric field convergence has been studied theoretically by Solanki and Steiner (1990a,b) and has also been inferred from γ – ray directivities by MacKinnon and Brown (1989,1990). Solanki and Steiner (1990) use an active region model in which material within a flux tube is at a higher temperature than the surrounding chromopshere and find that there comes a point where the external pressures on the flux tube cannot contain even the weakest fields. The tubes then expand rapidly, and at a height of about 800 to 1000 km the fields merge and form a 'canopy' with a nearly horizontal base. MacKinnon and Brown infer the field convergence from the distribution of γ – ray bremsstrahlung continuum bursts on the solar disk. These bursts occur almost exclusively on the solar limb. Bremsstrahlung γ – rays are highly beamed in the direction of motion of the emitting particles, which on the limb are travelling in the local horizontal direction in a locally vertical magnetic field - i.e., mirroring, which happens at the deepest point in their trajectories. The location and strength of convergence therefore afect the intensity and angular distribution of observable γ - rays. Modelling has placed constraints on the field - "All of the strengthening of the field cannot occur in too narrow a region, neither just above the photosphere nor just below the transition region, and the field strength in the coronal part of the loop must lie within a range of values, never being as large as half the photospheric field B_1 nor so small as $10^{-2}B_1$".

The model of Solanki and Steiner gives a much more rapid convergence than is inferred from the results of MacKinnon and Brown. It seems plausible in the anisotropic chromosphere that flux

tube material is hotter than its surroundings, making magnetic canopies observeable in active regions. But possibly in the heated flare atmosphere in which γ - rays are formed the temperature distinction between flux tube and non-flux tube material is lost meaning that extreme examples of canopies would not occur during this period. As it moves back towards its pre-flare active region state (see chapter 1) it is possible that during this phase the temperature difference between magnetic and non-magnetic material will be once more established leading to the formation of the canopy again. We do not test an extreme canopy model but will investigate both rapidly and slowly converging field structure, employing the form of field used by MacKinnon and Brown. A loop co-ordinate system (r,θ,s) is defined where r is the distance from the loop axis, θ is the azimuthal angle and s is the distance along the loop axis from the top of the loop. By the time the loop enters the chromosphere the loop axis is the local vertical (neglecting loop tilt) so we rewrite MacKinnon and Brown's equation 8a having replaced s by the co - ordinate z - the vertical distance down from the top of the chromosphere.

$$B_z(z) = B_o + \frac{(B_1 - B_o)}{p_2 - p_1}[p_2 x'^{p_1} - p_1 x'^{p_2}] \qquad 3.5$$

where $x' = z\backslash z_o$ and z_o is the depth of the chromosphere, and p_1, p_2 are constants describing the field convergence. p_1 controls the depth at which convergence occurs and p_2 controls the rapidity of convergence. B_1 and B_o are the photospheric and chromospheric fields. Such an explicit form for the field variation is necessary when solving the Fokker-Planck evolution equation for the particle distribution.

§3.1.5 The Fokker - Plank Evolution Equation and its Solution

In treating the problem of mirroring electrons we consider the evolution of a particle distribution. Since the angular dispersion of the beam distribution is important in calculating the polarization it will generate, we prefer not to use any method involving average beam quantities - neither an average pitch angle - as in the mean scattering treatment, nor an average particle energy, as is employed in the treatment of a monoenergetic proton beam in the previous chapter (successfully, since protons do not scatter significantly). Instead we use a novel method developed in the astrophysical context by MacKinnon and Craig (1991) to solve the Fokker - Planck equation for the particle distribution. Below we will introduce this equation and describe the method of solution.

Let the distribution function have the general form $f(z, E, \mu, t)$ where z is the distance co - ordinate, v is the speed, μ is the pitch angle and t is time. The equation for the evolution of the distribution function is given by

$$\frac{df}{dt} = \frac{\partial f}{\partial t} + D_z f + D_v f + D_\mu f = 0 \qquad 3.6$$

where the $D's$ are partial differential operators on the function which can in general vary with all of the parameters z, v, μ and t. This equation can only be solved knowing the boundary condition $f(t=0) = f_o(t, z, v, \mu)$. In a steady state, (and we will treat the generation of impact polarization as a steady state problem) the equation we have instead is the time integral of (3.6). Let the differential operators in spatial and velocity co - ordinates be grouped into one operator $\mathcal{G}$. Then the time - integrated equation is

$$\int_0^\infty \frac{\partial f}{\partial t} dt + \int_o^\infty \mathcal{G} f dt = 0 \qquad 3.7$$

At $t = \infty, f = 0$. At $t = 0, f = f_o$. Defining the time - independent distribution function

$$F = \int_o^\infty f dt \qquad 3.8$$

gives the steady state equation with, instead of boundary conditions, a source term, i.e.,

$$\mathcal{G} F = f_o(z, v, \mu) \qquad 3.9$$

Solving the evolution equation with a boundary condition and then integrating over time is equivalent to solving the steady state equation with a source function equal to the spatial part of the injection function. This is understandable if one considers what integration over time means, when evaluated at a particular spatial point. If at point z_i one counts into bins all the particles passing with a given velocity and pitch angle, from a single injection event, over all time, the resulting particle distribution will be the same as if one counted, for a short time, particles arriving from a constantly renewing source with the same spatial and energy dependence as the injection function. In the steady state all stages of evolution of continuous injection function are present, at a point, simultaneously.

Therefore we can approach the solution of the steady state equation via the time - dependent equation, and calculate the distribution function at chosen z_i's by integrating over time the solution at z_i of the time dependent equation. We will not derive it here but the particular form of time dependence to be solved in the case of a mirroring population undergoing Coulomb collisions is (see eg Kovalev and Korolev 1981, Hamilton, Lu and Petrosian 1990)

$$\frac{\partial f}{\partial t} + \mu v \frac{\partial f}{\partial z} - \frac{4\pi e^4 \Lambda n}{me^2} \frac{\partial}{\partial v}\left(\frac{f}{v^2}\right) - \frac{4\pi e^4 \Lambda n}{me^2} \frac{\partial}{\partial \mu}\left((1-\mu^2)\frac{\partial f}{\partial \mu}\right) + \frac{v}{2}\frac{\partial}{\partial \mu}\left((1-\mu^2)\frac{\partial lnB}{\partial S} f\right) = 0 \qquad 3.10$$

The first two terms in this expression are the time and distance derivatives, the third and fourth describe the energy loss and pitch angle scattering due to Coulomb collisions , and the final term describes the change in pitch angle due to magnetic field convergence. S is the distance along a field line. We also specify a boundary condition, in terms of the injected energy spectrum and

pitch angle distribution. Equation 3.10 can not be solved analytically. The two usual methods employed in the solution of Fokker - Planck type equations are scattering treatments and Monte Carlo simulations. The former, as described briefly already involves following the evolution of a particle having the mean properties of the entire particle ensemble. Ambiguities exist in this method. For example, when defining the mean pitch angle is it appropriate to use $\cos < \theta >$ or $< \cos\theta >$? Or indeed, is it more appropriate to work with the sine of the pitch angle? In addition, defining mean quantities means that detail is lost as is illustrated in MacKinnon and Craig (1991). In this paper the spatial distribution of energy deposited by an electron beam in a mean scattering treatment is compared with that generated by the 'stochastic' method (which is what will be employed in this chapter) and, not surprisingly, if a single energy value is attributed to the entire distribution at a particular point, all particles will deposit the bulk of their energy at the same depth, at an infinite local rate, whereas a genuine distribution encompassing a range of energies will show a spread in the depths at which individual particles lose most of their energy. According to equations 9a in Emslie (1978) the energy deposition rate in a thick - target calculation depends on the inverse of the particle velocity, so the fact that the stochastic treatment of energy deposition reveals a large spread in deposition rate by a monoenergetic beam with a unique value of pitch angle, which is not seen in the mean scattering treatment, indicates that details of the velocity distribution are lost if a mean scattering treatment is used. Although it might be expected (depending on the particular implementation of the mean - scattering treatment) that the mean value of the velocity distribution would be the same as the single value of velocity coming out of the mean-scattering method, the spread of the function is very important in the problem of excitation of $H\alpha$, since the excitation cross section is strongly dependent on v. We will not in fact study a mono-energetic beam, as did MacKinnon and Craig, but have some initial distribution over velocity. This will smear the differences between the mean-scattering stochastic method, but these differences will probably still be important. Additionally the mean-scattering treatment, by its nature, does not allow for any spread in pitch angle θ, the other factor which affects the resulting polarization, via the anisotropy term $b(v)$. In a mean scattering treatment there is only one value of the anisotropy factor at a given depth, but in the real situation, each division in velocity of the distribution function will have its own anisotropy factor, and it is not clear how, or if, the two cases are related.

The second method, the Monte Carlo method, as used by Bai (1982) in his calculation of electron transport in a fully ionised plasma, involves the construction of a large ensemble of particles each with an assigned velocity and pitch angle (according to some initial condition). The paths of the individual particles are followed in a stepwise manner, with the average pitch angle and energy evolution, over a given step distance modelled by analytic approximations at each position chosen

as a step.

The stochastic method, used by Craig and MacKinnon, is closest to the Monte Carlo method in that it uses individual particle paths to build up a picture of the overall distribution function, but without resorting to approximations for the variations of pitch angle and energy. Instead, the solution is based on the equivalence of a Fokker - Planck (F-P) equation with a set of stochastic differential equations. The statistical basis of the method is described in Gardiner(1985) and we give here only a sketch argument. A F-P equation is one of the type

$$\frac{df}{dt} = \frac{\partial f}{\partial t} + \frac{\partial}{\partial x_i}(A_i f) + \frac{1}{2}\frac{\partial^2}{\partial x_i \partial x_j}(B_{ij} f) \qquad 3.11$$

- having a drift term with coefficient (A_i) and a diffusive term with coefficient ($B_{i,j}$). Let the co-ordinates x_i make up a vector $\underline{x}$. The distribution function f at a time t and at vector $\underline{x}$ is related to f_o at $t_o \underline{x}_o$ via the conditional probability $p(\underline{x}, t \mid \underline{x}_o, t_o)$ i.e.,

$$f(x,t) = f_o(\underline{x}_o, t_o) p(\underline{x}, t \mid \underline{x}_o, t_o) \qquad 3.12$$

The solution of the diffusion equation

$$\frac{\partial}{\partial t} p(\underline{x}, t \mid \underline{x}_o, t_o) = \frac{1}{2}\frac{\partial^2}{\partial x^2} p(\underline{x}, t \mid \underline{x}_o, t_o) \qquad 3.13$$

is given by

$$p(\underline{x}, t \mid \underline{x}_o, t_o) = \frac{1}{\sqrt{2\pi(t - t_o)}} e^{-(\underline{x} - \underline{x}_o)^2 \backslash 2(t - t_o)} \qquad 3.14$$

and describes a *Wiener process*, $\underline{W}(t)$ - the spreading by diffusion of an initially sharp distribution. This is the solution of the diffusive part of the F-P equation. It can be shown that the F-P equation is formally equivalent to the set of equations

$$d\underline{x} = -\underline{A}(\underline{x}, t) + \underline{\underline{B}}^{\frac{1}{2}}(\mathbf{x}, \mathbf{t}) d\underline{W}(t) \qquad 3.15$$

$\underline{A}$ being a vector containing the drift terms in the F-P equation and $\underline{\underline{B}}$ being a tensor containing the diffusive terms. These are called the random or stochastic differential equations. The path of a single particle can be followed by timestepping equations 3.15 and, at each timestep, calculating a new random $\underline{W}(t)$ to simulate the diffusive part of the transport process. If many particle paths are calculated the distribution function can be built up, and examined at a position z_i by simply binning the particles arriving at there according to their velocity and pitch angle. Obviously the distribution generated will be subject to errors $\sqrt{}$ N on N, the number of particles found in a particular bin, since the scattering is a random process. And the distribution will be better the more particles that are followed. The advantage of this method over the Monte Carlo method (as used in Bai 1982) in this particular application is that analytical approximations for scattering

etc, which are easy to use in a uniform medium, are not appropriate when the medium is, like the transition region and chromosphere, one in which density and temperature are varying rapidly over small length scales. The stochastic method can deal with individual consecutive scattering and is simple to adapt for non-uniformity of the relevant atmospheric parameters. It is also computationally very simple to implement and understand.

The stochastic equations to be solved in the case of electrons mirroring and undergoing Coulomb collisions are

$$dz = \mu v dt \qquad 3.15a$$

$$dv = \frac{-4\pi e^4 \Lambda n}{m_e^2 v^2} dv \qquad 3.15b$$

$$d\mu = \left[\frac{-8\pi e^4 \Lambda n}{m_e^2 v^3} + \frac{v}{2}(1-\mu^2)\frac{\partial ln B}{\partial z}\right] - \left[\frac{4\pi e^4 \Lambda n}{m_e^2}\frac{(1-\mu^2)}{v^3}\right]^{1\backslash 2} r(t)dt \qquad 3.15c$$

As outlined above, a Wiener process is in fact the Gaussian distribution with mean zero and in this case, because of the form of the equations, variance two. Therefore $r(t)$ for individual particles is a number drawn at random from this Gaussian. The computational process for following a single particle is as follows. The particle's initial velocity and pitch angle are prescribed by being drawn from some initial distribution function. An analytic form for the magnetic field variation is chosen - although this is solely because detailed experimental data does not exist - the stochastic method will cope easily with interpolated data, as it does in fact when using chromospheric structure data. A time-step is chosen, and the position, velocity and pitch angle of the particle are stepped on by values Δz, Δv and $\Delta \mu$ according to equations 3.16. The atmospheric parameters for the new particle position are calculated by evaluating the interpolation between the semi - empirical data points of Machado *et al*, in the same manner as is used in chapter 2, and the timestepping process is continued. It is a simple matter to examine the pitch angle and velocity of every particle arriving at a chosen value of z, the position in the atmosphere, and bin it accordingly, thus building up an approximation to the distribution function. The smoothness of the distribution function is improved as the size of the steps is reduced, and the number of test particles increased.

§3.2.1 General Method of Calculation and Test of Stochastic Simulation

Above we described the time-stepping procedure which is used to advance the distribution and count up the electrons into energy and angle bins. Now we describe how the polarization fraction is calculated from the resulting distribution . First of all we must realise the computational limitations of this method. Although simple, it is numerically intensive and takes rather a long time to run, therefore it is not possible to examine the distribution at closely spaced points through

the atmosphere - rather we look only at one or two positions of importance. In principle of course an examination of the distribution function with as much spatial resolution as in the thick - target proton beam model is possible, but very lengthy to compute. We will be able to make a reasonable approximation to the truth by locating the region in which the majority of non - thermal emission originates and examining the electron distribution function in this region. Providing that the distribution function does not change too rapidly over this chosen region, our values for the non - thermal emission should be a reasonable approximation. The level 1 hydrogen density must be high, but the optical depth low. Of course, the optical depth, as we calculate it, depends on the population of level 2, which decreases with increasing height in the atmosphere, and population of level 1 does the same thing, as is shown in figure 3.2. Our criterion for choosing the region in which the majority of non-thermal radiation originates is that it lies above the optical boundary, and that its extent is that distance in which the level 1 number density decreases by a factor of 10. In figure 3.2 , we see that the density at the position of the optical boundary is $\sim 2 \times 10^{11}$ cm^{-3}, and that it drops by an order of magnitude in a distance of 10^5cm. We shall assume that this narrow slab has a density equal to the density at its centre, which is 1×10^{11} cm^{-3}. We assume also in our calculations that all beam electrons throughout the slab have the same distribtion function as those in the centre of the slab (that is at 1.4285×10^8 cm above the photosphere and that all non-thermal electron excited emission comes from this region. It is anticipated that over distances as small as 10^5 cm the distribution function does not change significantly, compared to the changes due to transport in the overlying material. Important in polarization calculation is the ratio of non-thermal to thermal radiation. Although we only calculate the non-thermal radiation in a narrow slab we shall use the values for thermal radiation from the previous chapter, which have been integrated over the entire depth of the chromosphere. This will provide us with a lower limit to the magnitude of the polarization fraction. Still, it will be correct to about 10% since the number of level 1 particles has the most noticeable effect on the non-thermal intensity, and we are taking into account the region in which the vast majority of level 1 hydrogen atoms are located.

Before calculating the polarization resulting from these simulations we should look at some numerical results and see whether they are consistent with what we would expect physically. The result of one run of the stochastic simulation is an array of numbers of particles, divided in pitch angle and velocity, at a chosen height. An example of such an array is given in table 3.1. The array is set out with particle pitch angle horizontally and particle energy vertically. This simulation was made using 5000 particles, a maximum particle energy of 100keV and an initial pitch angle at injection of 0.8. This is the distribution as it appears at a height of 1.4295×10^8 cm above τ_{5000} - i.e just before Hα becomes optically thick. The field convergence is gentle, rather than of the 'magnetic canopy' version, and is described by the parameters $(p_1, p_2) = (2, 3)$ and $(B_c, B_p) = (300, 1200)$.

It will be noticed that the sum of all the entries does not add up to this number. Physically, as the distribution evolves, some particles will thermalise and be lost from the total population of the beam. As the timestepping advances in the stochastic simulation, the energy of some test particles will be reduced to zero (really the ambient thermal energy) through Coulomb scattering, and here the timestepping calculation stops. Therefore, when examined as a function of depth it is evident that the total beam particle population need not be conserved. Note that the distribution function spreads in angle at the low energy end of the spectrum - the table of particle numbers at their point of injection has values only at the initial pitch angle injection. The angles are in fact increasing - because of the magnetic field convergence the electron pitch angle increases, but because of scattering not all the pitch angles change by the same amount. The angular distribution of the high energy part of the population is not significantly affected by either the scattering or the field convergence. The number of particles in each energy bin has decreased due to the effect of scattering but we see that at high energies, there is no spread in pitch angle.

We test a couple of extreme cases. If we choose values for the field parameters so the field does not in fact converge, we should find that the distribution function remains essentially at the same pitch angle right through the atmosphere, with only perhaps a little scattering at the low energy end. On the other hand, if we reduce the density of the medium, the scattering should reduce to zero, but the convergence remain. If density is increased, the scattering will become significantly larger. Figures 3.3 a,b,c show the 2-d plots of particle distributions for runs with combinations of field parameters corresponding to these situations. In figure 3.3a, the convergence parameters are (14,15) which correspond to a slight convergence very low in the atmosphere. 3.3a is plotted at a position high in the atmosphere - at 1.4285×10^8 cm, and it is evidently not drifting in mean pitch angle at this point, although scattering is still present - the distribution function is spreading. In figure 3.3 b, the convergence parameters are the same as were used to generate table 3.1 but the atmospheric density is one order of magnitude less than the density in the MAVL F1 atmosphere. Note that the effect of field convergence is present without the spread in the distribution function, as we expect. If we increase the density by an order of magnitude over the MAVL F1 atmosphere, as in figure 3.3c, we see that the scattering effect becomes very large. So although we only test models using the F1 atmosphere we anticipate that, because if the increased scattering, higher mean beam energies would again be necessary in model F2 for a given polarization fraction to result.

From the particle distributions which we will calculate it is possible to evaluate the polarization Stokes' parameters according to the equations given in §1.2.6. (Note that if the distribution function of the mirroring and scattering particles is cylindrically symmetric then we can again use

the Stokes' Q and I parameters to fully describe the polarization. The magnetic field configuration which we have chosen is symmetric about the local vertical, so any convergence effects will not introduce asymmetry into the distribution, and neither will the scattering part, so we are safe with this method.) The distribution function is first normalised to 1 by dividing each bin entry by the total particle number. Calculating the Stokes' parameters involves evaluating the moments of the distribution function, given by equation 1.2.11. Note that in this equation, J_n is in fact $J_n(v)$. Therefore at a chosen height we evaluate the integrals over pitch angle as a function of velocity. Since we have only discrete values of the particle distribution function it is necessary to evaluate the integral as a sum - this will inevitably result in errors on the values of the J_n's. The values of $v\sigma(v)$ have been calculated at evenly spaced points, which we use in a Trapezoidal approximation to the full integral.

$$T(f) = \Delta v \Sigma_{i=1}^{n-1} f(x_i) + \frac{h}{2}[f(x_1) + f(x_n)] \qquad 3.16$$

where the points at which the function is defined are $(x_1, x_2 \ldots, x_n)$, separated by h. The standard error on this simple trapeziodal rule is of the order of $h^2 f''$ where f'' is the second derivative of the function.

§3.2.2 Variation of Parameters

In this problem there are several parameters which we can vary. First of all the initial pitch angle of injection primarily affects the sign of the polarization fraction generated. The shape of the distribution - i.e. horizontally or vertically peaked, at the particular energy of the electron, is the only thing that determines the sign. The electron distribution when scattering and being guided by the converging magnetic field moves always towards higher values of pitch angle until such times as the electrons are of such a low energy that they are completely thermalised by collisions and isotropised. We are interested only in high energy electrons - higher than the energy at which the polarization fraction changes sign from positive to negative at any rate, since electrons of too high an energy are scattered too rapidly. Therefore we are interested in horizontally peaked distributions, although it is possible that a distribution with initial pitch angle 0° - i.e. injected directly along the field, can be scattered and deviated from their paths by a sufficiently large amount that their distributions become horizontally peaked. But it is likely that at high energy, initially beam-like electron distribution will not do this in the chromosphere unless the convergence conditions are extreme. In addition, to get polarized radiation at a significant level, the convergence would all have to occur above the neutral hydrogen - rich layer, which is a rather narrow part of the atmosphere. We are mostly interested in distributions which start off with a significant pitch angle - e.g a μ of 0.7 or less. Secondly we can vary also the shape of the field - to control the exact position at which the majority of the change in the distribution takes place. As mentioned

before there are two differing scenarios which are worth testing here, which will probably lead to quite different results - the gentle expansion of fields as deduced from Gamma-ray directivities by MacKinnon and Brown (1989, 1990), and the magnetic canopy scenario where the expansion is rapid. We will vary conditions to result in rapid and gently convergences and in addition we shall vary the absolute magnitudes of the coronal and chromospheric fields, since these also affect the field convergence shapes. Figures 3.4 a-f show the range of field shapes studied.

For the initial particle distribution we use a uniform distribution over some interval, whose maxiumum range is to be specified, and is our third variable. Note that using the stochastic method it is quite simple to adapt the initial input distribution so that it has for example a power-law variation as is commonly found in solar physics - or a normal distribution - it is merely a matter of assigning appropriate initial energies to each of the particles whose stochastic trajectories are to be followed. But we choose the uniform distribution as a simple example) To generate the initial particle energies the NAg routine G06DAF is used, to pick numbers at random from a uniform distribution. We must decide on the upper energy of the electrons which we study - the 511keV anihilation line present in solar flares indicates that electrons of this energy must be present although possibly not in large numbers. Hard X-ray measurements indicate the presence of large numbers of electrons with energies of around 100-200 keV and lower. We shall test with a maximum energy of 500keV and also 100keV.

§3.2.3 Variation of the Initial Pitch Angle of the Distribution.

For this study we shall hold the particle energy constant, firstly at 100keV, and secondly at 500keV. We use the MAVL flare F1 atmosphere and parameters $(2, 3)$ to describe the field convergence. According to the work of MacKinnon and Brown this limits the value of the coronal to photospheric field to the range $0.25 - 0.45$. Since the effect of field convergence will be seen best with the largest possible ratio of photospheric to coronal fields we shall use values (300,1200). The pitch angle cosine is varied between 0.2 and 1.0. For each set of parameters the stochastic simulation is run, and we show the plots of the distribution as a function of pitch angle and particle energy at the location 1.4295×10^8 cm in figures 3.5. for selected parameter values. The total polarization fraction which we will calculate comes from the narrow slab at this position, as defined above. Looking at figures 3.5 and 3.6 we see that distributions which start out more beam-like are, at these energies, and with the chosen gentle field convergence, not changed significantly. Although there is evidently change in the distribution at the low energy end of the particle spectrum ($E < 30keV$), the polarization fraction will be dominated by contributions from the great number of high energy particles whose energy and pitch angle have not been changed.

In addition we calculate the intensity of Hα radiation emitted by the electron distribution at each of depth points. This must be multiplied by the total beam flux and the mean particle energy to obtain the total beam energy. since we are considering only uniform distributions, the mean energy is the median energy. As in chapter 2, the criterion for the polarization to be visible at the direction - corrected level $P_{obs} = 5.5\%$ is

$$\frac{P_B I_B}{I_B + I_{th}} > P_{obs} \qquad 3.17$$

where I_B and I_{th} are the beam-generated and the thermal intensities. Using the value of thermal intensity calculated for the MAVL atmosphere in chapter 2 we plot in figure 3.7a,b the polarization emitted for a variety of values of total beam particle number flux. We see that the magnitude of the polarization fraction is higher (both on the positive and negative sides of the graph) for the higher injection energy. Because the mean energy of particles exciting Hα radiation increases, the magnitude of the polarization fraction of the photons they excite also increases (being on the negative side of the curve in figure 1.15), and although the cross section decreases, the behaviour of the polarization evidently dominates. Note also that the polarization fraction changes with depth. If it is positive then it becomes more so, and if it is negative it becomes less so, reflecting the tendency of the distributions to increase in pitch angle as traverse the atmosphere. It is possible to have a polarization fraction of a few percent for a beam flux of between 10^{10} and . 10^{11} ergs cm^{-2} s^{-1}, or a total beam energy of $\sim 10^{32}$ and 10^{33} ergs injected for the duration and over the area of the biggest flare, since the polarization fraction is ultimately limited by the form of the distribution in the hydrogen-rich layers. There is no more severe a problem with the energy budget for this model than with the proton beam model, but (see discussion at the end of the chapter) there are still questions to be answered regarding the timescales emerging from the trapped electron models, and how the polarization area may realistically be increased from the 10^{17} to 10^{18} cm^2 which is calculated in some cases (e.g. Canfield 1991) for the magnetic loop footpoint.

§3.2.4 Variation of the Field Convergence Parameters.

In this investigation we keep the initial pitch angle of injection constant, vary the form of the field convergence in a ordered way. The field is described by p_1 which controls the height at which most of the convergence takes place, and p_2 which controls the sharpness of the convergence. Initially we keep the sharpness parameter constant and vary the position of convergence. We expect that as the convergence position is lowered, the polarization fraction will decrease for a given pitch angle of injection. Figures 3.4 show the field convergence patterns for the external field lines, and there is a line drawn across the figures at the position of the maximum emission. The gradient of the

field line at this point $\frac{dB}{dS}$ enters into equation 3.10 - if it increases then the effect on the particle paths is more pronounced. The gradient of the field line as drawn in the diagrams is of course not the field convergence gradient, in fact the smaller the gradient of the field line, the larger the field convergence. As can be seen, most of the field patterns are vertical or nearly vertical at the point of maximum emission - only the fields resulting from convergence parameters $(1, 5)$ and $(1, 10), (2, 10)$ slope significantly inwards here. We therefore expect that most of the polarization fractions for a given p_2 will be only slightly different, but that there will be a marked difference when using the rapidly converging field. This is because if the position of the majority of polarized emission is above the region of strong convergence, then the particle distribution will not change in pitch angle before exciting Hα , but if the strengthening occurs above here then the pitch angle will be increased. The region from which the bulk of Hα radiation emanates is very close to the top of the atmosphere and the convergence occurs on a scale which is compared to its dimension, so the effect of the convergence will not be great.

The polarization resulting for a single value of pitch angle (0.4 or 0.8) is studied. The distribution is uniform with upper limit 100keV. The total beam flux used is 2×10^{18} electrons cm^{-2} s^{-1}, or a total beam energy of 10^{33} ergs. Figure 3.8a also graphs the result for an upper limit of 500keV ($5 times 10^{33}$ ergs), which is rather large but is included for the purpose of illustrating how insensitive the polarization fraction is to beam energy (above some lower threshold corresponding to the minimum energy necessary to reach the neutral hydrogen rich layers $\sim$ 25 keV in flare model F1). Looking first at constant $p_2 = 5$ (figures 3.8 a and b), we see that indeed the most marked increase is at the low p_1 values, but that the decrease here is only a matter of 5% or so of the maximum. Evidently this factor is not as important as the initial pitch angle at injection in determining the distribution at subsequent positions. We end up with much the same results - at an injection pitch angle cosine of 0.4, we get 4% polarization and at a value of 0.8 we have a polarization of 6.6%. There is once again only a small variation with energy - a slight increase in the fraction (althought this was not studied at $\mu = 0.8$ since it was evident that any modification would not be large enough to change the sign of the polarization fraction.) Although we have not tested the full range of parameter p_1 we can see that there is an effect on the polarization fraction from changing the convergence position. Now let us use a new value for the convergence strength - $p_2 = 10$. Figures 3.9a and b illustrate the results of these calculations. The modulus of the polarization fraction has, both for low and high μ values increased by a few tenths of a percent polarization over the low convergence strength situation, as we expect from the increase in the gradient of the field lines at the emission point, visible in figures 4 c and d. But for such a large change in this convergence parameter the variation in polarization fraction is disappointingly small, and we suspect that it will be necessary to use quite extreme values for the convergence position

and strength ($p_1 \ll p_2 \ll 1$) for field convergence to be able to radically alter the distribution function at the position of maximum Hα emission.

With these studies we confirm that a high convergence factor, high in the atmosphere, is necessary for the generation of polarization with a positive sign, but that, although there is a visible effect on the polarization faction when the field convergence is changed, the value of the pitch angle at injection is still the dominant factor.

§3.2.5 Changing the value of the Magnetic Fields.

In the previous section we worked with field values of 300 Gauss in the corona, and 1200 Gauss in the chromosphere, which were based on the limits set by the MacKinnon and Brown (1990) models, for the parameters (2,3). Although we can vary the shape and position of convergence by changing (p_1, p_2), the strength is decided by the ratio of the coronal to the photospheric values. Of course, a field with strengths 300 Gauss at the corona and 1200 Gauss at the photosphere has the same shape, for a given (p_1, p_2) as a field of (100,400) Gauss, but a field with values (100,1000) Gauss has a different convergence for the same parameters. In addition, the $\frac{1}{B}\frac{dB}{dz}$ term appearing in the Fokker - Planck equation depends on the absolute value of the coronal field and also on the difference between photospheric and coronal fields. We shall change the absolute values of the field and also increase the ratio - we use values of (100,1000). The work of MacKinnon and Brown, implies that the corresponding radius of the footpoint of the loop is decreased to 10^7 cm. This means a single loop injection area even smaller than the polarization area of 10^{19} cm^2 which is observed, but we shall in any case see what the effect of changing the field is, because there is no real physical reason why the footpoints should not be somewhat larger. With these new field values we repeat the calculations from section 3.2.3 - the pitch angle is varied and the other parameters kept the same, with the values they had this previous section. The beam flux used is 10^{14} electrons cm^{-2}s^{-1}. We plot the results of this investigation alongside those obtained using the previous field strengths (figure 3.10 a,b). We see once again that there is a small increase all round in the absolute values of the polarization fraction, which is mirrored in the change in the field line gradient. But it is the pitch angle of injection which continues to dominate the polarization fraction.

Note that there is one additional parameter which we have not varied. Only a single form of density distribution (as given in the MAVL model) has been used. The density distribution is important not only for the energy variation of the electron beam but in addition for the pitch angle variation - previous work has not considered this aspect, so by using a non-uniform distribution we have

made some advances. But it would be interesting to see what combination of scattering density and field convergence is most efficient at varying the distribution of injected particles so that they do perhaps eventually mirror. This chapter did aim to find a mirroring distribution, but within the parameters already tested we have only been able to find relatively small perturbations to the initial distributions - deviations by a few degrees - for a wide range of field parameters. We expect that only a large change in the density distribution can affect the particle paths enough to make them mirror. We see from figure 3.3c that an order of magnitude increase in the total particle density has a large effect on the particle distribution, and increases in density at locations of high field convergence could possibly further enhance this.

§3.2.6 Discussion and Results

Discussion of Errors on the Polarization Fractions

Before we can properly interpret the results of these calculations we must properly account for the various sources of uncertainly in our calculations. Throughout chapter 2 we used experimental values for cross sections and polarization fractions which we are aware have errors associated and which result in uncertainties in the calculated values for observed polarization fractions. We have never calculated the effects of these errors, because all results are affected in the same way by them, and we can be sure that, apart from computer generated errors in, for example, NAg routines, the method is free from uncertainties - i.e., were we to run the calculation several times there would be no 'spread' in the results. However, in the work of chapter 3 we calculate the polarization from a particle distribution which is noisy, and if we were to run the calculation several times, a mean result would emerge but there would be a spread in it, even if the atomic data were absolutely precise. This is the 'counting noise' associated with the stochastic method. If one run of the code generates a bin with N particles in it, the uncertainty in the occupancy of that bin is $\sqrt{N}$. For these high energy electrons studied, the lower energy bins with high numbers of particles will contribute most significantly to the final polarization result, since the cross section decreases with energy whilst the polarization fraction has more or less a constant value at energies above 1keV. These bins have, in general, 100 - 500 electrons in them, corresponding to a fractional noise error of 0.05 to 0.1. So for subsequent runs of the code we would expect the results to differ *unavoidably* by this amount. When we run the code with a variety of field convergence parameters we see variations in the final polarization results which are not much larger than this - i.e., a few tenths of a percent change in polarization on a level of a few percent. So we need to be careful about attaching significance to these variations. Strong changes in the field shape at the region of strong emission, e.g. going from (1,5) to (4,5) shows up as changes above the noise level, but the fractional

change in the results when the convergence parameter is varied from (2,5) to (4,5) is only $\sim$ 1%, so we cannot really say for sure, that there is a systematic variation, although we suspect that there will be. To reduce the errors it is necessary to run the code following a higher number of particle paths - but to reduce the error to the level of 1% when the energy range is divided into 10 bins say, it is necessary to get 10000 particles average in each bins, which corresponds to 100,000 test runs. And this is not even allowing for divisions in angle, in which case the numbers would have to be further increased. So although we can estimate the lengths to which we must go to limit the intrinsic spread in this method, it is not actually worth carrying out the calculations since the changes we expect to see are small anyway. The large variations in polarization fraction with the field parameters are evident with the present calculations and they are sufficiently good indicators of the general trends in the model that we do not feel it necessary to increase (from 5,000) the number of particles in our runs.

Results of the Trapped Electron Model

We have performed simulations of the development of a population of electrons trapped in a magnetic bottle in a collisionally thick atmosphere. Using reasonable field parameters, we have found that it is possible to generate a positive polarization fraction of a few percent with a total energy budget very similar to that required by the proton beam model. We find that there is a slight variation of the polarization fraction with absolute field strength and convergence parameters, but this is only pronounced when the variations are such that the shape of the field is changing rapidly in the narrow Hα emission region at the top of the chromosphere. Variations in the field shape at low positions in the atmosphere are not 'seen' by the trapped electrons. The fraction obtained with the parameters we have tested just makes the threshold value (5.5%) necessary to explain the observed polarization. This is when an injection pitch angle of 78° from the vertical is used. Smaller pitch angles give smaller positive, or negative polarizations. We have not yet investigated the full range of possible field parameters - for example the magnetic canopy model of Solanki and Steiner (1990) would give more rapid convergence of the field, higher in the atmosphere, and with such models the range of pitch angles which can result in positive polarization fractions will be increased. But even the limited examples which we have studied demonstrate that it is easily possible for a trapped population of electrons to explain the polarization observations, with no more serious an energy budget problem than was encountered in the proton beam model.

There are still caveats of course. The first of them is that the large area of the observed Hα region is still not a natural result of this model - as with any model associated with the initial injection of energy into the chromosphere. The usual estimates for footpoint injection areas is $10^{17} - 10^{18}$ cm^2,

as found for example, in the work of Canfield (1991) on the ratio of Hα to hard X-ray emission. The convergence model of MacKinnon and Brown, developed to explain γ - ray distributions employs similar size footpoints, and the convergence parameter which we used are related to the footpoint sizes. For larger footpoint flares it is not known (although it could be calculated) what field convergences are necessary to explain the γ - ray observations, however we could still make the γ - ray and Hα field requirements agree if necessary, since we have seen that for distributions with a large pitch angle at injection, the polarization fraction is relatively insensitive to the field convergence. But additionally, it is possible that the emission comes from a large number (up to a few tens) of loops, possible as seen in Hα magnetic arcade type flares, firing off at similar times. This may be a strange situation geometrically, but there is certainly no energy constraint on it.

The second caveat is of course the timescale of the polarization. The increase in the time for which electrons are present in this model as compared to the 'single pass' picture of the electron flare depends on the trapping efficiency. In the work we have done so far the particles are being affected by the field but are not yet mirroring, although with the field convergences and the pitch angles which we use they most certainly will mirror, at some deeper region. We can see from the adiabatic invariant what the field ratio should be in a non-scattering environment for our electrons of pitch angle 0.4, which have the correct properties to cause the polarization. Of course, the chromosphere, as we have said, is not a non-scattering atmosphere, but for electrons of 100keV or more, figure 2.6 shows that the beam energy is not substantially reduced by scattering until the electron beam has traversed a column depth of $\sim 10^{21}$ cm^{-2}. Of course the particles are being deflected during their passage, but the tendency of both field convergence and scattering is to increase the particle pitch angle thus increasing the polarization. 10^{21} cm^{-2} is equivalent to approximately 10^8 cm of chromospheric material in the F1 model, so we require the field at a depth of 10^8 cm to be sufficiently strong that particles with an initial pitch angle of 0.4, injected in a coronal field of $\sim$ 300 Gauss, be reflected. Using the adiabatic invariant it is easily calculated that this critical field is only $\sim$ 360 Gauss, which is only a very moderate strengthening at this point, and corresponds to a decrease in the 'radius' of the flux loop by $\sim$ 10%. A stronger field convergence means that the particles will of course mirror farther up, and therefore will not have lost so much of their kinetic energy in collisions at this point, and there is the possibility that the mirroring process can occur a number of times. However, taking a loop of length 10^9 to 10^{10} cm, the loop crossing time of a 100keV electron is less than a second, and unless the field convergence is sufficiently high in the chromosphere that the electrons lose, through collisions, only a very small fraction - say one tenth of one percent, of their initial energy, on each loop crossing, repeated mirroring could not result in the timescales of 10^3 seconds observed. There would have to be some continuous injection of energetic electrons into the loop to replace those lost - this could maybe be

achieved through sustained reconnection. But other examples of long-lived particles in the solar corona already exist - namely the long-timescale proton events mentioned earlier.

In conclusion then, in terms of sign and magnitude of the polarization and the energy of the beam our findings indicate that the trapped electron model of the generation of impact polarization is capable of explaining the observations as well as the proton beam model. For the model to work one must inject electrons at an angle of $> 78°$ to the axis of symmetry of a converging vertical flux tube. We have studied injection of a uniform energy distribution of electrons, at a unique pitch angle, but do not anticipate that changing to a power law, or other energy distribution will significantly affect the results, provided that the electrons have, for the most part, energies of around. There remains work to be done on alternative field configurations, and pitch angle distributions, rather than unique injection angles should be investigated, but at present the model is yielding satisfactory results.

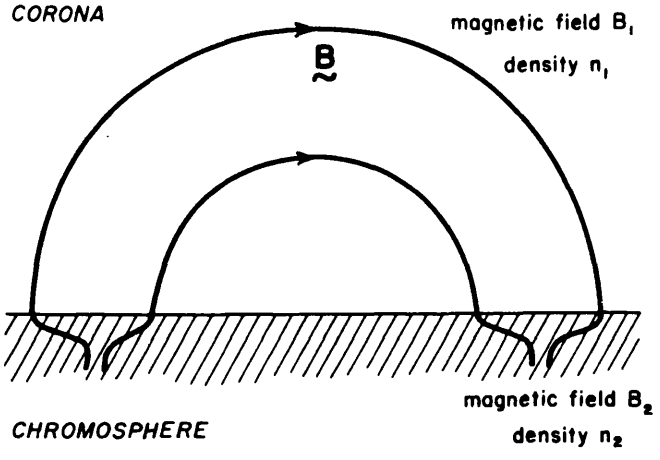

Fig 3.1 Solar coronal loop - the magnetic trap.

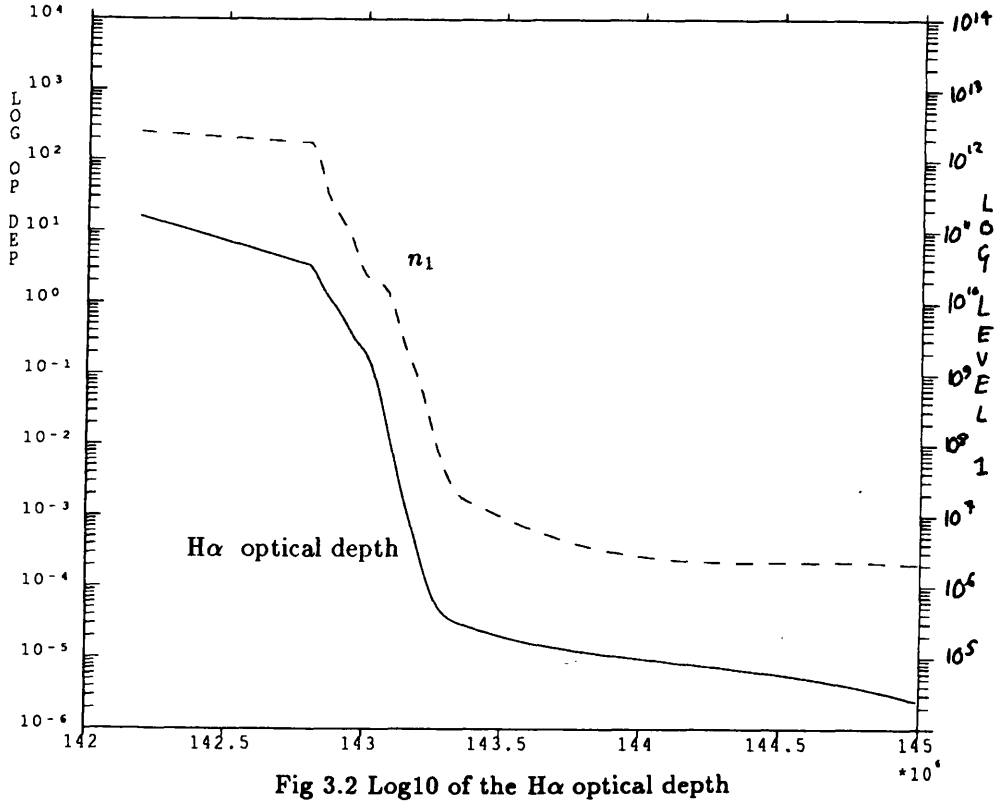

Fig 3.2 Log10 of the Hα optical depth
and hydrogen level 1 number density
as a function of height (flare F1).

0	0	0	0	0	0	0	0	6	97	7	0	0	0	0	0	0	0	0
0	0	0	0	0	0	0	5	170	52	0	0	0	0	0	0	0	0	0
0	0	0	0	0	0	0	144	286	0	0	0	0	0	0	0	0	0	0
0	0	0	0	0	0	0	358	20	0	0	0	0	0	0	0	0	0	0
0	0	0	0	0	0	0	486	0	0	0	0	0	0	0	0	0	0	0
0	0	0	0	0	0	0	507	0	0	0	0	0	0	0	0	0	0	0
0	0	0	0	0	0	0	445	0	0	0	0	0	0	0	0	0	0	0
0	0	0	0	0	0	0	464	0	0	0	0	0	0	0	0	0	0	0
0	0	0	0	0	0	0	544	0	0	0	0	0	0	0	0	0	0	0
0	0	0	0	0	0	0	480	0	0	0	0	0	0	0	0	0	0	0

Table 3.1 Example result of a stochastic simulation,
binned vertically in energy and horizontally in pitch angle.

Fig 3.3 Particle distributions generated with extreme field convergence parameters and atmospheric densities.

field convergence = (14,15)

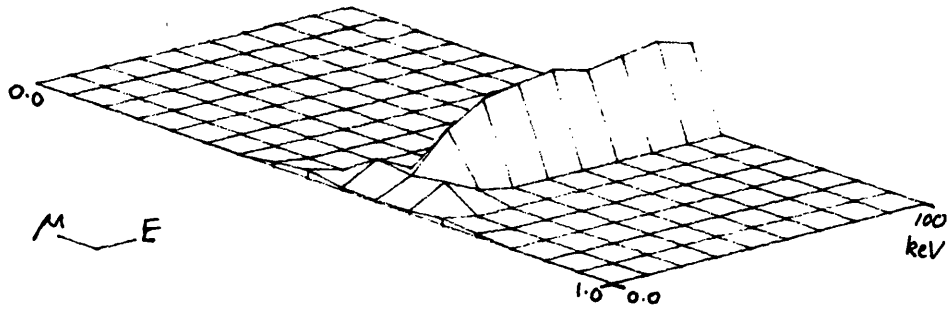

density = 10× MAVN model F1 density

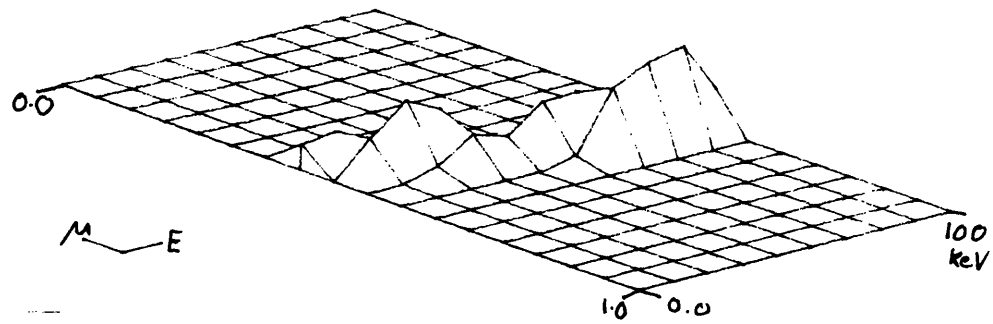

density = 0.1× MAVN model F1 density

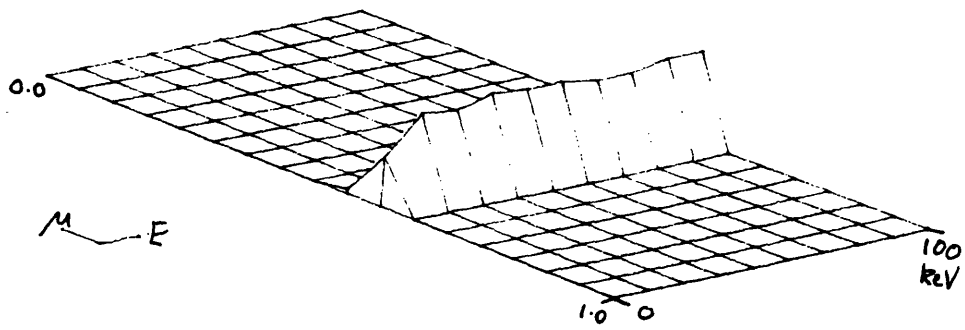

Fig 3.4 Field convergences.

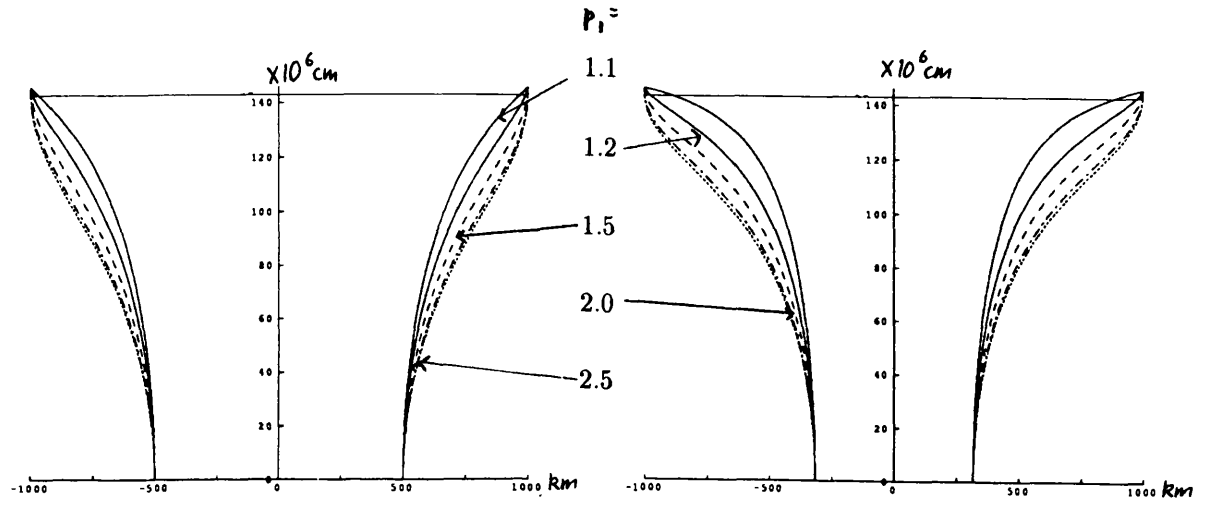

(a) $p_2 = 3, (B_0, B_1) = (300, 1200)$ (b) $p_2 = 3, (B_0, B_1) = (100, 1000)$

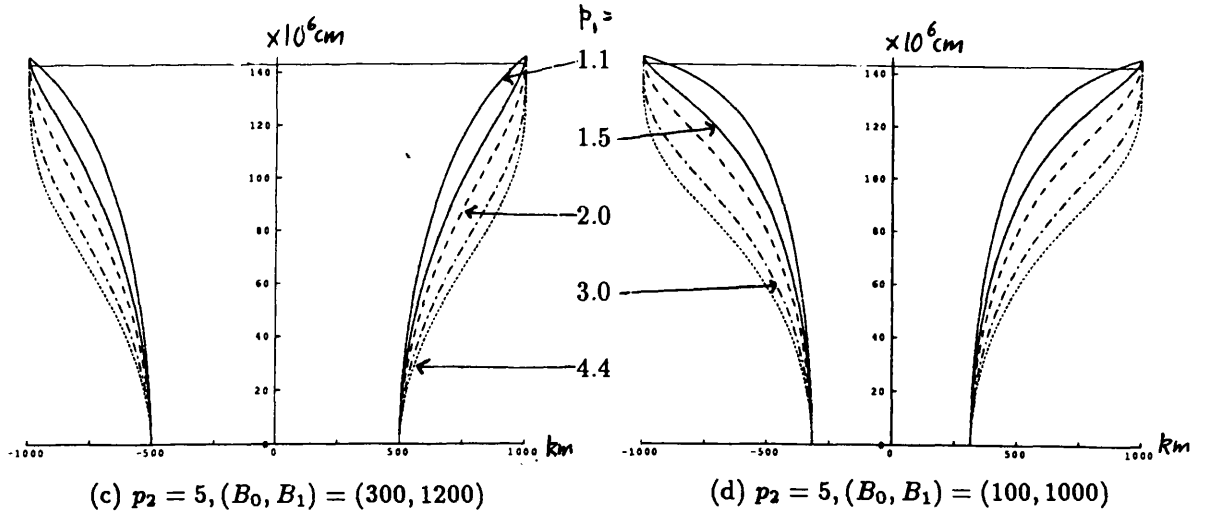

(c) $p_2 = 5, (B_0, B_1) = (300, 1200)$ (d) $p_2 = 5, (B_0, B_1) = (100, 1000)$

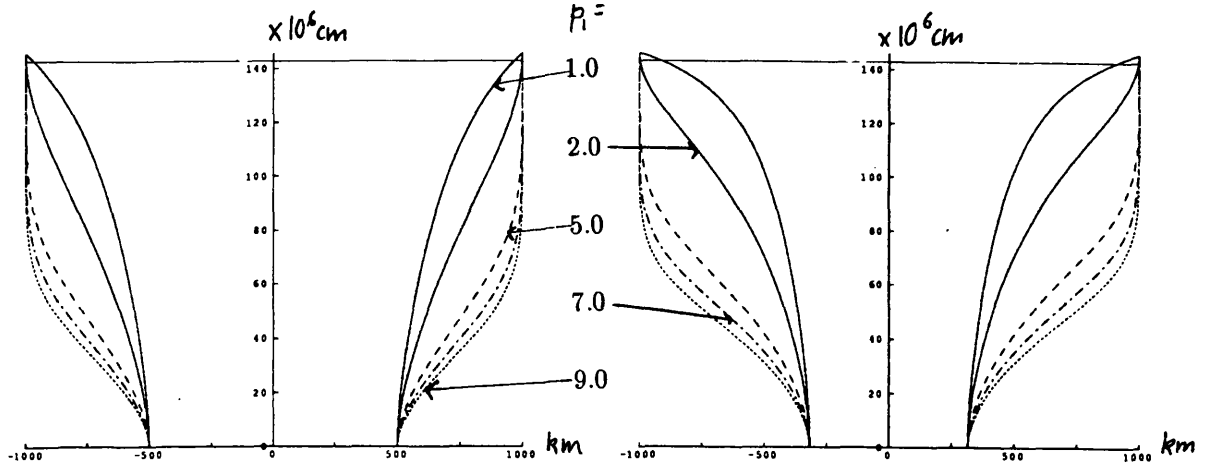

(e) $p_2 = 10, (B_0, B_1) = (300, 1200)$ (f) $p_2 = 10, (B_0, B_1) = (100, 1000)$

Fig 3.5 Particle distribution functions at $h = 1.4295 \times 10^8$ cm for a variety of initial pitch angles.
Maximum injection energy = 100keV.

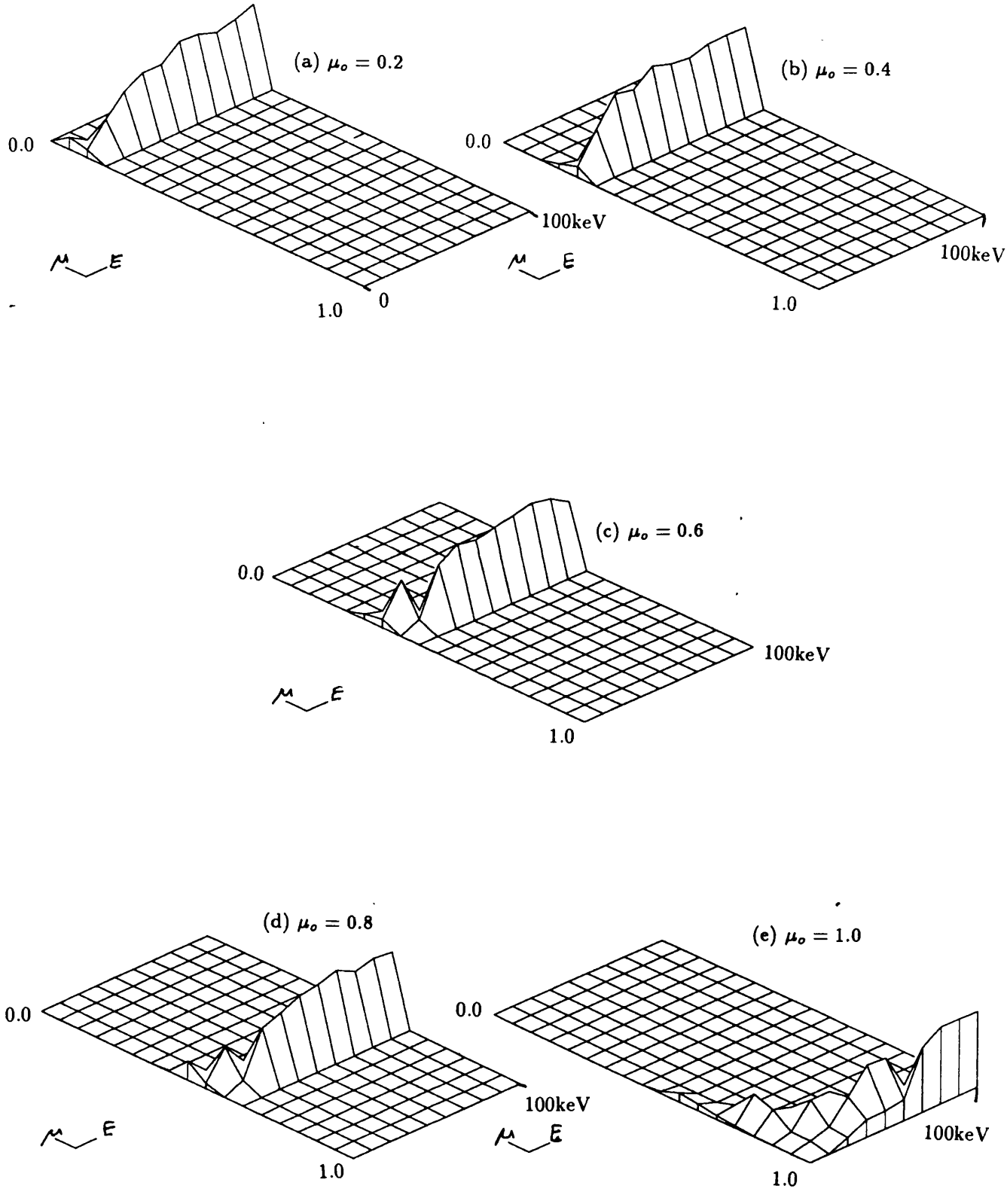

Fig 3.6 Particle Distribution functions at $h = 1.4295 \times 10^8$ cm for a variety of initial pitch angles.
Maximum injection energy = 500keV

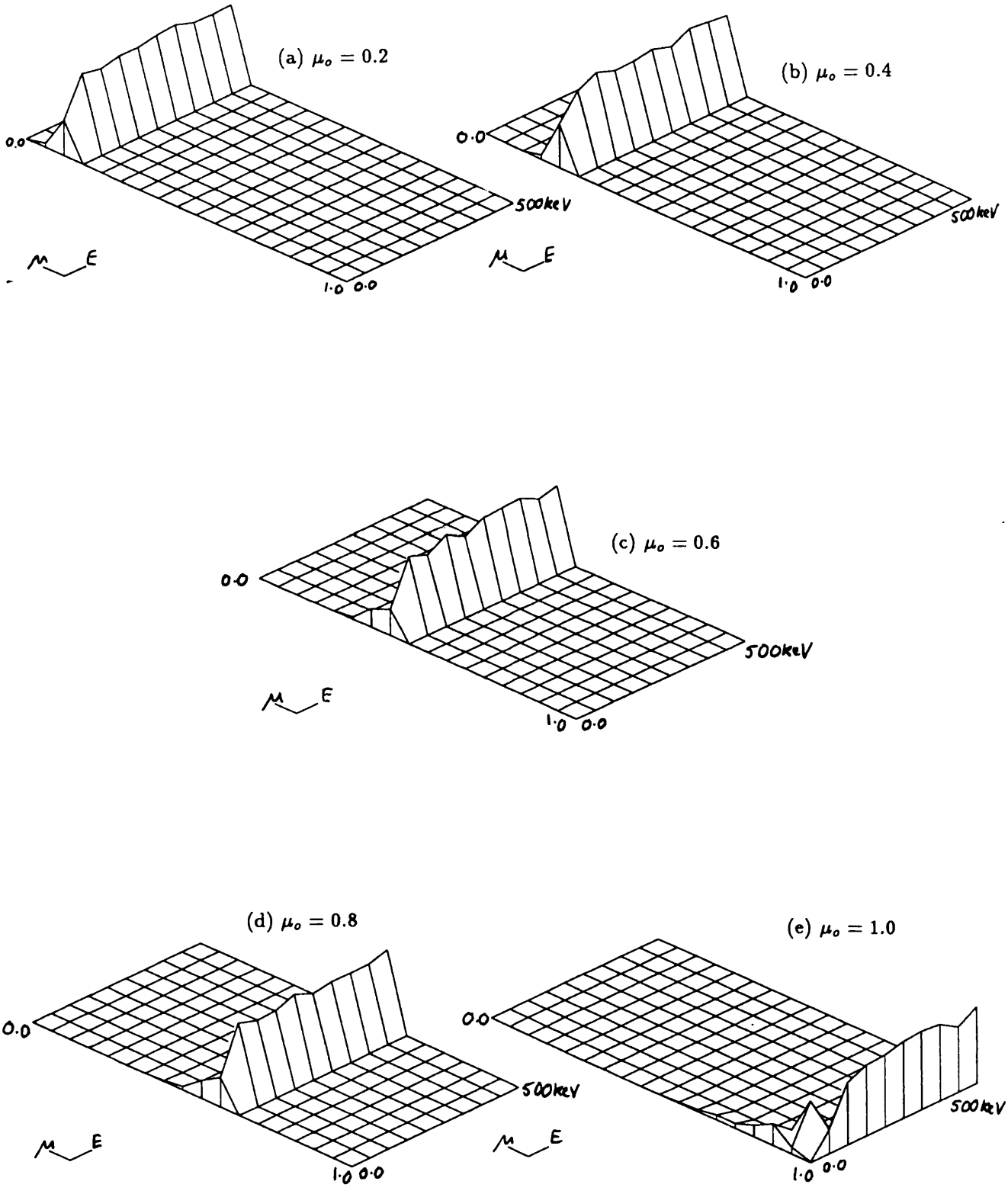

Fig 3.7a Net polarization as a function of initial pitch angle.
$(p_1, p_2) = (2, 3), (B_0, B_1) = (300, 1200), E_{max} = 100keV$

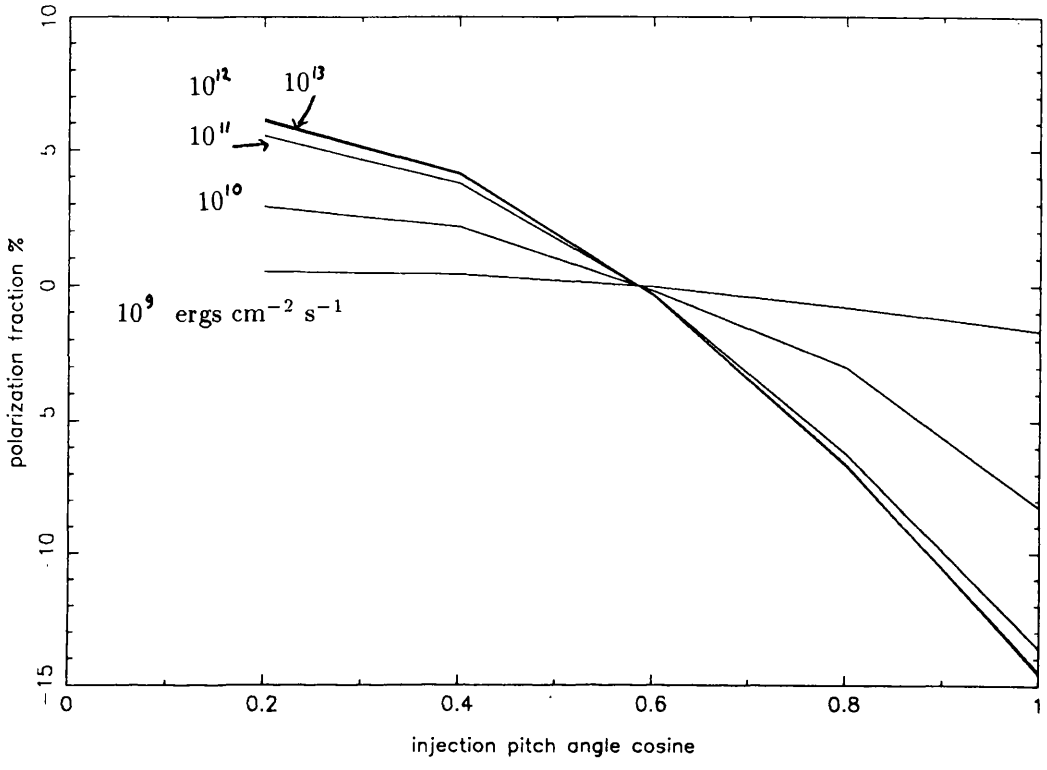

Fig 3.7b Net polarization as a function of initial pitch angle.
$(p_1, p_2) = (2, 3), (B_0, B_1) = (300, 1200), E_{max} = 500keV$

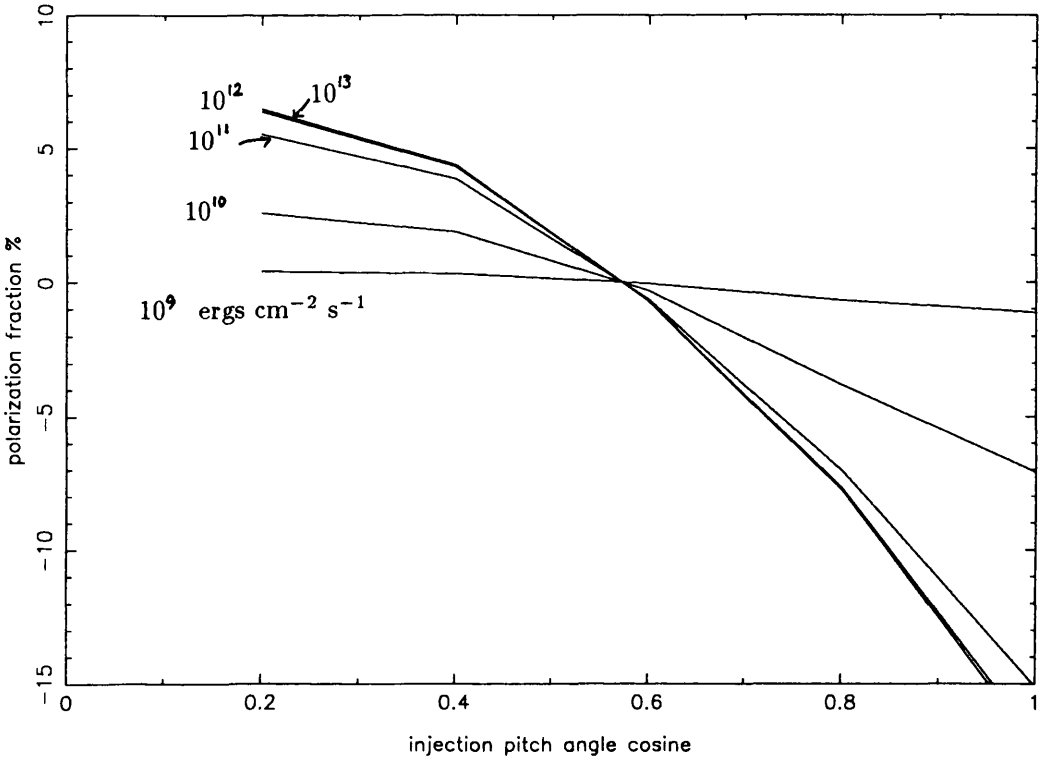

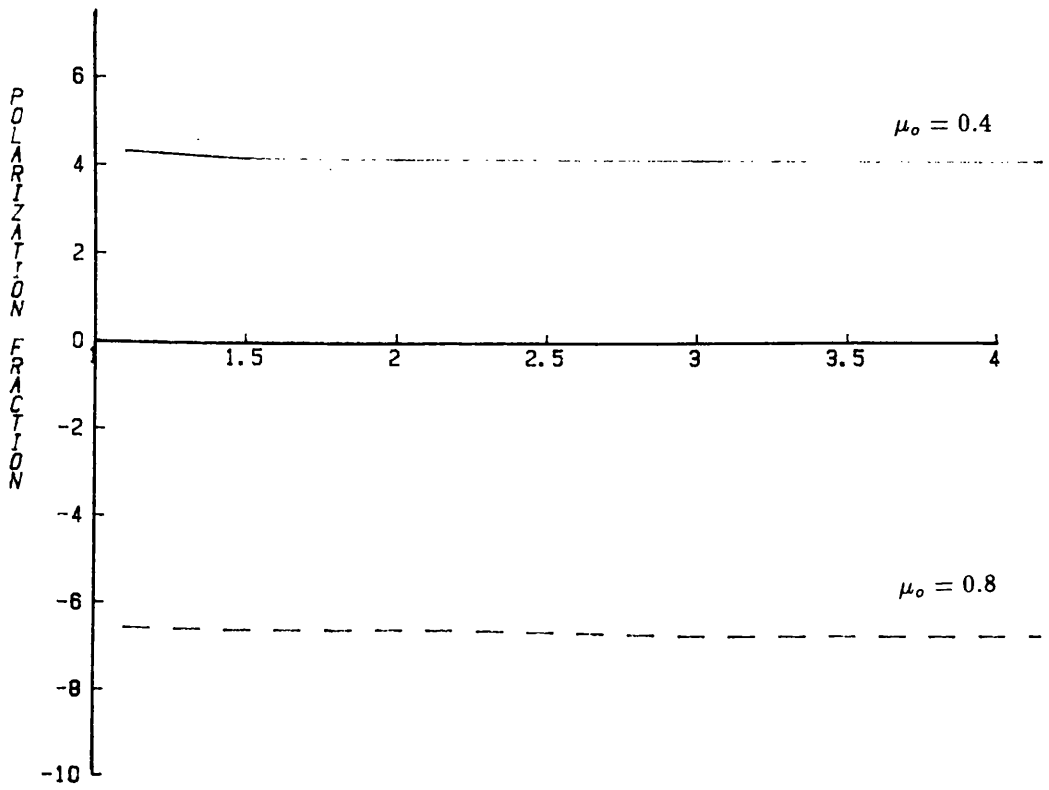

Fig 3.8a Net polarization as a function of p_1.

maximum energy = 100keV

$p_2 = 5$

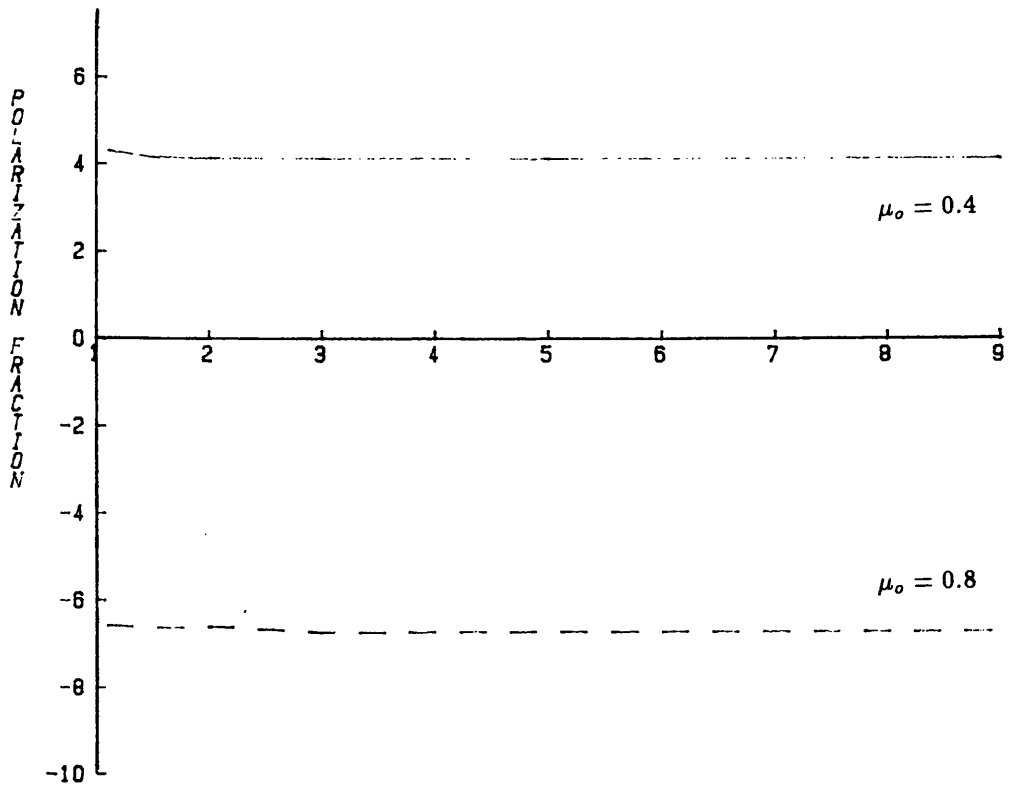

Fig 3.9a Net polatization as a function of p_1.

maximum energy = 100keV

$p_2 = 10$

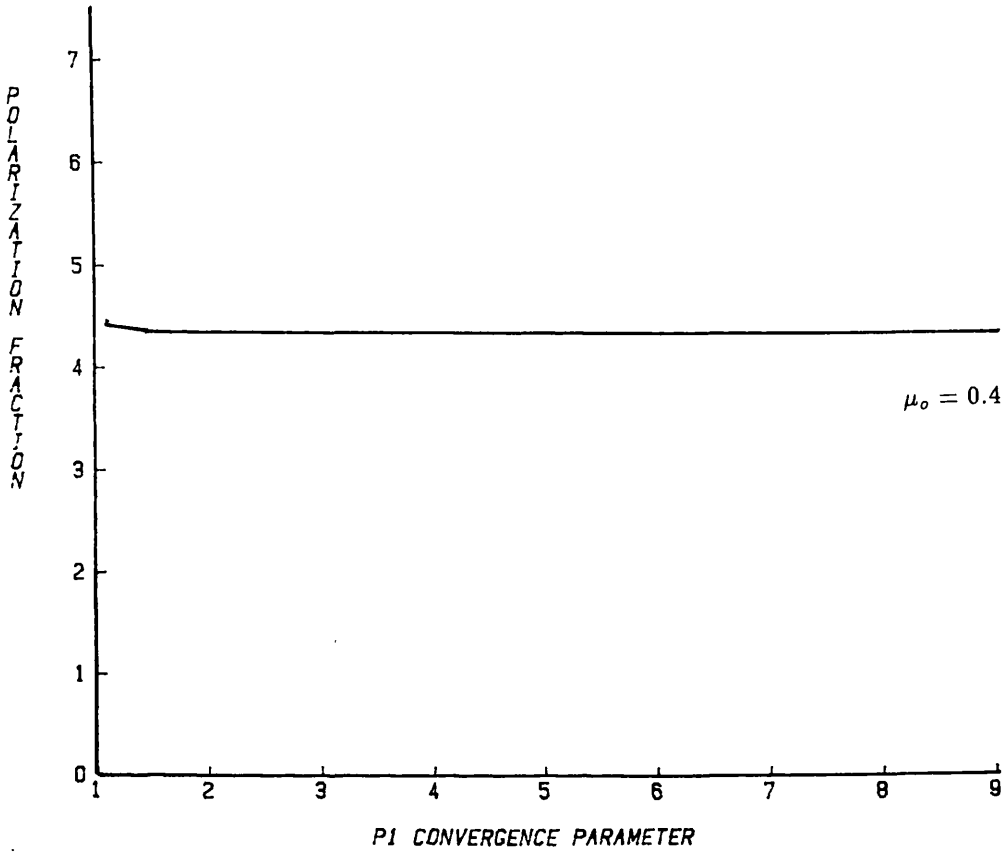

Fig 3.9b Net polarization as a function of p_1
maximum energy = 500keV
$p_2 = 10$

Fig 3.10a Net polarization as a function of initial pitch angle
for two sets of coronal and chromospheric field strengths.
$(B_0, B_1) = (300, 1200) and (100, 1000), E_{max} = 100 keV$

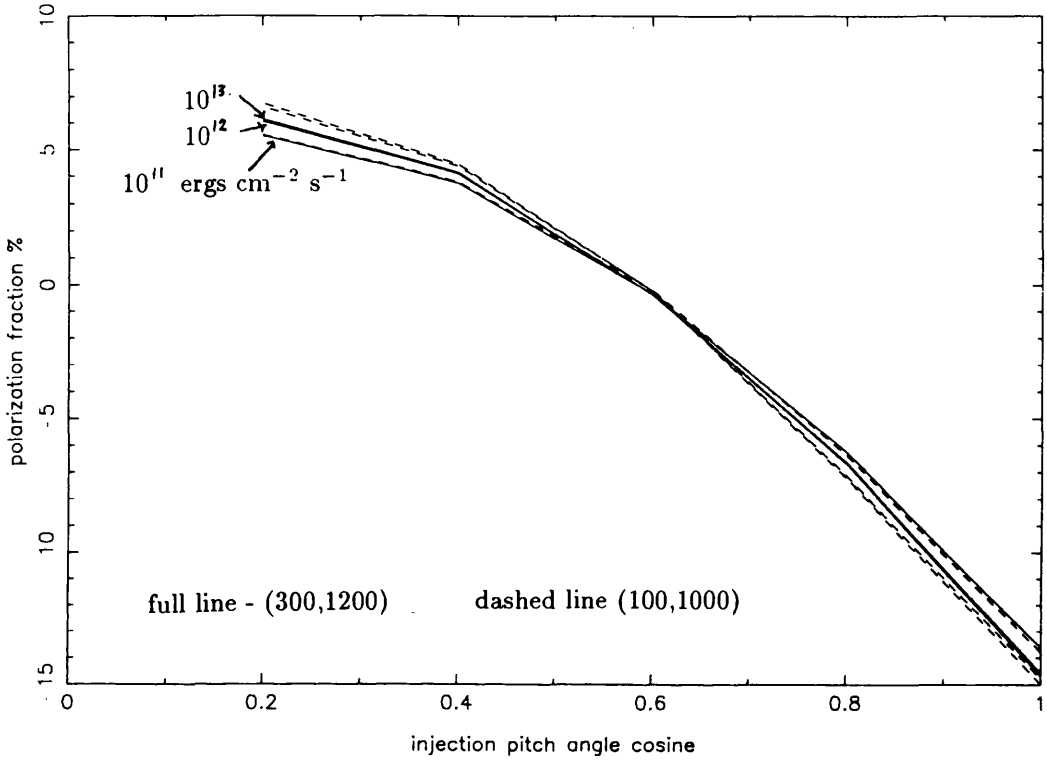

Fig 3.10b Net polarization as a function of initial pitch angle
for two sets of coronal and chromospheric field strengths.
$(B_0, B_1) = (300, 1200) and (100, 1000), E_{max} = 500 keV$

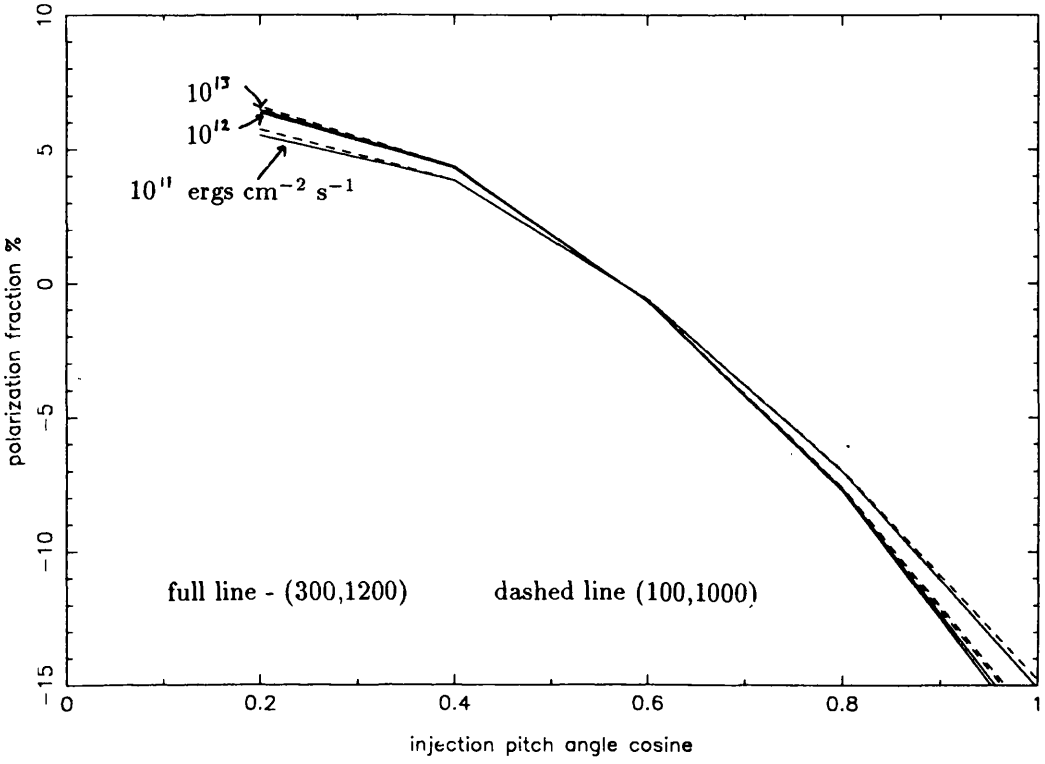

§4.1.1 Introduction

In the previous two chapters we have studied the generation of impact polarization by various forms of beam - the monoenergetic and power law proton beam, and the mirroring electron beam, and have discussed the results and their implications, dismissing particular sets of parameters, or entire models, using only the criterion of total energy necessary to reproduce the observations. But it has been mentioned in Chapter One that there is a problem in using any form of beam from the corona in the model of the excitation process. Beams from the corona, involved with powering the flare, are associated with the flare impulsive phase, which, except in the rare cases of extended hard X-ray flares, occurs on short time-scales and involves the input of beam energy over a relatively small area. If the polarization is caused by such a beam then we expect to be able to reconcile the duration and area of the polarization observations with the typical duration and area of the impulsive phase observations. There is always the possibility that the flare in which the polarization was observed was unusually large in its energy, duration and area, but unless this is the case, the parameters seem considerably in excess of what is reasonable for the impulsive phase. Also the characteristic beam - driven impulsive phase hard X-ray signature is not present in all of the flares exhibiting impact polarization. Hénoux *et al*(1990) and Hénoux (1990) claim that during the time of the polarization observations in the flares of 11th July and 17th, no HXR bursts were recorded in the SMM HXR burst spectrometer. Additional observations by Metcalf *et al* (1992) do show a hard X-ray burst - highly variable but with an overall duration of 10 minutes, occuring at the same time as an observation of polarized Hα emission. In this event there evidently is some connection between the primary release process and the process causing the polarization. It is not possible from this data to see whether the polarized emission continues beyond the end of the HXR impulsive signature. Despite this incidence of an obvious coincidence in time, we feel it is necessary to explain the other events in which no such correlation is evident. We are motivated therefore to seek an alternative explanation for the observations, which does not rely on any part of the impulsive flare - instead we investigate the possibility that processes occurring in the gradual part of the flare are the source of polarization.

§4.1.2 Flare Time and Area Scales

As has already been mentioned in Chapter One, the entire flare process, from the time when an active region brightening is observed through to when the atmosphere has returned to its initial state, can be split into three intervals.

1) The pre-flare phase - lasting for minutes or hours around the region where the flare will occur. Effects include, for example, indications of rearranging magnetic fields appearing as the brightening of active region prominences or filaments , and also an EUV and soft X - ray brightening of active region plasma, indicating a slow transfer of magnetic energy.

2) The impulsive phase - lasting at most a few minutes, when intense, energetic and rapidly varying nonthermal emissions indicate the release of the magnetic energy stored in the sheared magnetic fields above the active region.

3) The gradual phase - lasting many minutes, and exhibiting a variety of thermal emissions from the atmosphere which has been heated by the impulsive phase. Emissions peak some time (a few minutes) after the impulsive phase. During the gradual phase, bulk plasma motion (evaporation) occurs, and through various mechanisms the atmosphere relaxes to its pre - flare state, probably with some continued gradual energy input.

The duration of the impulsive phase is evident in the hard X - ray profiles resulting from various satellite expeditions, but the area of the region through which the energetic particles pass as they enter the chromosphere can only be inferred, since it is in general unresolved, or very poorly resolved by present observations. It is obvious that the 30 minutes or so of polarized emission observed in the July 17th 1982 flare can not be easily explained by a standard flare model impulsive beam which, according to hard X-ray observations, typically lasts for less than five minutes. There exist, as has been mentioned previously, rare examples of extended hard X-ray bursts (Vilmer*et al*, 1982) lasting $\sim 10^3$ seconds, but according to these authors the extended part of the emission is thought to be Bremsstrahlung radiation from a perfectly trapped, low density population in the corona, rather than from a thick-target precipitating flux. There is no evidence of precipitating beams lasting longer than the impulsive phase.

Consider now the precipitation area. Canfield*et al* (1990) investigate the ratio of hard X-ray emission from the corona to simultaneous Hα emission from the impulsive phases of five flares, and using a thick target model of the impulsive phase (not including trapping), deduce a mean precipitation area for non-thermal electrons of $(1.4 \pm 1.0) \times 10^{17}$ cm^2. We have supposed in the previous two chapters that the Hα impact polarization is generated by beams from the corona, either of protons or electrons, which are guided into the chromosphere by magnetic structures - presumably similar to those present in the five flares studied by Canfield *et al.* If this is the case then it is difficult to explain the difference between the electron precipitation area derived by Canfield *et al*, and the precipitation area, of at times as much as 3.6×10^{19} cm^2, forced by the assumption of a beam driven model of Hα Impact Polarization.

In contrast to this gloomy picture for beam interpretations we present now certain facts about the later phases of the flare, which fit very nicely with the polarization observations. During the gradual phase the solar atmosphere, heated by the release of stored magnetic energy in the

impulsive phase, adjusts radiatively and hydrodynamically, gradually dissipating the energy and returning to its pre - flare state. The process is mapped in various emissions - in soft X-ray lines for example, as mentioned in §1.1.6, and in Hα lines, as mentioned in §1.1.5. Brightening in soft X-rays indicates an increase in the thermal emission measure, as hot material from the chromosphere moves into the corona. This motion is confirmed in soft X - ray line blue shifts, although the precise interpretation of these line shifts is a matter of some debate, as will be discussed briefly in §4.1.3. Work has been carried out by Antonucci *et al* (1990 a,b) to analyse the line shifts, which are found to correspond to the evaporation of material into the corona simultaneously with an increase in the area of the flare Hα bright patch to as much as 5.8×10^{18} cm^2 for around five minutes. In addition to the soft X-ray observations there is evidence of the response of the atmosphere in Hα upflows with a duration of a hundred minutes. We have in previous sections studied the generation of polarization by high energy beams. However, low velocity directed particle motions, such as chromospheric upflows will also be capable of producing polarization, if the particle energy is greater than the excitation threshold (12.1eV). Evidently, processes happening during the gradual phase occur on time and area scales which are compatible with the polarization observations. We shall investigate whether chromospheric evaporation is a possible means of driving the atomic impact polarization process.

§4.1.3 Chromospheric Evaporation

According to the thick target beam model of solar flares, deposition of energy in the atmosphere by particle beams during the impulsive phase occurs over a very short timescale, and also, because of the rapid increase in atmospheric density in the transition region, over a very small distance. If the rate of heating by such a large and rapid input exceeds the rate of cooling by radiation and hydrodynamic expansion an explosive evaporation of the chromosphere occurs, forcing material into the coronal flare loop (Fisher*et al* 1985). One observational signature of this is blue shifts in soft X-ray lines. Alternatively, if the input flux is low enough that the plasma can cool gradually (for example, input from a bottled population of particles, as has been studied in chapter 3) no such explosive process need take place although some gentle evaporation will always occur. Blue shifts in soft X-ray lines, confirming the explosive evaporation scenario, have been observed in the impulsive phase of solar flares, for example, using the Bent Crystal Spectrometer on the SMM satellite. Antonucci*et al* (1990 a,b) report observations in Ca XiX and Fe XXV, and Doyle and Bentley(1986), Doschek(1988) also observe CaXiX. That these observations indicate upwards-directed bulk motion of chromospheric plasma is not in dispute (see NASA conference publn 2439 Energetic Phenomena on the Sun, chapter 4, for a full discussion of the physics involved). However the exact form which the upflow of material takes is still a topic of considerable debate. Antonucci

et al (1990) fit their observations with a three-component plasma (three different velocities, three different temperatures) - explaining the line-shape as a composite of emission from a component moving at about 600 kms^{-1}, one at about 300kms^{-1}, and a third, long-lived component moving at around 100kms^{-1}. However it is not very realistic to describe the plasma by discrete components, even if they do fit the line-shape. Emslie and Alexander (1987) use the electron-heated, hydrodynamical model of Nagai and Emslie (1983) to illustrate that a multi - thermal plasma, having a temperature and velocity gradient along the loop length, when viewed at a variety of angles can, by a combination of red- and blue-shift effects, reproduce the observed line profiles. The upflow velocities used in this interpretation are from the Nagai and Emslie model and lie between 200 and 1100 km s^{-1}, with the velocity in the principal soft X-ray source being 200km s^{-1}. The interpretation of the observations by Emslie and Alexander is more physically reasonable but we should point out here that it is by no means decided that explosive evaporation need be driven by an electron beam. In fact evaporation can be caused by any form of heating if sufficiently strong.

The observations used by Antonucci *et al* were of a large flare (optical class 3B) of two-ribbon type occurring on April 24th 1984. The timing of the blue-shift observations is most interesting. The initial impulsive phase of the flare is characterised by a large blue shift in the CaXIX and the FeXXV lines, interpreted by Antonucci *et al* as an upflow with velocity as high as 800 kms^{-1}. This lasts for around 1 min (see fig 4.1 (from Antonucci)) at a time, but it appears that the process which leads to the emission of this blue-shifted radiation occurs repeatedly, with about 1 minute between each instance of very high velocity emission. We reproduce table 1 from Antonucci *et al* (1990, b) which indicates that the onset of evaporation occurs within 25 seconds of the time of increase of the Hα emitting area, and that this area increases to between 1.2 and $4 \times 10^{19} cm^2$ - which appears to correspond well to the area and time variation of Hα polarization. Still, although the time variation is about right, the timescale of this rapid evaporation is again somewhat short for our requirements. However a lower blue shift component, identified with a low velocity component is also present, with a velocity of order 100 kms^{-1}, for a period of 100 minutes so there is obviously no problem if we want a long-timescale atmospheric response. As well as these observations there have been many other reports of evaporation in solar flares, although there are not so many gradual phase as impulsive phase observations. Among those that do exist are Acton*et al* (1982) who make Hα and soft X-ray observations of the large flare of 1980 May 7, 1456, and arrive at values of $v = 10 - 20$ kms^{-1} during the impulsive phase of the flare and $v = 10$ kms^{-1} during the gradual phase (timescale 5-6 minutes). Schmieder et al (1987) interpret sustained sustained (up to $\sim$ 5 hours) Hα blueshifts observed in post-flare loops during the gradual phases of 3 large flares as gentle evaporation with velocity up to 10 kms^{-1}. Zarro and Lemen (1988) report impulsive phase evaporation of 350 ± 50 km s^{-1} in the 1985 Jan 23 0725 flare, followed by gradual phase

evaporation at a velocity of 60 km s^{-1}, decreasing to zero over 15 minutes. These are found to be consistent with heating by thermal conduction from the reconnection site in the corona.

The evaporation of the solar atmosphere in response to an impulsive beam has been studied numerically by Nagai and Emslie (1984). They find that a steep hydrodynamic shock forms, which moves upwards in about a minute, from the base of the chromosphere to the apex of the loop from which the heating beam originated. This large upwards momentum is compensated for by a downwards propagating front. We are not so much interested in the very early, extremely high velocity part of the motion, as in the situation which arises in their model after 120 seconds, once the beam input has ceased and when the thermal phase of the flare would begin. The hydrodynamic models indicate that at this time there still exist, in the upper chromosphere sections of material with upwards velocity of 100 km s^{-1}. This velocity lies within the range of velocities found experimentally during gradual phase evaporation. The temperature of the atmosphere is $\sim 10^7$ K, therefore material in the flow will be ionised. It is feasible that such ionised flows, moving through material with some neutral content could generate impact polarization. This is possible in two ways - firstly if a fragmented or channelled flow penetrates the upper regions of the chromosphere, and secondly, if a diffusive flow of particles occurs - for example in a thermal conduction front. In the following sections we discuss the former process - the fragmented or channelled flow, in which case we are dealing with relatively high flow velocities - $\sim 10^7 - 10^8$ cm s^{-1}. The basic requirement for the production of Hα impact excitations is that charged particles move relative to neutral particles with a velocity greater than the level 3 excitation energy of 12.1 eV, and with an anisotropic distribution. The threshold energy corresponds to a velocity of only 5×10^6 cm s^{-1} for protons, or 2×10^8 cm s^{-1} for electrons, so a flow of evaporating material of the typical velocity suggested by observation and modelling has ample energy to enable this process to occur. To have relative motion between the flow material and the atmospheric material we need some interpenetration of flow and static atmospheric material - the area over which this can happen is optimised by having the flow material separated into discrete filaments, a process that could occur by one of a number of physical mechanisms. Without yet proposing a fragmentation mechanism, we can calculate the fraction of the atmosphere which must be involved in the flows. This will depend on various factors - the intensity and polarization of the radiation from each part of the the atmosphere (flow, static or interpenetrating), the geometry of the system and the surface area of each component.

§4.1.4 Atomic Data

Before being able to calculate the emission intensities and polarization we need to discuss the

atomic data to be used in the calculations. When dealing with flow velocities of $\sim 10^7$ cm s^{-1} and temperatures of 10^7K the typical proton speed will be less than 1keV, so we desire atomic cross sections for very low energy interactions. We will in addition require polarization fractions at low energies and in this section we describe the source of these atomic parameters. In some cases the typical proton energies which we consider are less than 1keV. The level 1 to level 3 excitation cross sections at very low proton energies have not been measured - the lowest energy published by Lüdde and Dreizler (1983) is 1keV, and this is for the overall transition, rather than excitation to individual angular momentum sub-levels. We attempt to estimate the total excitation cross section at energies below 1keV by assuming that at threshold energy (i.e. 12.1 eV, the excitation energy of level 3) the excitation cross section goes to zero, and above threshold, varies linearly with energy up to the value of 4×10^{-19} cm^2 reported by Lüdde and Dreizler, so that a straight line relationship may be used. We are also forced to assume, when calculating the sub-level excitation cross sections, that excitations to each of the levels 3s, 3p and 3d are in the same proportion as for the lowest energy data point where we have the full information available. The lowest energy data point we have is at E = 25.3 keV (for protons) and at this point the levels 3s, 3p, 3d are excited in the approximate ratio 4:1:8 (including the coefficient describing the proportion of level 3p electrons de-exciting with the emission of a Hα photon). The total $1 \rightarrow 3$ cross section is equal to the sum of the three with the appropriate coefficient (c.f §1.2.4).

The polarization fraction also proves problematic, since the nearest experimental data point is for electrons and is at an equivalent proton energy of 27.5 keV. This energy is really rather high compared to the typical energies with which we are dealing in this instance. In any case it is not clear that we can use electron impact polarization data at low proton energies. The interaction between low-energy protons and neutral hydrogen atoms will not be simple to describe, and probably does not proceed by the same mechanism as an electron - neutral interaction, since the pair are thought to pass through a "quasi - molecular" state. Indeed it has been proposed that the polarization resulting from such low energy excitations be used as a diagnostic for the orientation and energy level of such states. The path is not clear here, but we expect that at energies close to threshold we may calculate polarization using the theoretical argument as given in §1.2.5 - i.e., that in the limit of excitation of a neutral with angular momentum = 0 by a threshold energy particle, the resulting angular momentum must also be zero, allowing us to determine which of the magnetic substates may be populated, and hence what the polarization fraction is. Calculated in this way, the polarization fraction is $\sim$ 45%. It is expected that the result of any "quasi-molecular" interaction will be to reduce the polarization fraction, but it is impossible to say by how much. We will bear in mind that some reduction is expected.

§4.1.5 Competing Excitation Processes in the Evaporation Scenario

There are three important regions, each of which must be considered when calculating the polarization resulting from the fragmented evaporation model. Firstly there is the static material, whose temperature and density structure is modelled in the MAVN atmosphere. The calculation of the emission from this region has already been described in §2.1.4. Secondly there is the upflowing region which is split into two - the volume in which the flow and static material interpenetrate, and the volume in which they do not. The flow temperature is higher than the temperature of the ambient material, and for temperatures above $\sim 1.5 \times 10^5$K (mean electron energy $\sim$ ionisation energy of hydogen) we may consider it completely ionised in which case the only emission coming from the region where there is no interpenetration is due to recombination emission - the expression for this has been given previously. In the region of interpenetration we have a drifting Maxwellian meeting an essentially static neutral hydrogen target (static since the thermal diffusion speed of particles in from the static surroundings is much less than the drift speed). The Hα excitation depends on the temperature and density of the interpenetrating neutrals and of the flow particles, but the polarization resulting depends in addition on the anisotropy of the flow distribution. This varies with the temperature and therefore the mean particle speed, of the Maxwellian in the global rest frame of the flow. For example, if the flow temperature is 10^5K then the mean proton speed is only 3×10^6 cm s^{-1} in which case the addition of a flow velocity of 10^7 cm s^{-1} makes the distribution function extremely anisotropic, whereas at a temperature of 10^7K and a mean proton thermal speed of 3×10^7 cm s^{-1} the degree of anisotropy is not nearly so great. To be able to work out the relative importance of contributions from all three types of material (i.e., static, interpenetrating and pure flow material) we must know the optical behaviour of each. This has already been calculated in §2.1.5 for the static component, under the assumption that optical depth is due to level 2-3 absorption, but there is no reason why in the interpenetration region the Hα optical depth should be the same, since this depends on the population of level 2 hydrogen which may be changed by collisions with flow particles etc.

Emission from the Interpenetration Region - Optical Depth Effects

Since the temperature and density in the upflowing region is different from that in the static region, we expect that the optical properties of the material will be different. In particular, it is likely that it will be possible to see "deeper" into hotter material - i.e., the position of the optical boundary would be lower. As was demonstrated in Chapter 2 the radiation intensity depends very crucially on the position of the optical boundary relative to the region in which neutral hydrogen density is high. Therefore we must calculate the optical depth (dependent on the number density of level

2 hydrogen) in the upflowing region. We can only arrive at the level 2 population by writing the level 2 rate equation - balancing the number of particles that are excited into level 2 per cubic centimetre per second with the number that are de - excited, since in a steady state there must be an equilibrium between these two quantities. The rate equation will involve many terms, and in fact one cannot properly solve for one level in isolation - one should solve the simultaneous equations for all levels up to some cut-off, but this is of course not within the scope of this thesis. Still, by making some judicious approximations we will be able to arrive at a reasonably accurate answer. We list below the processes contributing to the population and de-population of level 2 in the interaction region, indicating which are more significant and which may be neglected in our calculation. The approximate number of level 2 particles per second per cubic centimetre which are created or destroyed by a process is given below that process.

Level 2 Populating Processes Operating in the Interpenetration Region.

1) Excitation of level 1 hydrogen by collision with flow electrons.

$$n_1 n_e \int v_e \sigma_{1\rightarrow 2}(v_e) f_e(v_e) dv_e$$

2) Excitation of level 1 hydrogen by collisions with flow protons.

$$n_1 n_e \int v_p \sigma_{1\rightarrow 2}(v_p) f_p(v_p) dv_p$$

3) De-excitation from level 3 and above following collision with flow particles.

$$\int_v \Sigma_{j=3}^{\infty} n_j \sigma_{j\rightarrow 3} v f(v) dv$$

4) Spontaneous de-excitation of level 3 and above (eg, Hα emission).

$$\Sigma_{j=3}^{\infty} n_j A_{j,2}$$

5) Recombination of flow electrons and protons onto level 2.

$$n_e n_p \alpha_2$$

6) Photo - excitation of level 1 particles to level 2.

$$n_1 B_{1,2} J_{\nu 2-1}$$

7) Drift of level 2 particles in from the ambient plasma

$$N_2 v_{drift}$$

Level 2 Depopulating Processes Operating in the Interpenetration Region

1) Collisional excitation from level 2, to upper levels, by electrons.

$$n_1 n_e \int v_e \Sigma_{j=2}^{\infty} \sigma_{2\rightarrow 3}(v_e) f_e(v_e) dv_e$$

2) Collisional ecxitation from level 2, to upper levels, by protons.

$$n_1 n_p \int v_p \Sigma_{j=2}^{\infty} \sigma_{2\rightarrow 3}(v_p) f_p(v_p) dv_p$$

3) De-excitation to level 1 following collisions with flow particles

$$n_2 n_p \int_v \sigma_{2\rightarrow 1} v_c o l l f(v) dv$$

4) Spontaneous emission out of level 2. (Lymanα)

$n_2 A_{2-1}$

5) Photo-excitation out of level 2

$n_2 \Sigma_{j=3}^{\infty} B_{2,j} J_{\nu j-2}$.

All the excitation and de - excitation terms must balance, but some are of smaller size and can be neglected. We now describe the calculation of each term.

Process 1), collisional excitation from level 1 by flow electrons will be important when the flow temperature is greater than 5×10^4K, since at lower temperatures the mean thermal energy of the particles is less than the necessary excitation energy, and only a small portion of the high energy tail of the Maxwellian will be able to excite level 2. At higher temperatures of 10^5 to 10^7 K the energy of the majority of particles is sufficient for excitation of level 2, but instead of explicitly calculating the excitation by the Maxwellian, we calculate the excitation at the mean thermal speed, $v_{th} = \sqrt{(2kT \backslash m_e)}$. (At 10^6 and 10^7 K the electron thermal velocity $\sim 10^8 - 10^9$ cm s^{-1}, is much greater than the flow velocity, therefore we do not expect the distribution to be changed significantly by the addition of a drift term of order 10^7.) At these velocities the Born approximation for the excitation cross section can be used. Values of this at a range of energies are given in Vainshtein (1965).

Process 2) Collisional excitation by flow protons raises problems whose treatment will be discussed in section 4.1.7 - namely that the distribution function of the protons when viewed in the rest frame of the level 1 particles which are being excited is no longer a Maxwellian, but neither is it adequately described by a purely vertical flow. However, we are not actually interested in the anisotropy of level 2 excitations, merely in how many there are, so it will suffice to use the proton velocity which has the largest associated population - found by calculating the zeroth moment of the distribution functions at various temperatures. The level 1 to level 2 excitation cross sections at a proton energy of 1keV is given in Lüdde and Dreizler and the required cross sections calculated by extrapolating to zero cross section at threshold energy.

Process 3), collisional de-excitation from level 3 and above will occur more slowly than spontaneous de-excitation, therefore we neglect it. Similarly, process 2) of the *de*-population processes - collisional de-excitation from level 2 to level 1 will occur more slowly than spontaneous de-excitation and is neglected.

Process 4) When calculating spontaneous de-excitation to level 2 we will consider only the de-excitations from 3 - 2 since we do not have data on the populations of overlying levels in the static atmosphere. The Einstein coefficient for this process is 4.39×10^7 s^{-1}.

Process 5) is recombination onto level 2 which is calculated using the appropriate recombination coefficient (see equation 1.2). The recombining population is the flow electrons and protons and the temperature which appears in equation 1.2 is the flow temperature.

Photo-excitation processes, such as number 6) have not been previously considered in this thesis, and we can only state what we believe to be a reasonable estimate of the magnitude of this effect, since a proper radiative transfer calculation is beyond the scope of his section. To calculate the number of excitations from level 1 to level 2 by Lyman α photons we must know J_ν, the mean intensity of Lyman α photons. The mean intensity is the direction averaged specific intensity, I_ν. I_ν is the energy at frequency ν per unit time, passing through unit area, per unit solid angle per unit frequency, and for an isotropic radiation field $I_\nu = J_\nu$. J_ν is then simply the energy per unit frequency passing through unit area per unit time. Photons involved in the photo-excitation could come from both the flow material itself and from the surroundings. However the number of Lyman α photons emitted in the predominantly ionised flow is expected to be negligible in comparison with that from the surroundings. The energy in Lyman α emitted per unit area per unit time in the stationary atmosphere is the Lyman α cooling rate R, which is graphed in Machado *et al*, and peaks strongly at 50 ergs cm^{-3} s^{-1} between heights of 1.43 and 1.435 $\times$ 10^8 cm. To calculate an upper limit to J_ν assume that all Lymanα radiation generated in each section of static material is emitted through the boundary to the adjacent flowing material. Consider a geometry in which the fragmentation is in the form of strips (see fig. 4.2). For the change in optical depth to have any noticeable effect it is necessary to have the distance h to the new optical boundary of the same order as the width w_f of the flow channels, and also to have the width of the flow channels of the same order as the width w_s of the static part (see later). The area of the boundary between a flowing strip and a static strip is $h\sqrt{A_f}$. The total energy emitted in Lyman α in one of the flowing channels is $\delta h R w_s \sqrt{A_f}$ where δh is the thickness of the emitting region. Therefore the energy passing through unit surface area per unit time from the static to the flow region is $\sim \delta h R w_s \backslash h$ and the mean intensity is obtained by dividing this by the frequency of the radiation, viz

$$J_\nu = \frac{\delta h R w_s}{\nu h} \sim \frac{\delta h R}{\nu} \qquad 4.1$$

since $w_s \sim h$. The Einstein B coefficient is related to the A coefficient thus

$$B_{1,2} = \frac{2h\nu^3}{c^2}\frac{g_2}{g_1}A_{2,1} \qquad 4.2$$

where g_1 and g_2 are the degeneracies of levels 1 and 2, and n_1 is the number of particles in level 1 in the material surrounding the flow, from the Machado *et al* paper.

Process 1) of the de-population processes, collisional de-excitation from level 2 to upper levels, involves an infinite sum which can be approximated by the first few terms. Again the speed of the bulk of the shifted Maxwellian protons is used in the calculation of proton excitation, and the mean thermal electron speed is used in the electron calculation. We consider only the 2-3, 2-4 and 2-5 cross-sections - this will be sufficient, since the 2-6 cross section is less than 1% of the 2-3

cross section (in the Born approximation, at electron velocities of $\sim 10^8 - 10^9$ cm s^{-1} (Vainshtein 1965)).

With these expressions we can calculate, as a function of height, flow temperature and velocity, what the equilibrium number density of level 2 hydrogen atoms is, and therefore the variation of optical depth with depth in the interpenetration region. Figures 4.3 and 4.4 show the variation of these parameters for a variety of temperatures, when observing vertically downwards. As we might have expected, the position of $\tau = 1$ changes with temperature - as the temperature increases the height at which the atmosphere becomes optically thick decreases - it is possible to see farther into the hotter material. At a flow temperature of 10^5 K, the atmosphere is optically thick below a depth of 1.41×10^8 cm. At 10^6K this position is 1.35×10^8 cm, whereas in the higher temperature cases the atmosphere is still optically thin at heights of 1.275×10^8 cm. So the total emission escaping from the interpenetration region will be very much higher than the emission from the static part. This is because lowering the optical boundary position increases the volume of material whose emission in Hα reaches the observer, and at low positions in the atmosphere the neutral hydrogen number density is high. The effect of this decrease in optical depth on the resultant polarization will be significant, provided that the flow channels are wide enough. The width of the channels is important because (see fig 4.2) emission is over 4π steradians, and if the channels are narrow then the effect of decreased optical depth would only be seen when looking vertically down the channels - viewing at an angle (which we do in the flare observations) would then reveal little difference since the path which the majority of photons would take to reach an observer viewing at an angle would be through static, high optical depth material. However, if the horizontal and vertical dimensions of the flow channels are similar, a larger proportion of polarized photons will escape through low optical depth material.

Emission from the Non-interacting Flow Region.

A highly ionised flow generates predominantly recombination emission, but one with some neutrals generates collisional emission also. Flows of temperatures of 10^6 and 10^7K can be quite safely assumed to be completely ionised, since the mean thermal energy of particles at this temperature is far in excess of the ionisation energy of hydrogen (which corresponds to a temperature of 1.58×10^5K) so all radiation is due to recombination. A flow at 10^5 K is however not completely ionised. To get an idea of the ratio of recombination to collisional excitation we must calculate the ratio of the number of atoms in level 3 or above to that in levels 1 and 2. The number of neutral

hydrogens in state nL in a plasma of temperature T is given by the Saha - Boltzmann equation;

$$\frac{n_i n_e}{n_{nL}} = \frac{1}{(2L+1)}\left(\frac{2\pi m_e kT}{h^2}\right)^{\frac{3}{2}} e^{E_i \backslash kt} = g(T) \qquad 4.3$$

E_i being the ionisation potential of hydrogen and h being Planck's constant. If we assume a plasma in which the number of electrons equals the number of protons in their free state and also combined in neutral hydrogen then this equation can be rewritten for the ionisation fraction x. It is not straightforward however, since all levels will be populated to some extent, and we must therefore sum over all levels nL. The resulting form is

$$\frac{1-x}{n_p x^2} = g(T)\Sigma_n n^2 e^{\frac{E_i - E_{nL}}{kT}} \qquad 4.4$$

Formally the sum diverges when high n states are considered - an unphysical situation which can only be avoided by the assertion that high levels are less populated than their L.T.E values because of disturbing influences of other particles. We are only interested here in recombination and downward cascade, and hence in the population of the levels lower than 3 relative to the population of all states with n equal to or higher than 3. This latter quantity must be less than or equal to the total number density of protons (bound and free) in the plasma, and we can then set a limit to the ratio, although not work it out exactly. From 4.3 we have

$$\frac{n_{1s} + n_{2s} + n_{2p}}{n_p} = n_p\left(\frac{h^2}{2\pi m_e kT}\right)^{\frac{3}{2}}\left[e^{E_i \backslash kT} + 4e^{E_i \backslash 4kT}\right] \qquad 4.5$$

where n_p is less than the flow density of 10^{11} cm $^{-3}$, and the ratio of level 1 and 2 atoms to the total proton number density is therefore less than 1.413×10^{-11} at a temperature of 10^5K. So most Hα emission will follow recombination and downwards cascades to level 3. A similar calculation demonstrates that only 10^{-22} of those atoms in all states with n less than 20 are in level 10 or below. Since at n = 20, the energy of the orbital electron is only 0.25% different from ionisation energy, it is a reasonable approximation to say that the 10^5 K plasma is completely ionised, in which case we need only calculate recombination emission. The expression for then recombination coefficient to level 3 hydrogen (from which de-excitation to level 2 follows) is

$$\alpha_3 = \frac{6.26 \times 10^{-6}}{27T^{\frac{3}{2}}} exp\left(\frac{1.74 \times 10^4}{T}\right) E_i\left(\frac{1.74 \times 10^4}{T}\right) \qquad 4.6$$

This is then multiplied by the electron and proton number density to give the emission per unit volume per unit time.

Table 4.1

Temperature	Recombination Intensity
10^5 K	5.95×10^7 cm^{-3} s^{-1}
10^6 K	4.28×10^6 cm^{-3} s^{-1}
10^7 K	2.20×10^5 cm^{-3} s^{-1}

Compared to emission from the static and interpenetrating part the intensity of this emission is negligibly small. We can say therefore that the polarization fraction visible from the region overall will depend predominantly on the ratio of polarized and unpolarized emission in the interpenetration region, which we shall now calculate.

§4.1.6 Calculation of Polarization from the interpenetrating region

As previously pointed out, the distribution function of the flow particles involved in the excitation of the ambient neutrals is a drifting Maxwellian, and both the electron and proton components will give rise to excitation though only the proton component will generate polarized emission, as the electron component will be very isotropic. At a temperature of 10^5K, the lowest temperature we consider, an electron has a mean thermal velocity of 5.5×10^8 cm s^{-1} and the addition of a flow velocity of a mere 10^7 cm s^{-1} will not make the distribution function significantly anisotropic. Likewise with the higher temperature cases. The electron emission is therefore calculated using the methods of §1.1.4, viz

$$n_e n_1 \int_\chi^\infty v\sigma_{1\to 3} f(v) dv$$

The proton distribution function is a different matter. Since the thermal velocity of protons is considerably smaller than that of electrons the presence of a flow *will* cause a significant anisotropy in the distribution, when viewed in the rest frame of the surrounding material, for flow temperatures less than about 10^8 K. To properly calculate the polarization resulting from this anisotropic distribution we must calculate the moments of the distribution and use them in the equations for the Stokes' Q and I parameters, as was done in Chapter 3 First of all let us write down the terms involved in the calculation of the relative intensities of proton and electron emissions.

$$\frac{I_p}{I_e} = \frac{n_p n_1 \int_{v_p} J_0(v_p) v_p \sigma(v_p) dv_p}{n_e n_1 Q(v_{exc}) v_e \sigma_{v_e}} \qquad 4.7$$

where v_p, v_e are the proton and electron thermal velocities, σ_{v_p}, σ_{v_e} are the cross - sections at these velocities and $Q(v_{exc})$ is the fraction of particles in the electron thermal velocity with energy sufficiently high to excite Hα radiation. It is a reasonably good approximation to use the mean

thermal velocity to calculate the total *electron* generated emission, but we cannot do the same for proton emission. In the rest frame of the drift the bulk of particles have the proton thermal speed, but since the static distribution is completely isotropic, the addition of a uni-directional drift component of similar (or greater) magnitude to the thermal component results in a distribution to which one can no longer easily assign a mean velocity value. We work therefore with the moments of the proton distribution function. The zeroth moment at a particular velocity is related to the number of particles at that velocity, as the zeroth moment is the integration of the velocity distribution function over pitch angle and the integral of the zeroth moment over velocity is then equal to 1. Also, the quantity $Q(v_{exc})$, the fraction of electrons with velocity greater than the excitation energy for Hα is approximately equal to 1 for distributions at a temperature of 10^6 or above (and has value 0.6 for a 10^5 K distribution). Since in the flow $n_p = n_e$ we can approximate the polarization obtained from a drifting electron and proton Maxwellian by

$$p \sim \frac{b(v)P_{beam} \int_{v_p} J_0(v) v_p \sigma(v_p) dv_p}{Q v_e \sigma_{v_e}} \qquad 4.8$$

$b(v)P_{beam}$ is here the polarization obtained from a distribution with anisotropy factor $b(v)$ under conditions in which a completely unidirectional distribution would generate P_{beam}. We can see from equation 4.8 that to have an appreciable polarization fraction from the interpenetration region we must confine our interests to regimes of high flow velocities at relatively low temperatures, since the electron thermal velocity is so much larger (a factor of $\sqrt{(m_p \backslash m_e)}$ times) than the proton thermal velocity. A high flow velocity but low temperature flow will mean firstly that the proton anisotropy factor will be large and secondly that the proton velocity with the drift term added is significantly larger than its thermal value, whilst the electron thermal velocity is kept as small as possible. In addition, we wish to maximise the proton excitation cross section which, at the typical proton speeds we discuss here (10^7 to 10^8 cm s^{-1}) is increasing with velocity.

Now we shall calculate the anisotropy of the drifting proton Maxwellian, using the moments of the distribution function. In the rest frame of the flow the particle distribution function is given by the Maxwellian corresponding to the distribution temperature.

$$f(v) = \frac{4}{\sqrt{\pi}} \left(\frac{m_e}{2kT} \right)^{\frac{3}{2}} v^2 e^{\frac{-m_e v^2}{2kT}}$$

However, in the rest frame of the ambient static chromospheric material every particle has a component of velocity, v_d, added in the flow direction, which we call z. Splitting the velocity in the flow frame into its $x-, y-$, and $z-$co-ordinates we have;

$$v_x = v \sin\theta \sin\phi$$

$$v_y = v \sin\theta \cos\phi$$

$$v_z = v \cos\theta.$$

where (θ, ϕ) are the pitch angle and azimuth. Now let us add v_d to the $z-$ component transforming into the rest frame of the static surroundings. From figure 4.5 we can see that

$$v^2 = v'^2 + v_d^2 - 2v'v_d \cos\theta'$$

v' and θ' are the speed and pitch angle that a particle originally at (thermal) speed v, pitch angle θ now have. All particles in the thermal distribution with velocity v and angle θ (pitch angle cosine $= \mu$) will end up in the shifted distribution with velocity v' and angle θ' (pitch angle cosine μ'). To calculate the moments of the distribution function we need to find out how many particles at speed v' have angle θ'. Every particle that ends up at (v', θ') belonged originally to the stationary Maxwellian, and was a member of the population at (v, θ). This population is calculated from the stationary distribution function and depends only on speed, since the Maxwellian is isotropic. So for every (v', θ') the original (v, θ) can be calculated and the number of particles at (v, θ) can be evaluated from the Maxwellian. This is then the number of particles at (v', θ') in the shifted distribution. So the numerical values of the moments as a function of velocity can be obtained by treating this set of values of the new distribution function and the corresponding pitch angles as data points to be multiplied by the pitch angle raised to the appropriate power (0 or 2) and integrated using NAg routines E02BBF and E02BEF, which interpolate and integrate functions defined at discrete points.

In practise the computation does not proceed in quite this way. Instead the stationary Maxwellian is evaluated at a large number of values of pitch angle ranging from 0 to 180° (in 300 divisions) and speed, ranging from zero to a few times the thermal velocity (in 200 divisions). The number of particles in a small interval around a position (v, θ) in velocity and pitch angle space is proportional to the value of the Maxwellian at that position multiplied by the volume of the interval. The volume of the interval is $\delta v \times \delta\mu \times \delta\phi$ although since a constant $\delta\phi$ transforms to the same, constant $d\phi$ under a $z-$ translation we ignore this variable. The number of particles at (v, θ) is then assigned to the new position (v', θ') in the shifted distribution, and can be binned into new velocity and pitch angle divisions (this time the angular range is divided into 30, and the velocity range into 20). This is not a particularly elegant method of calculating the shifted distribution, but is simple and rapid to run. Figures 4.6 - 4.8 show the results of calculations of shifted distributions for various values of flow velocity and temperature. These are polar diagrams, in which each closed curve is a contour of constant speed in the new distribution, the distance from the origin to any point at angle θ' on the constant velocity curve represents the number of particles at that speed and pitch angle.

We see first of all in figure 4.6c that at a temperature of 10^7 K corresponding to a proton thermal velocity of 4.06×10^6 cm s^{-1} most of the contours are circles, although with origins slightly shifted from zero. The distribution is not far from isotropic, except at very low and very high speeds. At low speeds the distribution predominantly occupies the "backward" hemisphere (curves 1,2,and 3) but as speed increases the constant speed contours become more circular in form, then develop a forward anisotropy in the form of an enhancement about the $z-$ axis (which is unfortunately covered by only one point in our choice of angular division. At velocities above 1.8×10^7 cm s^{-1} the distribution has become highly anisotropic, with all particles at these speeds confined to the "forward" hemisphere. However at the extreme high and low speed ends of the distribution there are not many particles; the majority of particles are in the fairly isotropic part , and we do not expect a high degree of polarization to result from this particular pair of parameters. But if we examine the distribution at lower temperature (10^6K, figure 4.6a) - a thermal speed of 1.28×10^7 cm s^{-1} - we note that the distribution is far more concentrated in the forward hemisphere, and that at speeds above 4.5×10^6 cm s^{-1} forward peaks develop (curves 3,4,5), which 'merge' into a single forward peak as speed increases. Overall the distribution is more isotropic. Decreasing the temperature once more we find that all particles at all velocities are moving in the forward hemisphere within $\sim 45°$ of the z-direction, which will result in a high anisotropy factor and a correspondingly high polarization fraction for radiation generated by this distribution. Now let us return to a temperature of 10^7 K, but increase the drift speed. As one might expect, decreasing the ratio of the mean thermal proton speed to the imposed drift speed results in an increase in anisotropy of the proton distribution. For all parameters studied at a drift speed of 5×10^7 cm s^{-1} or above the distributions are very strongly forward peaked. The effect of changing this ratio is directly reflected in the anisotropy factor $b(v) = 3J_2(v) - J_0(v)\backslash 2J_0(v)$. $b(v)$ is zero for a completely isotropic distribution and 1 for a uniquely beamed distribution. All our distributions lie somewhere between the two, but in figs 4.9 - 4.11 we see $b(v)$ increasing as velocity increases. $b(v)$ does not appear explicitly in the formulation of the Stokes' parameters, but is closely related, therefore we can expect a similar type of increase in polarization fraction in Hα as the ratio of mean thermal to imposed drift speed decreases - assuming that the Hα excitation cross section remains constant, or is relatively slowly varying across the range of speeds which we consider.

We have already noted the fact that the graphs indicate the number of particles at a given speed - the area enclosed by a contour of constant speed, being the integral of the distribution function over pitch angle, is proportional to the number of particles at that speed. The zeroth moment of the distribution function has the same property. From the diagrams we see that, for example, the dominant contribution to emission from a 10^6 K plasma with drift velocity 10^7 cm s^{-1} is from protons with a velocity of 1.2×10^7 cm s^{-1} From 4.9b this corresponds to an anisotropy factor

of 0.33. We can estimate therefore that the emission from the proton component of the shifted Maxwellian has approximately one third of the maximum polarization value of 45% i.e. 15%. To properly calculate the total emission by the proton component of the distribution function we use the zeroth moment. The total emission by protons at velocity $v \rightarrow v + dv$ and at position z is

$$\Delta I(v) = J_o(v) n_p n_1(z) \sigma_{1 \rightarrow 3}(v) dv$$

which must then be integrated over velocity to obtain the emission per cm^3 per second. Figure 4.12 shows the result of this calculation. As can be seen, the emission follows the distribution of level 1 hydrogen atoms through the atmosphere, which is as we would expect since this is the only thing which we are allowing to change with depth. Above a position of $\sim 1.43 \times 10^8$ cm emission from protons in the interpenetration region is far lower than in the static part. Below $\sim 1.43 \times 10^8$ emission from the interpenetration region increases enormously, and is far higher than in the static region. This is because in the static region the emission intensity is very highly dependent on the temperature of the medium, which decreases to below excitation temperatures as position in the atmosphere is lowered. But the temperature of the flow is assumed to be constant with depth, and the emission per unit volume from the interpenetration region is much greater than from the static part. From figure 4.4 we see that the atmosphere is still optically thin in this region of high emission, therefore we can expect that the total emission from the flow per unit area at the surface will be significantly higher than that from the static atmosphere. It is likely that polarized emission will dominate over emission from the static part.

§4.1.7 Calculation of Interpenetration Area.

At the boundaries between the two components - one static and one moving - there is some mixing of the ambient hydrogen from the material surrounding the flow, and the flow protons themselves. This is where impact excitation will take place. The amount of impact excitation occuring depends on the flow particle speed and also on the volume of the solar atmosphere in which flow and static components mingle. The latter in turn depends on the distance by which the two components can interpenetrate. Since the charged particles of the flow are guided by the local magnetic field, once the flow is established, the flow particles will not penetrate farther than a gyroradius into the ambient material, which, in the case of a proton of velocity $\sim 10^7$ in the chromospheric field of 500 Gauss, is only 4×10^{-7}cm. This is certainly not very large, but the ambient hydrogen, not tied to the field, may diffuse into the flow at its thermal velocity, and will remain neutral until a collision with a flow particle ionises it, or strips it of its electron in a charge transfer reaction. Which one of these processes is dominant will depend on the relative velocity of charged and neutral particles. We mentioned before that expected ranges for flow velocity and temperature are $10^7 - 10^8$cm s

$^{-1}$, and $10^6 - 10^7$K - corresponding to mean particle energies of around 100eV to 10keV. The cross section for ionisation by electron has a maximum value (experimentally and theoretically) of $\sim 7 \times 10^{-17}$ cm^2. At proton energies of less than 40 keV the cross section for ionisation by proton falls below that for charge transfer (see Fite*et al*, 1960) therefore at our charge transfer between neutral and flow proton, with an experimental cross section of $\sim 1.5 \times 10^{-15}$ cm^2 is the predominant means by which neutrals are stripped of their electrons. Let the mean free path for undergoing charge transfer be $L_{c.t.}$. Then

$$L_{c.t.} = \frac{1}{n_p \sigma_{c.t.}} \qquad 4.9$$

where $\sigma_{c.t.}$ is the charge exchange cross section, and n_p is the number density of protons in the flow. The value of $\sigma_{c.t.}$ for transfer to the n=1 state at an impact energy of 1keV is 1.47×10^{-15} cm^2 (from Lüdde and Dreizler 1982). Although we expect that at lower energies the cross section for this process will be smaller, we can use the 1keV value to give a lower limit for the charge transfer distance. Using a flow proton density of 10^{11} cm^{-3} gives this lower limit as $L_{c.t.} = 7 \times 10^3$ cm. There are other processes operating as the neutral particle penetrates the flow. As it moves through, the neutral will also undergo collisions with flow particles that transfer momentum to it, so that eventually it will be moving with the flow. At this point there is no relative velocity between the charged and neutral component and there is no longer the possibility of impact excitation. Let the distance over which this momentum is transferred be $L_{m.t.}$. The distance which the neutral atom can diffuse into the flow and still be available for impact excitation (the interpenetration distance) is then $\min(L_{c.t.}, L_{m.t})$

The momentum transfer distance is the distance which a neutral will diffuse into an ionised flow before collisions with ambient particles cause it to be accelerated to the flow velocity. The diffusion velocity of the particle $v_{diff} = \sqrt{(2kT \backslash m_h)}$ will be of the order of $1 - 5 \times 10^6$ cm s^{-1} for a particle in the chromosphere - in the Hα rich layers it will be closer to 1×10^6 cms^{-1}. Transform now to the frame in which the flow is stationary. In this frame it appears that the neutral is moving very nearly vertically, in the direction opposite to the original flow direction, with a velocity nearly equal to the flow velocity i.e., $\sim 10^7$ cm s^{-1}, and the momentum transfer time is the time taken for it, in the flow frame, to slow down because of collisions with flow particles, since if we transform back to the original frame the neutral is now moving with the flow. The momentum exchange timescale is given by

$$\frac{1}{\tau_{m.t.}} = \frac{1}{\tau^e_{m.t.}} + \frac{1}{\tau^p_{m.t.}} \qquad 4.10$$

where e and p refer to electron and proton collisions. $\tau^e_{m.t.}$ is related to the momentum transfer cross section thus:

$$\tau^e_{m.t.} = \frac{1}{n_e v_f \sigma^e_{m.t.}} \qquad 4.11$$

and similarly for protons. The momentum and energy transfer cross section are also related via the scattering angle and scattering function of the electrons or protons, and it is simple to calculate in the Born approximation the energy and momentum change of each sort of charged flow particle in the collision. However it is not so easy to calculate the momentum and energy change of the diffusing neutral in this problem since simple treatments of electron scattering, like the Born approximation, assume that the neutral is a fixed scattering centre, and to include the motion of the neutral we must use more complex approximations. Also, in any given real collision, a fraction of the charged particle energy (if this is high enough) may go into exciting an energy level, and some will go into moving, giving momentum and energy to the neutral. A simple approximation we could make, ignoring the excitation effects, would be to treat the collision between neutral and charged particle as a simple "billiard ball" collision, in which case the majority of the momentum is transferred through collisions with the more massive proton, as opposed to the case of momentum transfer via the Coulomb interaction where the electrons are responsible for the majority of momentum transfer. If this is the case then the scattering function depends only on the effective radius of the particles (which in the case of a proton and a hydrogen atom we take to be the Bohr radius, $a_0 = 5.29 \times 10^{-9}$ cm^2. The momentum transfer cross section is then $\sigma_{m.t.} = \pi a_0^2$ and the momentum transfer distance $l_{m.t.}$ for a proton and electron number density of 10^{11} cm^{-3} is of the order of 10^6 cm. This distance is considerably larger than the charge transfer distance so between these two processes charge transfer will be the most important.

If the neutral were to be changed by charge transfer into a proton before it began to move with the flow, then another important quantity would be the momentum transfer cross-section for a proton in a hot target, since there would follow the possibility that it could be changed back into a neutral by charge transfer and become available again for excitation. As mentioned in §2.1.1 the energy of the beam or 'test' particle relative to the mean thermal energy of the particles of the target which it enters is an important parameter in calculating its stopping distance. There are three regimes of interest. When the energy of the test particle is much greater than both the electron and the proton thermal velocities the target is cold, when it is intermediate between the electron and proton thermal velocities the target is warm and when it is less than the proton thermal velocity the target is hot. Moving again to the frame in which the flow is static, the 'diffusing proton' has velocity around 10^7 cm s^{-1}. So the target will be warm if the flow temperature is around 10^5 K but will be hot if it is greater than this. (The flow temperature is the temperature of the Maxwellian in the global rest frame of the flow.) The expression for the rate of change of diffusing proton velocity parallel to its original direction is given in Tamres *et al* (1983) and is

$$\frac{dv_{\|}}{dt} = -(\nu^p + \nu^e)v_{\|} \qquad 4.12$$

where

$$\nu^j = 2\Psi(X_j)\nu_o \qquad 4.13$$

$$X_j = \left(\frac{m_j}{m_p}\right)\left(\frac{E}{kT}\right) \qquad 4.14$$

$$\nu_o = \frac{4\pi e^4 \Lambda n_p}{(2m_p)^{1\backslash 2} E^{3\backslash 2}} \qquad 4.15$$

$$\Psi(X_j) = \frac{2}{\sqrt{\pi}} \int_0^{X_j} t^{\frac{1}{2}} e^{-t} dt \qquad 4.16$$

$\Psi(X_j)$ is an incomplete Gamma function, $\gamma(3\backslash 2, X_j)$ which can be expressed as the summation of a series, viz

$$\gamma(a,x) = \frac{\Sigma_{n=0}^{\infty}(-1)^n x^{a+n}}{n!(a+n)}$$

If X_j is very large the upper limit of the integral in 4.8 tends towards infinity and $\gamma(3\backslash 2, X_j)$ tends to the value of the complete gamma function, $\Gamma(3\backslash 2) = \frac{\sqrt{\pi}}{2}$ therefore $\Psi(X_j) = 1$. If the target is cold then both $\Psi(X_e)$ and $\Psi(X_p)$ are approximately 1, giving the simple cold target results of equations 2.11. If the target is warm X_e is large but X_p is small, in which case it is necessary to use the series expansion. Since X_p is much less than 1, the first term in the expansion is sufficient, and we arrive at

$$\Psi(X_p) = \frac{2}{\sqrt{\pi}} \frac{2}{3} X_p^{\frac{3}{2}} \qquad 4.17$$

this leads to the energy equation seen in 2.24. If the target is hot then there is a similar expansion for $\Psi(X_e)$, and the equation for protons in a hot target is , after a little reduction

$$\frac{dv_{\|}}{dt} = \frac{2\pi e^4 \Lambda n_p v^2}{E^2} \frac{4}{3\sqrt{\pi}} \left[2 + \left(\frac{m_p}{m_e}\right)\left(\frac{E}{kT}\right)^{3\backslash 2}\right] \qquad 4.18$$

The approximate momentum loss time, δt, in such a situation is then given by

$$\delta t \sim v_{\|} \frac{\delta v_{\|}}{\delta t} \sim \frac{\sqrt{(2m_p)}}{2\pi e^4 \Lambda n v_{\|}} \frac{3\sqrt{\pi}}{4} \left(\frac{m_e}{m_p}\right)^{1\backslash 2} (kT)^{3\backslash 2} \qquad 4.19$$

$v_{\|}$ is the velocity of the proton in the rest frame of the flow $\sim$ flow speed. $L_{m.t.}$ for this charged particle $\sim \delta t \times v_{diff}$, and is given in the table below,for different values of the flow temperature, along with the other relevant length scales discussed above. Since we are in the hot target regime we use the charge transfer m.f.p. - it is the shortest relevant lengthscale and therefore provides a lower limit to the interpenetration area and hence to the polarization fraction.

Table 4.1

Process	Temperature	mean free path
charge transfer	$10^5 - 10^7$K	$5 - 10 \times 10^3$cm
hard sphere scattering	$10^5 - 10^7$K	10^6cm
warm target	$< 10^5$ K	1.3×10^3 cm
hot target	$10^6 - 10^7$K	$1.8 \times 10^4 - 5.6 \times 10^5$cm

§4.1.8 Results and Discussion.

Having now described the relevant excitation processes and the manner of their evaluation we now summarise the numerical results of the calculations for a number of values of flow velocity and temperature. Below are the intensities and polarization from the interpenetration region.

Table 4.2

Velocity	10^7	2×10^7	5×10^7	10^8
T = 10^5				
Proton emission	2.21×10^{17}	2.10×10^{18}	1.45×10^{19}	-
Pol'n fraction	39.9%	42.34%	44.5%	-
Electron emission	1.11×10^{21}	1.11×10^{21}	1.11×10^{21}	1.11×10^{21}
Net polarization	0.01%	0.08%	0.57%	-

Velocity	10^7	2×10^7	5×10^7	10^8
T = 10^6				
Proton emission	6.06×10^{17}	2.75×10^{18}	1.26×10^{19}	1.63×10^{20}
Pol'n fraction	26.7%	30.0%	42.55%	43.4%
Electron emission	1.47×10^{21}	1.47×10^{21}	1.47×10^{21}	1.47×10^{21}
Net polarization	0.01	0.05 %	0.37%	2.77%

Velocity	10^7	2×10^7	5×10^7	10^8
T = 10^7				
Proton emission	9.15×10^{20}	1.22×10^{20}	3.0×10^{20}	1.09×10^{21}
Pol'n fraction	13.9%	19.09%	32.4%	38.7%
Electron emission	7.6×10^{21}	7.6×10^{21}	7.6×10^{21}	7.6×10^{21}
Net polarization	0.17%	0.31%	1.07%	5.55%

It is evident in a low temperature flow, of 10^5 K, with a flow velocity of 10^7 cm s^{-1} that although the proton part of the distribution function is sufficiently highly anisotropic to produce a polarization fraction of 40%, the intensity of radiation from proton-hydrogen interactions is negligibly small compared with that from electron-hydrogen interactions, which are of course unpolarized. The polarization is therefore swamped. The difference in emission is due mainly to the difference of particle velocity, which appears in equation 4.7. If we keep the same drift velocity value but increase the temperature to 10^6 K, the polarization fraction from the protons decreases as we would expect, and in addition the component of emission from the electron part of the distribution function increases, as now the mean electron thermal energy is 86eV. By far the larger part of the electron distribution is capable of exciting Hα emission. However the proton contribution increases also, because the excitation cross section increases with proton energy. At a drift speed of 10^8 cm s^{-1} we find that our polarization fraction is almost 3%. As the temperature goes up still farther to 10^7K again the proton and electron contributions are enhanced and the polarization fraction decreases. However at 5×10^7 cm s^{-1} the proton emission is sufficiently intense to allow the polarized component to be visible at a level of 1% over the electron component, whilst at a drift speed of 10^8 cm s^{-1} the polarization produced increases to 5.5%. In summary, for polarization to be visible from the upflowing regions at a level of the order of 1% we require that the flow velocity is greater than $\sim 5 \times 10^7$ cm s^{-1} and the temperature around 10^7K, depending on the flow velocity. We note that with these parameters the bulk kinetic energy of the evaporative flow ($\sim 0.5 n_p m_p v_d^2$) is of the same order as the thermal energy ($\sim n_p kT$) as we would wish in a plasma which is expanding because it has been heated.

As can be seen from table 4.2 the intensity of emission from the interpenetrating region is significantly larger than that from the static part - $\sim 10^3$ times larger, therefore the only real constraint which we have on the geometry of the evaporation is that the surface area of static chromosphere should not exceed $\sim 10^3$ times that of the evaporating region, and also that the area taken up in flows should be similar to that which is static, for the increase in optical depth in these regions to have a significant effect. As was demonstrated in §4.1.7 the interpenetration distance is of the order of 10^3 to 10^4 cm, depending on the temperature of the surrounding material and the flow velocity. Given then that only a small part of the upflowing material is actually emitting polarized Hα , we shall now examine whether is it possible , within the constraints outlined above to have a sufficiently high total Hα intensity - fitting for an active region, and still be able to see polarised Hα radiation at a level of a few percent.

Let the areas of static sun, flow channels, interpenetration distance and total flare be A_s, A_{uf}, A_{int} and A_f respectively. Let the intensity of radiation from each of these regions be I_s, I_{uf}, I_{int} and

I_f. P is the polarization fraction generated in the interpenetration region. We can then write the constraints.

$$A_s + A_{uf} + A_{int} = A_f \qquad 4.20a$$

$$A_{uf} + A_{int} \sim A_s \qquad 4.20b$$

$$I_s A_s + I_{uf} A_{uf} + I_{int} A_{int} = I_f A_f \qquad 4.20c$$

$$\frac{P I_{int} A_{int}}{I_{uf} A_{uf} + I_{int} A_{int} + I_s A_s} = 5.5\% \qquad 4.20d$$

$I_f = I_s$ since the static model is based on the total flare value of intensity. In addition, we calculated that the maximum Hα intensity generated by recombination emission in the upflowing (but not interpenetrating) region is 10^7 cm^{-3} s^{-1}, therefore even if the flow was optically thin right down to height zero - i.e. the top of the photosphere - 1.46×10^8 cm down from the top of the chromosphere - the total emission per square centimetre at the surface of the non-ineterpenetrating region would still be at least an order of magnitude below the total emission per square centimetre of the surrounding static sun, which, from the thermal excitation calculation of §2.1.4 emits at a rate of $\sim 5 \times 10^{16}$ cm^{-2} s^{-1}. Also, this maximum value of 10^7 corresponds to a low temperature flow, at 10^5K, and we see from the table of results that it is not possible to generate sufficient polarization using a flow at this low temperature anyway, so in fact the recombination emission rate would be one or two orders of magnitude down on this maximum value. So since $I_{uf} \ll I_s$ and since we have specified that the total flow plus interpenetration area must be similar to the static area (4.20b), we may neglect the second term on the left hand side of equation 4.20c. Let $I_{int} = f I_s$. Then from 4.20a

$$A_s + f A_{uf} = A_f = A_{uf} + A_{int} + A_s \qquad 4.21$$

For large f, $A_{int} = A_{uf} \backslash f$. This means that the interpenetrating regions need only be a small fraction of the total upflowing region, which is good news because the interpeneration distance d as calculated in §4.1.7 is rather small compared to the length scales of $\sim \sqrt{10^{19}}$ cm, which is the typical linear dimension of the Hα -bright structure. Let us now put some numbers into these relationships. First of all we determine the value of f, the ratio of photon number fluxes from the interpenetrating to the static region We are only interested in flows which generate a polarization of at least 1% in the interpenetration region, corresponding to velocities and temperatures in the range $5 \times 10^7 - 10^8$ cm s^{-1}, $10^6 - 10^7$K. The typical total intensity of radiation from this region at the surface is $10^{20} - 10^{21}$ cm^{-2}s^{-1}, whilst that calculated from the static atmosphere of MAVL is $\sim 5 \times 10^{16}$cm^{-2}s^{-1} - therefore $f \sim 10^3 - 10^4$. The absolute values of the area quantities are then

$$A_f \sim 10^{19} cm^2$$

$$A_s \sim 5 \times 10^{18} cm^2$$

$$A_{uf} \sim 5 \times 10^{18} cm^2$$

$$A_{int} \sim 5 \times 10^{14} - 5 \times 10^{15} cm^2.$$

To achieve these conditions the flow must be fragmented into a certain number N of discrete channels. We are in a position to calculate N, in the model where the flow is arranged in strips, or one in which the channels are in the form of cylindrical filaments. 1) An individual strip has area $A_f \backslash 2N$, and the interpenetrating part of the flare has area of $\sqrt{A_f} \times d$ where d is the interpenetration distance. The total interpenetrating area must total $\sim 5 \times 10^{14} - 5 \times 10^{15}$ cm^2, therefore with $N \backslash 2$ strips - each having 2 edges along which interpenetration can occur, we arrive at a fragmentation number of 150 to 1500. Note that our additional condition that the distance h from the chromospheric surface to the $\tau = 1$ optical boundary be approximately equal to the width of each channel (and therefore each strip, w_s) limits us to the lower end of this range - fragmentation numbers of order 10^2. $N \times w_s$ must be approximately equal to 10^9 cm and $h = w_s = 1.84 \times 10^7$ cm (T = 10^7) or 1.09×10^7 cm (T = 10^6). 2) A cylindrical channel has radius R, and the interpenetration region around the boundary of the channel $A_{int} = 2\pi R \delta R$. There are N such channels, so $R = 10^{10 \rightarrow 11} \backslash N$ using the limitation on interpenetration area given above. The total upflow area is $\sim 5 \times 10^{18}$ cm^2, consisting of N channels each of area πR^2 so $\pi R^2 N \sim 5 \times 10^{18}$ cm ^{2}. Therefore in this model of cylindrical upflows the fragmentation number varies between 60 and 6000. Our additional condition in this case is that the radius of the flows should be approximately equal to the distance to the optical boundary, and this gives the same range of permissible fragmentation numbers. Note that in this calculation we are assuming that the optical depth in the flow region has not changed because the geometry of the flows has changed (recall that the calculation of specific intensity was performed for a strip geometry). We do not expect that it will, since when comparing the size of terms in §4.1.5 the photo-excitation term - the only one that is affected by the geometry - is generally negligible in comparison to the other excitation terms. In both of the above geometries the resulting discrete structures have length scales of $\sim 10^7 - 10^8$ cm, which is just at the limit of the smallest scales resolvable on the sun in Hα . There are a number of means by which fragmented upflows could be generated - the Rayleigh Taylor instability is discussed in §4.1.9. But fragmentation is also advocated in the context of initial acceleration mechanisms. If hard X-ray bursts from solar flares are predominantly non-thermal $e^- p^+$ Bremsstrahlung then the work of Holman (1985) suggests that at least 10^4 oppositely directed channels are required to exist in the particle acceleration region for a sufficiently high energy beam accelerated by electric fields to be stable and able to propagate from the region. This is only a requirement of Holman's model - (i.e., *if* the hard X-ray signature is non-thermal then there must be fragmentation) rather than a prediction based on

a proposed acceleration mechanism, however it does indicate to us that under certain plausible acceleration conditions there must be fragmentation. The fact that the fragmentation we demand is lower than the lower limit set by Holman's requirements should not worry us unduly, since it is possible that filaments will merge to some extent when the beam has left the acceleration region and as the free-streaming distributions become more isotropised when they encounter the denser regions of the low corona and chromosphere. Had our required filamentation been higher than that predicted in the Holman model we would have had a problem. There exists, in addition, work by Winglee *et al* (1988) who use a numerical code to simulate the transport of energy by an electron beam in a 2-d flaring flux loop. Results from this work also suggest a filamentation of the driving beam, associated with the necessity to have return currents to keep the beam stable. It appears that in a 2-d simulation, as the beam - return current system evolves, enhancements and depletions of electrons appear (if beam and return current are not cospatial) which accelerate plasma ions across field lines - in the plane perpendicular to the beam direction, which cause the beam to fragment on a scale of the order of the ion gyro-radius in the local magnetic field. This condition appears during the evolution of the system rather than being a pre-requisite for a particular model to work, but must be treated with caution since it is the result of a 2 - d simulation which (unless the beam is in fact a sheet - like structure) is inappropriate.

The important fact to emerge from this discussion is that there is a number of situations in which filamentation appears naturally or is a requirement of a testable model. Above we have only discussed filamentation of an energetic beam from the corona although the generation of filamented upflows is possible also. Linear Polarization observations are incapable of distinguishing between these two diametrically opposite directions from which the target could be excited.

Total Energy Requirements of the Flow - Driven Model.

As in the case of the beam-driven model we calculate the total energy that is contained in flows. The total kinetic energy is equal (to 1 part in 10^3) to the kinetic energy of the protons.

$$v = 5 \times 10^7 \text{ cm s}^{-1},\ E_{tot} = 5.64 \times 10^{20} n_p \text{ ergs}$$

$$v = 1 \times 10^7 \text{ cm s}^{-1},\ E_{tot} = 4.61 \times 10^{21} n_p \text{ ergs}$$

Apparently using our density value of 10^{11} cm $^{-3}$ we have a similar problem as occurs in the beam-model. The total energy required is similar to that occuring in a very large flare, and in the latter high velocity case is greater. However we have no need to abandon the model here since it is possible to reduce the density of the flow and still have the interaction regions generate the same degree of polarization, and have enough leeway in the total intensity to allow the total polarized intensity

to be visible over the thermal background, without requiring an inordinately high fragmentation number.The total intensity in Hα generated by protons is equal to the total interpenetration area multiplied by the total flow generated intensity. The total intensity per unit volume is directly proportional to the flow density and therefore decreases with it. However the interaction area increases as we decrease flow density, since the area depends on the interpenetration distance - the distance which a neutral travels before being turned into a proton via charge exchange, and this is inversely proportional to the flow density. So the product of intensity and area does not change as density is changed. It is possible therefore to have a flow of lower density - say 10^{10} cm^{-3} which generates visible polarization, but has a smaller total energy requirement.

§4.1.9 A Possible Fragmentation Mechanism - the Rayleigh-Taylor Instability.

It is important that there is relative motion of the evaporating material and that which lies around it. So it is necessary that the structure overlying the slow shock region is not totally disrupted, but that some of the flow material can penetrate. To avoid the problem of disrupting the flare atmosphere with a flow, and losing the neutral hydrogen layer we propose the following picture. We know from the theoretical hydrodynamical models of Nagai and Emslie, that the formation of a high temperature hydrodynamic shock in the evaporating atmosphere is possible. Such shocks are subject to instabilities, such as the Rayleigh-Taylor Instability, in which the front fragments, and the fragments "run away" in front of the bulk of the shock. (see schematic diagrams 4.12) This mechanism has been proposed (Gull 1973, 1975) as being responsible for the observed filamentation in expanding supernova remnants, as they sweep the interstellar medium up in front of them, and under appropriate conditions may lead to the filamentation of the evaporating solar atmosphere. Such filaments could pierce the neutral hydrogen layer before the rest of the slow shock 'catches up'. The material in the fragments is travelling at a greater velocity than the remainder of the shock (see below) and it is at the boundary between these channels and the ambient material that impact excitations may take place. Below we consider the relevant parts of the theory of formation of the Rayleigh Taylor Instability. This instability occurs at the boundary between two fluids in a net accelerating field, where the denser fluid lies 'on top of' the less dense fluid. It is most familiar as the gravitational instability occuring when, for example, ink "fingers" through water. In the solar case we posulate a simple model in which evaporation occuring as a result of localised heating of the atmosphere produces a horizontal moving supersonic front, which acts to accelerate the material in front. According to the Supernova remnant model of Guil (1973) the material, being accelerated supersonically, cannot disperse and accretes in front of the shock. Across the boundary, pressure balance must be maintained, which requires that the gas density in the material behind the shock increases to form a contact discontinuity, and it is this discontinuity,

in the presence of the decelerating force provided by the accreted matter, that becomes Rayleigh Taylor unstable. The result of this process in a supernova remnant is that filmanets of material proceed ahead of the bulk of the expanding shell. Such filaments are readily observable (van den Berghe*t al* 1973)).

There is the additional complication in the solar case of the magnetic field which threads the chromosphere and corona. This modifies the manner in which material can move, depending on its orientation to the moving front. The effect of a magnetic field lying parallel to the evaporation front is as of a surface tension - damping out small wavelength oscillations but allowing larger ones to grow. A magnetic field perpendicular to the material boundary has the opposite effect - hindering large oscillations and permitting small ones. We can explain this effect in the following way. The onset of fingering requires that dense material from 'above' moves past less dense material below, which requires a distortion of the field lines to the side. A long wavelength perturbation requires the motion of a large quantity of material - a large distortion of the field lines and hence a large curvature force, which is resisted by the field.

Rather than write down and solve the dispersion relation in the general case, we shall simply state the equation for the growth rate n of perturbations of wavenumber k, in the case of a magnetic field perpendicular to the evaporation front.

$$n^3 + 2k(\sqrt{\alpha_1} - \sqrt{\alpha_2})n^2 + k(2k + \alpha_1 - \alpha_2)n - 2k^2(\sqrt{\alpha_2} - \sqrt{\alpha_1}) = 0 \qquad 4.22$$

α_1, α_2 are $\rho_1 \backslash (\rho_1 + \rho_2)$ and $\rho_2 \backslash (\rho_1 + \rho_2)$ where ρ_1 and ρ_2 are the densities of material 'above' and 'below' the boundary - with reference to the net gravitational, or accelerating field g. In this equation n the growth rate is expressed in units $g \backslash V_A$ s^{-1}, and k in units $g \backslash V_A^2$ cm^{-1}, where V_A is the local Alfvèn wave speed.

$$V_A^2 = \frac{B^2}{4\pi(\rho_1 + \rho_2)} \qquad 4.23$$

The chromospheric Alfvèn velocity is calculated using typical chromospheric field strengths of 500 to 1500 Gauss, with a proton number density of 10^{11} to 10^{12} cm^{-3} . To be able to use the equation in the form written above we also need a value for the net accelerating force acting on the evaporating material. According to the paper by Gull (1973), as material builds up ahead of the shock, it produces a net deceleration of the post-shock material at the contact discontinuity. The post-shock gas could equivalently be thought of, in the rest frame of the accreted material as accelerating outwards. Alternatively consider the situation in the frame of the post shock material. The density in here increases towards the contact discontinuity. Since this material is all moving at essentially the same velocity (provided by the expansion power) in the rest frame of the shock the post-shock material looks like a hydrostatic atmosphere with 'gravity' directed outwards. The

gravitational force g is given by $g \sim v_s^2 \backslash h$ where v_s is the sound speed in the material and h is the scale height of the discontinuity. This provides us with a means of estimating g.

Suppose that energy released during a flare is deposited in a narrow region of the atmosphere where the density increases rapidly - in the MAVL model F1 this occurs between 1.425 and 1.435×10^8 cm - the density increases by an order of magnitude in 10 km. There is a similarly rapid density increase in quiet sun models. According to the Nagai and Emslie model this part of the atmosphere can be heated to $10^6 - 10^7$ K, therefore the sound speed $v_s = \sqrt{(kT \backslash m_p)}$ is around $1 - 5 \times 10^7$ cm s^{-1}. For the accretion of matter to occur the expanding material must form a shock - i.e., must be moving faster than the sound speed which observations - observations suggest that this is possible. According to Gull, once the ratio of matter accreted by the shock to that which is moving behind the shock is of the order of 0.01 the boundary becomes Rayleigh - Taylor unstable. Therefore if the 10km thick layer of average density 10^{12} protons cm ^{3} is driven out by expansion, it is necessary to accrete 10^{16} protons per cm^2 of 'surface' of the shock. This is a large number, however if the evaporating material is moving at just above the sound speed - say 5×10^7 cm s^{-1} sufficient material will be accreted when the shock has moved into a further kilometer of overlying material (at a density of $\sim 10^{11}$ protons cm^{-3}) - taking less than a hundredth of a second. So after only a very short time the shock - front of the evaporating material is potentially Rayleigh-Taylor unstable. Putting h, the scale height of the material building up behind the shock-front less than the dimension of the evaporating part of the atmosphere, and $v_s = 10^7 - 5 \times 10^7$ cm s^{-1} gives a value for the effective gravitational field in the post-shock material as $10^8 - 2.5 \times 10^9$ cm s^{-2} .

In addition we require the Alfvèn velocity for this region. From equation 4.23, using field strengths and densities as given above, $V_A \sim 1 - 3 \times 10^8$ cm s^{-1}. So wavenumbers in eqution 4.22 are measured in units of $g \backslash V_A^2 \sim 1.1 \times 10^{-9} - 2.5 \times 10^{-7}$ cm^{-1} whilst growth rates are measured in units of $0.33 - 25$ s^{-1}.The velocity of growth perpendicular to the the boundary is proportional to e^{nt}, and clearly we must have $n > 0$ and $n^2 > 0$ for the perturbations to grow. It is evident that perturbations on all scales can grow, but at different rates. Our upper limit to wavelength is 10^9 cm as mentioned already but we really wish to know about the growth of instabities of scales of $10^7 - 10^8$ cm, corresponding to wavenumbers $10^{-8} - 10^{-7}$ cm^{-1}. Depending on the temperature, density and field in the shock region these wavenumbers correspond to a range of $0.1 - 100$ in the units described above. There are low and high energy approximations to the solution of the cubic 4.22, unfortunately our wavenumbers cover the entire range so for most sets of parameters it is necessary to solve 4.22 fully. The solutions for temperatures of 10^6 and 10^7, and wavelenghts 10^7 and 5×10^7, at suitable density, are plotted in figures 4.13 a,b. Evidently instabilities of this size can grow rapidly - timescales of between about 0.1 and 10 seconds - with longer wavelength instabilities

taking longer to develop. It has not been studied here but Chandrasekhar demonstrates than as the ratio of 'upper' to 'upper + lower' density increases, the growthrate also increases, so with a more extreme density discontinuity the perturbations would develop even faster.

We have demonstrated that Rayleigh - Taylor instabilities with the wavelengths we require *can* develop on short timescales, but there are two problems which we must address before being able to say that this process is a likely fragmentation process. Firstly, since it is necessary to have a supersonic front if the instability condition is to be reached, the front itself might very rapidly attain the neutral hydrogen layers and would either push them upwards or disrupt them entirely. However if the growth of perturbations is rapid enough and on a large enough scale it is possible that the flow of material and therefore kinetic energy from the shoch boundary would slow the shock down (so that it is no longer a shock!). If in this time the amplitude of the perturbations became large enough for them to become "channels" to the less dense upper chromosphere it is possible that material would continue to flow upwards along these channels, and in removing thermal energy from the heated region, halt the global expansion of the heated gas. Secondly, we are interested in relatively long wavelength perturbations but of course all wavelength perturbations can potentially occur. Shorter wavelengths grow on shorter timescales and longer wavelengths on longer timescales (if the other atmospheric parameters are kept the same). Note however that if the wavelengths are more than about an order of magnitude longer than the $\sim 5 \times 10^7$ cm perturbations that we have looked at already this would be perturbations on the same scale as the entire evaporating region which are of no interest. Also, it turns out that the dependence of timescale on wavelength is not very great - repeating the calculation of growthrate for a perturbation of size 10^5 cm we find that the growthrate is reduced only by a factor of ~ 1.5 when the field is small, and not at all when the field is large (corresponding to the asymptotic limit). The velocity of particles in the perturbations grows initially at the rate $\exp(nt)$. But when the distorted perturbation front is more than one wavelength removed from the existing shock front it is not clear how the growth of the instability will proceed (see fig 4.14) - indeed Gull suggests that in the case of supernovae, once the Rayleigh-Taylor filaments become extended they are themselves subject to other instabilities associated with the laminar flow of material in the filament past the interstellar matter. In the solar case it is also possible, indeed probable, that perturbations become similarly unstable once they become too extended. A $\lambda = 10^5$ cm perturbation would, by this argument, be subject to other instabilities once the perturbation front had penetrated just a few kilometers into the atmosphere above the shock (only a few times its wavelength). But a large wavelength ($\lambda = 10^7$ cm) perturbation, by virtue purely of its size, would not reach the same distorted and unstable condition until it had grown in amplitude to a few times 10^7 cm. If we suppose that the shock forms at a height of between 1.425 and 1.435×10^8 cm, and the transition region (in the MAVL

model) is at 1.46×10^8cm then evidently a large wavelength perturbation would retain its identity at least until the perturbation front had reached the transition region. At this point it is possible that flow from the heated regions to the upper region becomes established along the channels provided by perturbations, as was proposed earlier.

We do not present this as anything other than speculation, however there is definitely a case for believing that growth of perturbations on too small a scale will not last long - with the parameters we use certainly not as much as a minute, whereas there is the possibility that larger wavelength perturbations will more permanently affect the structure of flow from the heated area of the atmosphere to above the transition region - resulting in filamentation which would last for as long as it took for the heated region to cool.

§4.1.10 Discussion and Conclusions of the Fragmentation Model

We find that it is possible to generate impact polarization at the level of at least 1% by the interaction of a drifting Maxwellian (of particle density 10^{11} protons cm^{-3}) with a static surrounding atmosphere we require that the temperature of the drift material be $10^6 - 10^7$ K with a velocity of $5 \times 10^7 - 10^8$ cms $^{-1}$. For polarization generated in the interaction region to be visible despite the diluting effect of the surrounding material we require that the flow is fragmented into $10^2 - 10^3$ seperate channels, interacting with the surroundings around their edges. There is evidence that flows of this velocity occur on the sun during flares - Antonucci *et al* (1990) record evaporation velocities of 8×10^7 cm s^{-1} having a duration of $\sim$ 5 minutes and a periodic time variation on a scale of 1.5 minutes. In addition, theoretical work by Alexander and Emslie (1987) on the response of the chromosphere to heating by an electron beam suggests that upflow velocities of as much as 11×10^8 cm s^{-1} are possible in the low corona, if considering a multithermal plasma model of evaporation. The Antonucci *et al* observations identify an Hα brightening in the chromosphere with an area of up to 4×10^{19} cm^2 occurring at the same time as the high velocity occurs, agreeing with the area scales over which Hα polarization is observed to occur, suggesting that chromospheric evaporation can occurs on a sufficiently large scale to associate it with the source of the polarization. However the timescale remains a problem - the Antonucci et al observations of chromospheric upflows last for only 5 minutes or so. The suggestion of these authors that the successive 'firing' of a number of loops could lead to the observed periodic variation of the calculated upflow velocity can in principle be extended to a larger number of loops firing over a longer timescale. We note that the degree of polarization observed by Hénoux *et al* varies with a period of the order of 1 minute - as do the velocity measurements, which indicates that the two processes may be linked. The two sets of observations are consistent with an atmosphere responding to a

periodic energy input with a periodically varying atmospheric evaporative motion, which generates impact polarization, but they are, of course, also consistent with the polarization being produced by interaction of the injected particles as they move downwards. In this latter case however, we are returned to the problem of chapter 2 - the energy required in this case is too large for all but the biggest of flares, and unlike in the evaporation - driven model, it cannot be reduced to a value which is more reasonable.

Recall that because of the geometrical effects of viewing the flaring regions at an angle one needs a polarization fraction of 5.5% in the 90° direction to see a fraction of 2.0% from Earth. Within the parameters we have tested we only just attain this polarization level. This is due primarily to the dilution of proton generated polarized emission by electron generated un-polarized emission from the same region. In addition we recall that the possibility of depolarization due to molecular interactions may occur - further lowering the polarization fraction calculated. However, in our calculations we have made two assumptions which will affect the results - probably not by an order of magnitude, but possibly by a few percent polarization. The first is the low energy approximation we use for the proton excitation cross section and polarization fraction. Recall that we assume that the cross section goes linearly to zero from 1keV to threshold excitation energy. It is not obvious that this need be the case - it is possible that the cross section increases with decreasing energy for some way below 1keV before turning over and decreasing to zero. Until experiments or reliable theoretical calculations over the very low energy range are performed we cannot be sure about the cross section behaviour. Our second assumption is that the electron generated emission is unpolarized - an approximation which was made for a speedy calculation, and is correct when we have flow temperatures of around 5×10^6 or 10^7. But in cases where the flow temperature is small - 10^5 K but the flow velocity is large, - 10^8 cm s $^{-1}$ the electron distribution can be significantly anisotropic - in this case the typical thermal speed is only twice the flow speed, so we could expect that the electron distribution will generate polarization also. Although the mean electron energy at 10^5 K is lower than the Hα excitation threshold there is still $\sim$ 0.6 of the total particle population with sufficient energy to excite the transition. The majority of these will have threshold or near-threshold energies and therefore would excite Hα photons with polarization fractions equal to the threshold value. This electron distribution looks, to all intents and purposes, the same as a proton distribution of drift velocity $\sim 2 \times 10^7$ cm s^{-1} temperature 10^7 K and we would expect the same degree of polarization to result from both. According to table 4.2 this is is 19.09 %. Of course the intensity of emission from a 10^5 K flow is slightly lower than those from higher temperature flows, 10^{19} photons cm^{-2} s $^{-1}$, - but only slightly, therefore it is not necessary to increase the fragmentation. The drawback to this particular form of evaporation is that it is not easy to see how one could have a thermally - driven evaporation where the average particle kinetic

energy is so much greater than the average particle thermal energy. If we move to higher flow temperatures the electron distribution will still be slightly anisotropic, but not significantly so, compared to the proton distribution. Of course, above a certain value of electron energy - around 500eV corresponding to a distribution temperature of $\sim 6 \times 10^6$ K, the polarization fraction is negative, but with a corresponding mean thermal speed of 1.7×10^9K the anisotropy introduced by the flow is small and the magnitude of the polarization fraction will be tiny. So although there is in fact a reduction in the total polarization from the interpenetration region because of this, it will be so small as to be negligible.

We conclude that the process of bulk flow of charged particles constrained by a magnetic field through a neutral target, coupled with the ability of neutrals from surrounding material to diffuse across the field lines into the flow, can produce impact polarization at a level of a few percent (when viewed at 90° to the flow direction). In the solar atmosphere it would be possible to observe such polarization above the Hα level of the surroundings because the absorption in Hα in the region where flow and static mingle is reduced as a result of the increased temperature and increased excitation in the flow. However, with present values for atomic data and reasonable flow temperature and speed, the fraction generated, although having a value of a few percent, is of the same order of magnitude but in general smaller than that observed. Nonetheless, since it is a process which is energetically permissible, and also has the potential to explain the area scale of the polarization observations, it should remain a likely candidate for the source of the polarization, at least until improvements in atomic data at low energies rule it out altogether. It is necessary to have the flow fragmented if the area in which generation of polarized radiation takes place is to be large enough, but there are theoretical suggestions that fragmentation will take place in particle beams which heat the chromosphere and it is possible that a non-uniform heating rate could generate fragmented evaporation. Although the parameters which we have chosen as being representative of conditions in the evaporating solar chromosphere (on the basis of theoretical and observational work) result in a polarization fraction which is slightly too low, it would be possible with more extreme parameters to generate the polarization fraction that is observed - which does require higher fragmentation but is certainly not to be ignored for this reason. To sum up, we consider that whilst failing to explain the polarization observations using the present values for atomic parameters, the flow-driven model cannot be ruled, out on the grounds that there is still considerable uncertainty in the atomic physics at low energies. We have demonstrated that the total energy and fragmentation in the flow are consistent with flare values. At values of temperature and density which are consistent with those observed and inferred the flow driven evaporation model fails by a factor of 2-3 to explain the observations, whilst at more extreme flow parameters, agreement can be reached between the results of the model and the observations.

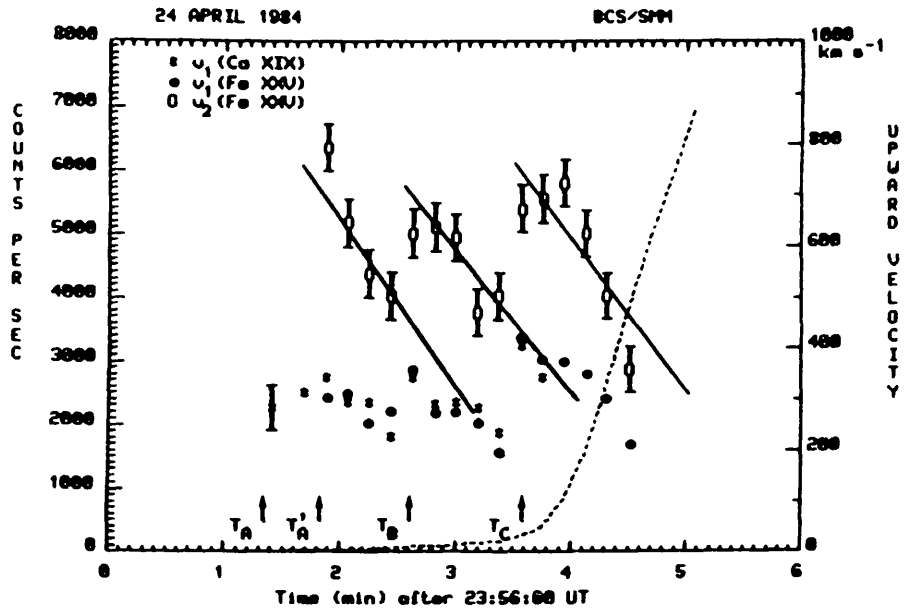

Fig 4.1 Blue shift velocities as a function of time
(Antonucci *et al* 1990)

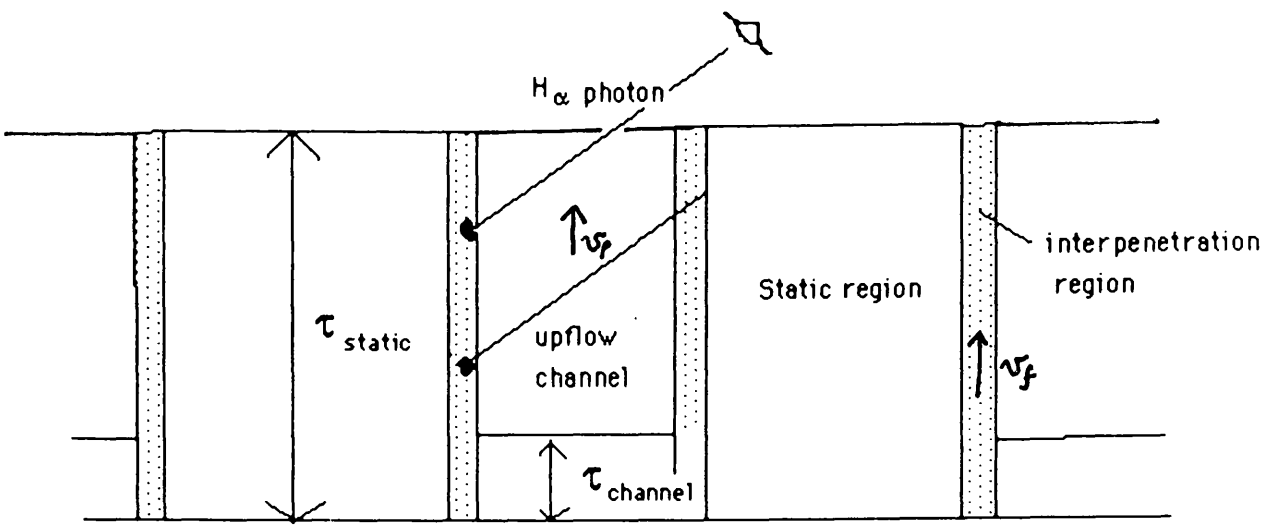

Fig 4.2 Suggested fragmentation of evaporating material into channels.

Fig 4.3 Variation of level 2 occupancy in interpenetration region

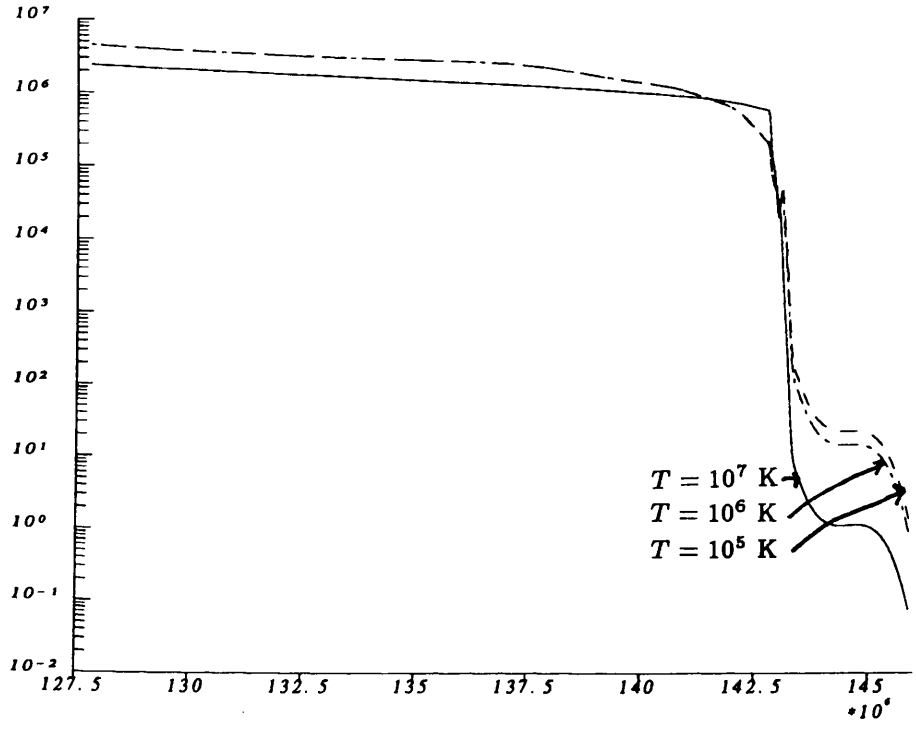

Fig 4.4 Variation of optical depth with position in interpenetration region

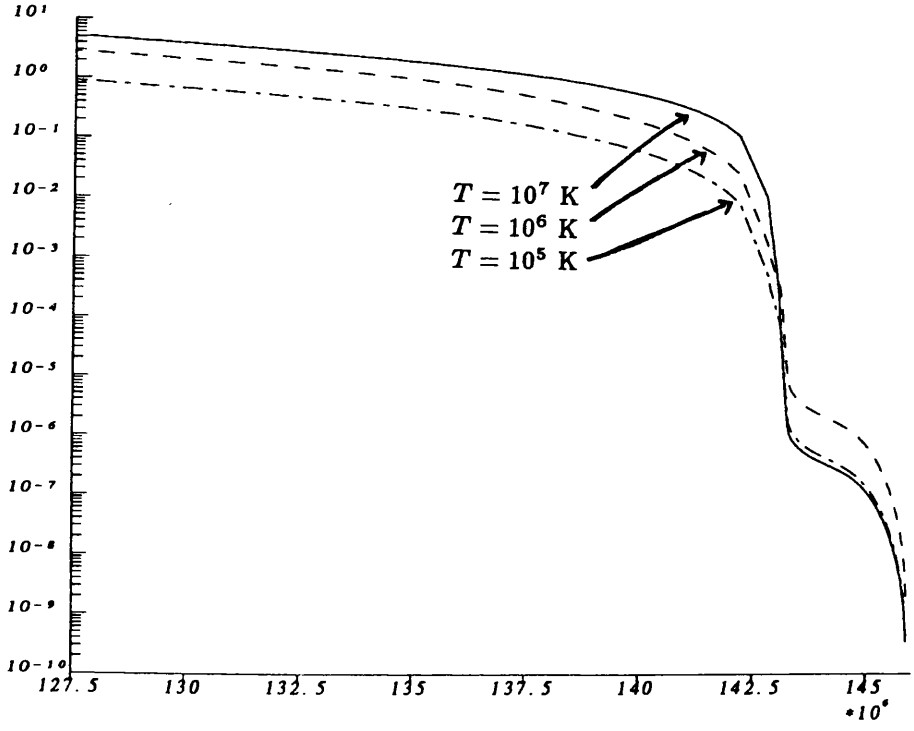

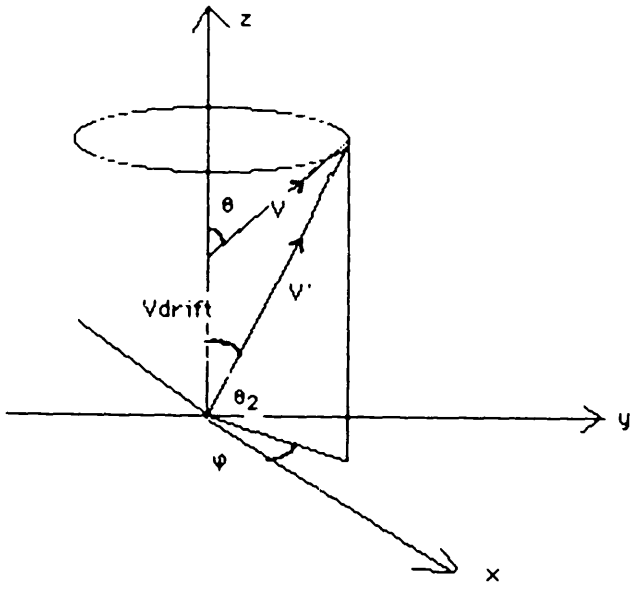

Fig 4.5 Geometry of transformation of flow particle velocity to static frame.

Fig 4.6 Distribution functions of flow particles in velocity space.

Bulk flow velocity = 10^7 cm s^{-1}

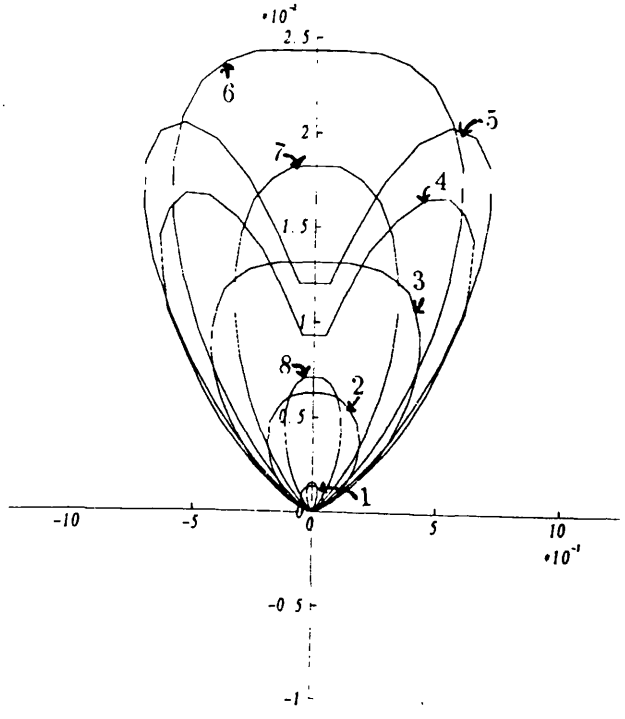

T = 10^5K

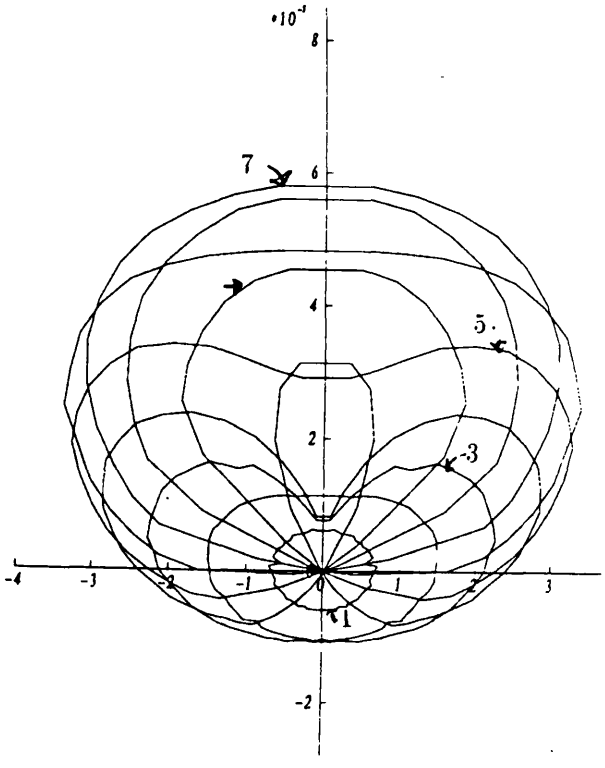

T = 10^6K

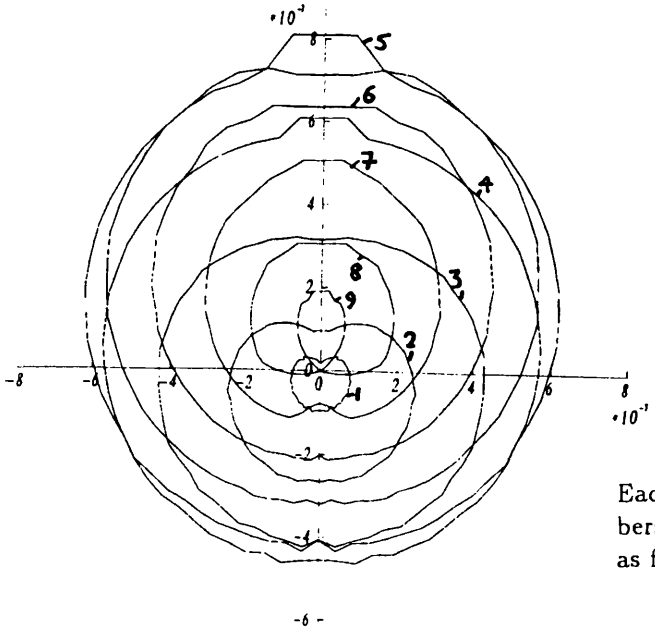

T = 10^7K

Each line is a contour of constant speed. The numbers, i, associated with the lines indicate the speed as follows.

Fig 4.6a. speed = $i \times 1.5 \times 10^6$ cms^{-1}

Fig 4.6b. speed = $i \times 2.0 \times 10^6$ cms^{-1}

Fig 4.6c. speed = $i \times 3.0 \times 10^6$ cms^{-1}

Fig 4.7 Distribution functions of flow particles in velocity space.
Bulk flow velocity = 5×10^7 cm s^{-1}

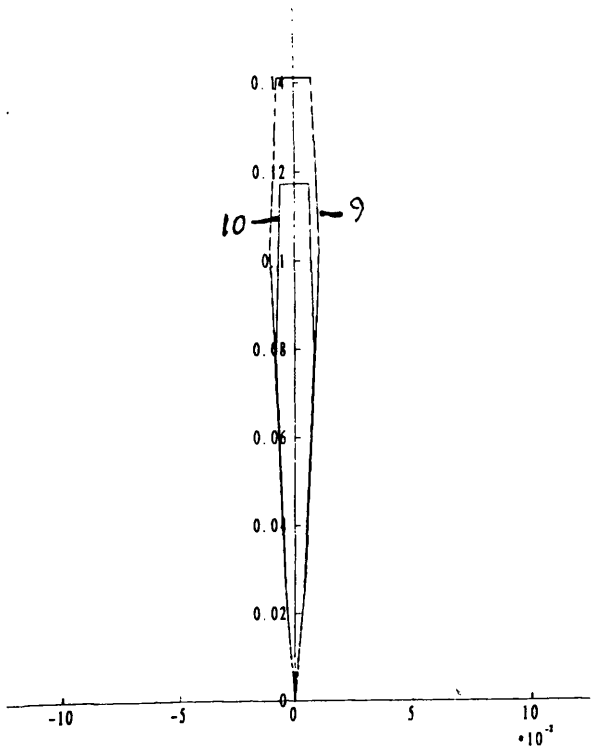

$T = 10^5$K

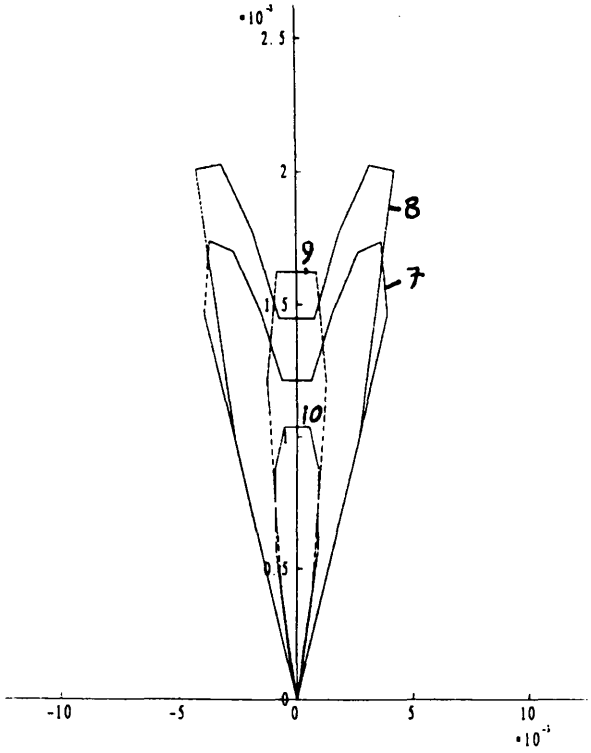

$T = 10^6$K

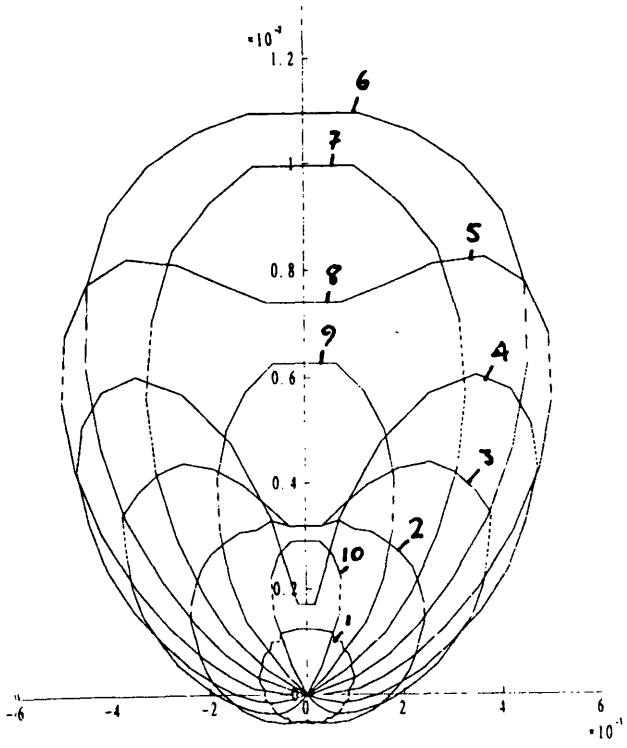

$T = 10^7$K

Fig 4.7a. Speed = $i \times 5 \times 10^6$ cms^{-1}

Fig 4.7b. Speed = $i \times 5 \times 10^6$ cms^{-1}

Fig 4.7c. Speed = $i \times 10^7$ cms^{-1}

Fig 4.8 Distribution functions of flow particles in velocity space.
Bulk flow velocity = 10^8 cm s^{-1}

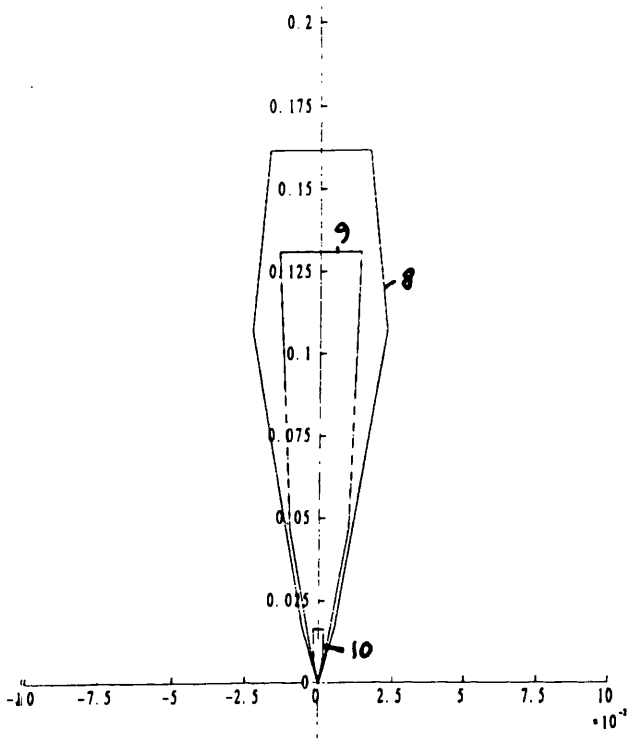

T = 10^6K

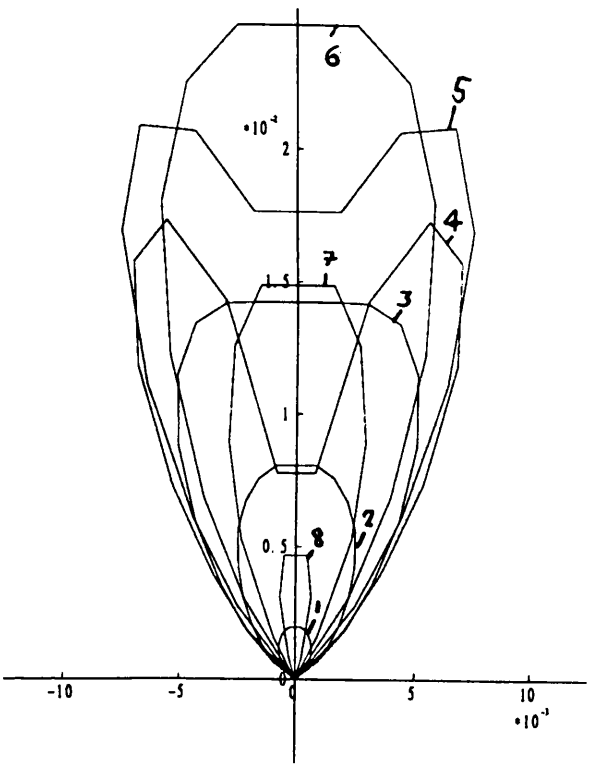

T = 10^7K

Fig 4.8a. Speed = $i \times 10^7$ cms^{-1}

Fig 4.8b. Speed = $i \times 2 \times 10^7$ cms^{-1}

Fig 4.9 Anisotropy factor of flow particles.
Bulk flow velocity = 10^7 cm s^{-1}

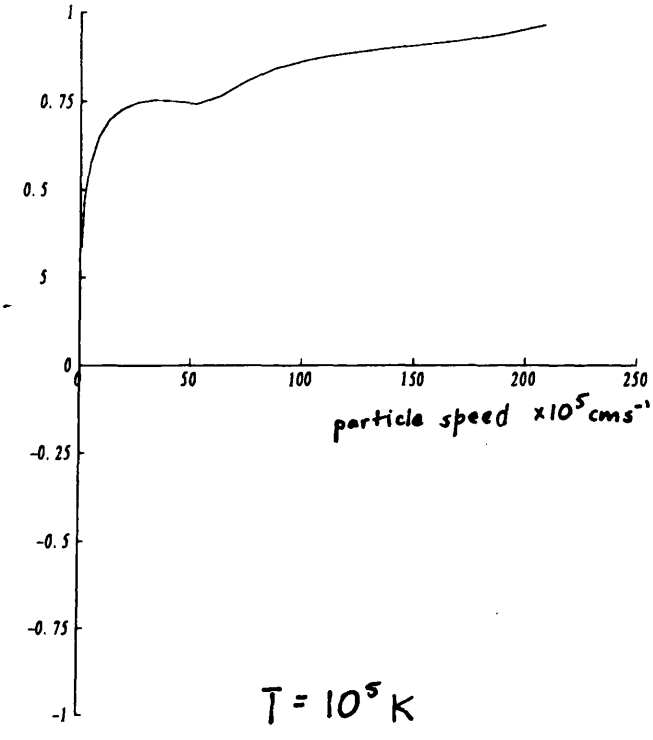

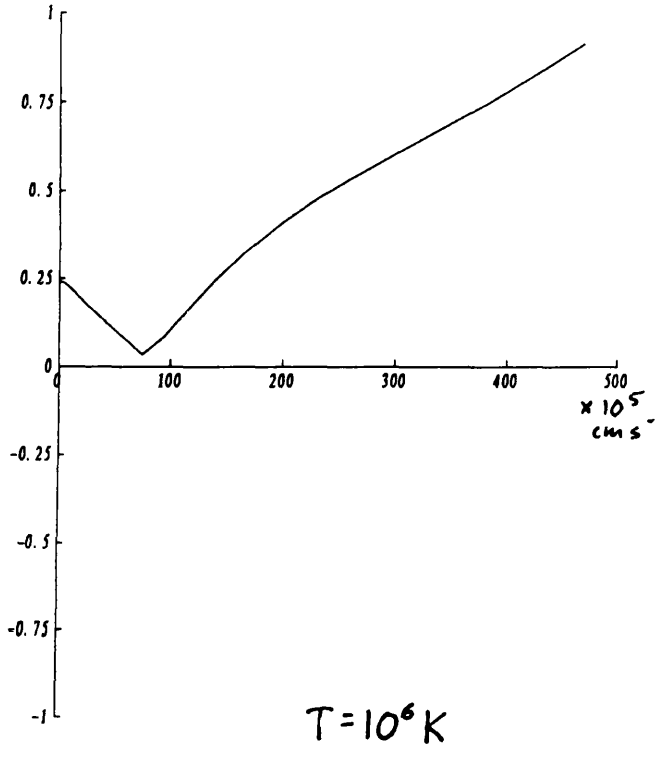

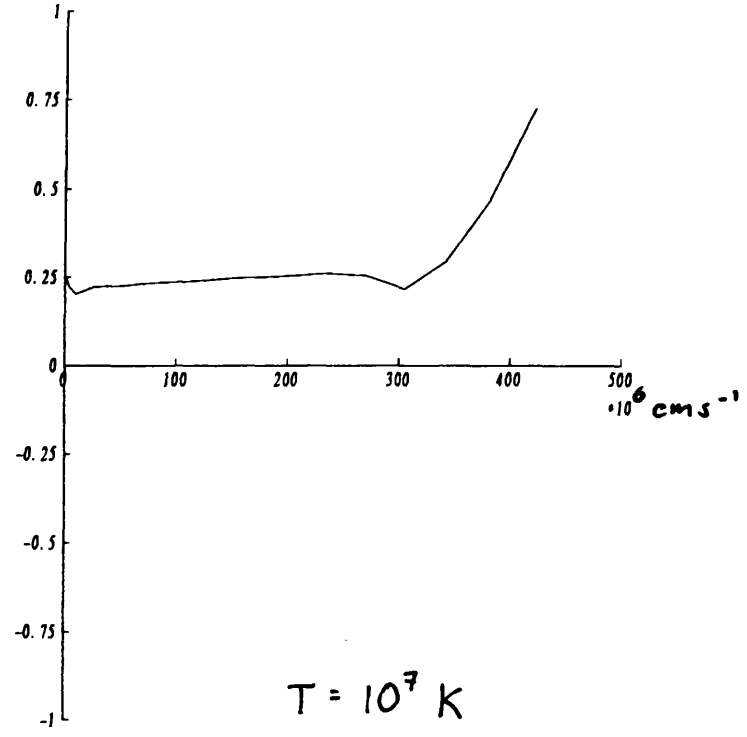

Fig 4.10 Anisotropy factor of flow particles.

Bulk flow velocity = 5×10^7 cm s^{-1}

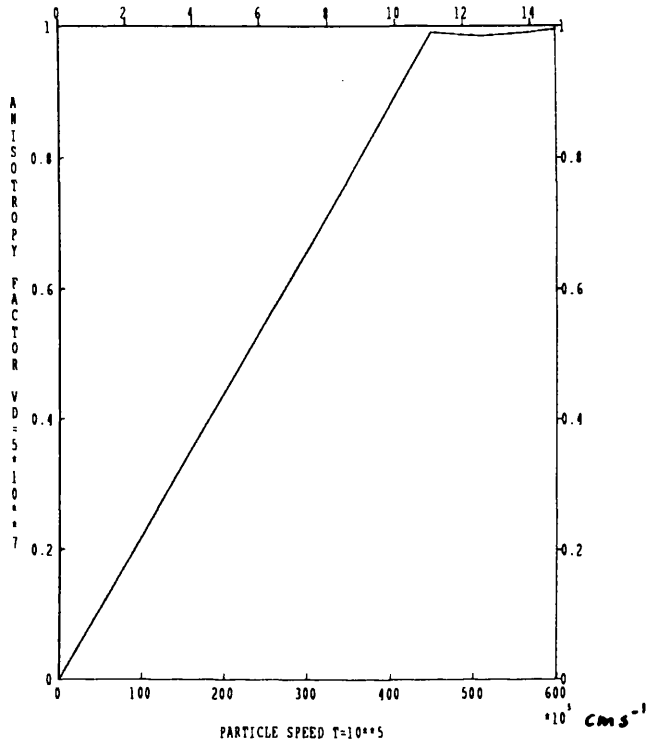

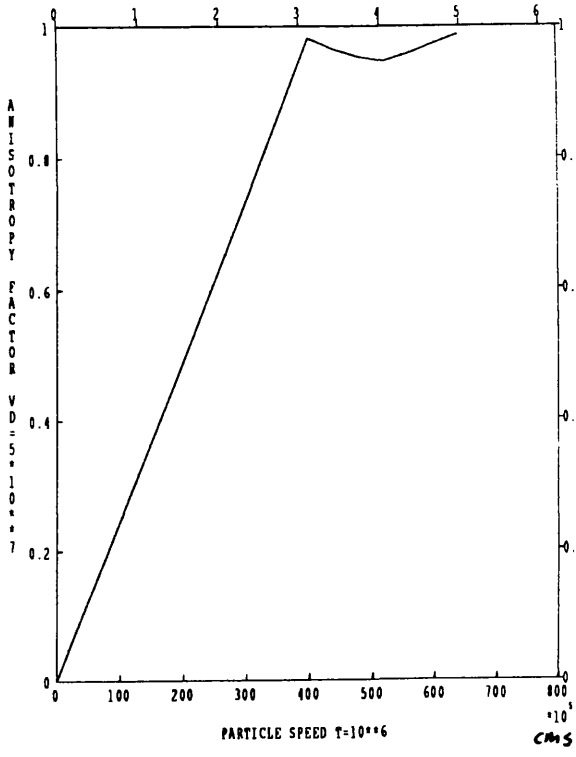

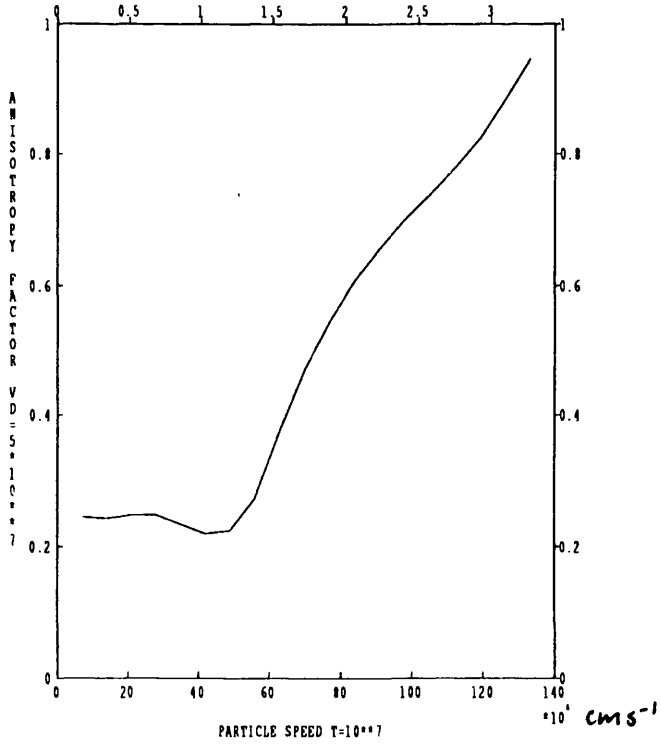

Fig 4.11 Anisotropy factor of flow particles.

Bulk flow velocity = 10^8 cm s^{-1}

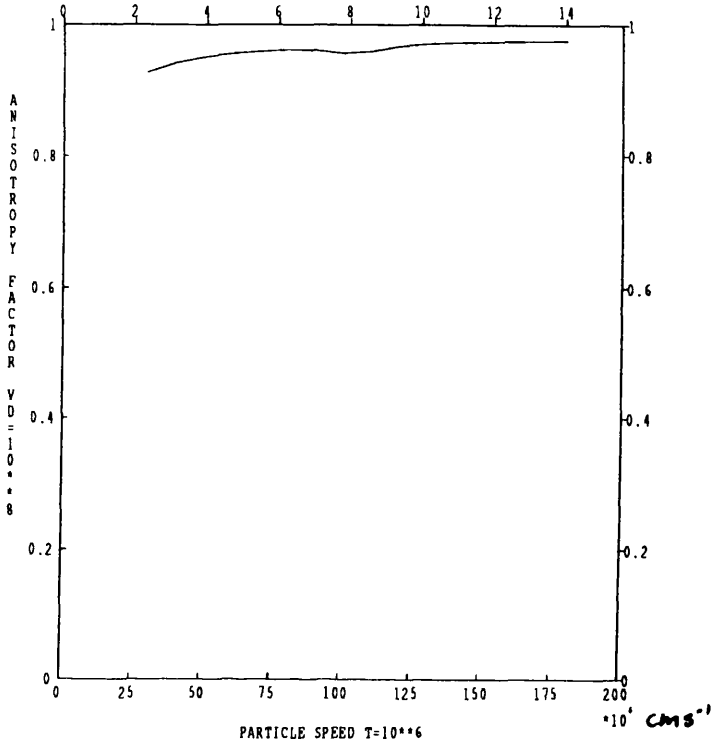

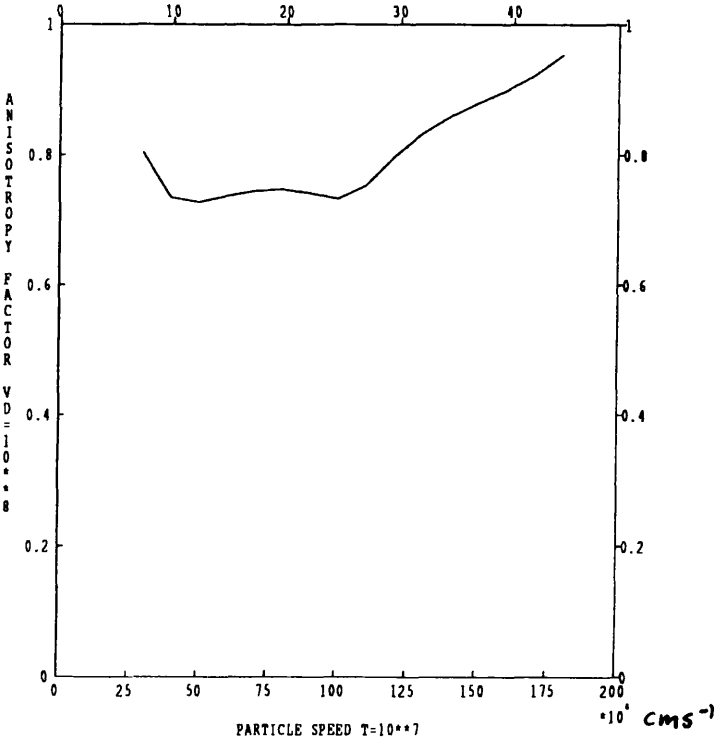

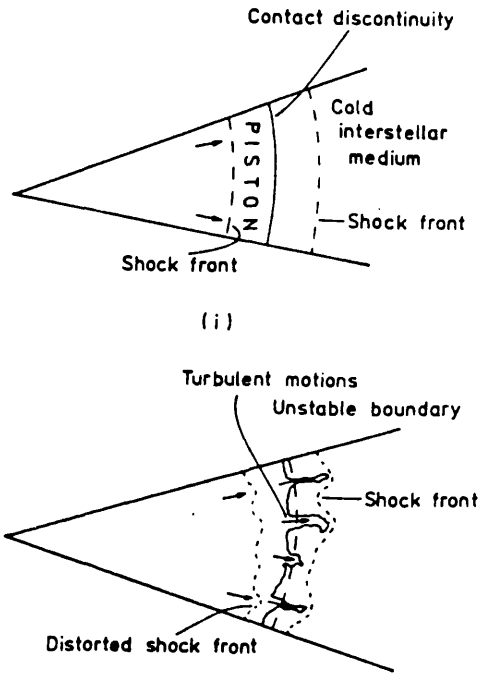

Fig 4.12 Rayleigh-Taylor instability in a supernova remnant.
From Gull (1973)

Fig 4.13(a) Growthtime of a Rayleigh Taylor instability of wavelength 10^7 cm, as a function of transverse field strength.

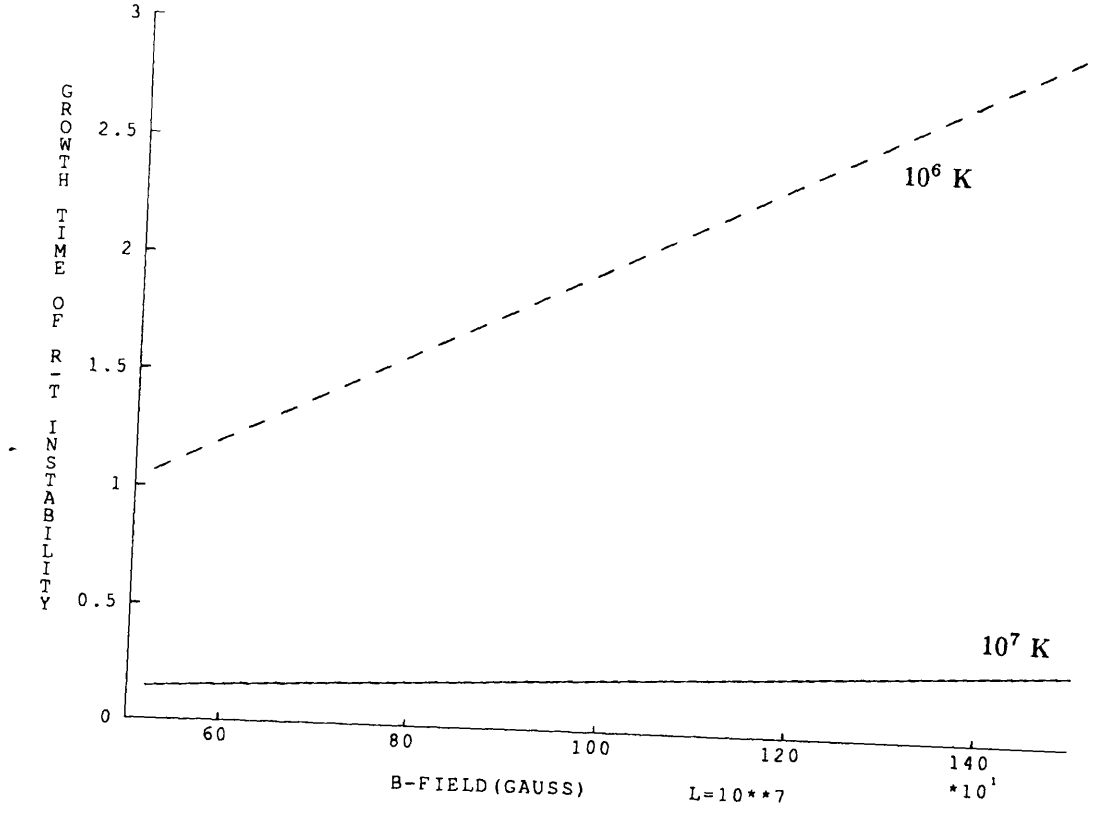

Fig 4.13(b) Growthtime of a Rayleigh-Taylor instability of wavelength 5×10^7 cm, as a function of transverse field strength.

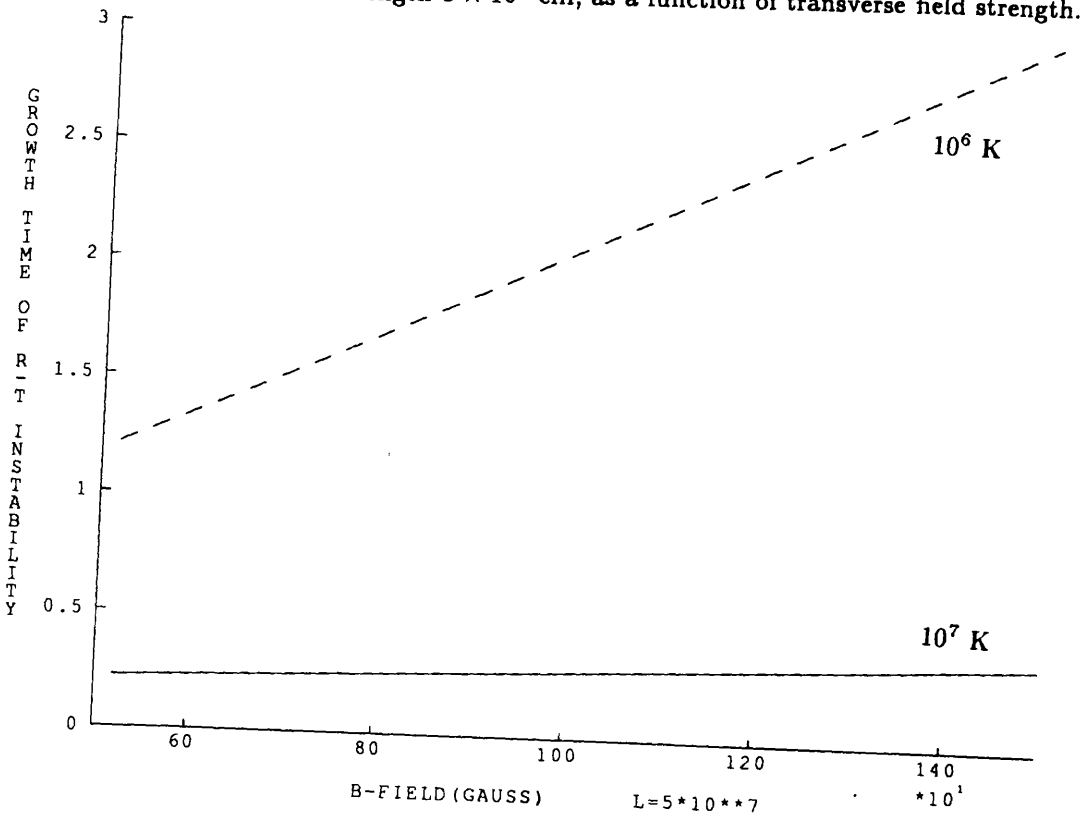

Chapter 5. Line Impact Polarization in other Astrophysical Objects.

§5.1.1 Introduction.

The basic conditions necessary for the excitation of polarized line impact radiation are simple - the motion of an anisotropic distribution of charged particles through a target containing a fraction of a neutral element. In particular, since hydrogen is such an abundant element, we might expect to see Hα impact polarization in a variety of astrophysical objects. An obvious one to consider in the light of the work of previous chapters is flares on stars other than the sun. Dwarf Me type stars exhibit strong emission in the Hα line, and from the rapid changes in their photometric inensities are known to undergo flaring activity, involving large fractions of the stellar surface ($\sim 0.05\%$, De Jager 1986) - far more energetic activity than occurs on the sun - the total flare energy can be up to 10^{37} ergs. DMe stars are known also to have cool, dense, hydrogen-rich atmospheres, and there is speculation that flares on these stars are driven by proton rather than electron beams (Van den Oord 1988), which would make them ideal candidates for impact polarization.

Secondly, compact objects frequently have particle streams or flows associated with them. For example, in AM Her objects - accreting white dwarfs - the presence of 100keV protons in polar accretion streams is inferred from cyclotron observations (Thompson, 1986). Additionally, the environments of pulsars - rotating magnetised neutron stars are rich in structure - streams, flows and winds. The interaction of the pulsar wind with its environment may prove an interesting problem in Hα polarization studies, since such winds are observed to generate Hα signatures in their interaction with their stellar environment, and at present a debate exists about the composition of the wind (protons or electron - positron pairs) which polarization could help to answer.

A further area of investigation is that of particle jets, which are observed to be ejected from many astrophysical objects, for example on galactic scales (radio jets from active galactic nuclei for example) and also on smaller, stellar scales. Matter is observed to be ejected from some central source, usually in diametrically opposite directions. Such particle streams could interact with material surrounding their source, generating impact polarization in the interaction. The observation of impact polarization in distant sources, where geometry is not known, could be particularly useful, since information on both energy and geometry are contained in the resultant emission, although one would have to have some idea about one of these two parameters to be able to pin down the other via impact polarization observations. But, for example, since the polarization has only 2 'states' - parallel or perpendicular to the beam direction - which occurs depends only on whether the beam energy is greater or less than some critical energy - it may be

possible to pin down the system geometry quite unambiguously if other energy diagnostics can tell us roughly what the typical particle energy is. In particular we will consider the use of Hα impact polarization as a potential diagnostic tool in the case of the strange stellar object SS433.

§5.1.2 SS433 - a Stellar Jet System.

SS433, a seemingly unique stellar object, has presented workers with many theoretical and observational puzzles regarding its composition, geometry, power source and means of regulation. It shows emission at all observed wavelengths (with some wavelengths being absorbed by the large quantity of Galactic material lying in the line of sight). At radio wavelengths emission appears to be collimated into two oppositely directed jets. The system is thought to be as depicted in figure 5.1 - a Roche-lobe overflowing star losing matter to a compact object - a black hole or a neutron star - in an accretion disc. In the direction perpendicular to the plane defined by this disk matter is ejected at high velocity. The strongest optical emission is in the Hα line, although at first it was not clear that this was in fact the emission line as all wavelengths were so far Doppler shifted from their rest positions. The shift corresponds to a velocity for the emitting material of 0.26 of the speed of light. This velocity remains constant to within less than 1% over the radiating lifetime of the material which is 1 to 2 days (c.f. e.g. Zwitter*et al*, 1989). It is believed that the jets are actually in the form of discrete blobs or "bullets" emitted by some central source, being somehow ejected at a highly regulated velocity. The means of acceleration is not certain, but whatever it is it must produce these essentially mono-energetic bullets. The source of luminosity of the bullets is also somewhat of a puzzle which has been dealt with by Brown *et al* (1991). The bullets cannot be self-luminous. In the Hα line alone they are extremely bright - an emission rate of $\sim 10^{35}$ ergs s^{-1}. As already mentioned they radiate for 1 to 2 days. If they were composed completely of hydrogen and each hydrogen atom emitted one Hα photon (thus cooling the bullet from Hα emission temperatures) then the observations impose a requirement on the total number of hydrogen atoms of 10^{46} atoms per bullet, which, when emitted once a day and moving with a velocity of 0.26 of the speed of light amounts to a total kinetic energy of 10^{42} ergs per second, which is comparable to the power of a galactic nucleus. Such an unreasonably high energy demand has prompted workers to search for an alternative power source for the Hα luminosity, sustainable over the lifetime of the bullets. In Brown *et al* 1991 various sources of power are investigated and summarised, including heating by radiation from the source of the bullets (although photometry and polarimetry indicates that a sizeable fraction of the bolometric luminosity of the system originates in the stellar companion to the bullet source), conversion of internal fluid motion of the bullet, and extraction of the bullet's kinetic energy via the interaction between the bullet and the dense stellar wind from a companion, whose presence has been demonstrated by analysis of the stationary component of the emission

spectrum. The work of Brown *et al* has isolated this latter mechanism as the most likely source of bullet power, but for a rather narrow range of bullet parameters - i.e., bullet masses $\sim 10^{25}$ g, densities $10^{11} - 10^{12}$ electrons per cc, and for wind mass loss rates of $10^{-6} - 10^{-3}$ solar masses per year. Radiative heating is deemed implausible on energetic grounds, unless the radiation were strongly beamed along the direction of the bullets' motion, and the conversion of bulk internal motions is somewhat limited by the observed narrowness of the Hα lines - a bullet with sufficient turbulent energy to power the observed emission would generate an Hα line with a width in excess of that which is observed.

Despite the small allowable parameter regime in the wind heating model, it is thought to be the most likely candidate. We investigate in the following section a possible test of the model. Spectrometry has revealed than in the vicinity of the bullet source there exists a dense stellar wind, emanating from an unseen companion. Presumably this wind would be in a highly ionised state, as is the solar wind (the outer layers of the sun streaming along the open coronal magnetic field lines). The wind particles when interacting with the bullets do so in a kinetic rather than a bulk fluid manner, since the mean free path of a wind proton as seen in the bullet rest frame is comparable with the dimensions of the bullet itself. Direct proof of such particle - particle interactions would help pin down the heating process. The bullets themselves we assume to be composed predominantly of hydrogen. Brown *et al* in their calculation take the bullets to be completely ionised, with all line emission coming from recombination, but this is not necessarily the case. Line radiation can of course be thermally generated by collisions between neutral hydrogen and ambient electrons. We shall investigate the possibility that radiation emitted by the bullets in their interaction with the stellar wind is polarized by impact excitations, and investigate the polarization as a function of bullet conditions. The range of likely temperatures can be constrained by noting that there is no clear evidence for emission in the He II line, but strong emission in HeI. (Zwitter *et al*) This leads to a value of between 5,000 and 40,000K, although a smaller temperature range is more likely (10,000 to 20,000K) because of the behaviour of the cooling function around this range. At such temperatures we would expect a high proportion of neutral hydrogen atoms to be present, since the hydrogen ionisation energy corresponds to a temperature of $\sim 10^5$ K. The expected sizeable fraction of neutral hydrogen and helium atoms present in the bullets will interact with the stellar wind and as they do there are a number of non-thermal emissions which we might expect as a result of the wind-bullet interaction. Firstly, as mentioned already, as a potential low energy diagnostic in the solar case, the emission of a Doppler - shifted Lyman α photon following charge capture onto a proton is one possibility. However, at relative speeds of 0.26c, we are talking about interaction energies of 34MeV, in which case we are no longer confined to low energy diagnostics. Indeed, energies are sufficiently high that nuclear interactions may

be important - particularly the emission of Gamma ray lines following collisions of high energy protons with various elements present in the bullet. Such lines are observed and used as high energy particle diagnostics in the sun. Thirdly, the the generation of impact excited line emission is a distinct possibility, and since the bullets move through the wind at 0.26 of the speed of light, in the bullet rest frame the wind particles appear to be a highly collimated charged beam, in which case we would expect impact emission to be polarized, providing not only an indication that atom-proton collisions are occurring, but also giving geometrical information on the bullet-wind system.

Of these three potential diagnostics impact polarization is the one most likely to bear fruit. Lyman alpha radiation, lying in the ultra-violet part of the spectrum is greatly extinguished by material lying in the line of sight, which is, unfortunately, the Galactic plane. Gamma ray lines from SS433 are expected to be very weak, and severely broadened by recoil Doppler Broadening (c.f (e.g.) Brown et al 1987). Impact polarization would arise from all neutral species present in the bullet, but since hydrogen is the most abundant element we concentrate on the excitation of the Hα line. Although we have previously studied Hα impact polarization as a low energy proton diagnostic, the cross section for excitation by particle impact however remains at a reasonable size up to the very high energies of the wind particles in the bullet frame (according to the high energy Bethe approximation, c.f. fig 5.4), and the Hα line from SS433 is evidently not extinguished. We describe below the calculation of polarization fraction as a function of bullet parameters.

§5.1.3 The Polarization Calculation

To wind protons with an energy (relative to the particles of the bullet) of some 34MeV, the bullet presents a cold target, since its temperature is estimated to be $\sim 10^4$ K. We do not have a model for the distribution of material throughout the bullet, as we do when dealing with model solar atmospheres, but Brown (1971) showed how the total rate at which a collisional process occurs can be calculated independently of the distribution of material. The wind protons in the frame of the bullet form a unidirectional beam, with impact energy of E_o at the "front" of the bullet. The number of Hα photons from **a single proton** in this beam as it traverses the collisionally thick target which the bullet presents is given by

$$L_{p,H\alpha} = \int_{E_1}^{E_0} \sigma_{H\alpha} dN_H \qquad 5.1$$

where $\sigma_{H\alpha}$ is the Hα excitation cross section, N_H is the total column depth traversed by the wind proton of particles which are in level 1 or 2 (from which they can be collisionally excited to level 3). $\epsilon_{H\alpha}$ is the energy of an Hα photon and E_1 is the Hα excitation energy. This equation can also

be written in terms of the total collisional energy-loss cross section $\sigma_c(E)$:

$$\int_{E_1}^{E_0} \sigma_{H\alpha} dN = \int_{E_1}^{E_0} \frac{\sigma_{H\alpha}}{E\sigma_c(E)x_1 dE} \qquad 5.2$$

x_1 is the fraction of bullet hydrogen in level 1 and 2. This depends on the thermodynamic state of the bullet. $\sigma_c(E)$ is the average cross section over all species in the target - assuming that it is composed entirely of hydrogen in an arbitrary ionisation state. It is given by

$$\sigma_c(E) = \frac{2\pi e^4}{E^2(x\Lambda - (1-x)\Lambda')\left(\frac{m_p}{m_e}\right)} \qquad 5.3$$

where Λ, Λ' are as defined in §2.1.1 Evidently the ratio $\sigma_{H\alpha}\backslash\sigma_c(E)$ is important in this formulation. $\sigma_{H\alpha}$ is a total Hα excitation cross section, which, in this case, is composed of a normalised sum of excitations from level 1 and from level 2 hydrogen atoms. In L.T.E the ratio of level 2 atoms to level 1 atoms is sufficiently small that their contribution to the total level 3 population can be neglected, despite the fact that the excitation cross section for $2 \rightarrow 3$ excitations is approximately 10^2 times higher than the cross section for $1 \rightarrow 3$ excitations. But we will study also a case where the level 2 population is determined by collisional excitation, and is different from its L.T.E. value. We describe later the calculation of this normalised cross section in the non-thermal and thermal cases.

To find the total polarization we must include the polarization fraction $p_{H\alpha}$ in the integral in equation 5.2, and define a fraction $\eta(E_0)$ which has dimensions of polarization fraction, and is given by

$$\eta(E_0) = \int_{E_1}^{E_0} \frac{\sigma_{H\alpha} p_{H\alpha} x_1}{E\sigma_c(E)} dE \qquad 5.4$$

The polarization fraction is, as in the solar case, diluted by any emission from the bullet which is thermally generated. Since we are assuming that the only energy **supply** is from the wind-bullet interaction, the thermally generated emission can be no greater than the kinetic energy of the wind intercepted by the bullet surface. Let the thermally generated luminosity from each wind proton be $L_{th,H\alpha}$, in which case the **maximum** possible number of Hα photons from each proton is $\frac{E_\alpha}{\epsilon_\alpha}$. Using the definition of $\eta(E_0)$ the total polarization fraction if the bullet is optically thin to Hα and if all beam energy is converted to Hα - thermal or non-thermal, is

$$P_{H\alpha} = \frac{\eta(E_o)}{x_1 \int_{E_1}^{E_0} \frac{\sigma_{H\alpha}}{E\sigma_c(E)} dE + \frac{E_\alpha}{\epsilon_\alpha}} \qquad 5.5$$

If f is the fraction of the total wind power that goes into producing Hα emission (via either collisional or thermal excitation) then the polarization fraction can finally be written

$$P_{H\alpha} = \frac{x_1 \eta(E_o)}{x_1 \int_{E_1}^{E_0} \frac{\sigma_{H\alpha}}{E\sigma_c(E)} dE + \frac{E_\alpha}{f\epsilon_\alpha}} \qquad 5.6$$

The average value of the polarization fraction times the excitation cross section apperaring in equation 5.3 is the sum over states of individual substate cross-sections.

$$\sigma_{H\alpha}p_{H\alpha} = \Sigma_n\Sigma_l(f_n\sigma_{n\rightarrow 3l}p_{3l}) \qquad 5.7$$

It can first be split into excitation to the different substates of level 3 - 3s, 3p and 3d. Each of these can be excited from the 1s, the 2s and the 2p states (the excitation cross sections in the Born and Bethe approximations are graphed in figure 5.3). The total cross section must be weighted to take into account the fraction of the total population initially in each state. We are integrating in equation 5.2 with respect to the level 1 column density, and must therefore multiply the $n = 2s$ substate cross sections by the fraction $n_{2s}\backslash n_1$ (and likewise for level 2p) - otherwise we will be overestimating the contribution from level 2. The weighted cross section for excitation to the 3s state, for example, is given by

$$\sigma_{3s} = \frac{n_{1s}\sigma_{1s-3s} + n_{2s}\sigma_{2s-3s} + n_{2p}\sigma_{2p-3s}}{n_{1s}} \qquad 5.8$$

In L.T.E. the level occupation numbers depends on the ratio of the potential difference between the lower and upper states to the material temperature, but this will be modified in a non-L.T.E. situation. Generally, for two discrete states i and j

$$\frac{n_i}{n_j} = \frac{g_i}{g_j}\frac{b_i}{b_j}e^{E_{i,j}\backslash kT} \qquad 5.9$$

which is the Boltzmann occupation relation. g_i, g_j are the degeneracies of states i and i, which for a state with angular momentum quantum number l is $2l + 1$ - therefore the 3d state has degeneracy 5, etc. $E_{i,j}$ is the difference in energy between levels i and j. The quantities b, the departure coefficients, describe the variation of level populations from in non- L.T.E situations - in L.T.E all b's are equal to 1. These factors will be used in later calculations but let us first concentrate on the L.T.E. situation. Using the Boltzmann equation we can write, eg,

$$n_{2s} = n_{1s}e^{-10.2eV\backslash kT} \qquad 5.10$$

Therefore the complete cross section can be written

$$\sigma_{3s} = \sigma_{1s-3s} + e^{-1.2\times10^5\backslash T}\sigma_{2s-3s} + 5e^{-1.2\times10^5\backslash T}\sigma_{2p-3s} \qquad 5.11$$

and likewise for the total 3p and 3d cross sections. The individual cross sections contained in this sum must be calculated at very high interaction energies - 34 MeV. In the case of those upwards transitions which are the reverse of optically allowed downwards transitions the cross section calculated using the Bethe approximation is used (see MacFarlane 1974, and §1.2.5). Other cross sections are calculated in the Born approximation. The polarization fraction appearing in expression 5.4 for η is also calculated in the Bethe approximation, as given in equation 1.15

Finally we also require x_1, the fraction of all hydrogen (ionised plus neutral) in level 1. The Saha - Boltzmann equation (equation 4.3) takes us near to this.

$$\frac{n_{nl}}{n_p n_e} = (2l+1)\left(\frac{2\pi m_e kT}{h^2}\right)^{-\frac{3}{2}} e^{\chi\backslash kT}$$

We require $(n_{1s}+n_2)\backslash(n_p+n_{1s}+n_2+...)$. As mentioned before there are problems at certain temperatures in making the sum on the denominator of this expression converge so instead we can say that

$$x_1 < n_{1s}\backslash(n_p+n_{1s}+n_2) = \left(\frac{n_p}{n_{1s}}+\frac{n_{1s}+n_2}{n_{1s}}\right)^{-1}$$

now

$$\frac{n_p}{n_{1s}} = \frac{1}{n_e}\left(\frac{2\pi m_e kT}{h^2}\right)^{\frac{3}{2}} e^{-\chi\backslash kT} > \frac{1}{n_{bullet}}\left(\frac{2\pi m_e kT}{h^2}\right)^{\frac{3}{2}} e^{-\chi\backslash kT}$$

since $n_e < n_{bullet}$. Therefore

$$x_1 < \left(\frac{n_p}{n_{1s}}+\frac{n_1 s+n_2}{n_1}\right)^{-1} < \left[\frac{1}{n_{bullet}}\left(\frac{2\pi m_e kT}{h^2}\right)^{\frac{3}{2}} e^{-\chi\backslash kT}+\frac{n_1 s+n_2}{n_1}\right]^{-1} \qquad 5.12$$

So x_1 so it now has a definite upper bound and can be used in equation 5.6.

§5.1.4 A Non-L.T.E. Bullet

Let us now consider now the case where the bullet is not in L.T.E, but level populations are determined chiefly by a small number of transitional processes. Krolik and McKee (1978) in a paper on quasar emission line spectra, give expressions for population ratios under a variety of material conditions. The major distinction made is between excitation by a radiation field and excitation by particle collisions. We will look at the case where upwards excitations are due to collisions with thermal electrons rather than by photo - excitation, since in this wind - heating model we do not expect a large radiation field. In addition, the collisional excitation model is appropriate for a dense medium, which the bullet material is. Downwards transitions are due to radiative recombination and spontaneous de-excitation. Note however that the equilibrium is not determined by the properties of the wind except indirectly, through the amount of heating it delivers and hence the temperature of the bullet. The fact that we use the collisional expression means only that we expect the radiation field to be a small perturbation to the level populations whereas the collisions of thermal particles (irrespective of how they got their energy) has a large effect. So particle collisions excite level 2, which is also populated by recombination and downwards transitions. The emission of a Lyman α photon depopulates level 2. The population of level 1 is also changed by the dominance of collision - induced transitions, and in this regime is given by

$$\frac{N_{1s}}{N_p} = 557 T_4^{-1.4} exp(15.78(T_4^{-1}-1)) \qquad 5.13$$

T_4 is the temperature of the material in units of 10^4K. The other factor of interest is the ratio $N_2\backslash N_p$ which Krolik and McKee give as

$$\frac{N_2}{N_p} = \frac{5.5 \times 10^{-22} T_4^{-0.8} N_{e,8}}{\epsilon(\tau_{Ly\alpha})} \qquad 5.14$$

$n_{e,8}$ is the electron number density in units of 10^8. $\epsilon(\tau_{Ly\alpha})$ is the escape probability for a Lyα photon and depends on the geometry of the object. Osterbrock (1965) gives the form of the function for a spherical structure.

$$\epsilon(\tau) = (\pi^{\frac{1}{2}}\tau)^{-1}[(ln\tau)^{\frac{1}{2}} + 0.25(ln\tau)^{-\frac{1}{2}} + 0.14] \qquad 5.15$$

τ of course being the optical depth of the bullet material. It is thought that the spectrum of the entire SS433 system peaks in the UV region (Zwitter et al, 1989) but the detailed line structure will probably never be observed. We cannot know for certain whether the bullets are optically thin or thick, however, if we assume that the optical absorption cross section is the line centre absorption cross section as defined in §2.1.5 we can estimate the optical depth. The line centre absorption cross section a_0 for Lyman α works out as

$$a_0 = \frac{4.41 \times 10^{-18}}{T^{1\backslash 2}}$$

where D is the linear dimension of the bullet. This can be estimated. Brown *et al* (1991) quote reasonable bullet masses of 10^{24}g. We will assume, for ease of calculation, that the bullets are spherical, although the observations cannot actually distinguish between spherical structures which emit for about 1 day, or structures elongated to "a day long" along the projection of their axes of travel (Brown et al 1991). So if the typical bullet density is $10^{11} - 10^{12}$, the typical dimension is $1.12 \times 10^{12} - 5.23 \times 10^{12}$ cm. The total optical depth τ of the bullet is then simply given by

$$\tau = \frac{4.41 \times 10^{-18} n_1 D}{T^{1\backslash 2}} \qquad 5.16$$

n_1 is the number density of hydrogen in level 1 which depends of course on the bullet temperature. We cannot get this explicitly but can calculate a limit to it. If we say that the bullet is a pure hydrogen bullet then $n_{bullet} = 10^{11-12} > n_{1s} + n_p$. Therefore

$$n_{1s}\left(1 + \frac{n_p}{n_{1s}}\right) \ll 10^{11-12}$$

$$n_{1s} \ll \frac{10^{11-12}}{\left(1 + \frac{N_p}{N_{1s}}\right)} \qquad 5.17$$

which is calculated as a function of temperature. Figure 5.3 shows the Lyman α line centre optical depth as a function of temperature for bullet densities of 10^{11} and 10^{12} particles cm^{-1}, and

it is evident that with these parameters, and within the temperature range that we study (2,000 to 20,000K) the bullets are completely optically thick to Lyman α radiation, although they are becoming optically thinner as the temperature increases. But it is possible that this is not the correct source of Lyman α opacity and that the bullets are not completely optically thick to the radiation, therefore we shall also present results for Lyman α optically thin radiation.

From the above expressions we calculate x_1 and the ratio of level 2 to level 1 hydrogen, the final form for which, under conditions of collisional excitation, with the level 2 population determined by equilibrium between recombination and Lyman α emission, is

$$\frac{n_2}{n_{1s}} \sim \frac{5.5 \times 10^{-24} n_e T_4^{\frac{1}{2}}}{\epsilon(\tau) exp(15.78(T_4 - 1))} \qquad 5.18$$

Note that there is no distinction between 2s and 2p states, but if we assume that the ratio of these states is given by the ratio of the state degeneracies then we may again define an average cross section for excitation from both states.

The expressions for x_1 and $n_2 \backslash n_1 + n_2$ can now be inserted in expressions 5.11 and 5.6. Figures 5.4 shows the total Hα excitation cross section - that is the weighted sum of the substate cross sections where the weighting factors are appropriate to the physical conditions in the bullet, and the collisional energy loss cross section. We see that the energy loss cross section (lower line - n.b. for the sake of the appearence of this diagram we have actually plotted 10 times the energy loss cross section) is smaller than the excitation cross section over the range 500 to 30,000 keV although at some lower energy - probably a few keV - it will become larger. This cross section will actually change slightly with bullet temperature and conditions via the Coulomb logarithm, but here we have plotted the largest value it will take, which is for a completely ionised bullet. The various plots made are for the extremes of the range of bullet optical depth which we study - 10^{-1} and 100, with a bullet density of 10^{11} cm^{-1}. Figures 5.4a and 5.4b show the situation at low temperatures (2,000K). The upper line is in fact the two lines corresponding to the L.T.E. and non-L.T.E. conditions superposed. Numerically there is a small difference between these data but it is less than one part in ten million. Figures 5.4c and d show the same three lines for a temperature of 20,000K, and here we see that the ratio of level 2 to level 1 atoms has increased significantly and that the contribution of the 2 to 3 excitations is important in the non - L.T.E. situation. At increased optical depth the discrepancy between the results of the two models increases slightly, but once again this is only apparent in numerical results, in the 6th or 7th decimal place. We do not expect therefore that changing the optical depth of the bullet will affect the resultant polarization. We do however expect that the polarization from a non-L.T.E. bullet at high temperature will be greater than that from a bullet in L.T.E. but the difference will be small at low temperatures.

There is no variation of total cross section with bullet density. The total cross section depends amongst other things on the ratio of the various populations and this will not change as the density changes. But since in the L.T.E. case we have had to use an upper limit for the fraction of level 1 hydrogen rather than an absolute value, raising the bullet density will increase the upper limit, since the bullet density is a factor in the calculation of the limiting fraction.

§5.1.5 Results and Discussion

We calculate now the polarization fraction using equation 5.6. The integrations are done using NAg routine D01AJF - this is possible since we now have complete analytic forms for all the cross sections and polarization fractions. The results as a function of temperature appear in figures 5.5a and b, and here it is quite evident what effect the non L.T.E. distribution of states has. The lower lines are the L.T.E results - at a temperature of around 10^4 K the magnitude of the polarization fraction has decreased almost to zero as the hydrogen in the bullet becomes almost completely ionised. The lower of the two curves is the upper limit to the polarization magnitude if we have a bullet density of 10^{11} cm^{-3}, and the upper of these two curves corresponds to a density of 10^{12} cm^{-3}. The change in the polarization limit does not indicate any real change in physical processes occuring in the bullet - it just comes about because of the approximation we must make. From this graph we can say that if a wind-heated bullet is in L.T.E. with a temperature between 0 and 10^4 K, then it will emit polarization at a level of $\sim$ 10% (when the jets are seen side on, at 90° to the bullet direction of travel). Between temperatures of 8×10^3 and 1.2×10^4 K the polarization level drops from 15% to around 0.1%

The non-L.T.E. situation is quite different, and this is the uppermost of the three curves in figure 5.5a. The balance between recombination and collisional excitation leads to the population of level 1 and level 2 having a significantly higher than L.T.E. value. Therefore the polarization magnitude does not decrease nearly so rapidly - although it does do so slightly - and at the maximum temperature on the plot it still has a value of over 14 %. Figure 5.5b is an expanded section of figure 5.5a showing the beginning of this decrease and what looks like a single line is actually a superposition of results from calculations of the polarization with bullet optical depths ranging between 0.01 and 100 - there is no visible difference. So a wind - heated bullet in which the equilibrium within levels is between thermal collisions upwards and radiative recombination downwards will emit at a level of $\sim$ 15% over a temperature range of 0 to 2×10^4 K when seen at 90° to the bullet direction of travel.

Recall that the denominator in equation 5.6 has a term f multiplying the thermal excitation term.

Without doing any explicit calculations we can see that the effect of decreasing f - i.e. decreasing the fraction of the total wind energy (in the bullet rest frame) converted to thermal Hα - is to increase the polarization visible from the bullet. If the bullet is not optically thick to Hα then f can decrease considerably - indeed, in an L.T.E. gas between 2,500 and 20,000K the ratio of energy emitted in Lyman α to Hα is 20:1, therefore the magnitude of the polarization fraction would be substantially increased. It can never of course exceed the value given by $p_{H\alpha}$ in equation 5.4, which is $\sim$ 30%.

The polarization fractions calculated above are for bullets when viewed at 90° to their direction of travel and will be reduced somewhat since the SS433 system is not exactly "sideways on" to us. In addition, polarization, if observed, should track the motion of SS433 which precesses through an angle of 20° over a period of 164 days. This should also be the period of the variation in polarization fraction. We have only spoken so far about the magnitude of the polarization fraction but the direction is important too. We see that the polarization fractions are all negative, which means, given that the proton energies involved are 34 MeV, that the direction of the vector on the sky is perpendicular to the plane defined by the jet direction and the observer's line of sight. This along with the maximum value of the polarization magnitude obtained from the source should allow unambiguous determination of the geometry of the system at any time. Note that since we are dealing with a stellar object at considerable distance we must consider the effects of interstellar polarization or depolarization as Hα light from the source traverses the galaxy. Fortunately there is a way to estimate the effect of this. The central source on SS433 also emits in the Hα line, although not so strongly as the bullets, and we would expect that it will be intrinsically unpolarized or very slightly polarized in the broad band (Brown *et al*, (1987)). The component from the central source will not be shifted significantly from its rest wavelength and the components from the the bullets will be shifted in wavelength at either side of it. Any polarization appearing in the central Hα line, from the central source, will tell us about the interstellar polarization, allowing corrections to be made to polarization appearing in the shifted lines.

In conclusion we state that if the bullets of SS433 are heated by their kinetic interactions with a stellar wind we expect that they will emit polarized radiation at a level of around 15% although this fraction will be decreased by geometric and interstellar polarization effects. However it should be possible to correct for the effect of interstellar material and source geometry.

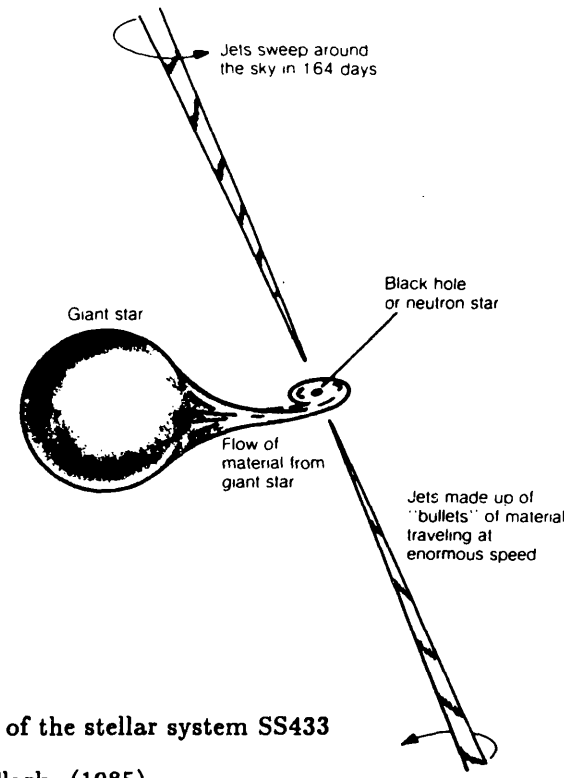

Fig 5.1 Visualisation of the stellar system SS433

From Clark (1985)

Fig 5.2 Bullet optical depth as a function of bullet temperature.

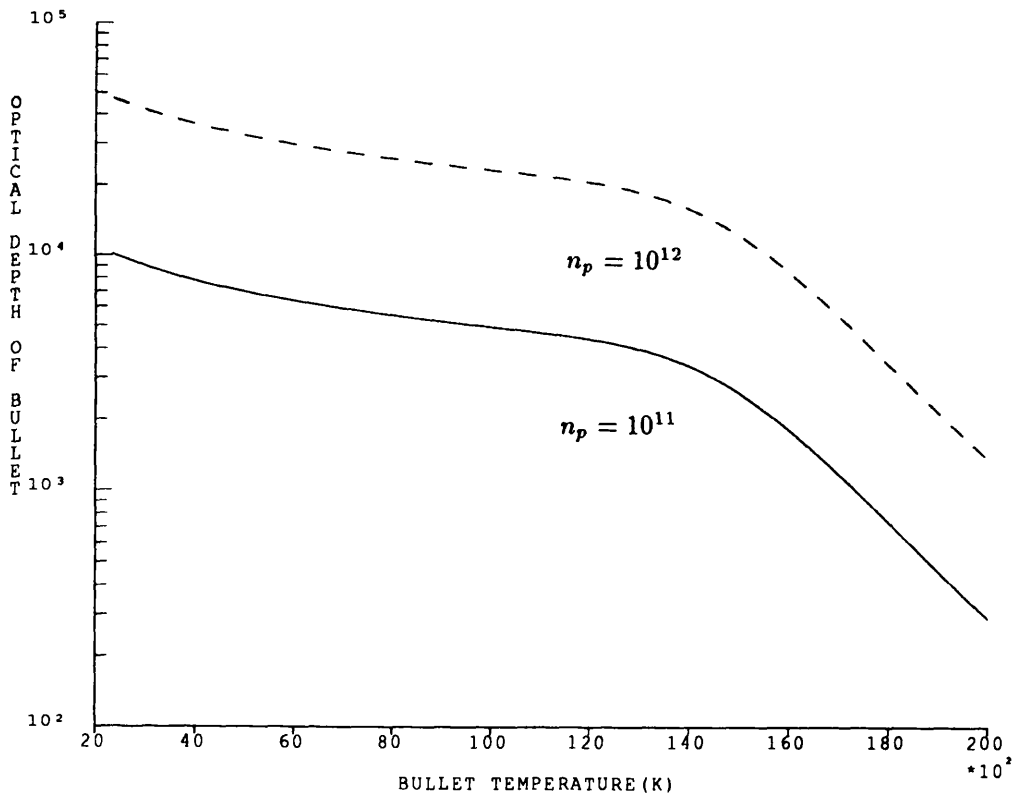

Fig 5.3 Level 3 hydrogen excitation cross section (high energy approximations)

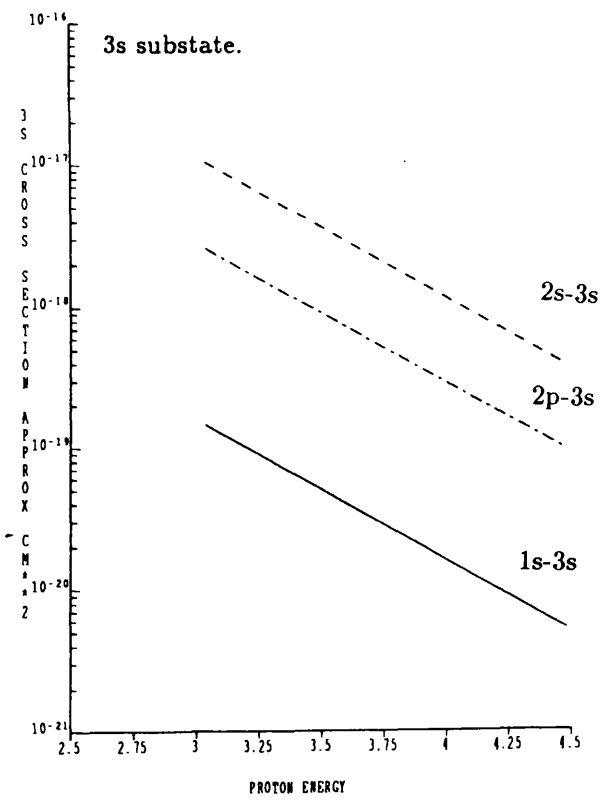

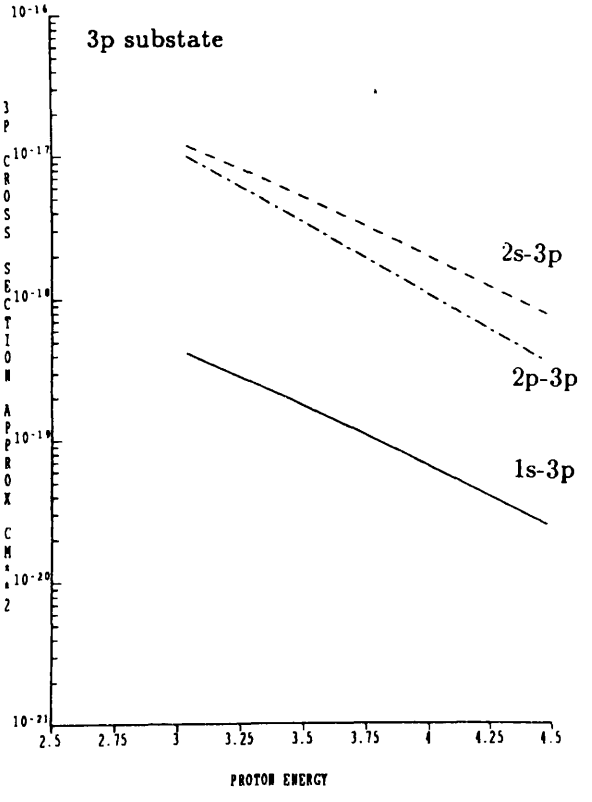

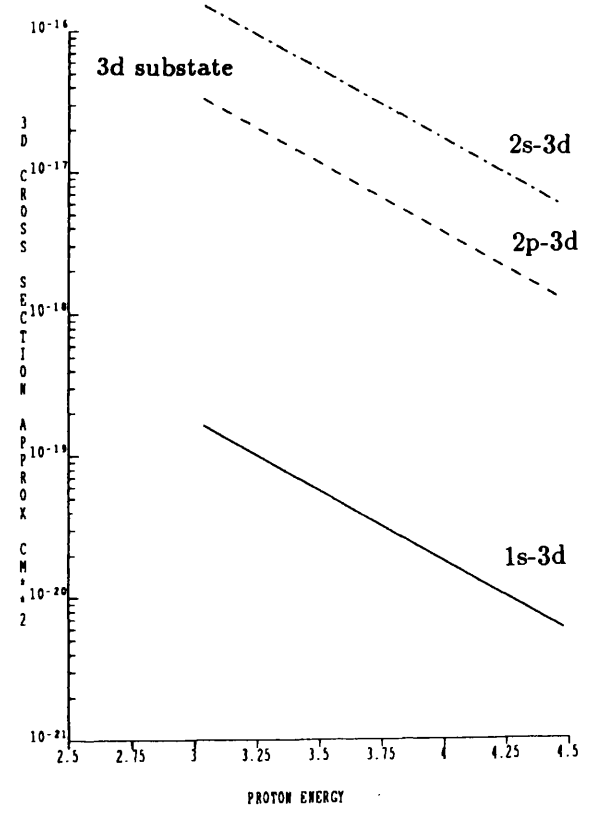

Fig 5.4 Total Hα excitation cross section (full line)
and 10× collisional energy loss cross section (dashed line).

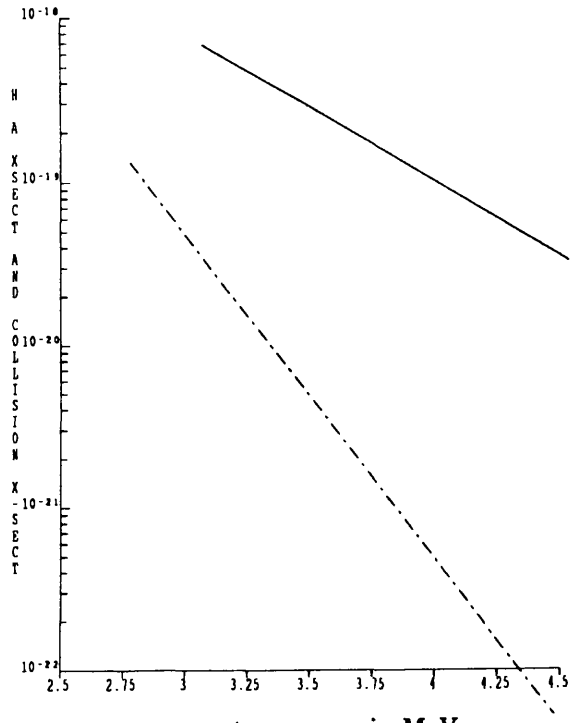

(a) optical depth = 0.01, T = 2,000 K

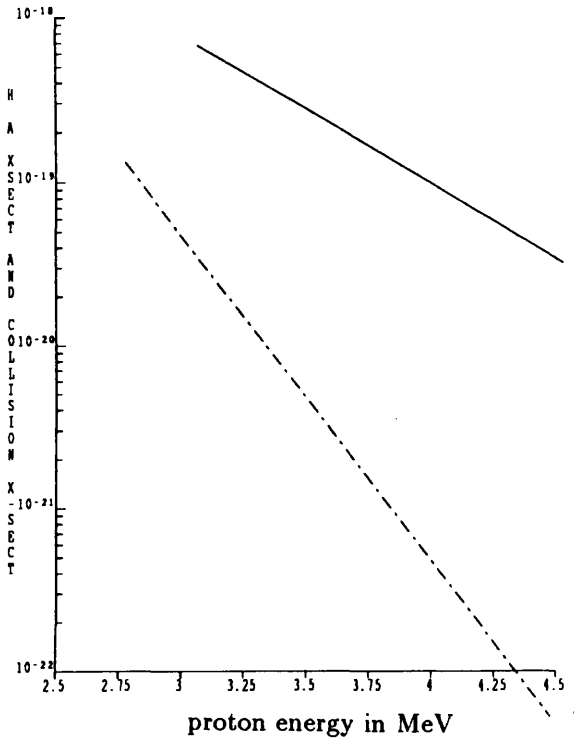

(b) optical depth = 100, T = 2,000

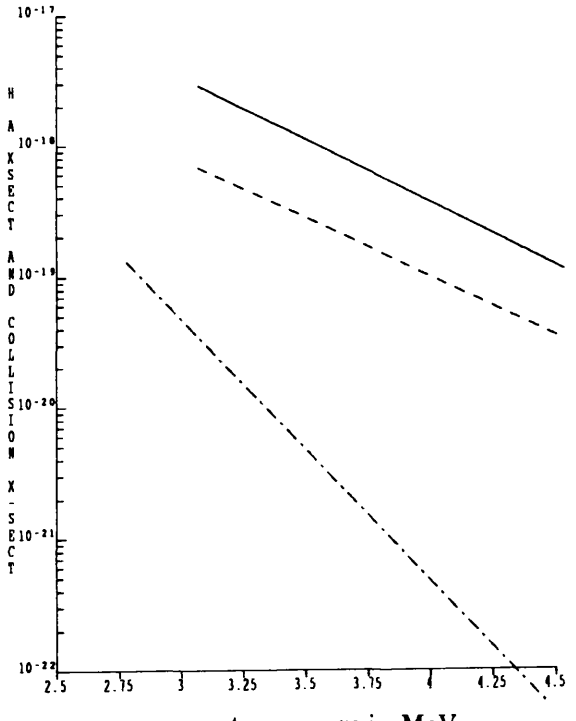

(c) optical depth = 0.01, T = 20,000

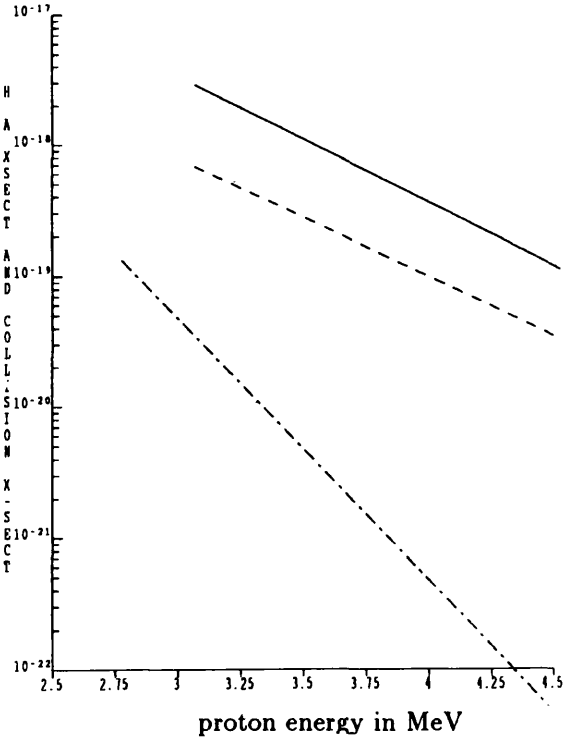

(d) optical depth = 100, T = 20,000

Fig 5.5 Net polarization fraction as a function of bullet temperature.

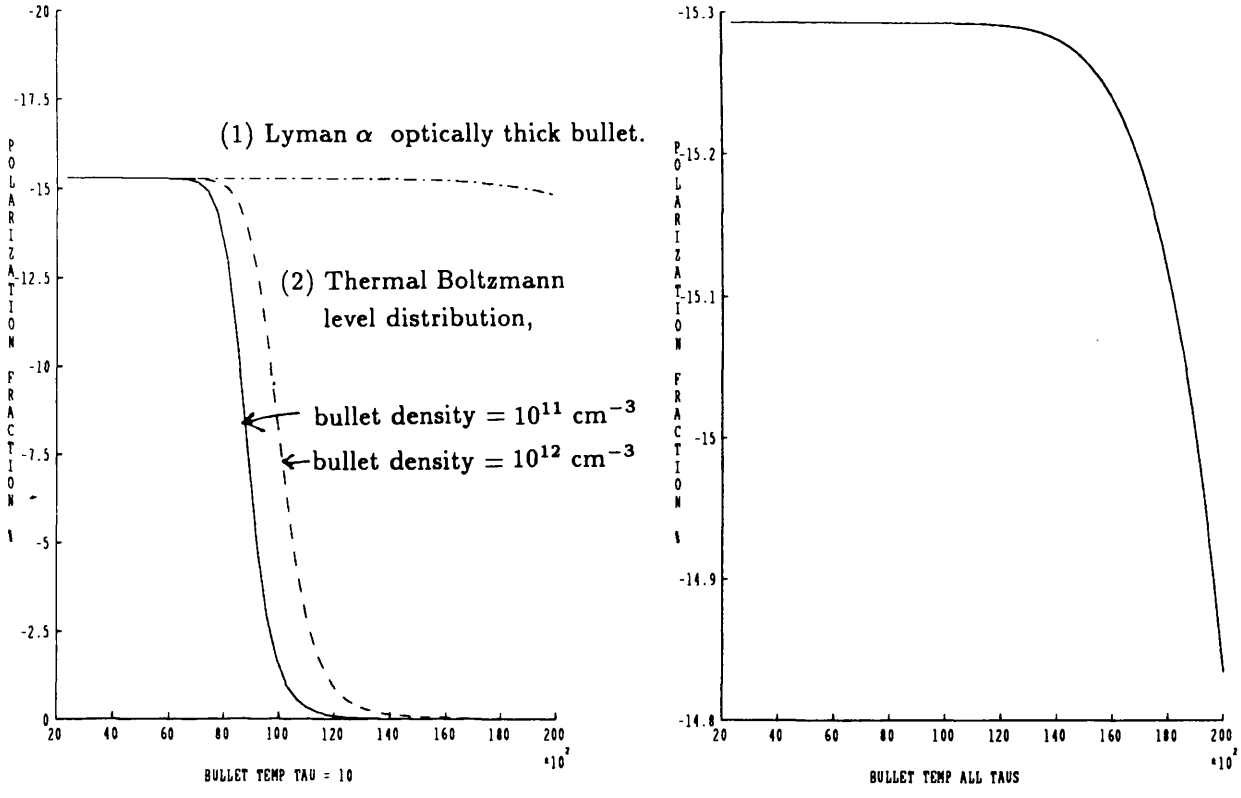

Chapter 6 Conclusions and Future Work.

In this final short chapter we will summarize the findings of this thesis, point out the areas in which problems still remain and consider some ways in which the work of the thesis may be extended and improved. We discuss first the shortcomings of the work already carried out before going on to suggest additional ways in which impact polarization may be useful in the solar and in the broader astrophysical context.

The Results of the Solar Work

The problem posed at the beginning of the thesis was to find a reasonable explanation for observations of polarization observed during certain solar flares, having a large duration and area. We investigated three principal types of model - the proton beam-driven flare, the mirroring electron model and the evaporation driven model. When tested under conditions representative of a flaring solar chromosphere (as described by the model atmospheres of Machado *et al* (1983)) all of the models have their shortcomings but to different extents. The first of the three, the proton beam - driven model, has been proposed by various authors (see Chapter 2) as a likely flare model, with certain advantages over an electron beam, and has been previously studied as a source for impact polarization, with favourable results. We show in Chapter 2 that although proton beams can indeed cause impact polarization for not unreasonable beam energy fluxes, the duration and the area of the observations place at best very strenous, and at worst totally unreasonable demands on the energy source for the flare. The principal reason for the difference between the conclusion at which we arrive and that reached by previous authors, is that previous authors treated the part of the flaring chromosphere in which impact polarization is principally generated as an isothermal medium with a temperature of 9×10^3K, whereas the model atmosphere which we use (also used by the previous authors) peaks in Hα emission at a temperature of $\sim 1.8 \times 10^4$K. Although this is not an enormous difference, the effect on the total Hα intensity is quite significant, increasing it by at least an order of magnitude. This increase in thermal radiation demands a significant increase in the beam-driven radiation to achieve the observed net polarization fraction and hence the beam-driven power over previous estimates. Primarily on this ground, but also on the basis that we do not expect the impact of beams from the corona, normally associated with the flare impulsive phase to occur over time - and area - scales as large as those seen in some polarization observations we have ruled out the proton beam as a likely candidate for impact polarized Hα generation in the case of these large polarized flares. Polarization in smaller flares might nonetheless still be explained by this model. We recognise however that since the basic requirement, namely that the impact generated polarized radiation be sufficiently intense to be visible over the ambient radi-

ation, is very dependent on the atmospheric model, it will really be necessary to test this scenario with a variety of atmospheric models, since it is possible that the range of parameters already tried is not sufficient. But since the proton beam precipitation is part of the atmospheric heating process the atmosphere must be heated to above the quiet sun atmospheric temperatures, so we suspect that for any reasonable atmosphere tried, the problem of competing with high thermal emission will remain.

The same must be said of the calculations of the other two models - energy requirements are always based in part on the competition between thermal and non-thermal emission, which depends on the atmospheric structure, but the other two models tested do have certain advantages over the proton beam model in that they agree with the time or area scales of the observations, or, with certain additional assumptions, with both. The trapped electron model investigated in chapter 3, in which electrons orbiting in a converging coronal field produce polarization upon arriving in the chromosphere with a distribution peaked in the local horizontal, can be incorporated into the coronal trap model of solar flares. From observations it appears that an electron population can be maintained in a converging coronal loop for reasonably long periods (at least a few minutes), with atmospheric flare signatures being a result of a proportion of the population which has leaked through the neck of the magnetic bottle. With this trapping model we find that if we inject the electron population into the magnetic bottle at a large pitch angle (greater than 75° or thereabouts) then for the limited range of field parameters which we have studied, we get a few percent polarization with an energy budget well within that of a small or medium sized flare. It can also explain the presence of polarization in flares both with and without accompanying hard X-ray signatures. The large area of the polarization observations still does not fall out naturally from this model, as standard ideas of energy injection suggest injection areas of one or two orders of magnitude smaller than is observed. But there is no fundamental objection on the grounds of energy to this model, as there is with the proton beam model, and it is overall a successful one.

The final model studied was the evaporating chromosphere. Here polarization is generated in the region in which a fragmented ionised flow and a surrounding, partially neutral and static atmosphere interact. We find here that using currently available atomic data the polarization resulting from the interaction is smaller than that observed but of the same order of magnitude, and is energetically possible. Also, as part of the slow response of the flare chromosphere to the rapid input of beam-energy, it may be possible to explain the area scales, and it is certainly possible to explain the time scales over which the polarization is observed. These calculations are once again model dependent and should be repeated with a number of different models. However, since the evaporation process, especially the slow evaporative flows which we use, are part of the

atmospheric cooling response, we do not only have the option of testing other high temperature atmospheres as in beam impact cases - cooler atmospheres may instead be more valid in this phase of the flare. A lower temperature atmosphere would mean of course that the energy condition (the necessary energy contained in the evaporating material) would become less stringent.

Although there have been certain qualified successes with the models tested so far, there remain aspects of the observations as yet not touched upon, and deficiencies on the treatments of which we are very aware. The aim of the thesis, and of all previous work, was to explain the presence of a polarization with a *mean* polarization level of 2.0% over an area of $\sim 2 \times 10^{19}$ cm^2. However it is very evident that although this is indeed the mean fraction, the variation in magnitude and direction at a given time, from pixel to pixel is large - see figure 1.1, and the variation with time of the number of pixels with polarization greater than a certain threshold level is also very great - over a period of 2 minutes the fraction can change from 0.1 to more than 0.4, and this change proceeds in a quasi-periodic manner. It is not at all the case that emission is steady, but for the first treatment of the problem - the calculation of energies an particle populations involved, it was adequate to average the polarization fraction and area. A satisfactory model of the process must of course include an explanation of the above-mentioned variations, and must also attempt to take into account various processes which we suspect will be important in the chromosphere but have as yet been ignored.

The most evident shortcoming of all the solar work carried out is that we have not included the effects of the transfer of polarized radiation through the solar atmosphere. We have attempted to account for the absorption of Hα photons by ambient level two hydrogen atoms, but have not dealt with the re-emission of Hα photons from these atoms, and the redistribution effect that results from the absorption and re-emission process. This whole process is known as resonance line scattering. Neither have we looked at the interaction of photons with atmospheric electrons, or Thomson scattering, which, as well as having an effect on the polarization of polarized photons, may, if there is some anisotropy in the distribution of the scattering electrons, cause initially unpolarized photons to emerge polarized from a scattering interaction. This is well studied in the theory of polarized Be stars, where anisotropies in the shapes and velocity fields of the stellar envelopes result in thermal radiation from the stellar surface emerging polarized. In his classic text on Radiative Transfer, Chandrasekhar summarises both resonance and scattering line polarization, and we quote directly his results. Below we present possible approaches to the transfer problems.

The Transfer of Polarized Radiation in the Solar Atmosphere - a Possible Approach.

We look first at the simpler of the two problems, scattering polarization, discussing first how it relates to the solar case and stating the relevant equations and their method of solution. Scattering of radiation from free electrons, or Thomson scattering, will certainly happen in the solar corona where material is very highly ionised, although relatively rarified - number densities of $\sim 10^{10}$ electrons cm^{-3}. But in the lower atmosphere also, even though it is not completely ionised, the electron density is significant - higher than the coronal electron density in fact - more like $10^{11}-10^{12}$ electrons cm^{-3}, and Hα photons from the low chromosphere will be scattered as they traverse this region. There is, as shown in figure 2.4, very little thermal Hα generation above 1.43×10^8 cm, nor is there a great deal of polarized non - thermal generation, on account of the reduction in the neutral hydrogen population above this point. The optical depth of the atmosphere (for absorption by level 2 hydrogens) also drops dramatically at this point, so it should be possible to consider the atmosphere are having a 'surface' at 1.43×10^8 cm, below which the vast majority of Hα radiation is produced and above which it is scattered in an electron rich - atmosphere (see schematic diagram 6.1). (n.b. This part of the treatment will not consider *at all* the processes occurring in the material below the surface in which resonance line scattering is occurring. Let the atmosphere be plane parallel, and let the distribution of electrons in the atmosphere be free from anisotropies (note that this will probably not be the case since the presence of a magnetic field orients the electrons along a preferential direction -see later. However an isotropic atmosphere will have the greatest depolarizing effect.) Let there in addition be no absorption or generation of Hα photons in the scattering region - a "pure scattering" treatment. Chandrasekhar gives the following expression for the transfer of radiation.

$$\mu\frac{d}{dt}\begin{pmatrix} I_l(\tau,\mu) \\ I_r(\tau,\mu) \end{pmatrix} = \begin{pmatrix} I_l(\tau,\mu) \\ I_r(\tau,\mu) \end{pmatrix} - \frac{3}{8}\int_{-1}^{1} \begin{pmatrix} 2(1-\mu^2)(1-\mu'2)+\mu^2\mu'^2 & \mu^2 \\ \mu'^2 & 1 \end{pmatrix} \begin{pmatrix} I_l(\tau,\mu') \\ I_r(\tau,\mu') \end{pmatrix} d\mu' \qquad 6.1$$

The variables I_r and I_l are the same as $I_\parallel$ and $I_\perp$ which were used in §1.2.2. So the Stokes' parameters I and Q with which we are accustomed to dealing, are given by

$$I = \frac{1}{2}(I_r + I_l) \qquad 6.2$$
$$Q = \frac{1}{2}(I_R - I_l)$$

The scattering optical depth in direction μ is τ, and in this treatment we must use the optical depth in the line of sight. In the previous chapters above the optical cut-off at $\tau_{H\alpha} = 1$ the atmosphere has been considered optically thin and this geometrical factor has not been important. μ is the cosine of the angle between the atmospheric normal and the line of sight, which depends on the flare position on the solar disc. Note that to calculate $I_l(\tau,\mu)$ and $I_r(\tau,\mu)$ we integrate over

all μ' at the source, corresponding to the redistribution of photons from all directions by scattering electrons. τ, the scattering optical depth, as calculated as before from the scattering cross section and the number density of scatterers in the atmosphere,viz

$$\tau = \int_S N_e(S')\sigma_T dS' \qquad 6.3$$

S is the total line of sight distance over which absorption takes place, and σ_T is the Thomson scattering cross section, given by

$$\sigma_T = \frac{8\pi e^4}{3m_e^2c^4} \qquad 6.4$$

which has a numerical value of 6.65×10^{-25} cm^2 We estimate the importance of free electron scattering by assuming an electron number density of 5×10^{11} cm^{-3} for the chromosphere, which has an extent of 3×10^8 cm above the layer where the Hα is generated, giving a column density of 1.5×10^20 cm^2. The coronal column mass is 3.14×10^{-4}, which is completely ionised, corresponding to a total electron column density of 2×10^20 cm^2. Therefore the total scattering optical depth is 2.3×10^{-24}, so we are probably only dealing with single scattering - i.e., the atmosphere is sufficiently optically thin that each photon is scattered once only. In addition, scattering of electrons from atoms occurs - this is called Rayleigh scattering, and the cross section fro this process is

$$\sigma_R = \frac{128\pi^4}{3\lambda^4\alpha^2} \qquad 6.5$$

α being the polarizability of the scattering atom. From Allen (1955) α is 6.6×10^{-25} cm^2. The value of σ_R for the scattering of Hα photons by hydrogen atoms is 3.16×10^{-25} cm^2 which, since the hydrogen number density is no higher than the electron number density, may be neglected in comparison to Thomson scattering. Of course we should have to use the actual density variation of the atmosphere, taking into account line - of - sight effects when calculating τ properly, but the values calculated above will give a general idea of the magnitude of the scattering effects. Equation 6.1 is an integro – differential equation, which must be solved numerically. The boundary condition that we impose is that at $\tau = 0$ (corresponding to the top of the Hα generating later - or rather the position at which the atmosphere becomes optically thick to Hα), the polarization fraction $P = Q\backslash I$ equals some non-zero value, which we can set depending on the model which we are using - i.e. proton beam, electron mirroring, evaporation (or any other) in either of the MAVL atmospheres. It is necessary also to have an initial distribution of intensities over angle cosine μ'. This is given in Hénoux *et al* (1983) for the Stokes' parameters Q and I. viz

$$I(\mu) = \frac{3I_T(1 - P_{90}\mu^2)}{3 - P_{90}} \qquad 6.6$$

$$Q(\mu) = \frac{3I_T P_{90}(1 - \mu^2)}{3 - P_{90}}$$

and using equations 6.2 we can calculate the angular variation of I_l and I_r at $\tau = 0$. This distribution function must be used in the integral part of equation 6.1, which for each of the two directions becomes

$$I_l; \quad -\frac{9}{8}\frac{I_T}{(3-P_{90})}\int_{-1}^{1}\left[(2(1-\mu^2)(1-\mu'^2)+\mu\mu'^2)(1-P_{90})+\mu^2(1-2P_{90}\mu'^2+P_{90})\right]d\mu' \quad 6.7a$$

$$I_r; \quad -\frac{9}{8}\frac{I_T}{(3-P_{90})}\int_{-1}^{1}\left[\mu'^2(1-P_{90})+(1-2P_{90}\mu'^2+P_{90})\right]d\mu' \quad 6.7b$$

These integrals can be performed analytically, and although the results are complicated, the effect is to turn equation 6.6a into an equation of form

$$\mu\frac{d}{d\tau}I_l(\tau,\mu) = I_l(\tau,\mu) + g(\tau,\mu)$$

where g and I are known at τ_0, providing boundary conditions, allowing the equation to be solved through the atmosphere, at a chosen viewing angle μ . There is of course a similar equation for I_r.

Let us now look briefly at the treatment of resonance fluorescence, which will be important in the optically thick part of the atmosphere. This problem is numerically very complex, and we can only give here theoretical results, and a very brief outline of how the problem might be approached. We are dealing with radiation which is linearly polarized, but the formulation of the equation includes the first circular polarization Stokes' paramter, U. However, all terms involving U will disappear, if we deal always with an atmosphere in which no circular polarization arises in the line - i.e., one which is plane parallel (locally) and in which any magnetic field is symmetric about the axis of the cylindrically symmetric beam diatribution The scattering of radiation occurs in the manner described by the equation

$$\mathbf{I}' = \left(\sigma\frac{d\omega'}{4\pi}\right)\underline{\mathbf{M}}\mathbf{I} \quad 6.8$$

where σ is the absorption cross section for the photon in the 'scattering' atom, $\mathbf{I}, \mathbf{I}'$ are vectors containing the 4 Stokes' parameters (according to Chandrasekhar's definition) of incident and scattered radiation and $\underline{\mathbf{M}}$ is the phase matrix, given by

$$\underline{\mathbf{M}} = \frac{3}{2}E_1\begin{pmatrix}\cos^2\Theta & 0 & 0\\ 0 & 1 & 0\\ 0 & 0 & \cos\Theta\end{pmatrix} + \frac{1}{2}E_2\begin{pmatrix}1 & 1 & 0\\ 1 & 1 & 0\\ 0 & 0 & 0\end{pmatrix} \quad 6.9$$

This is only a three by three matrix - the fourth Stokes' parameter is scattered independently of the others. The angle Θ is the angle between the direction of incident and scattered radiation. The terms E_1 and E_2 are constants depending on the initial value of the angular momentum quantum

number and the change δj of the transition.These have been calculated for certain transitions by Hamilton (1947). Evidently this scattering equation only describes the emission of radiation from one direction into another direction, and it will be necessary at some point to integrate over all directions of incident radiation, as in the case of Thomson scattering. Having found the appropriate scattering term it must now be included in the equation of radiative transfer for a plane parallel atmosphere in which photons are being generated, absorbed and scattered in one region. The general form for this is

$$\frac{-1}{N\sigma}\frac{d\mathrm{I}}{dS} = \mathrm{I} - \mathrm{F} \qquad 6.10$$

where F is the vector source function which encompasses all generation and scattering terms for each of the four Stokes' parameters. Such an equation would have to be solved numerically - a possible approach would be to perform a Monte - Carlo type of treatment, following the progress of individual photons from an appropriate initial angular distribution. But there is no doubt that a full treatment of the transfer of polarized radiation is a large and difficult project and would certainly merit a thesis all of its own.

The effect of Magnetic fields on Linear Polarization.

In the foregoing discussions we have neglected the possible effect of the chromospheric magnetic field on linearly polarized radiation. It will in fact affect both the generation and transfer of polarized radiation through its influence on the particle populations which generate and scatter radiation. The most well known effect that a magnetic field has on polarization is that of Faraday Rotation - the precession of the polarization vector about the magnetic field direction such that a photon of angular frequency ω is rotated by an angle $\Delta\theta$ over a distance d in a medium of electron number density n according to the equation

$$\Delta\theta = \frac{2\pi e^3}{m_e^2 c^2 \omega^4}\int_0^d nB_{\|}dS \qquad 6.11$$

where $B_{\|}$ is the magnetic field component along the line of sight. We will estimate the effect of this. In an atmosphere whose electron density is $\sim 10^{12}$ electrons cm^{-3}, with a magnetic field of $\sim$ 500 Gauss (in the upper part which is Hα optically thin) and an extent of $\sim 10^8$ cm, the rotation of the Hα line (angular frequency 2.9×10^{15} rads s^{-1}) the rotation is $\sim 5.6 \times 10^{-4}$ rads, or 0.03°. This is not enough to account for the variations of tens of degrees which are seen. The answer may lie with the generation of linear polarization, which is also known to be affected by the presence of magnetic fields, through the Hanlé effect (cf Tandberg-Hanssen and Emslie, 1988). In the presence of a magnetic field atoms will precess about the field direction. through the coupling of the total atomic angular momentum to the field. The precession period is given by

$$\omega = \frac{2\pi g_l \mu_B}{h}B \qquad 6.12$$

Where μ_B is the Bohr magneton and g_l is the orbital g factor for the atom. Because the plane of polarization of a photon emitted by an atom depends on the atomic orientation, the precession of the atom results in the precession of the polarization plane of those photons generated when the atom is excited and radiatively de-excites. The precessing atom can be considered as a harmonic oscillator with a damping term which represents the radiative lifetime of the atom. If the oscillator is being forced from the same direction as the field - e.g, by a beam of particles in the field direction, the radiation emitted is strongly polarized with the vector in this direction, as in the field – free case. But if the oscillator is being forced from a direction other than the field direction it is found that when viewed in the field direction the polarization depends on the field. If the radiative lifetime is very long compared to the precession period, the radiation from an atom observed along the magnetic field will be unpolarized since the oscillator describes a symmetric rosette about the field direction. If the precession period is approximately equal to the radiative lifetime then the rosette is asymmetric and the emergent radiation is polarized, but the polarization is reduced relative to the field free case,and the vector is rotated with respect to the direction of the exciting beam. If the precession period is much smaller than the radiative lifetime the atom has hardly any time to precess and the polarization is not very different from the field-free case. This theory has been studied for resonance polarization, where upper level excitation is by a polarized beam, however impact excitation is the same type of process and we would expect similar effects when a magnetic field is introduced in the case of impact polarization. Breit (1925) derived expressions for the change to the polarization magnitude and direction of emitted photons, not specific to any excitation mechanism, when a magnetic field is introduced. If we observe along the magnetic field, a line which, in the field free case is normally polarized by an amount p_o in a field of strength B now has polarization

$$p = \frac{p_o}{1 + (g\Omega_B \tau)^2} \qquad 6.13$$

where g is the Landé g factor for the upper level of the transition and Ω_b is the Larmor precession velocity for the electron. Also in this viewing direction, the angle of rotation of the linear polarization vector from its field-free orientation is

$$\Omega = \frac{1}{2}\tan^{-1}(g\Omega_b \tau) \qquad 6.14$$

For the Hα transition, $\tau = 2.27 \times 10^{-8}$s and $\Omega_B = eB\backslash 2m_e = 2.6 \times 10^{20}$, for a field of 1000 gauss , so the depolarization effect when viewing along the field direction will be severe - p will be practically zero.

What we draw from this discussion is that in the presence of a magnetic field, the polarization which we observe in the field direction depends amongst other things on the direction relative to the field direction from which the atoms have been excited. Although we assume that on a large scale the

beams doing the excitation are guided by the magnetic field in the corona and into the transition region, on the small scale of the turbulent chromosphere, the field direction may vary rapidly from one place to the next, with the result that depolarization may occur at certain positions when viewed from certain directions. Although the large scale coronal field in the form of loops is observed to be more or less perpendicular to the atmosphere, the convergence region (Chapter 3) and the region on the extremities of the loop footpoints need no be so ordered, so the direction of the precession axis and our viewing angle to it is highly position dependent. This provides a possible means of explaining the observed wide variation in the *direction* of the polarization vector. In addition since we in fact observe the combination of polarization components parallel and perpendicular to the direction of the exciting beam and the local field, the reduction in the component viewed in the field direction component could explain the variation in *magnitude* of the polarization fraction. If the Hanlé effect is significant, we might expect some correlation between the polarization magnitude and its direction - for example, low polarization fractions which are the result of viewing at an angle to a strong field would have arbitrary directions - having been rotated by the Hanlé effect. Areas of large polarization, where we view more or less down the local field, have not suffered significantly from depolarization and therefore their direction is preserved and is the same as in the field free situation. A study of such effects must be carried out.

(Note that Thomson scattering in the atmosphere is similarly affected by the presence of a magnetic field. This has been studied recently by Whitney (1991 a,b). Similarly to the Hanlé effect, the magnetic field serves to orientate the electrons with which initially unpolarized photons interact. Whitney studies the transfer of radiation using a Monte-Carlo simulation, following the progress of individual photons through an atmosphere in which scattering from free electrons takes place and finds that at low field strengths and high frequencies (of radiation) the linear polarization resulting from the scattering of initially unpolarized radiation is proportional to $(\omega_c \backslash \omega)^2$ where ω_c is the cyclotron frequency. So when dealing with optical wavelengths, where $\omega \gg \omega_c$ the effect will be very small, except in objects with very strong magnetic fields, eg, neutron stars.)

Time variations in the fraction of all pixels showing a high degree of polarization may have something to with the effects discussed above, since the Hanlé effect is capable of causing depolarization, but we would probably be better rewarded were we to investigate means by which the overall population of the

Extension of the Diagnostic Potential of Imapct radiation to Other Transitions.

Since every line transition, if excited by an anisotropic particle distribution, is polarized to some

extent, it may be possible to use a number of different lines excited during solar flares as beam or flow diagnostics. For example, linear polarization was observed during a flare at a level of 45% in the 1437Å line of silicon (Hénoux et al 1982), and is likely to occur in other lines, although the "efficiency " of generation will depend on the energy of the particles in the beam or flow. The cross section for excitation of a transition by particle impact varies with impact velocity, peaking at around the orbital velocity of the electron in the lower state of the upwards transition. This velocity varies from transition to transition. In a one electron atom the Bohr model predicts that it depends on the atomic number of the atom therefore the excitation cross sections of different atoms peak at quite different velocities. Although hydrogen is by far the most abundant element in the solar atmosphere, and Hα is a strong transition, there must be many other transitions which, if excited by a particle beam, are polarized in emission. It would be interesting, during the occurence of a flare, to investigate the linear polarization of various other atomic emission lines from the chromosphere and also from the corona, including other hydrogen emission lines. The Hβ line in particular should be polarized also since it is the result of excitation to the asymmetric $2p$ upper state, however because it is best excited by particles of the same energy as best excite the Hα transition, we will learn nothing more about the energy spectrum of the exciting distribution. If on the other hand we are able to observe impact polarization in other atomic lines we may be able to say something about the distribution of exciting particles at different energies. A factor of 3 in atomic number means a factor of approximately 10 in the energy at which the excitation cross section peaks, so with studies of polarization in other atomic species present in the solar atmosphere within the optical and UV ranges it may be possible to cover a range of excitation energies. We know that during the impulsive phase of solar flares, beams of some type do occur, whether electron or proton. In chapter 2, the combination of the orientation of the polarization vector and the fact that the beam distribution needed to be maintained throughout the dense chromosphere forced us to consider the proton beam, however the high energy electron beam, the favoured model for the solar flare process, must also inevitably result in impact excitations of atomic line and the presence of this phenomenon in lines of one electron atoms should be searched for. We suggest the study of hydrogen or other species which are in their second highest ionisation state with all but one electron removed, for the simple reason that it is still possible, by treating the atom as a Bohr atom, to calculate excitation cross sections and polarization fractions relatively easily, but since the atomic number is higher, the cross section will peak at energies higher than for the Hα transition. All elements at least up to nickel are visible in the solar spectrum, but the temperature of the corona, 10^7 K, corresponds more or less to the energy at which oxygen is in its penultimate stage of ionisation, so it may be possible to easily calculate expected polarization fractions for elements up to this. Elements with higher atomic numbers will not be in present in their penultimate ionisation states in large abundances, although with suitable data on cross

sections for excitation from lower ionization states we can go much higher in the periodic table. Consider for example the $1s2p - 1s^2$ transition in the 7th ionisation state of oxygen. It has a photon energy of 591 eV, which is in the UV range, and according to the Bohr theory, the orbital kinetic energy of the remaining electron is $\sim$ 6.5 keV. The excitation cross-section would then peak for particle energies of this order but the typical electron energy in the electron beam model is a few hundred keV and the cross section at these energies would still be quite small. If it the electron beam were in the form of a direct untrapped beam, the polarization fraction resulting would be negative - its direction would be perpendicular to the plane containing the beam direction and the line of sight, and would not appear in the beam-centre direction but in the direction of the projection of vector P $\times$ Q on the solar surface, where P is the vector in the beam direction and Q is the vector in the direction of the line of sight. If the more realistic coronal trap model, as investigated in chapter 3, is used, the polarization sign is not so clear cut, but polarization should be present to some extent in many atomic transitions. The potential for diagnostics of particle beam or flow processes at many energies in the solar atmosphere is large.

The possibility of observing line impact polarization in other astrophysical sources.

We have studied already the case of SS433, where is it suspected bullets of material interact with and are heated by a wind of protons from a companion star. In addition to this stellar source there are known to be large number of galactic sources exhibiting jet structures which may interact in a similar manner with the intergalactic medium. Emission from the termination of these jets in the ISM is frequently seen in radio and optical maps of sources and at these points thick - target particle - particle processes must be important. On a smaller scale there are a large number of binary stellar sources with cool interacting winds (Wolf - Rayet stars) and it was recently proposed (Brown, private communication) that the dynamics of the interaction of low energy, low velocity winds might be investigated using impact polarization. Extending to more exotic stellar objects, winds are also observed in pulsar environments (e.g. Tavani (1991)) and some of the scientific debate in this area centres on whether the wind is composed of protons or of electron - positron pairs. The wind is often observed to terminate in an Hα emitting region, probably indicating collional excitation of the interstellar medium. If the wind particle energy and density are known it should be possible to predict the Hα polarization fraction expected from a proton wind, or from an electron - positron wind - the two will be different because the stopping distance is different for the two particle masses (cf equation 5.3 where σ_c changes because of the inclusion or otherwise of the term $m_p \backslash m_e$.) This could, with suitable polarimetric observations go some way to answering the composition problem, which would in turn influence the theory of pulsar environments.

As can be seen there remains a large body of work to be tackled in the solar and in the wider astrophysical context of impact polarization. The phenomenon has certainly not yet benn properly exploited as a diagnostic although recent publications in the subject (e.g., Landi Degl'Innocenti 1992, Fineschi 1993) indicate that perhaps the astrophysical community is waking up to the diagnostic potential realised by Chambe and Hénoux in their paper of 14 years ago. Long may the interest continue.

References

Acton, L. W., Canfield, R. C., Ginkler, T. A., Hudson, S., Kiplinger, A. L., and Leibacher, J. W.: 1982, *Ap.J.* **263**, 409

Alexander, D.: 1990, *Astron.Astrophys.* **235**, 431

Antonucci, E., Dodero, M. A., and Martin, R.: 1990a, *Ap.J.Supp.Ser.* **73**, 137

Antonucci, E., Dodero, M. A., and Martin, R.: 1990b, *Ap.J.Supp.Ser.* **73**, 147

Athay, G. R.: 1985, in P. A. Sturrock, T. E. Holzer, D. M. Mihalas, and R. K. Ulrich (eds.), *Physics of the Sun Vol. II*, Reidel

Athay, R. G.: 1970, *Ap.J.* **161**, 713

Bai, T.: 1982, *Ap.J.* **259**, 341

Bhadra, K. and Ghosh, A. S.: 1971, *Phys.Rev.Lett.* **26**, 737

Brown, Carlaw, V. A., and Icke, V.: 1987, *Ap.Sp.Sci.* **143**, 153

Brown, J. C.: 1971, *Sol.Phys.* **18**, 489

Brown, J. C.: 1973, *Sol.Phys.* **28**, 151

Brown, J. C., Collins, G., and Cassinelli, J. P.: 1991, *Ap.J.* **378**, 307

Brown, J. C., Karlicky, M., MacKinnon, A. L., and van den Oord, G. H. J.: 1990, *Ap.J.Supp.Ser.* **73**, 343

Canfield, R. C. and Gayley, K. G.: 1987, *Ap.J.* **322**, 999

Canfield, R. C., Zarro, D. M., Wülser, J. P., and Dennis, B. R.: 1991, *Ap.J.* **367**, 671

Chambe and Hénoux: 1979, *Astron.Astrophys.* **80**, 123

Chandrasekhar, S.: 1961, in *Hydrodynamic and Hydromagnetic Stability*, Clarendon

Clark, D.: 1985, in *The Quest for SS433*, Hilger

Davidson, K. and McCray, R.: 1980, *Ap.J.* **241**, 1082

de Jager, C.: 1986, *Astron.Astrophys.* **156**, 95

de Jager, C. and Neven, L.: 1960, *Bull.Ast.Inst.Netherlands* **15**, 55

Doschek, G. A., Feldman, U., Kreplin, R. W., and Cohen, L.: 1980, *Ap.J.* **239**, 725

Doyle, J. G. and Bentley, R. D.: 1986, *Astron.Astrophys.* **155**, 278

Dulk, G. A. and MacLean, I. S.: 1978, *Sol.Phys.* **57**, 279

Durrant, C. J.: 1988, in *Atmosphere of the Sun*, Adam Hilger

Emslie, A. G.: 1978, *Ap.J.* **224**, 241

Emslie, A. G. and Alexander, D.: 1987, *Sol.Phys.* **110**, 295

Emslie, A. G. and Brown, J. C.: 1985, *Ap.J.* **295**, 648

Fineschi, S., Fontenla, J. M., MacNeice, P., and Ljepojevic, N. N.: 1991, in R. M. Winglee and B. R. Dennis (eds.), *Max '91 /SMM Solar Flares: Observations and Theory.*

Fisher, G. H. et al.: 1985, *Ap.J.* **289**, 414

Fox, G. K.: 1993, *M.N.R.A.S* **260**, 513

Franco, V. and Thomas, B. K.: 1971, *Phys.Rev.A* **4**, 945

Gabriel, A.: 1992, in J. T. Schmeltz and J. C. Brown (eds.), *The Sun - a laboratory for Astrophysics. NATO ASI no C373*, Kluwer

Gardiner, C. W.: 1985, in H. Haken (ed.), *Handbook of Stochastic Methods*, Berlin

Giampapa, M. S., Worden, S. P., and Linsky, J. L.: 1982, *Ap.J.* **258**, 740

Gull, S. F.: 1973, *M.N.R.A.S* **161**, 47

Gull, S. F.: 1975, *M.N.R.A.S* **171**, 263

Hagyard, M. J.: 1984, *Sol.Phys.* **84**, 13

Haisch, B., Strong, K. T., and Rodonò, M.: 1991, *Astron.Astrophys.*

Hamilton, R. J., Lu, E. T., and Petrosian, V.: 1990, *Ap.J.* **354**, 726

Hénoux, J. C.: 1986, in E. Stepanov and V. M. Odbriko (eds.), *Solar Maximum Analysis*, VNU Science Press

Hénoux, J. C.: 1990, *preprint*

Hénoux, J. C., Chambe, G., Semel, M., Sahal-Bréchot, S., Woodgate, B., Shine, D., Beckers, J., and Machado, M.: 1983a, *Ap.J.* **265**, 1066

Hénoux, J. C., Heritschi, D., Chambe, G., Machado, M., Woodgate, B., Shine, R., and Beckers, J.: 1983b, *Astron.Astrophys.* **119**, 223

Heritschi, D.: 1986, *Ap.J.* **311**, 474

Heyvaerts, J. H.: 1980, in E. R. Priest (ed.), *Solar Flare Magnetohydrodynamics*, Gordon and Breach

Heyvaerts, J. H., Priest, E. R., and Rust, D. M.: 1977, *Ap.J.* **216**, 123

Hippler, R., Madeheim, H., Harbich, W., Kleinpoppen, H., and Lutz, H. O.: 1988, *Phys.Rev.A* **38**, 1662

Holman, G.: 1985, *Ap.J.* **293**, 584

Hoyng, P., Brown, J. C., and van Beek, H. F.: 1976, *Sol.Phys.* **48**, 197

Hurford, G.: 1992, in J. T. Schmeltz and J. C. Brown (eds.), *The Sun - A Laboratory for Astrophysics. NATO ASI no C373*, Kluwer

Inokuti, M.: 1971, *Rev.Mod.Phys.* **43**, 297

Kane, S. R.: 1974, in G. Newkirk (ed.), *I.A.U. Symposium 57*

Kaupilla, W. E.: 1970, *Phys.Rev.A* **2**, 1759

Keller, C. U., Solanki, S. K., Tarbel, T. D., Title, A. M., and Stenflo, J. O.: 1990, *Astron.Astrophys.* **236**, 250

Khandewal, G. S. and Choi, B. H.: 1968a, *J.Phys.B.* **1**, 1218

Khandewal, G. S. and Choi, B. H.: 1968b, *J.Phys.B.* **1**, 1220

Kovalev, V. A. and Korolev, O. S.: 1981, *Sov.Astron.* **25**, 215

Krolik, J. H. and McKee, C. F.: 1987, *Ap.J.Supp.Ser.* **37**, 459

Li, P., Emslie, A. G., and Mariska, J. T.: 1989, *Ap.J.* **341**, 1075

Lin, R. P. and Hudson, H. S.: 1976, *Sol.Phys.* **50**, 153

Lüdde, H. J. and Dreizler, R. M.: 1982, *J.Phys.B* **15**, 2703

Machado, M.: 1985, *Sol.Phys.* **99**, 819

Machado, M., Avrett, E. H., Vernazza, J. E., and Noyes, R. W.: 1980, *Ap.J.* **242**, 336

MacKinnon, A. L.: 1989, **226**, 284

MacKinnon, A. L.: 1991a, *Astron.Astrophys.* **242**, 256

MacKinnon, A. L.: 1991b, *Astron.Astrophys.* **242**, 256

MacKinnon, A. L. and Brown, J. C.: 1989a, *Astron.Astrophys.* **215**, 371

MacKinnon, A. L. and Brown, J. C.: 1989b, *Astron.Astrophys.* **215**, 371

MacKinnon, A. L. and Brown, J. C.: 1990, *Astron.Astrophys.* **232**, 544

MacKinnon, A. L., Brown, J. C., and Hayward, J.: 1985, *Sol.Phys.* **99**, 231

MacKinnon, A. L. and Craig, I. J. D.: 1991, *Astron.Astrophys.* **251**, 693

Mahan, A. H., Gallacher, A., and Smith, S. J.: 1976, *Phys.Rev.A* **13**, 156

Margon, B.: 1984, *Ann.Rev.Ast.Astroph* **22**, 507

McClements, K. G.: 1990a, *Astron.Astrophys.* **230**, 213

McClements, K. G.: 1990b, *Astron.Astrophys.* **234**, 487

McConkey, J. W.: 1988, *J.Phys.B.* **21**, L317

McFarlane, S. C.: 1974, *J.Phys.B.* **7**, 1756

Melrose, D. B. and Brown, J. C.: 1976, *M.N.R.A.S.* **176**, 15

Metcalf, T., Canfield, R., and Wuesler: 1991, *preprint*

Mihalas, D.: 1978, in *Stellar Atmospheres*, Freeman Press

Moisewitch, B. L. and Smith, S. J.: 1968, *Rev.Mod.Phys* **40**, 238

Mott, N. F. and Massey, H. S. W.: 1965, *The Theory of Atomic Collisions*, Oxford University Press

Nagai, F. and Emslie, A. G.: 1983, *Ap.J.* **279**, 898

Osterbrock, D. E.: 1974, in *Astrophysics of Gaseous Nebulae*, San Fransisco

Park, J. T., George, J. M., and Peacher, J. L.: 1976, *Phys.Rev.A* **14**, 608

Percival, I. C. and Seaton, M. J.: 1958, *Phil. Trans. R. Soc.* **251**, 113

Peterson, L. E. and Winckler, J. R.: 1959, *J. Geophys. Res.* **64**, 697

Ramaty, R. and Murphy, R. J.: 1987, *Sp.Sci.Revs.* **45**, 213

Rees, D.: 1987, in W. Kalkoven (ed.), *Numerical Radiative Transfer*, Cambridge University Press

Schmieder, B., Forbes, T. G., Malherbe, J. M., and Machado, M. A.: 1987, *Ap.J.* **317**, 956

Shah, M. B. and Gilbody, H. B.: 1981, *J.Phys.B* **14**, 2361

Simnett, G. M.: 1986, *Sol.Phys.* **106**, 165

Simnett, G. M. and Strong, K. T.: 1984, *Ap.J.* **284**, 839

Smith, D. F., Chambe, G., Hénoux, J. C., and Tamres, D.: 1990, *Ap.J.* **358**, 674

Solanki, S. K. and Steiner, O.: 1990, *Astron.Astrophys.* **234**, 519

Spitzer, L.: 1962, in *The Physics of Fully Ionised Gases*, John Wiley

Sturrock, P. A.: 1968, in P. A. Sturrock, T. E. Holzer, D. M. Mihalas, and R. K. Ulrich (eds.), *Physics of the Sun vol II*

Svetska, Z.: 1976, in *Solar Flares*, Reidel

Syms, R. F., Dowell, M. R. C. M., Morgan, L. A., and Myerscough, V. P.: 1975, *J.Phys.B* **8**, 2817

Takakura: 1972, *Ap.J.* **00**, 0

Tamres, Canfield, R. C., and McClymont, A. N.: 1986, *Ap.J.* **309**, 409

Tandberg-Hanssen, E. and Emslie, A. G.: 1988, in *The Physics of Solar Flares*, Cambridge

Thomas and Athay: 1961, in *Physics of the Solar Chromosphere*, Interscience

Tsuneta, S., Takakura, T., Nitta, N., Okhi, K., Tanaka, K., Makishima, K.,

Marakami, T., Oda, M., Ogawara, W., and Kondo, I.: 1984, *Ap.J.* **280**, 887

Vainshtein, L. A.: 1961, *Opt.Spectrosc.(USSR)* **11**, 163

Vainshtein, L. A.: 1965, *Opt.Spectrosc.(USSR)* **18**, 538

van den Bergh, J. et al.: 1973, *Ap.J.* **227**, 26

van den Oord, G. H. J.: 1988, *Astron.Astrophys.* **207**, 101

Vernazza, J. E., Avrett, E. H., and Loeser, R.: 1988, *Ap.J.Supp.Ser.* **45**, 635

Vilmer, N., Kane, S. R., and Trottet, G.: 1982, *Astron.Astrophys.* **108**, 306

Vilmer, N., Trottet, G., and MacKinnon, A. L.: 1986, *Astron.Astrophys.* **156**, 64

Volwerk, M.: 1993, *J. Phys. Res.* submitted

Winglee, R., Pritchett, D. L., and Dulk, G. A.: 1988, *Ap.J.* **329**, 440

Wood, K. H., Brown, J. C., and Fox, G. K.: 1993, *Astron.Astrophys.* in press

Zarro, D. M. and Canfield, R. C.: 1989, *Ap.J.* **338**, L33

Zarro, D. M. and Lemen, J. R.: 1988, *Ap.J.* **329**, 456

Zwitter et al.: 1900, *Ap.J.* **0**, 0

Zwitter, T.: 1989, *Fundamentals of Cosmic Physics* **13**, 309